Experimental extrusion of tubular multilayer materials for Oxygen Transport Membranes

Kothanda Ramachandran, Dhavanesan

Publication date:
2014

Document Version
Publisher's PDF, also known as Version of record

PhD thesis:

Experimental extrusion of tubular multilayer materials for Oxygen Transport Membranes

PhD Thesis:

Experimental extrusion of tubular multilayer materials for Oxygen Transport Membranes

2014

By

Dhavanesan Kothanda Ramachandran

Supervisor: Dr. Andreas Kaiser, Senior Scientist, DTU Energy Conversion and Storage, Denmark.

Co-supervisor: Dr. Martin Søgaard, Senior Scientist, DTU Energy Conversion and Storage, Denmark.
Dr. Julie Glasscock, Scientist, DTU Energy Conversion and Storage, Denmark.
Dr. Frank Clemens, Group leader, Laboratory of high, EMPA, Switzerland.

Thesis examiners: Dr. Jean-Claude Grivel, Senior Scientist, DTU Energy Conversion and Storage, Denmark.
Dr. Farid Akhtar Associate Professor, Luleå University of Technology, Sweden.
Dr. Thomas Steenberg, CTO, Danish Power Systems, Denmark.

Financial support: OPTIMAC (No. 09 – 072888)

Published by: Department of DTU Energy Conversion and Storage, Risø campus, Roskilde, Denmark

Request report from: www.ecs.dtu.dk

ISBN: [978-87-92986-27-6] (electronic version)

Abstract

Inorganic oxygen transport membranes (OTMs) are of interest for high purity oxygen production and for integration into membrane reactors where oxygen is required at high temperatures. Doped ceria is an interesting material for an OTM due to its high phase stability under both oxidizing and reducing atmospheres and its high ionic conductivity. Designing and developing a high performance oxygen transport membrane involves scientific challenges associated with material development, ceramic processing and integration of materials in a multi-layer structure. In this work an asymmetric based oxygen transport membrane based on gadolinia doped ceria oxide, ($Ce_{0.9}Gd_{0.1}O_{1.95-\delta}$), (CGO) was developed on a tubular, porous support structure based on cost-efficient magnesium oxide (MgO). The porous support structure was prepared by thermoplastic extrusion using MgO powder, thermoplastic binders and graphite pore former. An optimization of the thermoplastic feedstock has been carried out with the aim of improving gas permeability and mechanical properties of the resulting MgO supports. The influence of three types of pore former (graphite with different shapes and sizes, and polymethyl methacrylate (PMMA)) on the mechanical strength and gas permeation of the extruded MgO porous supports was investigated for sintering temperatures between 1250 and 1400 °C. The gas permeability through the MgO supports during membrane operation was highly dependent on the total open porosity and on the size of pore necks. As expected, for all samples with different pore former type the permeability decreased with sintering temperature and decreasing total porosity. Only for the porous support prepared with flaky graphite did the total porosity and gas permeability increase with increasing sintering temperatures above 1300 °C. Scanning electron microscopy showed that for samples sintered above 1300 °C there was a growth of macro-pores and opening of bottle-neck pores, resulting in improved pore connectivity and thus improved gas permeability. Mercury intrusion porosimetry experiments confirmed an increase in the average pore size for samples sintered above 1300 °C, despite a significant decrease in total porosity.

The highest open porosity of 42.5 % and gas permeability of 4.7×10^{-16} m^2 was obtained for an MgO support with spherical graphite as a pore former. Implementing a bimodal pore size distribution (by using a mixture of two pore formers with an average size of 5.5 and 10.5 µm) it seems feasible to increase the gas permeation value to 4×10^{-15} m^2 and this route is also recommended for further studies. The characteristic strength of the MgO supports was characterized by Weibull measurements with a novel high temperature 4-point bending test method. The results revealed sufficiently high bending strength values of 60 MPa for the MgO support at an operation temperature of 850 °C, whereas the strength at room temperature was

77 MPa. The oxygen permeation flux on an asymmetric tubular CGO membrane, consisting of an MgO support (porous), catalytic layer on permeate side (NiO-CGO) (porous), CGO (dense), catalytic layer on feed side (porous, infiltrated nano LSC ($La_{0.6}Sr_{0.4}CoO_{3-\delta}$) particles on a porous CGO backbone layer), was tested at temperatures between 650 °C and 920 °C on a 30 mm long tube (inner/outer diameter of 9.8/11.4 mm) using atmospheric air and N_2, H_2 for feed and sweep side respectively. The oxygen permeation was 3.5 Nml min^{-1} cm^{-2} at 856 °C using a H_2 flow of 200 Nml min^{-1} on the permeate side. After subsequent oxidation and reduction (redox-cycle) of the Ni-CGO catalytic layer in the membrane, the permeation flux of the membrane improved significantly especially at low temperatures, reaching 4 Nml min^{-1} cm^2 at 850 °C. The improved performance is attributed to an improvement of the catalytic activity of the Ni-CGO structure after a redox-cycle. Finally, oxygen permeation tests on the asymmetric CGO membrane in methane/humidified hydrogen mixtures were performed which led to breaking of the membrane. Post-mortem analysis of the membrane microstructure by scanning electron microscopy (SEM) after the oxygen permeation test in methane indicated detachment of the catalytic layer on the permeate side, most likely due to carbon formation.

Resumé

En uorganiske iltseparationsmembran (eng. Oxygen Transport Membraner, OTM) kan anvendes til fremstilling af ren ilt samt til indbygning i membranreaktorer, hvor højtemperatur ilt er påkrævet. Doteret ceria er et muligt materiale som iltseparationsmembran, da det udviser stor kemisk stabilitet i både reducerende og oxiderende atmosfærer, og det samtidig har en høj ionledningsevne. Udviklingen af en højtydende OTM giver anledning til en række udfordringer indenfor materialeudvikling, keramisk fremstilling og integration af materialer i en multilagsstruktur. I nærværende projekt er der blevet fremstillet en tynd film OTM baseret på gadolinia doteret ceria ($Ce_{0,9}Gd_{0,1}O_{1.95-\delta}$, CGO) supporteret på et bærelag af en rørformig porøs struktur af magnesiumoxid (MgO). Den porøse bærestruktur er blevet fremstillet ved anvendelse af termoplastisk ekstrudering af en blanding af MgO, termoplastiske bindere samt grafit poredannere. I projektet er der blevet udført en optimering af den termoplastiske råmasse med det formål at optimere gaspermeabiliteten samt den mekaniske styrke af de porøse bærelag. Tre forskellige poredanner (grafit med forskellige former og størrelser samt polymethyl methacrylat (PMMA)) er blev testet, og deres betydning for den mekaniske styrke samt gas permeabiliteten af ekstruderede rør er blevet kvantificeret, hvor sintringstemperaturen af de ekstruderede komponenter har været mellem 1250 °C og 1400 °C. Det er blevet fundet, at gaspermeabiliteten for de forskellige fremstillet support afhænger af tilstedeværelsen af åben porøsitet samt størrelsen af kontaktarealet mellem to porer. Som forventet mindskedes gaspermeabiliteten samt porøsiteten for alle de undersøgte prøver med stigende sintringstemperatur. For det porøse bærelag, hvor der under fremstillingen blev anvendt grafit bestående af flager, blev det fundet, at gaspermeabiliteten øgedes med stigende sintringstemperatur. Skanning elektron mikroskopi viste, at store porer voksede og samtidig blev pore-pore halsen større, hvilket gav anledning til forbedret pore-pore kontakt samt gaspermeabilitet. Kviksølv porosimetry målinger bekræftede en forøgelse af porestørrelsen for prøver sintret ved mere end 1300 °C selvom den totale porøsitet mindskedes.

Den højeste åbne porøsitet (42,5 %) og højeste gas permeabilitet (4,7 $\times 10^{-16}$ m^2) af de fremstillede prøver blev opnået ved anvendelse af sfærisk grafit som poredanner.Ved at implementere en bimodal pore størrelsesdistribution (der blev anvendt to poredannere med en gennemsnitlig størrelse på 5,5 og 10,5 µm) kan gas permeabiliteten forøges med minimum en størrelsesorden. Den karakteristiske Weibull styrke og modulus blev også målt af de fremstillede support strukturer ved både stue- og højtemperatur i en 4 punkts

bøjemålinggeometri. Den karakteristiske Weibull styrke af supportstrukturerne blev målt til 60 MPa ved 850 °C, mens den ved stuetemperatur var 77 MPa.

I projektet er der blevet fremstillet en asymmetrisk membran bestående af et MgO support (porøst), katalytisk lag af NiO-CGO (porøst), CGO membran (tæt) og et porøst CGO lag, der efterfølgende blev infiltreret med den nominelle sammensætning $La_{0.6}Sr_{0.4}CoO_{3-\delta}$. Et 30 mm langt stykke af denne membran (indre/ydre diameter 9.8/11.4 mm) er blevet testet mellem 650 °C og 920 °C, hvor der er anvendt luft på fødesiden og N_2,H_2 og CH_4 på permeatsiden. Ilfluksen blev målt til 3.5 Nml min^{-1} cm^{-2} ved 856 °C, hvor der blev anvendt ren brint på permeatsiden. Efter en redox-cyclus, hvor membranen blev udsat for luft på begge sider og Ni dermed blev oxideret til NiO og efterfølgende reduceret igen til Ni, steg den målte iltfluks betydeligt ved især lavere temperatur. Dette er tilordnet til en forøgelse af Ni-arealet i det katalytiske lag. Til sidst i eksperimentet blev CH_4 og befugtet brint tilledt på permeatsiden af membranen, hvilket resulterede i at membranen fejlede. Efterfølgende SEM analyser indikerede at membranen var blevet adskilt fra selve supportstrukturen, hvilket muligvis skyldtes kulstofdannelse.

Preface

This work has been carried out at the Department of Energy Conversion and Storage, Technical University of Denmark (DTU), during the period 2011-2014. This project is part of a larger project called "Optimized Processing of Multi-material Architectures for functional Ceramics or OPTIMAC". The project was funded by the Danish Agency for Science, Technology and Innovation (FTP) (Contract No. 09 - 072888), which is a part of the Danish Council for Independent Research (DFF). OPTIMAC consists of three work packages (WPs) and this study is one of the sub projects i.e. SP-7 under WP-3, which focuses on developing tubular multilayer materials for oxygen transport membranes. The study has been supervised by Andreas Kaiser (Senior scientist), and co-supervised by Martin Søgaard (Senior scientist), Frank Clemens (Group leader, EMPA), Julie Glasscock (Scientist) and Marie Wandel (Senior scientist).

Working in a field of ceramic multilayered materials for developing an oxygen transport membranes is a splendid opportunity to discover my inner self and potential to bring things to its realization. My research would not have seen the light of the day if I had not received help and support of staffs and scholars of DTU at various levels of my research journey. No mere words of customary thanks are sufficient to recognize their contribution in my work and I pay my sincere thanks from the core of my heart as I am deeply moved by the ambience of DTU.

I am beholden to Dr. Andreas Kaiser for his unrivalled knowledge, constant guidance and kind support. I take this opportunity to express my deep sense of respect and personal gratitude to my supervisor Dr. Andreas Kaiser for his generous help and never-failing encouragement.

In the course of my research I received immense support and help from my co-supervisors Dr. Martin Søgaard, Dr. Julie Glasscock, Dr. Frank Clemens and Dr. Marie Wandel, whose inspiring guidance and valuable suggestions protected me from falling into unexpected errors for which I am eternally indebted to them.

Doing research at DTU is a pleasant experience and I richly benefitted by the support of the research members. I express my sincere and respectful thanks to Prof. Nini Pryds, and Dr. Severine Ramousse, for providing me an opportunity to work with the OPTIMAC project. It is a huge pleasure to give my sincere

thanks to Pernille Hedemark Nielsen for the extrusion experiments and preparation of SEM sample. I am also thankful to Marianne Nielsen for providing mercury porosimetry measurements.

I take this opportunity to express my sense of appreciation for all members in OPTIMAC project. Dr. De Wei Ni, Tesfaye Tadesse Molla, Raphaël Comminal and Dr. Vincenzo Esposito deserve special mention for their commitment. No amount of thanks shall be enough for the membrane group members and DTU colleagues; Prof. Peter Vang Hendriksen, Shiyang Chen, Dr. Jonas Gurauskis, Dr. Kawai Kwok, Dr. Bhaskar Sudireddy, Dr. Simona Ovtar and Dr. Alfred Junio Samson with whom I have enjoyed interacting with and received their help at various stages of my research work. I gratefully acknowledge the help from Dr. Astri Bjørnetun Haugen who devoted her time to proof-reading and correcting the entire thesis document.

I also want to extend my appreciation to my officemates at DTU. The moments I have spent with them and the interesting discussions we used to have will always remind me of my stay at DTU. My special thanks are due to all scientists and technical staff of Department of Energy conversion and Storage who helped me directly or indirectly with my research work.

Last but not the least, I am personally indebted to my beloved family members for their affection, cohesive help and support provided by them throughout, as always, for which my mere expression of thanks will not sufficient.

Place : Roskilde

Date : 28/08/2014

(Dhavanesan Kothanda Ramachandran)

List of publications

I. "Tailoring the microstructure of porous MgO supports for asymmetric oxygen separation membranes: Optimization of thermoplastic feedstock systems", **D. K. Ramachandran,** F. Clemens, J. A. Glasscock, M. Søgaard and A. Kaiser.

II. "The role of sacrificial fugitives in thermoplastic extrusion feedstocks on properties of MgO supports for oxygen transport membranes", **D. K. Ramachandran,** K.Kawai, M. Søgaard, F. Clemens, J. A. Glasscock and A. Kaiser.

III. "Low cost porous MgO substrates for oxygen transport membranes", **D. K. Ramachandran**, M. Søgaard, F. Clemens, B. R. Sudireddy and A. Kaiser.

IV. "Modeling constrained sintering of bi-layered tubular samples", TT Molla, **D. K. Ramachandran**, R. Bjørk, N. Pryds, A. Kaiser and Hl. Frandsen.

V. "Tubular multilayer fabrication and performance of a doped ceria oxygen membrane on a low cost MgO support", **D. K. Ramachandran**, M. Søgaard, F. Clemens and A. Kaiser.

The author's contributions

In **publication I,** the author was mainly responsible for carrying out the experimental work and data analysis, and for writing the manuscript.

In **publication II,** the author was mainly responsible for carrying out the experimental work and data analysis, and for writing the manuscript. K. Kawai was mainly responsible for mechanical testing and characterization of MgO supports.

In **publication III**, the author was mainly responsible for carrying out the experimental work and data analysis, and for writing the manuscript.

In **joint publication IV,** the author was mainly responsible for carrying out the experimental work to model the stresses developed during constrained sintering on tubular membranes by TT Molla. The experimental description and results were supplied by the author to TT Molla who wrote the complete manuscript.

In **publication V,** the author was mainly responsible for carrying out the experimental work and data analysis, and for writing the manuscript. M. Søgaard was responsible for the membrane flux measurement and data analysis.

List of abbreviations

BCFN	$BaCo_yFe_xNb_{1-y-x}O_{3-\delta}$
BSCF	$Ba_xSr_{1-x}Co_yFe_{1-y}O_{3-\delta}$
CCS	Carbon Capture and Storage or Carbon Capture and Sequestration
CGO	$Ce_{0.9}Gd_{0.1}O_{1.95-\delta}$
CGO-M	CGO Membrane layer
CGO-P	CGO Porous layer
DTA	Differential Thermal Analysis
FCC	Face centered cubic
GPa	Giga Pascal
kJ	Kilo joule
KN	Kilo newton
kPa	Kilo Pascal
kWh	Kilo Watt hour
LSC	$La_xSr_{1-x}CoO_{3-\delta}$
LSCF	$La_xSr_{1-x}Co_yFe_{1-y}O_{3-\delta}$
LSFG	$La_xSr_{1-x}Fe_yGa_{1-y}O_{3-\delta}$
LSFN	$La_xSr_{1-x}Fe_yNb_{1-y}O_{3-\delta}$
MgO	Magnesium oxide
MgO-S	MgO support layer
MIEC	Mixed-Ionic-Electronic conductor
MPa	Mega Pascal
mPa	Milli Pascal
MP-FL	Magnesium oxide thermoplastic feedstock with flaky graphite as a pore former
MP-PM	Magnesium oxide thermoplatstic feedstock with PMMA as a pore former
MP-SP	Magnesium oxide thermoplastic feedstock with spherical graphite as a pore former
Nm	Newton meter

Nml	Normal milliliter
OTM	Oxygen Transport Membrane
PMMA	Polymethyl methacrylate
pO_2	Oxygen partial pressure
POM	Partial Oxidation of Methane
PSA	Pressure swing absorption
PSD	Patricle size distribution
PVB	Polyvinylbutyral
PVP	Polyvinylpyrrolidone
RPM	Rotation per minute
SCF	$Sr_xCo_yFe_{1-y}O_{3-\delta}$
SCFZ	$SrCo_yFe_xZr_{1-y-x}O_{3-\delta}$
SEM	Scanning Electron Microscopy
SOFC	Solid oxide fuel cell
STP	Standard Temperature and Pressure
TEC	Thermal Expansion Coefficeint
TGA	Thermo gravimetric analysis
vol.%	Volume percentage
WIP	work in progress
wt.%	Weight percentage
ΔP	Pressure difference
µm	Micrometer

List of figures

List of tables

Index

1. Introduction

Carbon dioxide (CO_2) is a greenhouse gas which is largely emitted from chemical, power generation and cement industries that pollutes the environment. Carbon capture and storage (CCS) is one approach for reducing CO_2 emissions in an attempt to overcome current global warming issues. Power plants can be made more efficient and cleaner by combusting the coal using pure oxygen (oxy-fuel) instead of air [2,3]. Practically, pure oxygen is conventionally produced by cryogenic distillation in large scale or by pressure swing adsorption in small scale [4]. However, cryogenic distillation is a very energy consuming process which consumes an energy of approximately 200 - 240 kWh per ton O_2 with the highest energy penalty for integration into high temperature processes. Oxygen transport membranes are a promising alternative for integration in high temperature combustion processes due to their high selectivity for oxygen and significantly lower efficiency losses [5].

Cement production contributes approximately 5 % of the global CO_2 emissions (ref **Fig. 1**). One of the most appropriate concepts to reduce the CO_2 emissions from such point sources is the oxy-fuel combustion. The use of oxygen transport membranes to provide oxygen for different industries i.e. steel, cement and syngas production, can improve the energy efficiency in the production cycle and further in some cases facilitate an easier CO_2 capture and sequestration. For the CO_2 capture and sequestration it is highly advantageous if the flue gas contains only CO_2, H_2O (and impurities) and only little N_2 as the complex N_2/CO_2 separation is avoided and also the flue gas (CO_2) is much more applicable in schemes for recycling/reusing.

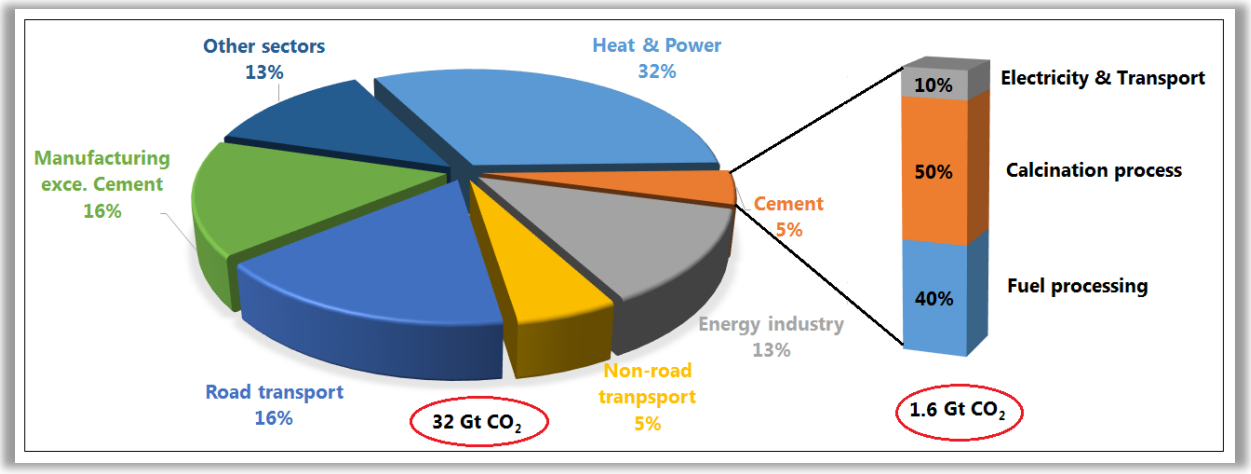

Fig. 1: Global CO_2 emission (source: www.WBCSD.org)

An Oxygen Transport Membrane is a gas-tight component permeable only to oxygen, giving 100 % theoretical selectivity. Use of such membranes can improve the energy efficiency of power generation from biomass gasification and reduce costs of CO_2 neutral transportation fuels made from biomass. The development of such membranes for these applications have been researched extensively in recent years to design high performance membrane modules [6] with utilization of ion conducting materials. Ion conducing ceramic membrane materials have certain advantages over polymeric materials such as high chemical and thermal resistance, mechanical stability at harsh environments and higher permeability. The main disadvantages of ceramic membranes are high raw material and manufacturing costs.

As a consequence, perovskite and fluorite structured ceramic membrane materials have been studied rigorously with a wide range of membrane thicknesses (50 to 2000 µm) and different configurations [7]. According to the Wagner equation, the oxygen flux of membrane can be increased by decreasing the thickness of the membranes [7]. In order to achieve fluxes that are of commercial interest for most of the large scale applications, it is clear that thin film membranes with thicknesses below <100 µm must be prepared. To produce such thin membrane and to improve mechanical stability, using a asymmetric membrane in which a thin membrane layer supported by thick porous layer would be an ideal solution [8]. Hence, the research and development of asymmetric configuration of mixed-ionic-electronic conducting (MIEC) membranes has been increased recently. However, there are many challenges associated with membrane preparation which needs to be fully addressed in order to get a functional membrane. The chemical and thermal behavior between the membrane and porous supports layer should be compatible with each other. Furthermore, the porous layer should be capable of supporting the membrane layer mechanically with sufficient gas permeability [9]. Also, compared to the membrane and catalytic layers that typically have thicknesses in the 10-30 µm range, the porous support structure will have a thickness in the range 500 – 1000 µm and thus constitute the majority of the component. It is thus clear that a low-cost material should be chosen for the support structure to compensate the membrane cost and ease commercialization.

This work describes the preparation and characterization of asymmetric, tubular thin film oxygen membranes for potential use in oxy-fuel combustion or syngas application, consisting of a mixed conducting fluorite structure, cerium gadolinium oxide (CGO $=Ce_{0.9}Gd_{0.1}O_{1.95-\delta}$), supported on a tubular, low cost porous magnesium oxide (MgO) substrate. Up-scalable laboratory fabrication processes, such as extrusion, dip-coating and co-firing of the ceramic layers were used for the preparation and demonstration

of asymmetric oxygen transport membranes, based on MgO supports, catalytic layers and a CGO membrane.

2. Background

Pure-oxygen conducting membranes and mixed ionic–electronic conducting (MIEC) membranes are the two types of ceramic membranes that can transport oxygen ions through the structure. For oxygen-ion conducting membranes, an external electric circuit needs to be connected to the membrane in order to transport oxygen ions across the membrane. In MIEC membranes the charge compensating electron transfer is done internally through the membrane layer. For both cases a chemical potential gradient is required as driving force for the flow of oxygen ions across the membrane. In other words, an oxygen partial pressure gradient across the oxide ceramic membrane at elevated temperatures causes the oxygen ion transport from one side to another side (high pO_2 to low pO_2) by diffusion through oxygen vacancies, maintaining the overall electrical charge neutrality [1,10–25].

2.1. Membrane materials

Fluorite and perovskite type oxides have been most widely used and investigated for MIEC membranes in different oxygen separation applications [7,11]. The perovskite structure (ABO_3) consists of the A-cation placed at the body center position (½, ½, ½) and the B-cation placed at cube corner position (0, 0, 0) and the anion is located in the face centered positions (½, ½, 0). An example for ideal perovskite structure is $SrTiO_3$. The transport of oxygen ions occurs by diffusion through oxygen vacancies in this crystal structure. The fluorite structure (ABO_2) comprises a face-centered cubic (fcc) packing, in which all cations are placed at the body center positions and only half of the anion sites are filled at the cubic corner, which leads to a high oxygen deficiency in the fluorite structure [7,11]. **Fig. 2** schematically presents the ideal crystal structure and diffusion paths of an oxygen ion for the fluorite structured material in (a) and (b), and the perovskite structured material in (c) and (d). More recently, dual-phase ceramic membrane materials have been investigated consisting of one phase which is responsible for oxygen ion transport and the other phase for electronic transport [26]. In some cases, dual-phase ceramic membranes can also be considered in order to improve the mechanical and chemical stability of membrane, which is difficult to achieve by one single-phase membrane [27].

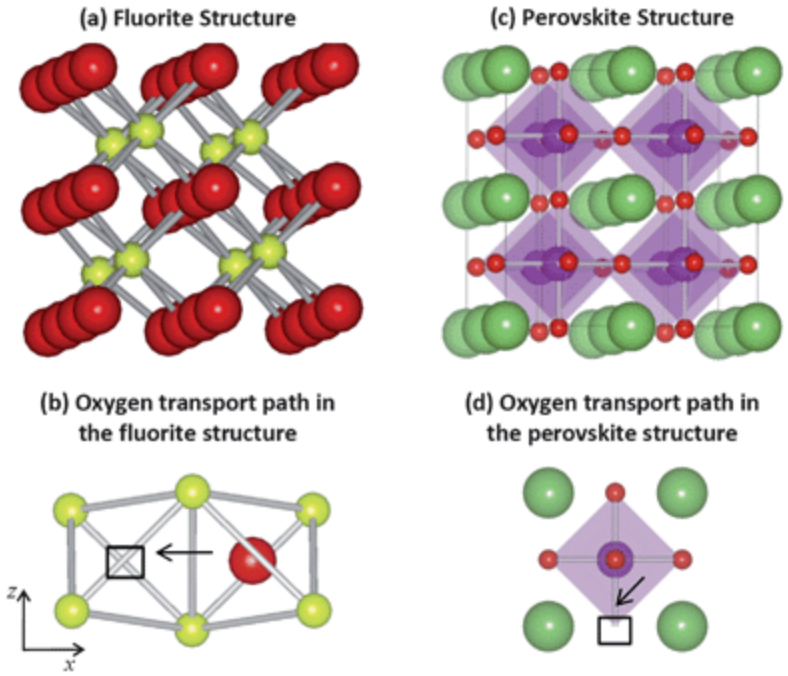

Fig. 2: Crystal structure and oxygen ion diffusion path in the fluorite structure (a and b), and in the perovskite structure (c and d), [28].

2.1.1. Asymmetric MIEC membranes

An asymmetric membrane configuration consists of a multilayer system in which a thin membrane layer is mechanically supported by a macro-porous layer. In order to have a successful asymmetric membrane, the support layer has to fulfill the following requirements, regardless of which fabrication technique is used [9].

- Mechanically stable at membrane application temperature;
- Thermally compatible, i.e. comparable thermal expansion coefficient (TEC) to membrane layer materials;
- Chemically stable during fabrication (sintering) and membrane application temperature and atmosphere;
- High gas permeability (sufficient gas supply to membrane reaction site)

In the asymmetric configuration, the high membrane performance (oxygen flux) can easily be achieved by reducing the thickness below the characteristic thickness [24,29], such that bulk diffusion never becomes the rate limiting step. As stated earlier, the oxygen permeation flux is inversely proportional to the membrane thickness when the oxygen transfer is limited by bulk diffusion, as demonstrated by the following equation:

$$J_{O2} = \frac{RT\sigma i.\sigma e}{16F^2 L(\sigma i+\sigma e)} \ln \frac{pO_2,high}{pO_2,low} \quad (1)$$

where J_{O2} is the oxygen permeation flux; R, the gas constant; T, the temperature; σi and σe are the ionic and electronic conductivity respectively; F, the Faraday constant; L, the membrane thickness and pO_2,high and pO_2,low are oxygen partial pressures at oxygen feed side and sweep side, respectively.

Oxygen transport membranes (OTMs) are an interesting new technology for the separation of oxygen from atmospheric air. The performance, efficiency and potential for market entry of an OTM is depending on several factors as sketched in **Fig. 3**.

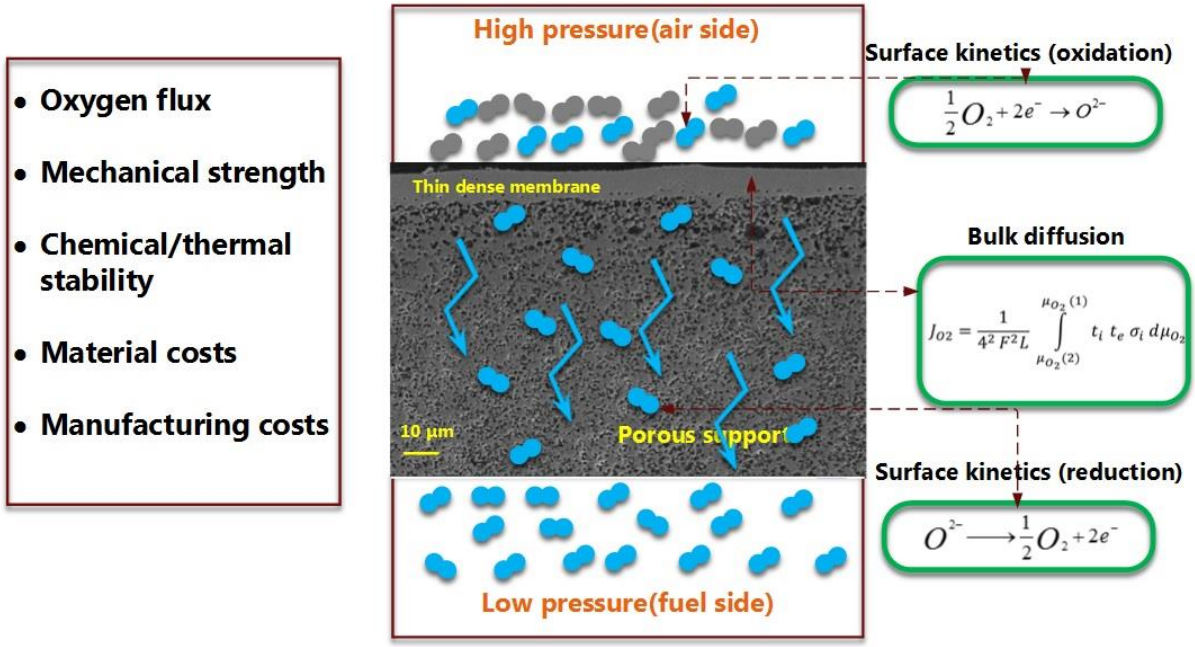

Fig. 3: The requirements for designing of an asymmetric membrane

Some of these factors, such as typical state of the art materials for membrane, support layers, catalytic layers, designs and performance parameters, are briefly reviewed in the next sections with focus on ceria based asymmetric OTMs most relevant for this work.

2.1.2. Oxygen transport mechanism in asymmetric membrane

Oxygen transport through asymmetric oxygen membrane involves five distinct steps which are tabulated in **Table 1**. The very first step is the mass transfer of oxygen/air molecules to the membrane surface for further electro-catalytic activity. The oxidation reaction will occur at the catalytic interface, resulting in dissociation of oxygen molecules into oxygen ions (O^{2-}) on the feed side. Once dissociated, the oxygen ions diffuse across the bulk membrane layer. The rate of oxygen transport can be accelerated by reducing the thickness or selecting a membrane material (composition) which has high oxygen vacancy concentration. Subsequently, the association of oxygen ions into oxygen molecules occurs at the permeate side of the membrane. Finally, the oxygen molecules will be transported across the think porous layer. The oxygen transport through the porous layers highly depends on the microstructure (porosity, pore size, pore connectivity) of the porous layer.

Table 1: List of steps involved in oxygen transport in porous supported asymmetric oxygen membrane

Step	**Transport**	**Controlling factor**
i. Oxygen supply to the membrane	Mass transfer of oxygen molecules to the membrane catalytic surface	Oxygen partial pressure
ii. Surface exchange kinetics	Dissociation of oxygen molecules into oxygen ions by electro-catalytic activity	Rate of dissociation of oxygen ions from O_2
iii. Bulk diffusion	Transport of oxygen ions through membrane	Membrane thickness and material composition
iv. Surface exchange kinetics	Association of oxygen ions into oxygen molecules by electro-catalytic activity	Rate of association of oxygen ions into O_2
v. Transport of oxygen through macro-porous layer	Mass transfer of oxygen from the membrane catalytic surface through macro-porous layer	Supports gas permeability Oxygen partial pressure

The diffusion of oxygen ions across the bulk membrane would be the rate-limiting step if the membrane thickness is above a characteristic thickness (presented schematically in **Fig. 4**, black line (2)). It is reported that most of MIEC materials have a characteristic thickness between 200–300 µm [15,16]. If the membrane thickness is reduced below the characteristic thickness, then the surface exchange becomes the rate-limiting step (shown in **Fig. 4**, red line (1)). However, the oxygen flux can be further increased by improving the surface exchange kinetics by integrating a highly permeable porous support and a highly efficient-catalytic layer prepared from nano sized particles [11]. It should be noted that the porous layer should have sufficient porosity and open structures so that oxygen molecules can be tranpsorted across the support very easily. Otherwise, the oxygen flux of the membrane will be controlled by the oxygen diffusion rate in the porous layer rather bulk diffusion in the membrane (schematically is shown in **Fig. 4**, white line (3)).

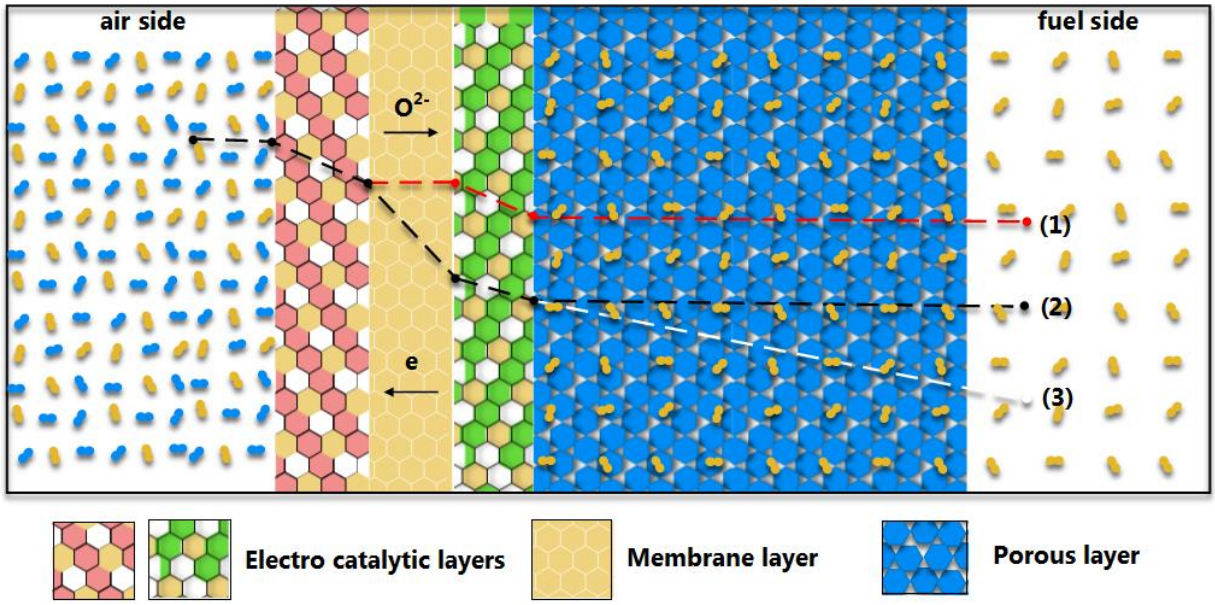

Fig. 4: Steps involved during oxygen transport in an asymmetric membrane, 1) oxygen transport controlled by surface exchange kinetics, 2) oxygen transport controlled by bulk diffusion, 3) oxygen transport controlled by gas diffusion through porous layer.

In order to improve the oxygen flux further, the kinetics of the catalytic layers (dissociation and association of oxygen molecules) has to be improved by using high performance electro-catalytic materials. It was widely researched and reported in the area of catalytic material development for SOFC application in order to improve very significantly electro-chemical oxidation/reduction activity at elevated temperature and also reduce the operation temperature [30–33]. It was found in the literature that the electro-catalytic layer can

be prepared with enhanced catalytic activity by infiltration of nano particles of these materials into porous backbone structures, since only small of amounts of material used will not diminish the total porosity of the structure. Hence, this novel route can be used to prepare high performance catalytic layers if integrated with high oxygen flux membranes [31]. F. Zhao et al. have reported that LSC catalytic layers prepared by this route shows remarkable performance in term of high resistance to thermal cycling and thermal shock, due to the use of impregnated nano catalytic particles rather than bulk particles [34].

2.1.3. Factors influencing the membrane performance

The membrane performance (oxygen flux) is not only related to membrane materials but it also depends on the membrane design & configurations and membrane operating conditions. In an asymmetric configuration, the porous support structure might have a considerable thickness (compared to the active membrane layer) and might therefore limit the gas transport. Hence, the support layer should have a microstructure that results in high gas permeabilities and sufficiently high gas transport. Furthermore, the support needs to have high mechanical strength. Another parameter which influences of membrane performance is the sintering conditions adapted during membrane preparation. In one study, C. Fan et al. reported that LSCF ($La_{0.6}Sr_{0.4}Co_{0.2}Fe_{0.8}O_{3-\delta}$) membranes sintered at 1250 °C and 1300 °C displayed different oxygen flux performance, due to the presence of impurities in the perovskite phase after sintering at 1250 °C. Hence, the optimization of the sintering cycle is an essential activity to ensure higher performance by reaching the desired microstructural development [17]. Another influential parameter on the membrane performance is the operating conditions in which the membrane has been tested. The temperature dependence of the oxygen flux through the membrane was studied between 700 and 925 °C for an alumina doped SCF ($SrCo_{0.8}Fe_{0.2}O_{3-\delta}$) membrane by C. Zhang et al. It was noticed that the oxygen permeation flux increases sharply with temperature from 0.04 to 1.06 mL (STP)/cm^2 from 700 to 925 °C which mainly due to acceleration in surface reaction kinetics and bulk diffusion [12]. This study reveals that the operating temperature plays a vital role in the oxygen permeation of the perovskite structured SCF membrane. It is also obvious that different flow rates of feed and sweep gas will influence the membrane performance. By varying the flow rate of the sweep gas, the oxygen flux can be decreased or increased in the effect of changes in oxygen partial pressure on the permeate side. [18]. Stability over the period at elevated operational condition is another important factor to be considered and studied when evaluating the membrane degradation. In the literature, it is reported that the oxygen permeation flux and membrane reactor performance has been reduced as function of time [19,20]. It is stated that the stability of a

$Ba_{0.5}Sr_{0.5}Co_{0.8}Fe_{0.2}O_3$ (BSCF) membrane deteriorated over the period and the membrane performance of CH_4 conversion decreases to 93 %, because BSCF membranes are unstable in CO_2 enriched atmospheres [19]. Moreover, BSCF materials are known to be susceptible to reduction of the cobalt ions into metallic cobalt under very low oxygen conditions [15,17]. Recently, it was reported that a thin CGO membrane exhibits good stability towards harsh operating conditions such as low pO_2 and CO_2 atmospheres, resulting in a high oxygen flux of 16 N ml min^{-1} cm^{-2} at 900 °C [1].

2.2. Membrane architecture of an asymmetric membrane

There have been some studies which are focused on designing favorable membrane architectures by using different geometries, i.e. planar, tubular, hollow fibers, and honeycomb structures, as shown in **Fig. 5.** However, each design has own merits and demerits. Various process/ fabrication methods have been employed to design asymmetric thin membranes on porous substrates. The selection of such technique also depends on the desired product shapes, complexity in structure and mechanical and chemical integrity. Planar membrane configurations can be prepared very easily using conventional fabrication techniques, i.e. hydraulic pressing or tape casting. However, membrane sealing is one of the critical tasks that existed in planar devices. Air Products USA has developed a refined planar configuration of asymmetric membrane through tape casting process. The advantages of their configuration is its ability to withstand the mechanical stresses caused by the compressed air, as it consists of central supported porous structures. Moreover, these modules can easily be scaled up [6]. Other designs such as tubular and hollow fibre designs can be manufactured using either extrusion processes or phase inversion methods. The high surface area to volume ratio of these configurations will provide high membrane performance and make them superior over planar devices. The sealing can also be done very easily in this case [35].

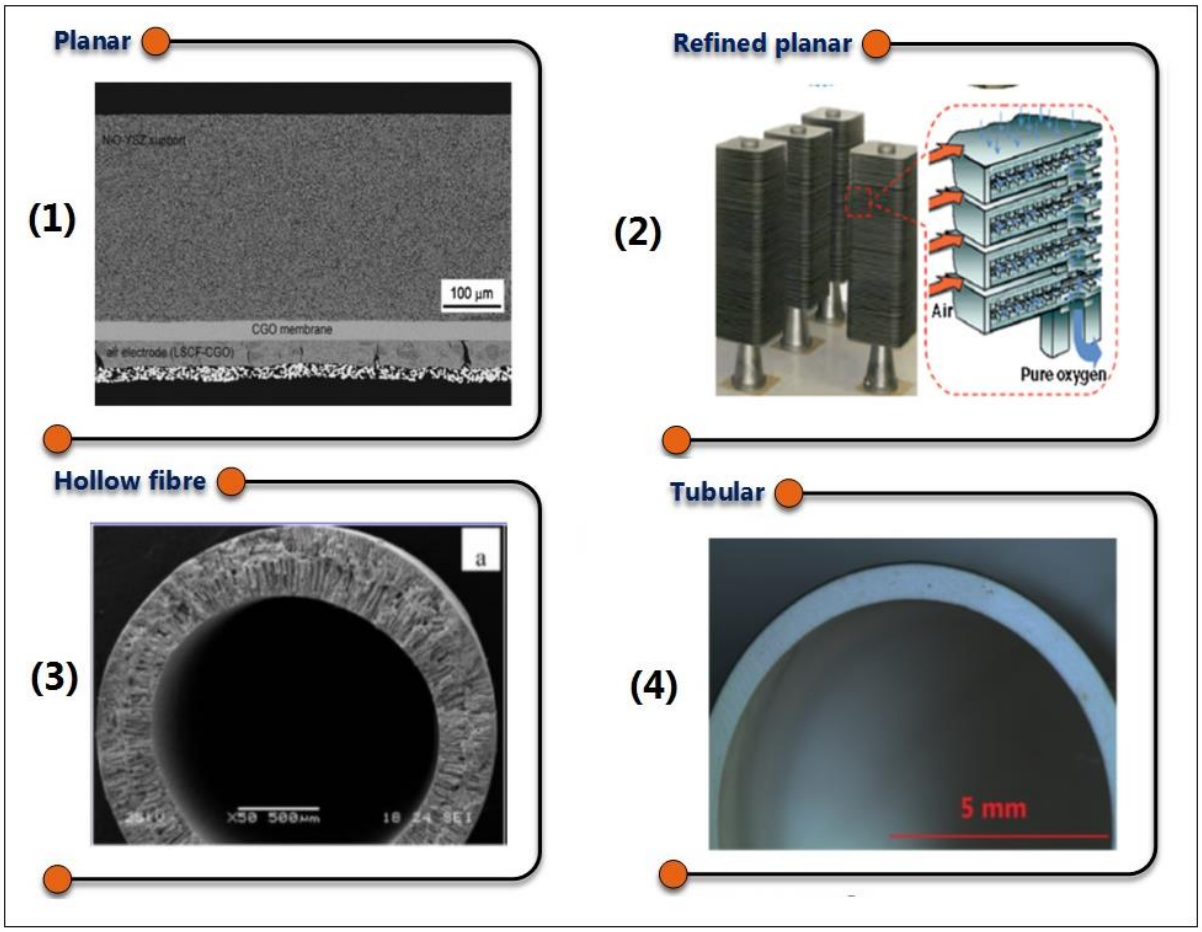

Fig. 5: Different type of configurations used for designing oxygen transport membranes, (1) a planar CGO asymmetric membrane [1], (2) refined Planar design for OTM [35], (3) asymmetric LSCF hollow fiber [36], and, (4) a tubular asymmetric CGO membrane supported by porous MgO [37].

2.3. Fabrication and performance of asymmetric OTMs

Fabrication of successful asymmetric membranes requires a very detailed understanding of physical, chemical, thermal and electronic properties of the material (porous and membrane layer) in order to overcome the challenges during multilayer fabrication and sintering. Matching the thermal expansion of the membrane and the support layer is one important aspect that need to be considered in order to avoid stress development during the sintering process.

2.3.1. Performance of single phase CGO membranes

Perovskite-structured compounds (i.e. BSCF) are interesting membrane materials which provide high oxygen flux. However, they have poor chemical stability at reducing atmospheres and very low oxygen partial pressure conditions [11]. Fluorite-structured gadolinium doped ceria (CGO) is another promising candidate material for oxygen transport membrane applications due to its high phase stability under both oxidizing and reducing atmospheres and its high ionic conductivity [1,18,38,39]. Choosing the appropriate shaping method is essential to influence the properties of the membrane materials through the microstructural development. Some of the techniques i.e. dry pressing, dip-coating and tape casting [17–19] are still used to fabricate thin and thick membrane layers. Much of the conventional techniques can be described as ceramic powder processing methods, which utilize prepared powders with a variety of binders and pressing techniques to form pellets [31]. The list of CGO membranes prepared using different fabrication techniques, including their sample thickness and membrane performance are presented in **Table 2.** As stated in section **2.2.2**, the membrane performance is not only dependent on the membrane material, but also the membrane configurations (thickness, shape) and operating conditions (temperature, pO_2 difference) etc.

From **Table 2,** it can be seen that different configurations of CGO membranes have been prepared with a wide range of thicknesses (10-1350 µm) and tested at different operation conditions. For CGO membranes in a self-supporting configuration (disk), thicknesses of only up to 500 µm can be achieved due to shaping and mechanical strength constrains. The highest flux of 5.95 $\times 10^{-07}$ mol s^{-1} cm^{-2} was achieved for a 500 µm thick disk-shaped membrane with an oxygen partial pressure gradient of 21 kPa/0.5 kPa. In the asymmetric planar configuration, an oxygen flux of 3.72 $\times 10^{-06}$ mol s^{-1} cm^{-2} was achieved at 820 °C for a sample thickness of 30 µm. The same performance was achieved with a membrane of similar thickness at 1000 °C, although the two membranes had slightly different type of porous layer material and the sweep gas used (which may develop differences in the pO_2 across the membrane). Another studies by A. Kaiser et al [1], reported oxygen fluxes of more than 16 Nml min^{-1} cm^{-2} (equal to 1.19 $\times 10^{-05}$ mol s^{-1} cm^{-2}) at 850 °C, using 30 µm planar asymmetric CGO membranes prepared by tape casting of different layers and subsequent lamination [1] by placing the membrane between air and humidified hydrogen with a pO_2 difference of 20 times. The membrane developed by A. Kaiser et al. showed high thermal and chemical stability at reducing syngas operation conditions [38]. The oxygen flux of 16 Nml min^{-1} cm^{-2} is considered to be the highest value achieved in term of asymmetric CGO membrane reported in the literature as per the author's knowledge.

These results motivated the author to consider further research on the fabrication and performance of CGO asymmetric membrane on tubular configuration.

Table 2 : Oxygen permeation flux of CGO based membranes

Membrane material	Temperature (°C)	JO_2 (mol s^{-1} cm^{-2})	pO_2'/pO_2''	Shape	Thickness (µm)	Support material	Process	Year	Reference
CGO20	850	6.00×10^{-11}	Air/---	Disk	1350	Self-supporting	Pressing	2003	[36]
CGO10	850	5.00×10^{-09}	Air/---	Disk	1250	Self-supporting	Pressing	2003	[36]
CGO20	950	5.95×10^{-07}	Air/He	Disk	500	Self-supporting	Pressing	2008	[37]
CGO10	---	---		Tubular	270-420	Self-supporting	Thermoplastic extrusion	2004	[38]
CGO10	600	---	Air/H_2-N_2	Planar	210	NiO/CGO10	Tape casting	2006	[40]
CGO10	820	3.7×10^{-06}	Air/H_2-steam	Planar	30	Ni-YSZ	Tape casting/ Pressing	2011	[35]
CGO10	900	1.19×10^{-05}	Air/H_2-steam	Planar	30	Ni-YSZ	Tape casting+ Lamination	2011	[14]
CGO10	1000	3.72×10^{-06}	Air/Argon-CH_4	planar	27	CGO	Tape casting+ Lamination	2011	[12]
CGO10	600	Run with fuel cell mode		Planar	10	Ni/CGO10	Pressing/ Electrophoretic infiltration	2005	[39]

CGO20 ($Ce_{0.8}0Gd_{0.2}O_{2-\delta}$), **CGO10** ($Ce_{0.9}Gd_{0.1}O_{1.95-\delta}$) JO_2 (mol s^{-1} cm^{-2}= 1.35×10^6 Nml min^{-1} cm^{-2})

2.3.2. Fabrication of porous support layers for asymmetric membranes

The microstructure (porosity and pore size distribution) of the porous layer of the membranes are highly dependent on the chemical nature of the starting powders, the particle size and distributions, the weight ratio of the ceramic powder to polymer binder, sintering conditions and densification behavior. To attain the desired microstructure, the right amount of pore former has to be included along with the ceramic. A data compilation of porous layers for asymmetric oxygen transport membranes prepared using different techniques with different thicknesses is presented in **Table 3**. The table lists membrane and support fabrication methods, materials used for both components, as well as thickness, pore-forming agent and pore size of the support. It should be noted that disk-based membranes, in which dry pressing technique is extensively used, have been widely researched to evaluate material performance (ref **Table 3**). However, the membrane thickness can only be reduced down to 150 µm by dry pressing method [40], where as other fabrication methods such as spin or spray coating are capable of producing thickness under 20 µm. Chang et al. produced crack-free dense MIEC membranes on porous supports via dry pressing, showing the O_2 flux to be ten times higher in the supported MIEC membrane than in the self-supported membrane, due to reduction of the thicknesses from 1000 µm to 200 µm (about 5 times) [41]. It was also reported in **Table 3** that different types of organic pore formers have been widely used in order to enhance the porosity (26 to 46 %) of the support layer.

Tape casting and extrusion processes are efficient fabrication techniques to prepare porous supports in an industrial scale. The tape casting processes have been extensively researched to design Planar membrane and SOFC devices [8,42–44]. However, a very limited research on tubular oxygen membrane with asymmetric configuration using extrusion have been reported [12,45]. The advantage of such a tubular geometry is that it provides higher surface area/volume and easier high-temperature sealing than Planar devices [12]. A number of other benefits include ease of manufacturing using extrusion and dimensional stability under temperature and oxygen activity gradients [46]. A study by W. Hsieh et al. [47] demonstrated that an electrolyte-supported tubular SOFC can be prepared using extrusion and dip-coating and thicknesses of 210 and 28-34 µm can be achieved for electrolyte and catalytic layers, respectively, with good adhesion between the layers. Another study by Z. Liu et al. [48] reported that a crack-free asymmetric tubular perovskite membrane with a thickness of 20 µm could be prepared using extrusion and spray drying. With the asymmetric design the oxygen flux performance was almost 1.35 times higher than with the

symmetric configuration, and the membrane was stable under low pO_2 conditions over 200 h. It is therefore evident that the membrane performance and stability could be improved by an asymmetric configuration.

In order to prepare such tubular membranes, high green strength and dimensional accuracy of the components is essential during shaping process and, the thermoplastic ceramic route is a suitable route to process such ceramic components. By this route, Defne et al. [13] have prepared a self-supporting tubular $LaFeO_3$ membrane with thickness of 250-470 µm. However, the fabrication method can be also used to design and fabricate thin planar, tubular and honeycomb structures with a high dimensional accuracy. The main disadvantage of the technique is the very critical and time consuming de-bindering process [49,50].

Table 3. Data compilation of the porous supports used in asymmetric membranes

Type	Membrane / Support material	Membrane / Support process	Membrane / Support thickness (µm/mm)	Pore former	Porosity (%)	Pore size (µm)	Year	Reference
Planar	LSCF/ LSCF	Slip casting / Dry pressing	200/1.5	Inorganic pore former		0.5	2001	[51]
Planar	$La_2NiO_{4+\delta}$/ Al_2O_3	Coating	40/xxx		40		2003	[52]
Planar	SFC/ SFC	Dry pressing	190/0.9	Carbon fiber	26		2005	[53]
Micro tubular	BCFC/ BCFC	Phase inversion process	175				2005	[54]
Micro tubular	LSCF/ LSCF	Phase inversion process	220				2005	[36]
Planar	YSZ/ NiO-YSZ	Coating/ Dry pressing	7/1.5				2006	[55]
Planar	SCFZ–0.4MgO / MgO–0.4SCFZ	Dry pressing	200/1.0	Active carbon		0.8	2006	[41]
Planar	LSFG/ LSFG	Tape casting	120/0.82	Cornstarch	28	1.9	2006	[42]
Planar	LSF-SFA/ LSF	Dry pressing	500/1.4	Graphite			2006	[56]
Planar	BSCF/ BSCF	Dry pressing	25/1.1				2007	[57]
Tubular	SCFA	Extrusion	900				2007	[12]
Tubular	LFC-LSFT	Extrusion	250-470				2007	[13]
Planar	GDC–LSFN/ Ni	Slip casting / Dry pressing	10/1.0		20-40		2010	[58]
Tubular	LSFN/ LSFN	Dry pressing	700				2010	[59]
Planar	BSCF/ BSCF	Tape casting	70/0.83	Cornstarch	34		2011	[8]
Tubular	SCFZ/ SCFZ	Spray coating /Extrusion	20/0.7	Inorganic pore former			2012	[48]
Planar	SDC–SDC/ SSAF	Dry pressing	800				2013	[60]
Planar	BSCF/ BSCF	Tape casting	800	Cornstarch	34		2013	[43]
Planar	CGO/ CGO	Tape casting	200/0.3	Graphite	43-46		2013	
Planar	BSCF/ BSCF	Tape casting	20/0.9	Cornstarch	40-41	1.6	2014	[44]
Planar	BSCF/ BSCF	Dry pressing	150-500/0.9	Organics	30		2014	
Planar	BCFN/ BCFN	Dip-coating/ dry pressing	20/0.98	Graphite	33	3.3	2014	[61]

From **Table 3**, it can be seen that most of the membrane configurations consist of the same material for both the membrane and porous support layer, in order to avoid stress induced from differences in the thermal expansion coefficient (TEC) [35]. Other than a TEC match, the support layer materials for asymmetric membranes should have a low material cost, high thermal and chemical stability in the harsh operating environment, and good mechanical properties at elevated temperatures [37]. Cheng Li et al. have reported the preparation of disk-shaped membranes supported on a low-cost support material such as aluminium oxide (Al_2O_3) [52]. However, alumina has too low thermal expansion of 8 $\times 10^{-6}$ $°C^{-1}$ [62], which makes it unsuitable as a potential support material for perovskite and ceria based composite membranes, which have high TEC value over 12 $\times 10^{-6}$ $°C^{-1}$. It is reported that another potential material such as magnesium oxide (MgO) satisfies these requirements [63,64] since it has a relatively high TEC), closer to the values for perovskite or ceria-based composites, and can thus be easily integrated with these membrane materials in multi-layered structures without failure during processing as a result of expansion mismatches [65]. Previously F. Valdivieso et al. demonstrated that MgO supports with large and stable pores can be obtained for application in long life fission products in which the porous supports should have thermal stability of porosity to avoid densification the temperature < 1600 °C [66]. H. Middleton et al. investigated the possibility using of porous MgO supports for membranes prepared via co-casting and co-sintering processes [67]. It was stated that the MgO support's porosity can be tailored to between 26 and 42 % porosity by altering the pre-calcination temperature of MgO powder from 1000 °C to 1200 °C. Moreover, it was given an indication that MgO supports show high structural stability even at very high temperature and that a wide range of porosity can be obtained by pre-treating the starting MgO powder. These are some reasons which motivated us to consider MgO as possible candidate material for the porous support layer in this PhD work on asymmetric CGO membrane preparation and testing. Moreover, to the author's knowledge studies are not available that deal with the preparation and testing of asymmetric tubular CGO membranes for use in syngas reactors or in similar applications. Hence, this work may fill the research gap in this area.

3. Objectives of work and outline of thesis

This thesis deals with the fabrication and characterization of asymmetric ceramic oxygen transport membranes (OTMs), based on a cheap porous support material (magnesium oxide, MgO) and a thin film ceria based oxygen membrane (cerium gadolinium oxide). Fabrication processes were chosen that are up-scalable and that allow cost effective fabrication of mechanically robust tubular multi-layers for use as oxygen transport membranes (dimensions of tubes: length 30-40 mm, diameter 10-11 mm and wall thickness 0.8 to 0.9 mm).

The thesis addresses several aspects in ceramic processing of such asymmetric oxygen transport membranes (OTM) which are discussed in different sections in the result section, and include:

(a) Fabrication of thin-walled tubes of a cheap, suitable and available support material by thermoplastic extrusion.

(b) Tailoring of the microstructure of the support structure, including the understanding of the relations between microstructure and gas permeability (to eliminate gas transport limitations), and to improve mechanical properties.

(c) Challenges that arise due to the simultaneous firing of porous (support) layer and dense membrane, such as stress development due to differences in densification rates.

(d) Preparation of fully functional tubular asymmetric oxygen transport membranes by dip-coating of catalytic and membrane layers on MgO support tubes for performance characterization (oxygen permeation tests).

A primary aim of this thesis was to establish a manufacturing method for producing porous MgO tubes by thermoplastic extrusion which would allow the fabrication of thin-walled (0.5 to 1 mm), form-stable structures with open porosities of 30 to 48 %. **Section 5.1** (**publication I)** summarizes the studies on the influence of the extrusion mass composition (feedstock) and sintering conditions on the resulting microstructure and properties of the MgO structure for the use as support in OTMs. Major parameters that are investigated are the concentration of thermoplastic binder, ceramic and pore former.

In **section 5.2 (publication II),** the microstructure, densification behavior, gas permeability and mechanical properties of the porous MgO support material was discussed as a function of pore former, pore former type and sintering temperature. Special emphasis was given to the characterization of the pore structure (e.g. pore size distribution) in the MgO support, using different techniques such as scanning electron

microscopy and Hg porosimetry. Additionally, the improvement in the permeability of MgO support from combining two fugitive pore formers (spherical graphite and PMMA) and economic analysis of MgO support were discussed in **section 5.3 (publication III)**.

Dip-coating experiments of green (unfired) MgO tubes with a thin membrane layer of CGO ($Ce_{0.9}Gd_{0.1}O_{1.95-\delta}$) were carried out to support the modeling of stress development during constrained sintering of such a typical bi-layered oxygen membrane structure. Validating these models were then possible by analyzing the data from the constrained sintering experiment of the two layers. The experimental part and some brief conclusions on the modeling results (from the thesis of TT Molla) are summarized in **Section 5.4 (a joint publication IV)**.

The final goal of this thesis (**Section 5.5, publication V)** was the preparation and testing of a full asymmetric, tubular MgO-supported CGO membrane under syngas operation conditions. For this purpose the CGO membrane and the suitable catalytic layers were applied on the MgO supports by dip-coating, followed by a co-sintering procedure. The challenge was to establish a homogenous coating on the outer tube surface for the different functional layers and to produce defect free gas-tight membrane samples after co-sintering.

4. Experimental methods

4.1. Raw materials processing

4.1.1. Raw materials

For preparation of porous MgO tubes by thermoplastic extrusion, MgO powder (Product #12R-0801, Inframat Advanced Materials, USA), pore former, a thermoplastic binder (Elvax 250, Du Pont, USA), paraffin wax (Sigma-Aldrich, USA) as a plasticizer, and stearic acid (Sigma-Aldrich, USA) as a dispersant were used. Three type of pore formers were used in the feedstock composition, namely: a graphite powder, flaky type (V-UF1 99.9, Graphit Kropfmühl AG, Germany) referred to as (FL), another graphite spherical type (TIMREX® KS6, TIMCAL, Switzerland) referred to as (SP) and PMMA (Poly methyl methacrylate, MR 10G, Exprix technologies, USA) referred as (PM). For preparation of the membrane and catalytic layers CGO (GDC-10 TC, 10 % Gadolium doped Ceria, Fuel Cell Materials), Nickel oxide (NiO-11316GNO, Novamet products, USA) was used.

4.1.2. Raw Materials Characterization (PSD, BET and SEM)

It is very important to characterize the properties of the starting raw materials, since powder properties will influence the following processing steps; i.e. powder dispersion/mixing, flow behavior (rheology) and especially sintering and the final microstructure. For measuring the particle size distribution (PSD) and the specific surface area, the powders were mixed with ethanol and de-agglomerated for 24 h using a ball mill. The dried raw and calcined powders of MgO, CGO and the graphite were dispersed with ethanol to measure the PSD with a particle size analyzer (LS 13320, Beckman coulter, Inc, USA). The Brunauer, Emmet and Teller (BET) specific surface area of the powders was determined using an Autosorb-1 analyzer (Quantachrome Instruments, USA). The morphology of the powders were investigated using a scanning electron microscope (SUPRA35, Carl Zeiss, Germany). A thermo-gravimetric balance (STA 409 CD, Netzsch GmbH, Germany) was used to study the decomposition behavior of the thermoplastic binder system (EVA, paraffin, stearic acid) and the graphite pore former in the MgO feedstock during de-bindering in air. The instrument was equipped with programmable temperature and gas change sequences. All experiments were conducted with a heating rate of 1 °C min^{-1} and an air flow of 100 ml min^{-1}.

4.1.3. Raw powder pre-conditioning

The uncalcined MgO powder had a very large surface area of 78 m^2/g (BET) and consisted of extremely fine (nanometric) primary particles that could not be fully de-agglomerated by kneading or pre-dispersion in

stearic acid. For better dispersion (easier de-agglomeration), the raw ceramic powders (MgO) were pre-calcined at 1000 °C with a heating rate of 100°C/h for 10 h to reduce the surface area of the powder from 78 m^2/g to 10.8 m^2/g. Further de-agglomeration of the pre-calcined MgO powder could then be achieved by milling and pre-coating with stearic acid. Stearic acid (37 ml) was dissolved in 1-propanol (1500 ml) and ball milled for 2 h to obtain complete mixing. Approximately 585 g of MgO was added to this mixture. The solvent was removed from the MgO slurry by drying on a hot plate for 24 h at 90 °C. This stearic acid coating helped to reduce the tendency of the fine MgO raw powder to adsorb water and agglomerate, and further improved the powder handling (e.g. significantly reduced dust formation during the kneading process).

The as-received CGO powder showed some level of agglomeration (small peaks on the sides of the main peak in the PSD graphs), but did generally have a smooth distribution centered on 1.46 µm (d50). After calcination at 1000 °C, the primary particle size had increased as expected, resulting in a broadened single particle size distribution with a d50 value of 2.14 µm. Another reason for the pre-calcining at 1000 °C was to closely match the shrinkage behavior to that of the MgO layer during co-sintering process.

4.2. Preparation of porous MgO support structures

In this study, the term "feedstock" refers to the mixture of thermoplastic and ceramic compounds used to prepare warm-pressed planar structures or extruded tubes. Previous studies [68] have shown that thermoplastic compositions designed for injection molding or thermoplastic extrusion can be shaped by warm pressing and give similar microstructures to extruded samples (when the process was carefully controlled). In material development and optimization of feedstock compositions it is therefore possible, and often convenient, to warm press samples for principal investigations instead of extruding the feedstocks, since this requires relatively large batch sizes (of 200 to 500 g).

4.2.1. MgO feedstock preparation

Two differently sized kneaders have been used to prepare the feedstock for two different shaping process i.e. warm pressing and extrusion. The Brabender N50 kneader (operating volume 55 ml) was used to prepare smaller batch size for warm pressing. The big kneader (Linden, Type BK20-Vol 500 ml, Germany) was used for preparing the feedstock for extrusion process.

After powder pre-treatment, all three types of ingredients (treated MgO powder, the graphite and the polymers, compositions as shown in **Table 4**) were weighed and added to kneader in the following order to achieve homogeneous mixing.

First, the kneader was heated to an operation temperature of 100 °C, filled with half of the amount of the MgO powder and allowed to run at low speed (10 RPM) to transfer heat to the MgO powder and break down larger aggregates. The typical curve of torque and temperature plotted against mixing time reveals a sharp decrease in stock temperature whenever cold material is added to the kneader. In the 2nd step, the polymers (Elvax 250 and Parafin wax) and the remaining MgO powder were added stepwise. After a homogeneous mixing of the mixture was achieved, the graphite powder was added. **Table 4** shows thermoplastic extrusion feedstock compositions prepared using the three different pore formers.

Table 4: Thermoplastic feedstock composition using different pore formers.

Code	Kneader Temperature (°C)	MgO content (Vol.%)	Polymer & additives (Vol.%)	Pore former (Vol.%)	Type of pore former
MP-FL	100	39	42	19	Flaky graphite
MP-SP	100	34	46	20	Spherical graphite
MP-PM	65	34	46	20	PMMA

Normally, the process of filling will take minimum 15 to 20 mins and varies based on the feedstock composition. If the recipe contains more polymers, it consumes less time for filling, vice versa more time in case of a higher solid loading. After filling, the mixture is kneaded for 30 mins at 30 rpm until a constant torque value of about >20 Nm is achieved. The typical torque curve is shown in **Fig. 6**. In phase 1, the torque started to increase due to addition of polymer in the kneader, in phase 2 the torque further increases due to addition of ceramic and graphite powder and decreases further when the polymer is thoroughly covering the ceramic particle, and in phase 3 the torque reaches a constant level indicating a homogenous mixture.

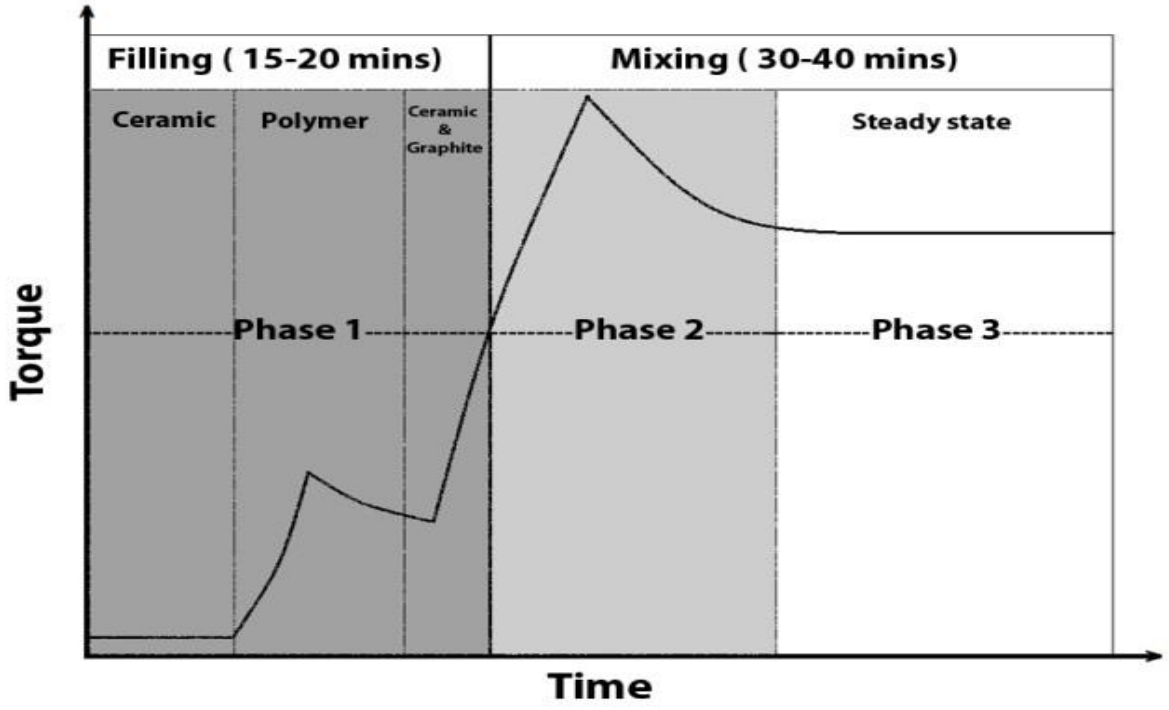

Fig. 6: Typical torque curve of a thermoplastic feedstock system.

4.2.2. Methods of feedstock characterization

The green densities of the warm-pressed and extruded samples were measured by the geometrical method and Helium pycnometry. The packing density of green (as-prepared) samples was calculated from the ratio between the measured green density and the expected green density (calculated by the density and volume fraction of each feedstock component) and compared to how well the particles are packed together. This was performed in order to verify the reproducibility of feedstock preparation.

A thermo-gravimetric balance (STA 409 CD, Netzsch GmbH, Germany) was used to study the decomposition behavior of different thermoplastic feedstocks (various combination of MgO, polymer and pore formers) during de-bindering in air. The instrument was equipped with programmable temperature and gas change sequences. All experiments were conducted with a heating rate of 1 °C min^{-1} and an air flow of 100 ml min^{-1}.

4.2.3. Warm pressing of porous MgO structures

For fast screening and characterization of the influence of the feedstock composition on the final properties, especially densification behavior and porosity, the different feedstocks were prepared in small quantities of about 50 ml in the mixer (as described above) and warm pressed into a rectangular shape with dimensions 35mm x 50 mm x 1-2 mm (width, length and height) using a Fortune Isostatic press (Model TP600) by applying a load of 100 KN at 100 °C. It was assumed that the final properties of the thermoplastic compositions were independent on the used shaping method (pressing or extrusion at 100 °C). Furthermore, extrusion of feedstocks requires batch sizes that are about 10 times larger than those for warm pressing, increasing the efforts (processing time and amount of material) beyond the scope of this study. Selected compositions were also extruded into tubular shape to investigate and compare the properties of pressed and extruded samples during processing and with respect to the final properties.

4.2.4. Extrusion of porous MgO tubes

Thermoplastic extrusion was used to shape support tubes as the process is capable of producing thin walled, form-stable substrates suitable for further membrane processing by dip-coating process. The extruder (Model 19/20DN Brabender, Germany) used dedicated oil baths to achieve the desired temperatures of 100 °C and 90 °C for the extruder chamber and die head, respectively. The feedstocks were shaped into tubes using a die assembly with inner and outer diameters of 12 mm and 14 mm, respectively. The die head temperature was always kept 10 °C lower than the chamber temperature to ensure form stability of the tube at the exit of the die. An extruder speed of 10 rpm was used for all experiments. Some of the polymeric pore former (PMMA) has a low melting point and it was necessary to optimize the extruder temperature to ensure a stable structure. I.e Feedstock (MP-PM) was extruded using lower temperatures (extruder chamber: 75 °C, die head: 70 °C) as the addition of a polymeric pore former produced a feedstock with lower viscosity. MgO, thermoplastic binders and graphite were used to develop thermoplastic feedstocks. These feedstock were designed to attain a desirable plasticity which make them easily extrudable at 100 °C due to high concentration of low melting polymers. Then, the MgO feedstocks were extruded into tubes (14 mm outer diameter and 1 mm wall thickness) using a Brabender extruder 19/20DN to prepare a porous form-stable structure with a uniform layer thickness. **Fig. 7** shows the image taken during thermoplastic extrusion process.

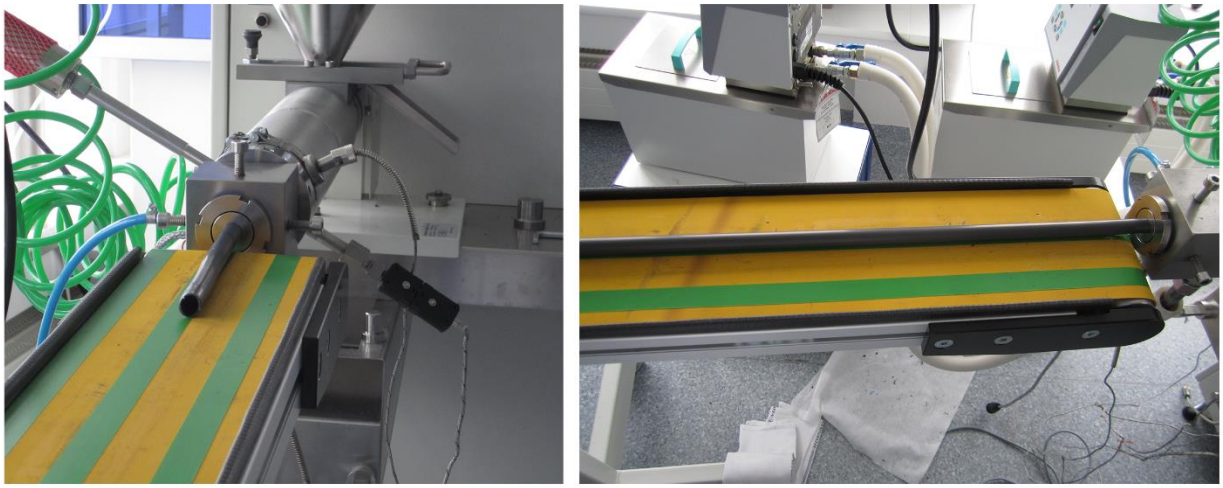

Fig. 7: Extrusion of a tubular device using a thermoplastic feedstock.

4.2.5. De-bindering and sintering of the porous MgO support

For the preliminary studies on feedstock development, the warm pressed/extruded tubes were de-bindered at different temperatures and heating rates as presented in **Fig. 8**. Additionally, selected compositions of warm-pressed and extruded samples were sintered at various temperatures between 1250 °C and 1400 °C in order to investigate the influence of the sintering temperature on the final properties. The de-bindering cycle was chosen based on the feedstock composition (type and quantity of pore former).

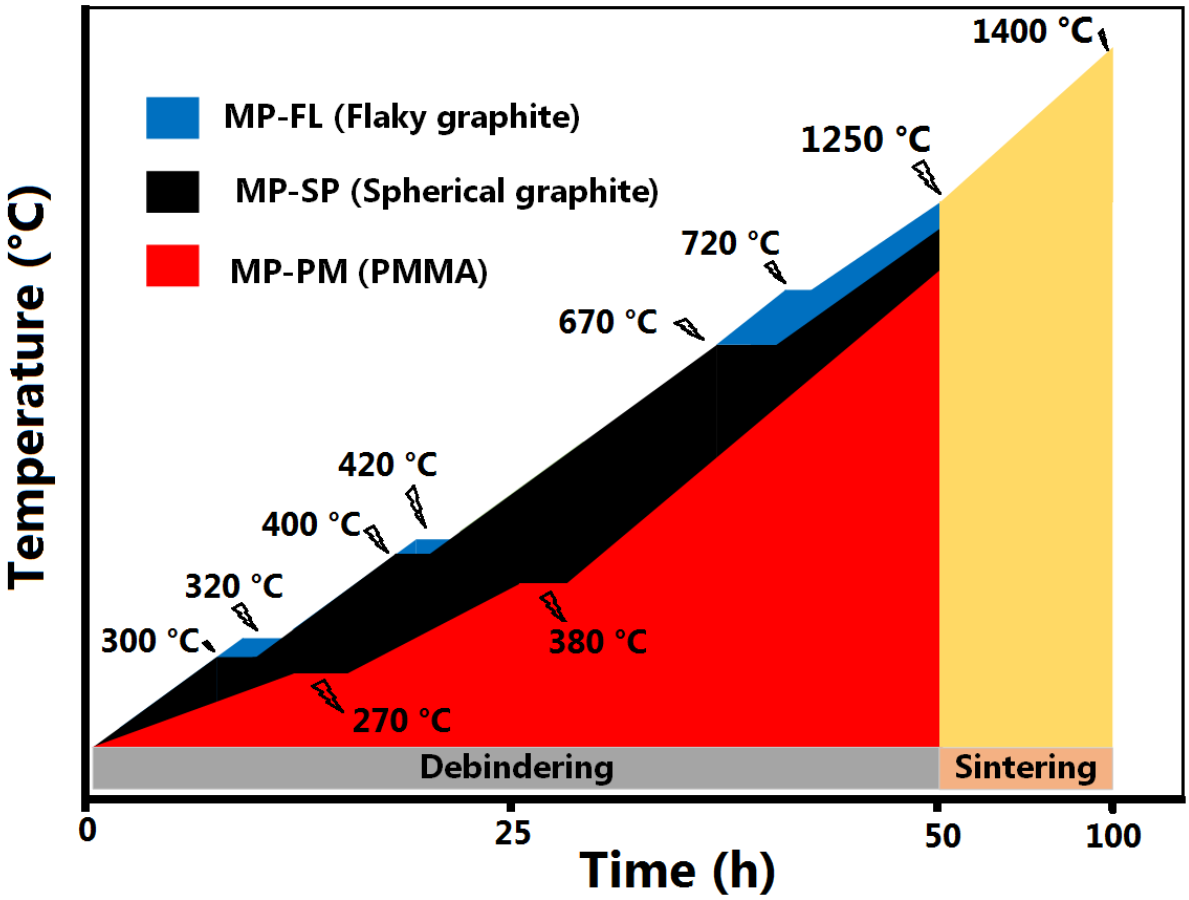

Fig. 8: De-bindering cycle derived from thermo gravimetric experiments for all three supports; MP-FL (Flaky graphite), MP-SP (Spherical graphite) and MP-PM (PMMA).

4.2.6. Characterization of MgO support structures

The properties of the different sintered MgO layers were characterized by Mercury Intrusion Porosimetry (MIP), Electron microscopy, Image analysis, Gas permeation and Mechanical testing, as will be described in detail in this section.

Porosimetry measurements were conducted using a Pore Master (PR-60 GT, Micromeritics, USA). Samples with weights of 0.9 to 1.1 g were measured in a penetrometer with a 5 cm^3 bulb volume and a usable Hg volume in the penetrometer stem of 0.392 cm^3, allowing for a maximum measureable pore volume of 0.366 cm^3. All measurements were run between 5 Pa and 420 MPa, translating into a measurement range of pore diameters between 240 µm and 0.003 µm [69].

The microstructure of the samples was studied using scanning electron microscopy (SEM) (SUPRA35, Carl Zeiss, Germany). The samples for the microstructural characterization were prepared using lap polishing with decreasing coarseness of sandpaper/polishing solution, where the last stage of polishing was with a 0.25 µm diamond paste.

For image analysis, the MAT LAB software was used to analyse the phase distribution of polished cross sections. It allows setting a simple threshold, applying limited pre- and post-processing steps and analysing the particle size distribution and interface area of the segmentation. The ultimate aim of this study is to compare the obtained result with mercury porosimetry experiment results [70].

Gas permeation measurements were carried out using an in-house built system. The setup consists of a gas supply unit, a testing chamber and a unit for measuring the flow of the gas that permeates the sample to be measured. The typical specimen size is a tubular supports with an area of approximately 10 to 20 cm^2. The thickness of the different porous MgO support samples varies from 0.85 to 0.90 mm. A pressure difference across the samples was created using an electropneumatic pressure controller (Tescom, ER3000, USA). The flow of permeated gas was measured using a flow meter (Agilent, USA). The measurements were made with a pressure difference ranging from 50 to 400 kPa at room temperature and with nitrogen as the permeate gas.

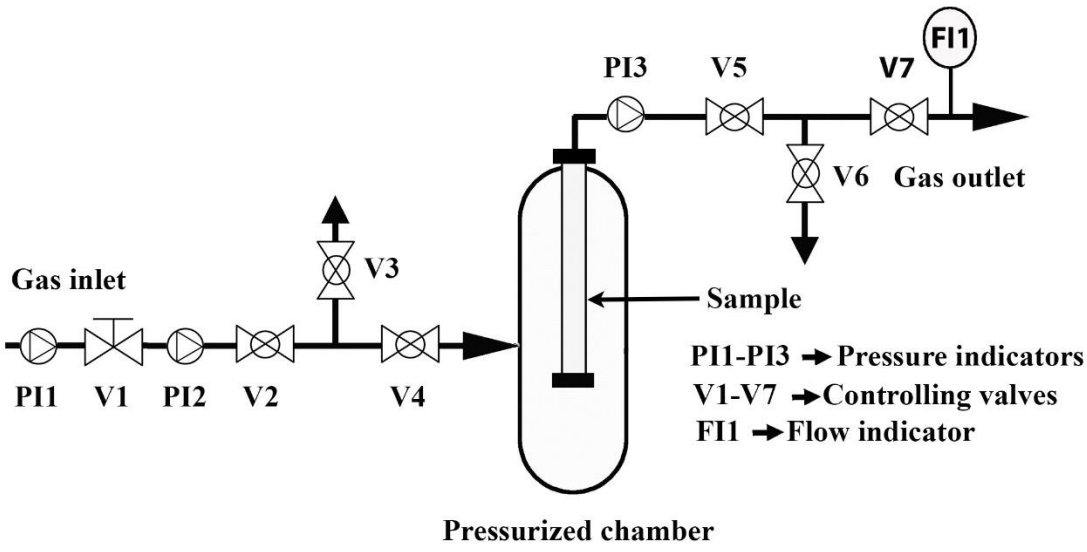

Fig. 9: Schematic diagram of gas permeation setup.

MgO tubes (MPG) sintered at different temperatures (1250 °C, 1300 °C, 1350 °C and 1400 °C) were glued at one end to a steel fixture and to a polymer composite enclosure at the other. Then gas permeation measurements were carried out in order to quantify the gas permeability using the Darcy equation:

$$j = -k/\mu \cdot \nabla P \qquad (2)$$

where, k is the permeability (m^2), j is the flux (m^3/m^2 .s), μ is the viscosity of the gas (Pa.s), and ∇P is the pressure gradient (pressure (Pa)/sample thickness (m)).

The mechanical strength was measured by a 4-point bending test of sectored specimens, which is a variant of the method developed in [46]. Sectored specimens were prepared by cutting the extruded tubes on the long axis into 4 quarters, each subtending an angle of 90°. The cut surfaces of the specimens were ground flat and then tested under four-point bending. A schematic of the specimen geometry and loading configuration is shown in **Fig. 10**. A large tensile stress zone is created in the middle bottom region of the specimen. The highest tensile stress is located away from the cut surfaces and therefore the measured strength data were not influenced by defects introduced by the machining.

All experiments were conducted using specially designed test equipment for continuous testing of multiple specimens under controlled environments. A schematic of the facility is shown in the literature [46]. The loading fixture is composed of a specimen holder, a rocking lever, and a T-stand. The specimen holder is controlled by an actuator (Parker, Model ET32) to move vertically through a connecting rod. The rocking lever sits on the T-stand which is placed on top of two Model 41/00005 load cells manufactured by RDPE. The entire fixture is housed inside a chamber with a furnace section that can be heated to high temperatures. All specimens were tested at room temperature and 850 °C in atmospheric air. The rate of downward movement of the actuator was 0.1 mm/s. The vertical displacement of the loading pins and the forces acting on the support pins were measured continuously.

The elastic modulus E was obtained from the load-displacement curve based on the Euler-Bernoulli beam theory,

$$E = \frac{P}{d}\frac{3La^2 + 2a^3}{6I} \qquad (3)$$

where d is the vertical displacement of the loading pins, P is the applied force, and I is the second moment of area of the specimen cross section.

To obtain the strength of each specimen, the maximum stress corresponding to the applied force at fracture was computed by the finite element method using the commercial software Abaqus [71]. The measured strength distribution was evaluated according to the conventional Weibull theory [72]. The probability of fracture P_f is given by

$$P_f = 1 - \exp\left(-\left(\frac{\sigma_{max}}{\sigma_0}\right)^m\right) \quad (4)$$

where σ_{max} is the maximum tensile stress in the specimen. The linear regression method was used to compute the two Weibull parameters, namely the flexural strength σ_0 and the Weibull modulus m.

Since the stress distribution in the specimen is multi-axial, the principle of independent action [73] was employed in calculating the effective volume. This principle assumes that the principal stresses act independently on fracture, which leads to an effective volume expression given by

$$V_{eff} = \int_V \left(\frac{\sigma_1}{\sigma_{max}}\right)^m + \left(\frac{\sigma_2}{\sigma_{max}}\right)^m + \left(\frac{\sigma_3}{\sigma_{max}}\right)^m dV \quad (5)$$

where σ_1, σ_2, σ_3 are the three principal stresses, and V is the specimen volume. The effective volume was determined numerically from the computed stress distributions from finite element analysis.

Owing to the statistical nature of the strength of ceramic materials, the Weibull parameters determined from a finite number of specimens invariably deviate from that of the parent population. The uncertainty in the measured Weibull parameters can be assessed by means of Monte Carlo simulations [74]. The confidence intervals for the measured flexural strength and Weibull modulus were determined after carrying out 10000 Monte Carlo runs for each set of tests.

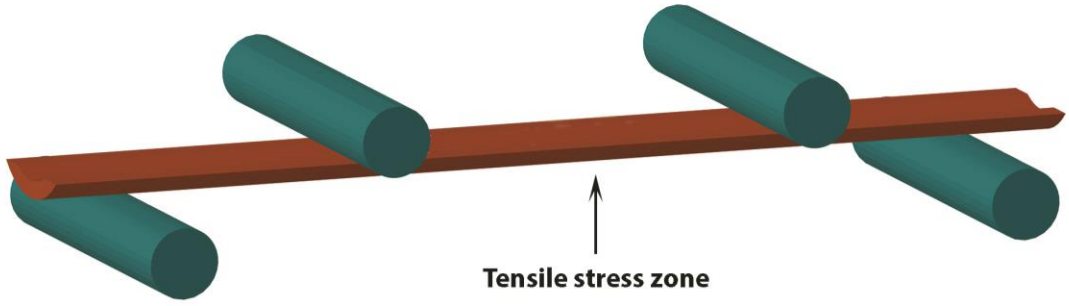

Fig. 10: Specimen geometry and loading configuration for strength testing.

4.3. Preparation and testing of asymmetric tubular membranes

This section describes the preparation of slurries for the active oxygen membrane layer (functional layer) and its application on MgO tubes by a specifically designed dip-coating process. **Fig. 11** ((a) shows a schematic of the prepared asymmetric tubular membrane architecture in which the porous MgO support was fabricated using thermoplastic extrusion and the membrane and catalytic layers were prepared through a dip-coating process from stabilized ceramic suspensions. This was followed by impregnation of catalytic material into the porous backbone on the outside of the membrane. **Fig. 11** (b)–(e) shows photographs of tubular membranes after each progressing steps. The process starts from the extrusion of tubes, followed by dip-coating and sintering of the catalytic layer (NiO-CGO), membrane layer (CGO) and porous CGO backbone layer for impregnation of nano particles of LSC.

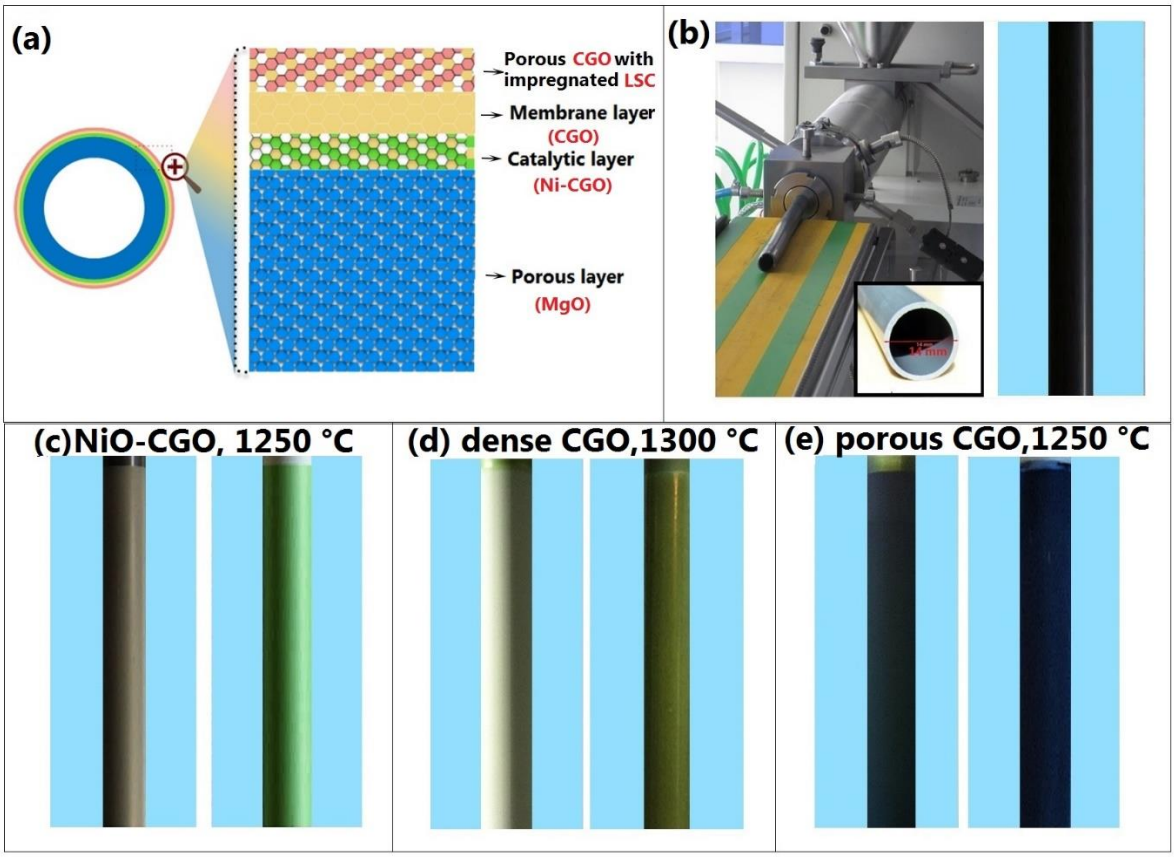

Fig. 11: (a) Schematic of the manufactured asymmetric tubular membrane including the used materials, (b) MgO tubes after thermoplastic extrusion, (c) Catalytic layer of NiO-CGO after coating and pre-sintering, d) Dense CGO membrane layer after coating and sintering, e) Membrane after coating and sintering of porous CGO layer with infiltration of LSC nano particles.

4.3.1. Slurry preparation for the dip-coating process

Three different slurries have been prepared: i) a CGO slurry for the dense membrane layer (CGO-M) ii) a CGO slurry for the porous infiltration layer on the feed side (CGO-P) iii) a NiO-CGO slurry for the activation layer on the permeate side. The slurry compositions are listed in **Table 5**. For the rheology measurement of dip-coating ceramic suspensions, a rheometer (MCR302, Anton Paar, Sweden) was used. For the dense CGO membrane preparation, a pre-calcined CGO powder (high solid loading -10 vol.% for better densification) was dispersed in an ethanol based suspension with polyvinylpyrrolidone (PVP) as dispersant and polyvinylbutyral (PVB) as binder. The resulting slurry for the dip- coating was homogenized by ball milling for 72 h. For the preparation of the catalytic layer on the permeate side, a NiO-CGO (60:40 wt.%) based cermet was used and the porosity will be introduced in the structure due to reduction of NiO to Ni. This NiO-CGO suspension (total solid loading 5-6 vol.%) was prepared with low viscosity in order to cover the MgO tube surface properly and to produce a very thin layer of coating. For the preparation of the catalytic layer on the feed side, a porous CGO backbone has been established from the porous CGO suspension using dip-coating process. This slurry contains about 20 wt.% of graphite pore former in order to create porosity. Later a LSC ($La_{0.6}Sr_{0.4}CoO_{3-\delta}$) solution for the impregnation process has been prepared from the respective nitrate solution of lanthanum (La), strontium (Sr) and cobalt (Co). The reason for using this technique is that the catalytic activity can be enhanced by infiltration of nano particles of these materials into porous backbone structure, since the small of amount material used will not diminish the total porosity of the structure. For the rheology measurement of dip-coating ceramic suspensions, a rheometer (MCR302, Anton Paar, Sweden) was used.

Table 5. Composition of NiO-CGO, dense (CGO-M) and porous (CGO-P) ethanol based suspensions.

Components	**NiO-CGO (60:40)**	**CGO-M**	**CGO-P**
Nickel oxide	5-6 vol.%	---	---
CGO (Low surface area) pre-calcined at 1000°C		10 vol.%	4-5 vol.%
Surfactant, PVP K10	3 vol.%	4 vol.%	5 vol.%
Graphite	---	---	20 vol.%
Binder, PVB K90	3 vol.%	5-6 vol.%	5-6 vol.%

4.3.2. Coating and co-sintering of the functional layers

For the dip-coating of the three functional layers, an in-house constructed dip-coater has been used. The dip-coating speed can be controlled accurately by a step engine, thereby allowing a very precise control of the thickness and evenness of the coatings. The coating speed of 2.5 mm/s was employed all the experiments. As shown in **Fig. 11**, the catalytic layer of NiO-CGO was coated on the green MgO tube and pre-sintered at 1250 °C, followed by dip-coating and sintering of the second functional layer of dense CGO and finally the porous CGO layer.

The porous MgO layer was prepared by thermoplastic extrusion of the feedstock containing ~66 vol.% of binder organics and fugitive pore former. In order to remove the organic media, a de-bindering and sintering cycle has been developed. **Fig. 12** shows the sintering steps for the MgO substrate and the co-sintering of the three functional layers such as the NiO-CGO layer, the dense CGO layer and the porous CGO layer. Optimized heating rates of 0.25 °C min^{-1} and 0.5 °C min^{-1} were used in the 1st cycle for the de-bindering and the sintering regime, respectively. A holding time of one hour at 300 °C, 400 °C and 670 °C was implemented during the de-bindering cycle to ensure complete removal of organic matter. The temperature was further raised to 1250 °C in order to initiate the partial sintering with the NiO-CGO layer, and to improve the mechanical strength for safe handling during subsequent dip-coating of membrane layers.

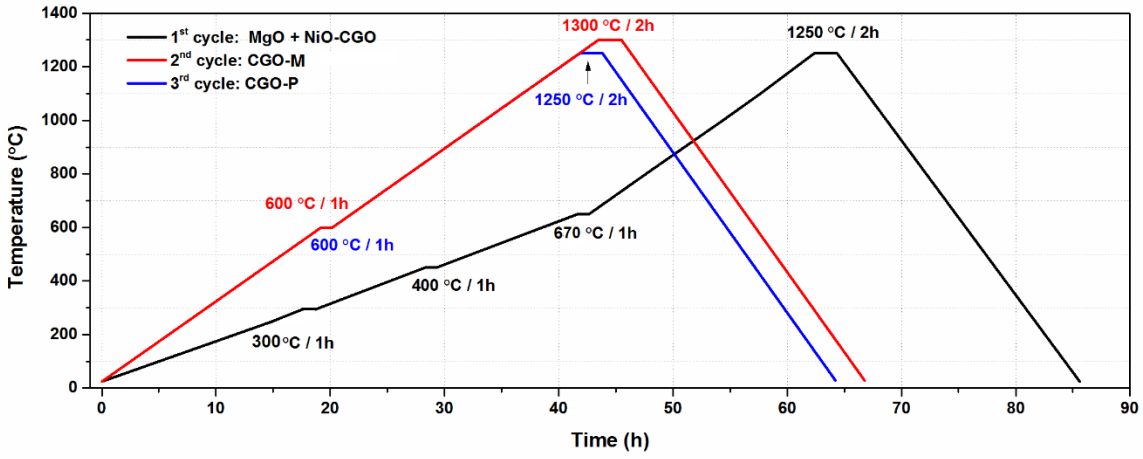

Fig. 12: De-bindering and sintering cycles used for co-sintering of tubular membrane.

Before coating of the membrane CGO layer, the pre-sintered sample was coated again with a single coating of the NiO-CGO suspensions in order to close any pores that may have developed during the pre-sintering

of the NiO-CGO layer. The CGO membrane suspension was coated on the outside with NiO-CGO layer two times to improve the chances of gas tightness of the dense membrane layer and to obtain a final sintered thickness of approx. 20 to 30 µm. After the coating, a heating rate of 0.5 °C min^{-1} has been employed for 2nd cycle, and a dwelling period of 1 h at 600 °C was applied to binder removal and later elevated to 1300 °C for 2 h (as shown in **Fig. 12**).

Finally, the outer (porous) CGO layer is dip-coated on the already sintered CGO dense layer. The component was sintered at 1250 °C for 2 h. Subsequently, an aqueous solution (1 M) of the nitrates corresponding to the nominal composition ($La_{0.6}Sr_{0.4}CoO_{3-\delta}$) was impregnated into the porous CGO layer 3 to 4 times and it was thermally treated at 200 °C after each impregnation. Finally, the infiltrated component was de-bindered at 400 °C to remove the polymer (surfactant, pluronic P-123) from the impregnated solution prior to the membrane testing.

4.3.3. Testing of asymmetric tubular membranes

An illustration of the oxygen permeation test setup is shown in **Fig. 13**. The tubular membrane is connected to alumina tubes via specially designed alumina transition pieces. The transition pieces and the sample are mounted at room temperature using a glass ceramic paste consisting of Na_2O: 17.8 mol.%, Al_2O_3: 9.4 mol.%, and SiO_2: 72.8 mol.% and an organic solvent. Upon heating to approximately 900 °C this glass ceramic paste can flow and seals the transition piece to both the membrane and the alumina tubes. The temperature near both ends of the tubular sample is monitored by two thermocouples located inside the transition pieces. Due to the length of the sample and the transition pieces, a temperature difference of approximately 10 °C was measured at high temperature (900 °C). The alumina tubes connecting the tubular membrane sample is connected to the gas supply system of the rig. The lower alumina tube connects to the gas supply system where a variety of gasses can be prepared/supplied. When there is a difference in the chemical potential of oxygen between the two sides, oxide ions will be transported through the membrane, resulting in a net flux of oxygen through the membrane. The difference in chemical potential is typically realized by flowing air to one side of the membrane (the feed side) and a sweep gas such as nitrogen or hydrogen to the other side of the membrane (the permeate side).

The upper alumina tube, in which the permeate gas flows, is connected to an oxygen partial pressure sensor and a mass flow meter. On the feed side of the membrane (outer side of the membrane) 30 NL/h (NL = Normal liters) air was flowed at all times. On the permeate side of the membrane different flows of nitrogen where utilized in order to characterize the membrane performance as a function of the flow rate. The oxygen

flux through the membrane was calculated using the mass balance from the flow of the sweep gas and the inlet and outlet oxygen partial pressures of the sweep gas from the equation 1 [39]. It should be noted that there is a slight overpressure inside the tube, therefore it is known that the quantity of gaseous oxygen that is transferred to the permeate stream via leaks/pinholes in the membrane is very limited.

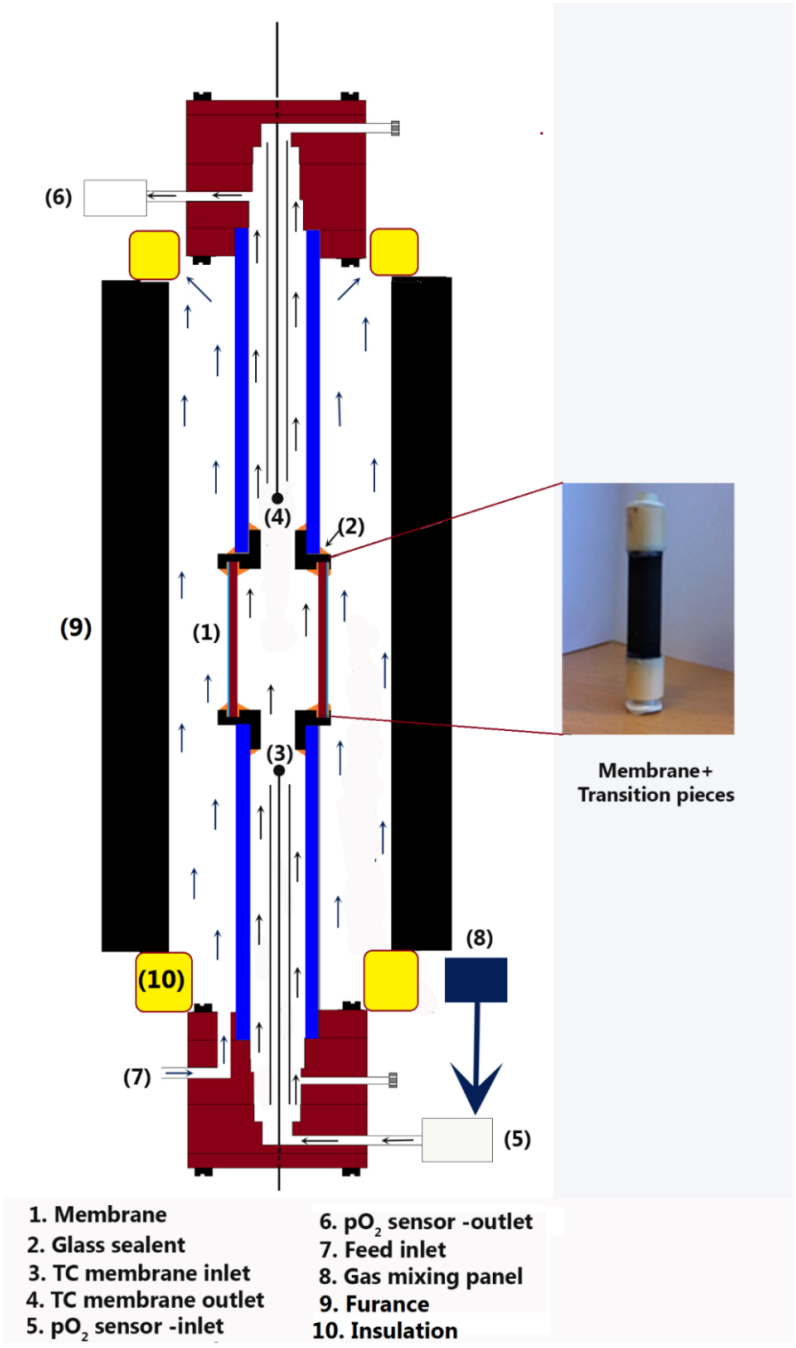

Fig. 13: Schematic of the membrane rig setup.

5. Results and discussion

This section will highlight the results on the development of an asymmetric thin film ceria membrane supported by a porous magnesium oxide support. Section **5.1** describes the considerations for the design of a thermoplastic feedstock composition that can result in MgO support tubes with required properties for use in the asymmetric membrane. Section **5.2** deals with the fabrication and characterization of MgO support structures and the effect of feedstock composition and sintering temperature. Section **5.3** describes how the use of two different fugitive pore formers can improve the gas permeability of the MgO support and also includes a cost analysis of the MgO support for further commercialization. Section **5.4** summarizes the fabrication and sintering of a full asymmetric membrane by application of dip-coated catalytic layers and the CGO membrane. Section **5.5** describes the results of oxygen permeation measurements on the asymmetric membrane.

5.1. Design of thermoplastic feedstocks for porous MgO supports

MgO feedstocks were prepared with different combinations of ceramic, polymer and pore former content in order to achieve form-stable components with the desired functional properties. **Fig. 14** shows a ternary compositional diagram used to visualize the feedstock development, where the fractions of ceramic (MgO), polymer and pore former are shown. For compositions with very high solids loading (MgO and graphite) of more than 65 vol.%, the feedstock could not be homogenized due to incomplete wetting of the polymer and a very high viscosity (referred to as the "unmixable region"). At very high polymer contents above 65 vol.%, especially at high ratios of polymer to ceramic, the MgO structure deformed or collapsed during the shaping or heat treatment; this region is labeled "form instabilities". In the region in the center of the ternary diagram (where the polymer and graphite content exceeded 65 vol.%) the prepared feedstocks were form-stable during extrusion, but the MgO structures were not mechanically stable after sintering. Hence, only the white area of the compositional diagram, representing successful samples, was investigated in further detail. The data points in this region illustrate the three strategies for systematically studying the feedstock compositions (1) varying the polymer concentration (red data points, samples MP1-5), (2) increasing the pore former concentration with a fixed MgO content (blue data points, samples PG2-3) and (3) increasing the pore former concentration with a fixed polymer content (black data points, samples MG2-4).

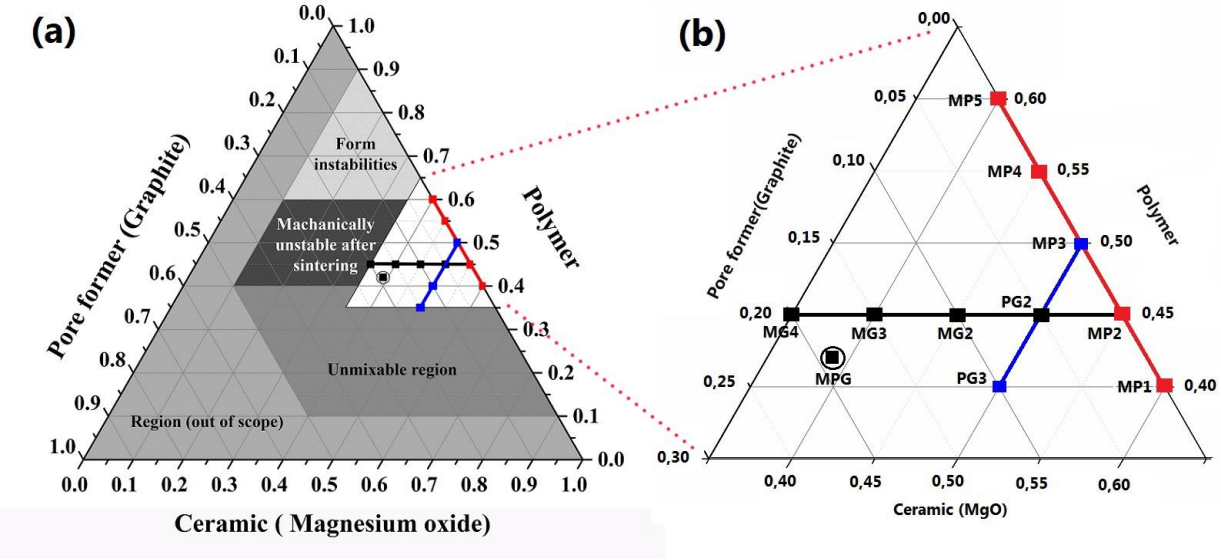

Fig. 14: (a) Ternary compositional diagram for thermoplastic MgO feedstocks, (b) the region of feedstocks suitable for the extrusion process.

5.2. Properties of MgO support tubes related to feedstock compositions and sintering temperature

For the preliminary studies on feedstock development, all samples were warm-pressed and sintered at 1275 °C for 2 h with a heating rate of 30 °C/h. The shrinkage, porosity, gas permeability, mechanical properties of the MgO support as a function of feedstock composition, sintering temperature and pore former type were discussed in this section.

5.2.1. Role of feedstock compositions

Fig. 15 summarizes the properties of MgO supports of different feedstock compositions after sintering at 1275 °C for 2 h. In **Fig. 15 (a)** as expected, the shrinkage and the porosity of the sintered MgO increased gradually from 15 % to 21 % and from 9 % to 18 %, respectively, with increasing polymer content from 40 % to 60 % (MP1-MP5). It is clear that the porosity can be adjusted by simply changing the powder/polymer ratio, which is an advantage of using thermoplastic processing. However, even at the highest polymer content of 60 vol.% (the limit for producing a stable ceramic structure), the observed porosity of 18 % is considered too low for sufficient gas permeability. Hence, the addition of a pore-former was required to

create additional porosity. In **Fig. 15 (a**) it can be also seen that the packing density of the green warm-pressed samples increased gradually with increasing polymer content, clearly indicating that the flowability of the feedstocks increased. **Fig. 15 (b)** shows the properties of the MgO support which is prepared with addition of pore former. In order to achieve high porosity values, the amount of pore former was gradually increased (replacing the polymer) at constant MgO powder concentration of 50 vol.%, as shown by the blue line in **Fig. 14**.

Fig. 15 (b) shows that the porosity could be significantly increased from 13 % to 31 % by the addition of 10 % graphite in the MgO feedstock. It can be seen that feedstock PG3 (with 10 % graphite) had a low packing density in the green state of 0.88. This indicates that (under the conditions used here for warm pressing), a polymer content of 40 vol.% is too low to achieve a homogeneous green body without small air inclusions. Hence, for this system, it can be concluded that the lower limit of the polymer content is above 40 % in order to avoid air inclusions in the feedstock and subsequent processing problems.

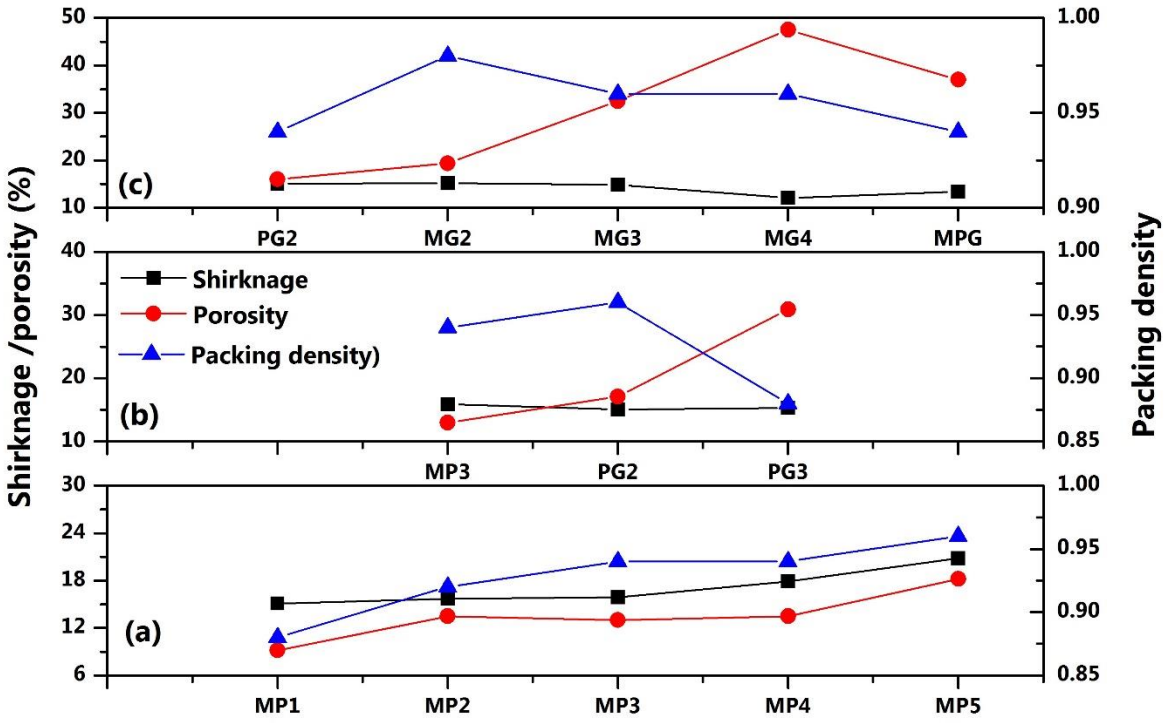

[a] Packing density is defined here as the geometrical green density compared to the expected green density calculated from the densities and concentrations of each component.

Fig. 15: Properties of MgO support layers with different feedstock compositions; (a) decreasing the polymer concentration (MP1-5), (b) increasing the pore former concentration with a fixed MgO content (MP3, PG2-3) and (c) increasing the pore former concentration with a fixed polymer content (PG2, MG2-4, MPG), sintered at 1275 °C for 2 h.

Thus, in a further part of this study the pore former content was increased linearly at a constant polymer content of 45 vol.%) and MgO supports properties were invested. **Fig. 15 (c)** shows the effect of graphite content (5 to 20 vol.%) on the properties of the sintered MgO (constant polymer content of 45 vol.%, sintered at 1275 °C). Meanwhile, the packing density of >90 % was achieved for all feedstocks. Also shown in a **Fig. 15 (c)** are the data for MPG (19 vol.% graphite) which lie between those for MG3 and MG4 with respect to graphite content and final porosity. This composition was selected for further study as its porosity was within the targeted range (35-40 %) and it showed the best overall behavior during processing (of the studied samples within the operational window shown in **Fig. 14**). Also, large quantities of MPG (hereafter called as MP-FL) could be easily processed and hence this composition was considered suitable for up-scaling of the process in the future.

The MgO supports need to be characterized to in order to evaluate their functionality as a support for membrane application. One very important property for application is a high gas permeability (in the order of 10^{-15} m^2) to ensure transport of gasses through the relatively thick porous ceramic support layer [1]. Furthermore, the microstructure of the support (porosity, pore size distribution) which influences the above properties is strongly depending on the fabrication [75], especially on the sintering conditions. The following section will discusses the relationship between sintering temperature and resulting microstructure of the MgO support.

5.2.2. Role of sintering temperature

In the case where the MgO support will be co-sintered with a membrane layer, the densification behavior of the support during sintering must closely match that of the membrane to avoid mechanical failures e.g. cracking or delamination. Another challenge is to select a co-sintering temperature where the membrane can be fully densified while keeping sufficient porosity in the support. Hence, it was necessary to investigate the effect of sintering temperatures (2 hours holding time) on the porosity of the MgO. This was done by sintering warm-pressed samples of MPG at 1250 °C, 1300 °C, 1350 °C or 1400 °C for 2 h and analyzing the resulting porosity by Hg porosimetry. The pore size distributions of the MgO supports measured from Hg porosimetry are shown in **Fig. 16**. For sintering temperatures of 1250 °C and 1300 °C bi-modal pore size

distributions with two distinct peaks are observed; the first peak with an average size below 0.1 µm and the second peak including pores above 0.3 µm. This second peak is present for all four sintering temperatures. It is obvious that with increasing sintering temperature (from 1250 °C to 1350 °C) the smaller pores are completely eliminated from the MgO skeleton. Therefore, the porosity below 0.1 µm will disappear with high sintering temperatures (1350 °C and 1400 °C). The pore size measured by Hg intrusion (**Fig. 16**) is significantly smaller compared to the microstructural observations [37]; this discrepancy can be explained by the formation of bottleneck pores (e.g. submicron pores) which connect the larger (micrometer range) pores. In the Hg porosimetry technique the pore size is calculated from the pressure required to push the Hg through the sample and hence the pore throat (smallest diameter of the pore) will give the measured pore size. It can be clearly seen that the pore throat size increased with temperature because of the densification of the MgO skeleton, and that the total porosity decreased with increasing sintering temperature until the sintering temperature reached 1350 °C. There was no further decrease in porosity observed at 1400 °C. The strong decrease in porosity in the temperature range 1250-1350 °C was a result of the elimination of the small pores in the MgO skeleton (as evidenced by the disappearance of the smaller pore size peak in **Fig. 16**).

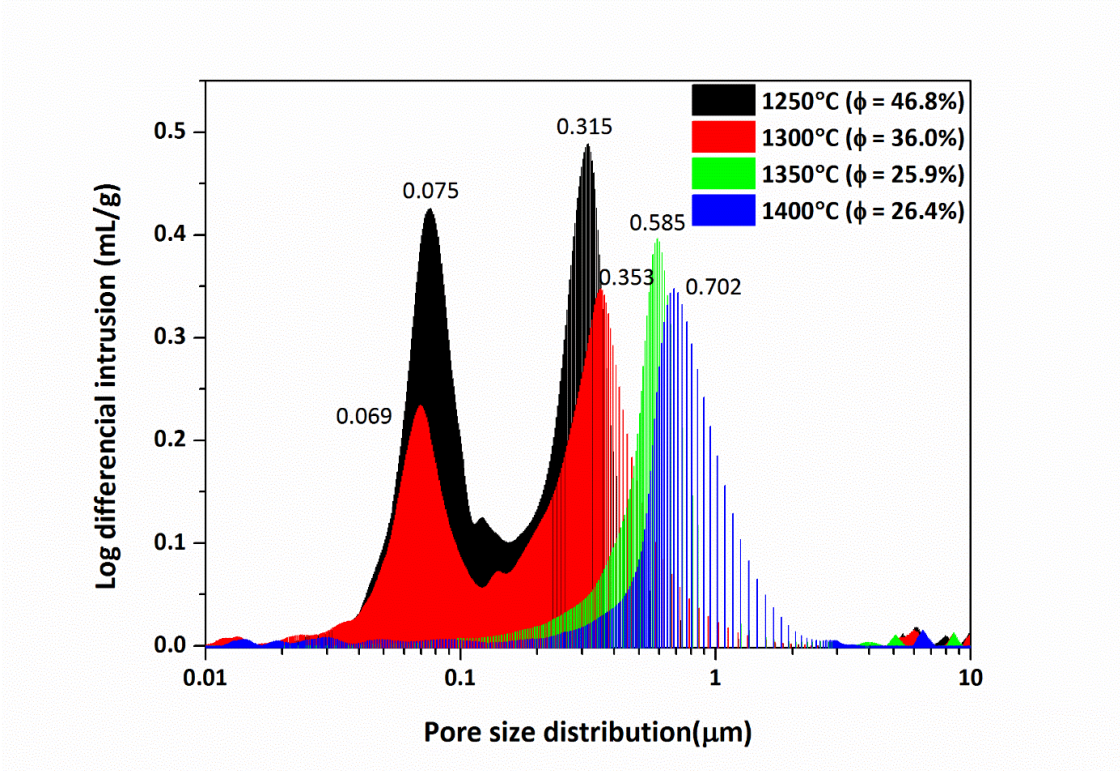

Fig. 16: Influence of the sintering temperature (T) on the pore size distribution of MgO supports (T = 1250 °C, 1300 °C, 1350 °C and 1400 °C at 2 h holding time). The corresponding open porosity is denoted by ϕ.

To conclude from this section, it can be stated that the feedstock compositions have been optimized with respect to the porosity and sintering behavior of MgO supports. The ratio between ceramic, polymer and graphite has been varied and investigated the influence MgO supports properties. A total porosity up to 36 % and an average pore size ~0.35 µm were achieved using a feedstock with 19 vol.% graphite pore former (particle size ~10 µm) at 1300 °C. A significant increase was also observed in the pore size through the porous MgO supports when the sintering temperature was increased from 1300 to 1400 °C. However, the gas permeability and mechanical properties of the supports need to be characterized in order to evaluate the support functionality. Therefore, further experiments are being undertaken to characterize these functional properties and also to enlarge the average pore size of the MgO supports prepared by extrusion using different type of pore formers (spherical graphite and PMMA), which will be discussed in the following section.

5.2.3. Role of pore former type

In this section the design and fabrication of porous MgO support structure produced by thermoplastic feedstocks using graphite (flaky, spherical), PMMA as pore former is described. Various thermoplastic masses (feedstocks) have been prepared (as described in section **4.2**) and the composition details can be found in section **4.2.1.**

In the previous section **5.2.2** we have shown that a total open porosities of between 26 % and 36 % can be achieved in MgO supports at sintering temperatures that might be sufficient for co-sintering of a full asymmetric MgO-supported CGO membrane at temperature between 1300 °C and 1350 °C. However, data of open porosity is by itself not sufficient to describe the required functionality for application in OTM. Since three different types of pore formers were used in the feedstock formulation, a study of binder removal (de-bindering process) was conducted to ensure form-stable and defect-free structures. A detailed evaluation of the thermal analysis (related to this de-binding study) is presented in **Publication II**. Thus, this section will provide a detailed discussion about the pore size distribution, gas permeability, mechanical strength and the microstructure of the porous MgO support material as a function of pore former type and sintering temperature.

5.2.3.1. Porosity and pore size distribution of MgO supports

The MgO supports were sintered for 2 h with different peak temperatures of 1250 °C, 1300 °C, 1350 °C and 1400 °C after implementing the de-bindering cycle shown in section **4.2.5.** Furthermore, the supports were studied by the mercury intrusion method to investigate the influence of open porosity and pore size distribution (**Fig. 17**). The highest porosity of 52.5 % was achieved for MP-SP at 1250 °C as seen in **Fig. 17 (**b), consisting of a large volume of small and big pores. In **Fig. 17**, it can be seen that the small pores (<0.1 µm) developed by decomposition of the low melting point polymers were eliminated with increased sintering temperatures, indicating how the support was densified by collapsing these small pores for all three supports. However, there is an indication of mean pore size enlargement with increasing sintering temperature. From **Fig. 17** (a) it can be seen that for MP-FL supports, the total porosity decreased with increasing temperature, except for the sintering temperature of 1400 °C where the average pore size increased from 0.60 to 0.68 µm at constant porosity. Therefore, it is thought that the MP-FL support sintered at 1400 °C should have better gas permeation properties than the support sintered at 1350 °C. In the case of MP-FL, **Fig. 17** (b) it shows a linear trend of decreasing porosity with increasing sintering temperature, and also a gradually increasing average pore size from 0.2 to 0.39 µm. Meanwhile, MP-PM, **Fig. 17** (c), showed very drastic changes in the pore size occurring between 1250 and 1300 °C by eliminating most of the micro pores (0.1 µm) and doubling average pore size from 0.16 to 0.30 µm while eliminating 24 % of total pore volume (porosity decreased from 38 to 29 %). The MP-PM support also shows a same trend with temperature like MP-SP, but the total porosity is reduced to almost half of that of MP-SP at 1400 °C and there is no significant pore size enlargement observed after 1300 °C. It eventually confirms that it has the least open pores and poor connectivity, which may resist gas permeation resulting in insufficient gas supply for the final application.

Fig. 17 (d) compares the pore size distribution of three MgO supports sintered at 1300 °C. The reason for considering this temperature is due to the possibility that suitable sintering and densification behavior can be achieved with thin CGO membrane for the final application. **Fig. 17** (d) shows the bi-model pore size distribution for MP-FL and mono-model distribution for MP-SP and MP-PM. Considering the average pore size and total pore volume, it can be assumed that MP- SP should have higher gas permeation value than other two supports since it has same pore size of ~0.33 µm and porosity of 5 to 13 % higher than other two supports.

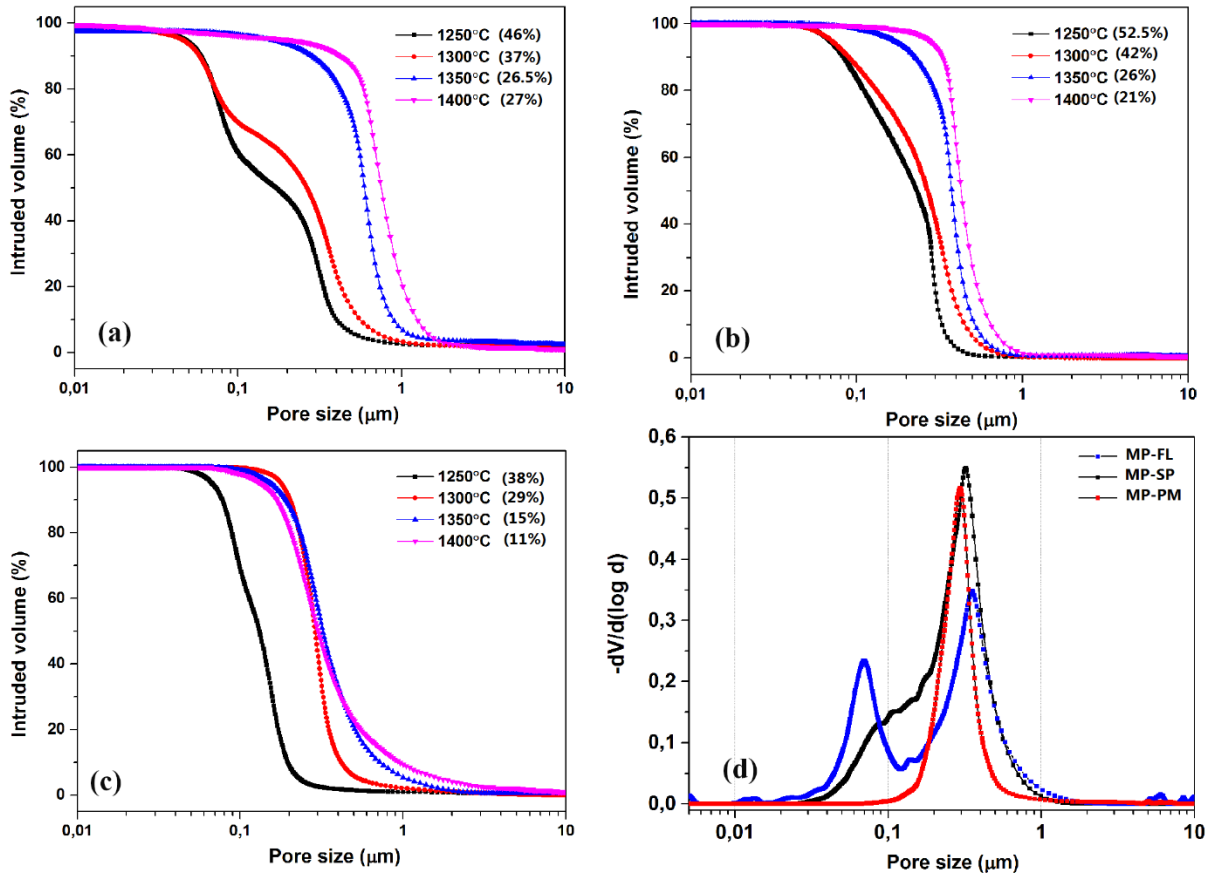

Fig. 17: The intruded volume in different pore sizes for different MgO supports, (a) MP-FL, (b) MP-SP and (c) MP-PM as a function of sintering temperature and (d) differential intruded volume against pore size distribution of the three supports. The corresponding open porosity is given in the brackets.

5.2.3.2. The gas permeability of MgO supports

The measured gas permeabilities and porosity of the MgO supports are presented in **Fig. 18** as a function of sintering temperature. This study indicates a strong correlation between the permeability and the open porosity, as expected. From **Fig. 18**, it is seen that the permeability is highest for the sample sintered at 1250 °C for all three cases, then it decreases strongly when increasing the sintering temperature to 1300 °C. Increasing the sintering temperature further to 1350 °C and 1400 °C increases the permeability again, such

that for the 1400 °C sintered sample it is almost at the same level as the sample sintered at 1250 °C for MP-FL supports. The reason for this behavior is due to the enlargement of the pores without an increase in the total open porosity. The decrease in permeability of the sample sintered at 1300 °C compared to 1250 °C originates from the decrease in porosity and the formation of randomly oriented larger elongated pores that may restrict the gas transport pathway.

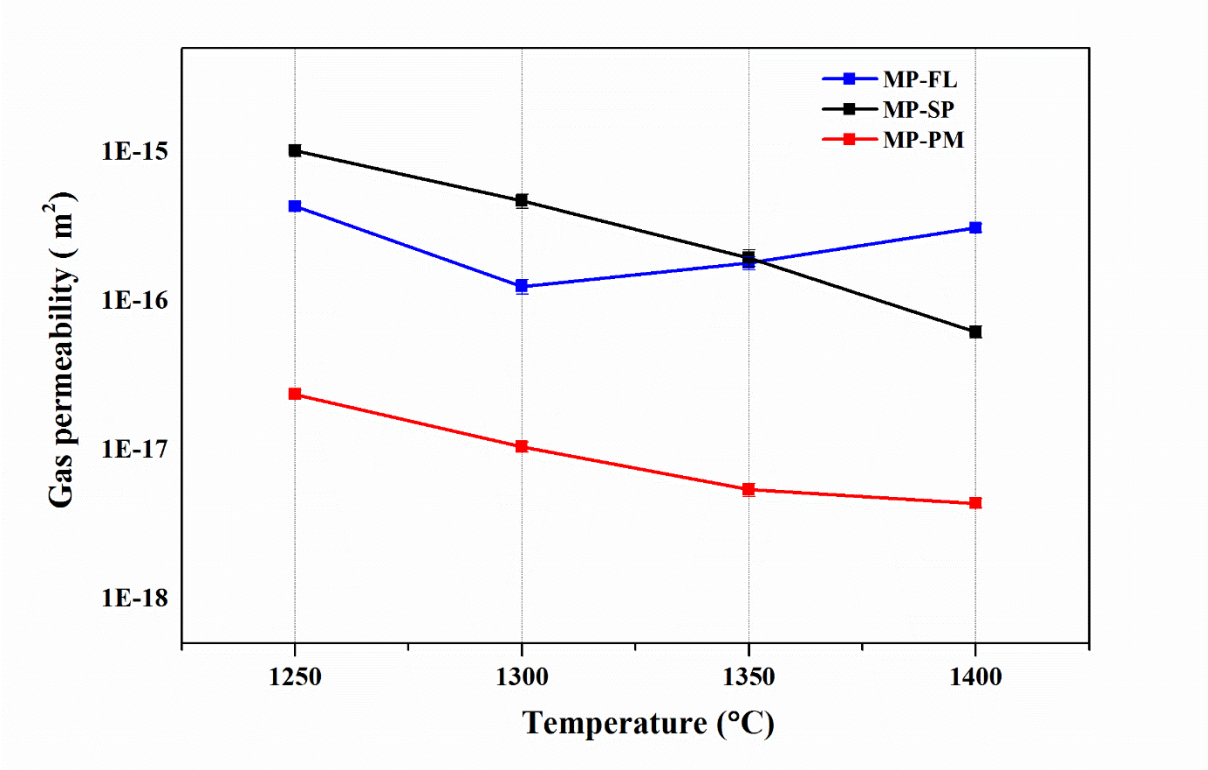

Fig. 18: The measured gas permeability at a ΔP of 2 bar as a function of sintering temperature of the MgO supports.

The decrease in the gas permeability of samples sintered at the higher temperatures is attributed to the decrease in open porosity and less pore connectivity; this may increase the resistance to gas flow. However, the MP-SP shows almost 40 % higher gas permeabilities than the MP-FL due to a high open porosity of 52.5 %, and it also depends critically on the microstructure (pore size, shape and interconnectivity (tortuosity)) [37]. At 1350 °C, both supports (MP-FL and MP-SP) had similar open porosities and also almost the same gas permeation value and pore size distribution (**Fig. 17** and **Fig. 18**). At 1400 °C MP-FL exhibits higher porosity and permeability than MP-SP, and also the mean pore size increases to 0.75 µm compared to 0.42 µm for MP-SP. It can be concluded that sintering the MgO support at high temperature improves

the pore size enlargement by sacrificing some open porosities. But this behavior is more significant for MgO supports with flaky graphite (MP-FL) than others two supports. In the case of MP-PM supports, the achieved permeability value was almost 1.5-2 orders of magnitude lower than for the other two MgO supports for all sintering temperatures (about 4.4 $\times 10^{-18}$ m^2 to 2.4 $\times 10^{-17}$ m^2). However, the highest gas permeation value of 4.7 $\times 10^{-16}$ m^2 was achieved for MP-SP at 1300 °C. Moreover, this type of MgO will be further investigated in order to optimize the pore former content using a combination of two pore formers such as a polymer (PMMA) and spherical graphite, which have different decomposition temperatures. We propose that this type of sample could be easily de-bindered and sintered without any shape instability and defects. However, the PMMA content can also compensate for some of the thermoplastic binder (Elvax), so it can be beneficial in two aspects where it acts as both binder and pore former, which ultimately enhances the plasticity, extrusion processability and improves the open porosity as well.

5.2.3.3. Assessment of mechanical behavior of MgO supports

With respect to the mechanical properties of supports for OTM, the number of studies is limited. Porous substrates made for membranes needs first to be characterized for mechanical properties in order to evaluate its suitability. There are some studies on BSCF materials for membrane application, and the elastic modulus and toughness of porous BSCF were reported for both room and operation temperature [46]. In other studies, a MgO substrate was considered as the porous support layer for the membranes, and fracture stresses of 36 ±6 MPa were obtained for a substrate with porosity of 36 ± 5 % [76] , which is similar to the value reported for porous CGO substrate [43]. For reliability considerations, the high temperature strength of the porous supports is the critical property to be characterized. This entails testing a large number (~30) of samples which is extremely time-consuming. For this reason, many reported strength values were based on a small sample size and are subjected to considerable uncertainties. Kawai et al. [46] proposed a testing methodology for tubular ceramics to circumvent the difficulty.

The mechanical properties of three porous MgO supports have been investigated at room and elevated temperature (850 °C) in order to analyze the mechanical stability of these components for final membrane applications. The fracture probability distributions at 25 ˚C and 850 ˚C are plotted in **Fig. 19** and **Fig. 20**, respectively.

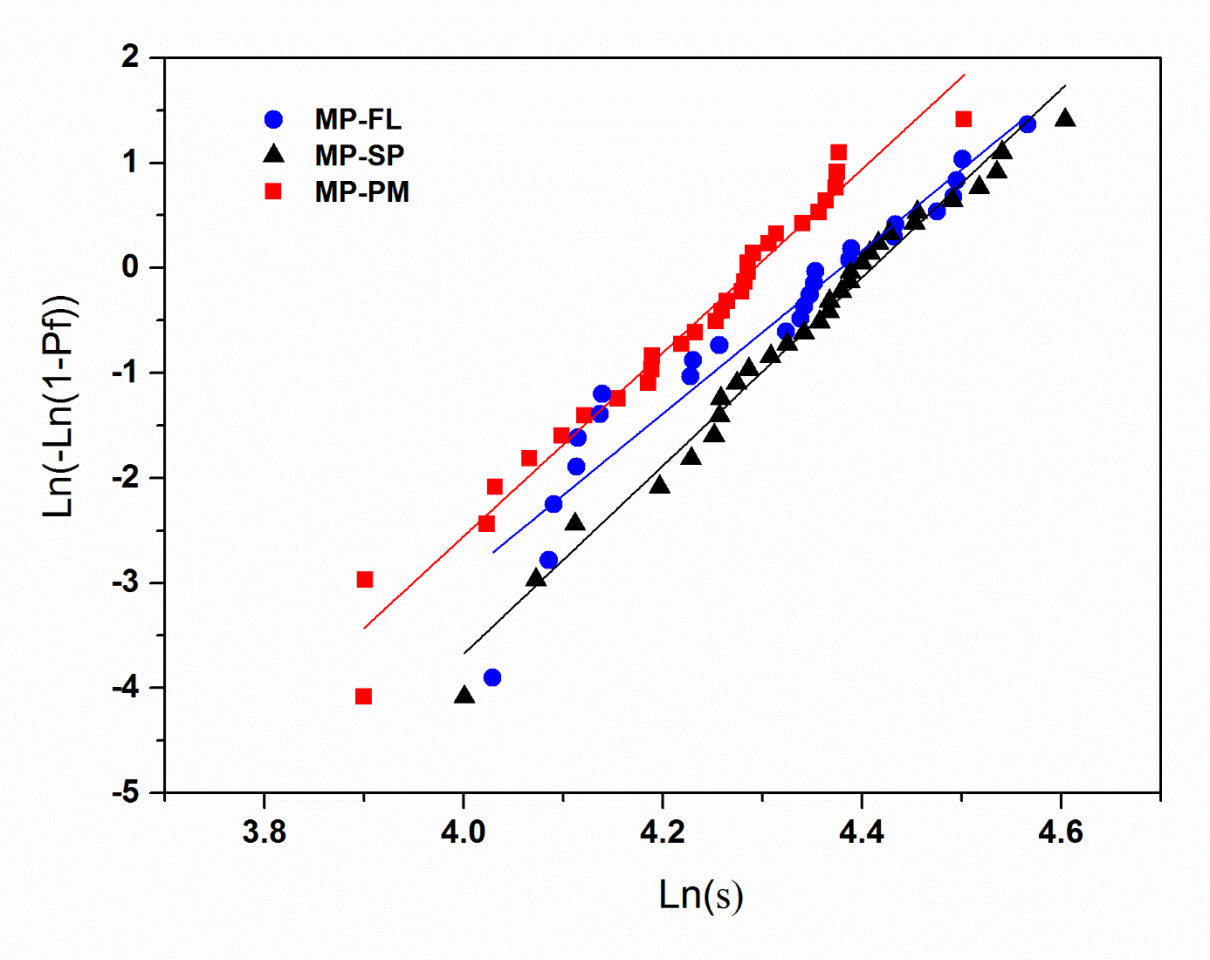

Fig. 19: Fracture probability of MgO supports at 25 ˚C for all three supports sintered at 1300 °C.

As shown in **Fig. 19**, the measured elastic moduli for MP-FL and MP-SP agree quite well with the empirical model. For MP-PM, the measured modulus is lower than what the empirical model predicted. The elastic moduli for the three types of supports decrease slightly with temperature, in the order of 7 - 9 GPa. For applications as support materials, a low elastic modulus is preferred, because a more compliant support induces smaller stresses in the membrane [64]. The Weibull moduli for MP-SP are the highest among the supports investigated. This suggests that the spread of flaw size distribution is the narrowest, which is desirable for such a component.

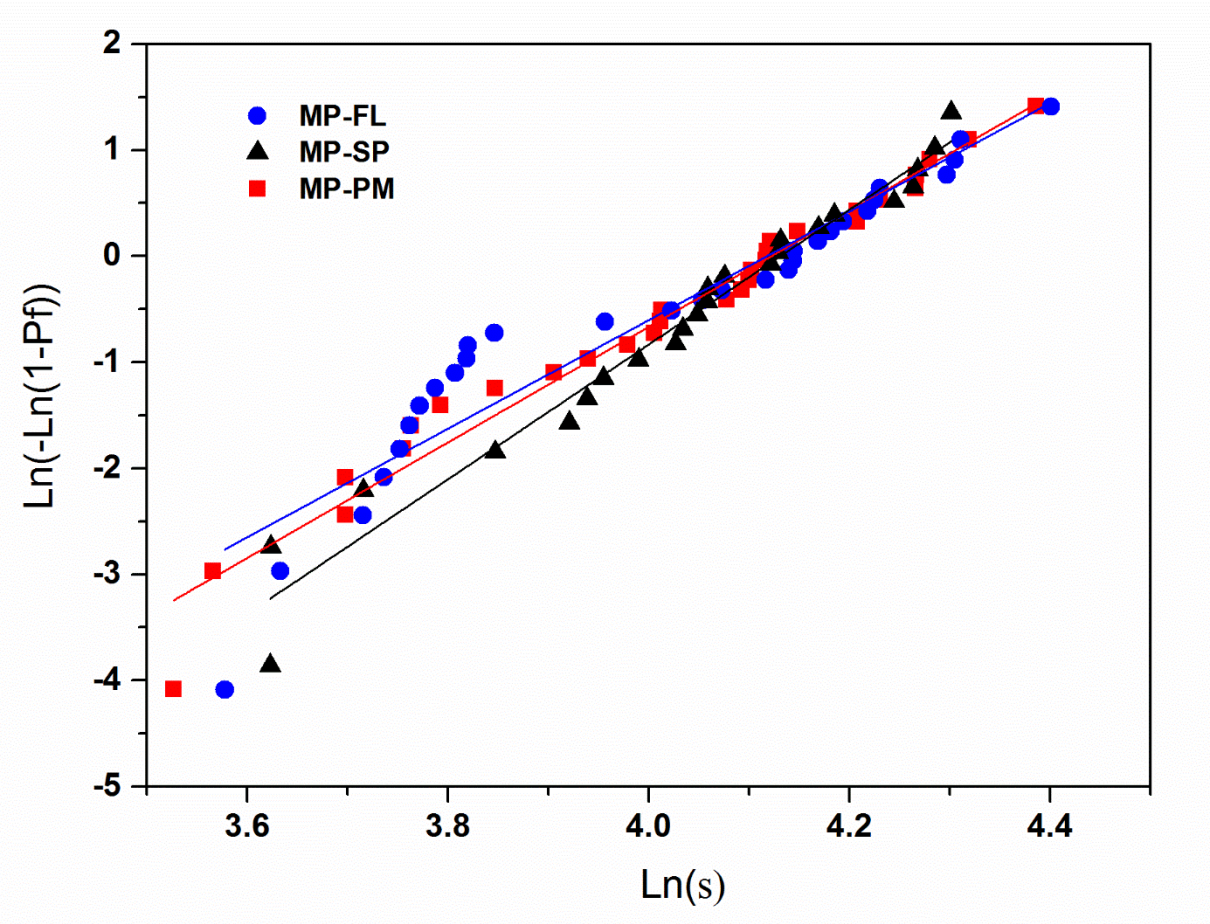

Fig. 20: Fracture probability of MgO supports at 850 ˚C for all three supports sintered at 1300 °C.

At room temperature, MP-FL and MP-SP have similar characteristic strengths with a difference within the statistical uncertainty. The porosity difference of 6 % between the two supports has little influence on the strength. Despite having the highest solid volume, the characteristic strength of MP-PM is lower than the other two supports. This is attributed to the large isolated pores which act as points of crack initiation.

The Weibull moduli at 850 ˚C were found to be lower than those at 25 ˚C for all three supports. The differences are however within the limits of uncertainty due to finite sampling. Since the Weibull modulus is a measure of the spread of the critical flaw size, it is not expected to correlate with temperature. Overall, the Weibull moduli for the three supports are typical for ceramics.

To correctly compare the characteristic strengths of different supports, the measured strength values at different effective volumes need to be scaled to the same effective volume using the relation:

$$\left(\frac{\sigma_0{}'}{\sigma_0''}\right)^m = \frac{V_{eff}{}''}{V_{eff}{}'}$$

where $\sigma_0{}'$ and σ_0'' are the characteristic strengths at the effective volumes $V_{eff}{}'$ and $V_{eff}{}''$.

Table 6 shows the comparison of characteristic strength of different supports scaled to the same effective volume of 10 mm^3. The characteristic strength of porous BSCFZ support reported in a previous study [46] is also shown for comparison. All supports show a decrease in characteristic strength going from 25 ˚C to 850 ˚C. The drop in strength is primarily due to the reduction in elastic modulus with temperature.

Table 6. Characteristic strength of porous supports scaled to an effective volume of 10 mm^3.

Temp (°C)	MP-FL	MP-SP	MP-PM	BSCFZ[46]
25	76.07	77.05	68.58	21.15
850	60.48	59.72	60.61	16.94

To summarize, the resultant MgO supports has decent gas permeabilities and sufficient mechanical strength which may perform successfully when it integrated into membrane. The evaluation of shrinkage and porosity of the membrane and support layer calculated by experimental and model will be discussed in the section **5.4.3.**

5.2.3.4. Microstructural analysis of porous MgO support structures

After mechanical testing, three types of MgO support's microstructures (polished cross sections) were investigated by electron microscopy, as shown in **Fig. 21**. All three different MgO supports show different microstructures due the different properties and particle sizes of the pore formers. Micrographs indicate that one support (MP-SP) has a better pore connectivity than the other which ideally enhances gas permeation value. The microstructure is an agreement with what expected from the gas permeation results in section **5.2.3.2**. In the case of MP-PM, there are some big isolated pores which can be easily visualized in **Fig. 21** (c). The weak pore network eventually deteriorates the gas permeation properties, which is the reason why MP-PM ended up with lower gas permeation value of 1.04 $\times 10^{-17}$ m^2.

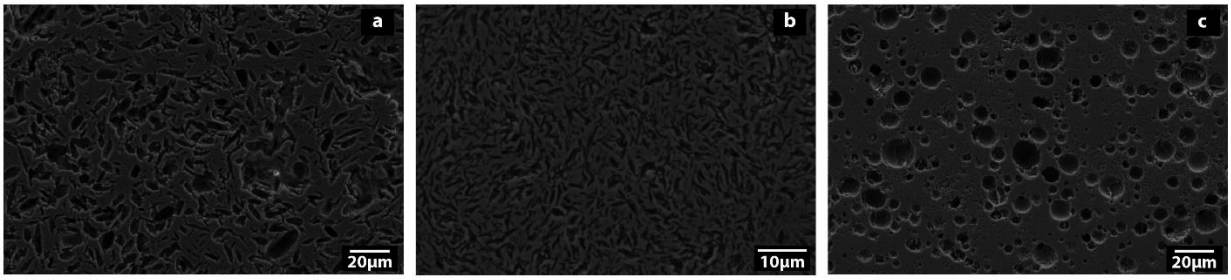

Fig. 21: SEM micrographs of polished cross sections of MgO supports sintered at 1300 °C a) MP-FL, b) MP-SP and c) MP-PM.

In order to calculate the mean pore size of the MgO supports from SEM 2D images, an image analysis code in MATLAB was used. This simply selected the right threshold point in order to distinguish two different phases; ceramic and pore boundaries. It is also well known that the pore size determined by Hg porosimetry indicates the pore neck size and always underestimates the real pore size which is shown in the SEM images. **Table 7** shows the mean size of pore former, pore size, pore neck size (Hg porosimetry) and neck to pore ratio for all three supports sintered at 1300 °C.

Table 7. The pore size characteristics of three MgO support sintered at 1300 °C.

Code	Pore former µm	Pore size (Image analysis) µm	Pore neck size (Hg porosimetry) µm	Size ratio (Neck to pore) %
MP-FL	11.3	10.3	0.36	3.5
MP-SP	5.5	2.8	0.34	12.0
MP-PM	10.5	7.9	0.30	3.8

As can be seen from **Table 7**, it is important to calculate the neck to pore ratio, as this value indicates how well the pores are connected with each other. It was observed that a higher neck to pore ratio of about 12 % was achieved for MP-SP whereas for the other two supports this ratio was under 4 %. Ultimately, the pore structure of MP-SP is beneficial in both ways; the smaller pore and larger neck size improves mechanical strength and gas permeability, respectively.

5.3. Enhancing the gas permeability of supports by different fugitive pore formers

Previous work on MgO supports with a porosity of 42 % have shown that for these structures a gas permeability (Darcy) of about 4.2 $\times 10^{-16}$ m^2 can be reached [37]. This needs to be improved to avoid gas transport limitations for membrane layers as we stated earlier. In this study, the MgO supports were prepared with two pore formers (a combination of PMMA and spherical graphite) and characterized further by measuring the gas permeation performance. Moreover, a detailed economic analysis on the commercialization of MgO support was carried out.

The feedstock was prepared with vol.% ratios of 1.2:1.5: 1 for MgO power, polymer and pore former, respectively, in which the spherical graphite to PMMA ratio is about 2:1. The kneaded feedstock was shaped into planar substrates and sintered at 1300 °C for 2 h and later used for characterization of porosity and gas permeability measurements.

5.3.1. Gas permeation performance

Fig. 22 shows the measured gas flux and the calculated permeability as a function of the pressure difference (ΔP) across the porous substrate. The measured gas flux versus the pressure difference curve showed an almost linear trend for all ΔP. Increasing the pressure from 25 kPa to 150 kPa, did not result in any changes in permeability, and there was no influence from the pressure gradient. An increase in gas permeability was observed when a pressure beyond 150 kPa was reached; this increase was attributed to increased gas access to small pores in the support which enhanced the gas permeation. It is well known that the gas permeation depends not only on the absolute percentage of porosity, but also critically on the microstructure (pore size, shape and interconnectivity (tortuosity)). The newly developed MgO substrates exhibit gas permeation values of about 4-4.5 $\times 10^{-15}$ m^2. In any case, the achieved permeability value of the porous MgO support in the present study is almost 7 to 8 times higher than the acceptable range. The high permeability measured on the MgO support forms the basis for further studies on integrating these substrates into high performance perovskite and fluorite based membrane materials.

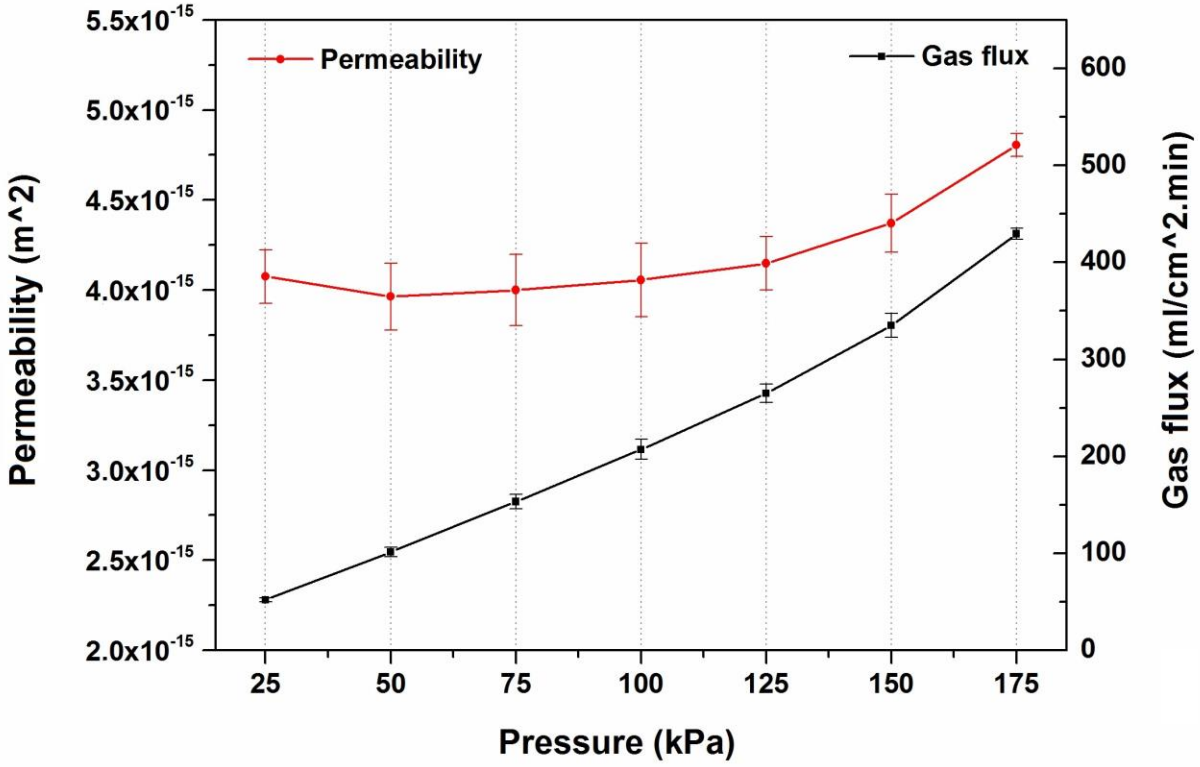

Fig. 22: The measured gas permeability and gas flow as function of ΔP from 25 to 175kPa.

To summarize, the porous MgO supports with high porosity of 55 % are prepared by the warm pressing method using pre-treated MgO powder. Spherical graphite and PMMA were chosen as pore-forming agents. The mean pore size of the porous MgO ceramics, sintered at 1300 °C, was about 0.65 µm. The microstructure indicates interconnected pores of a wide size range (0.1 to 10 µm), resulting in a high gas permeation value of 4-4.5 $\times 10^{-15}$ m^2, which is sufficient when integrated into a high performance perovskite and fluorite based membrane for syngas production environments.

5.3.2. Economic analysis

The cost analysis of porous MgO support was done by considering a small sized production facility located in India with monthly production capacity ~ 3 tones (2000 m^2) finished goods. To calculate the membrane cost, all costs involved in the production processes should be assessed carefully to make a better estimate, as presented in **Table 8.** The direct cost involves mainly the costs directly associated with the manufacturing of the product such as the cost of materials and routing (operation and manpower) cost). Moreover, indirect

costs (utilities, rent, audit and administrative staff) are included into the product cost, and is considered to be 50 % of WIP (work in progress) cost. Finally, membrane cost is assessed to be 150 $/m^2 including a pricing factor of 10. It was earlier reported that a clay based microfiltration membranes can be prepared with 61 $/m^2, in which only the raw material cost was considered to estimate the membrane cost [77]. A systematic cost analysis should including manufacturing and logistics cost while comparing the membrane cost to the commercially available membranes. In comparison with fluorite and perovskite materials, MgO is 15-30 times cheaper in terms of the material cost, making it a low-cost potential support material for asymmetric oxygen transport membranes [78]. More details on the cost analysis can be found in the **Appendix VI**.

Table 8. Membrane cost analysis from production of a sample size of 2000 m^2

Details	**Total for 2000 m^2 (USD)**	**Cost/m^2 (USD)**
Raw materials cost	12500	6.25
Process wastage (20 % of RM cost)	2500	1.25
Production cost	5000	2.5
Indirect cost (50 % of WIP cost)	10000	5.0
Total cost	30000	**15.0**
Pricing factor (5-10 times)		**(75-150 $)**

5.4. Fabrication of asymmetric ceria based membranes

The aim of this study is to develop a thin tubular asymmetric CGO membrane supported on a porous MgO structure. The porous MgO and functional layers (catalytic and membrane layers) were fabricated by thermoplastic extrusion followed by dip-coating. Ethanol based stable ceramic suspensions were prepared in order to achieve thin, uniform and defect free layers. The sintering regime has been tailored to completely remove binder and organics and to attain the desired microstructure development. Recently Liu et al. [48], demonstrated that a crack-free asymmetric tubular perovskite membrane with a thickness of 20 µm could be prepared using extrusion and a spray drying processing step and also stated that the oxygen flux performance was almost 1.35 times higher with the asymmetric configuration than the symmetric system. It is therefore evident that the membrane performance and stability could be improved by an asymmetric configuration. Hence, this section briefly discusses the fabrication and sintering of asymmetric ceria based membranes.

The fabrication of asymmetric tubular membranes consist of a number of process steps in which the porous MgO support (MgO-S) was first fabricated using thermoplastic extrusion and the membrane (CGO-M), the catalytic layer (NiO-CGO) and the porous backbone layer (CGO-P) were prepared through a dip-coating process (more details can found in **Publication V**) from stabilized ceramic suspensions. This was followed by impregnation of catalytic material into the porous backbone on the outside of the membrane. Since the preparation and characterization of the porous layer was discussed in the previous section, this section will only discuss the preparation and testing of the membrane layer.

In order to prepare a thin membrane layer, the stable ceramic suspensions for dip-coating have to be developed and the rheological properties of such suspensions have been characterized to give information on the expected quality of the layer thickness and the smoothness of the coated surface. The rheological measurements show that the highest viscosity of 37 mPa (at a shear rate of 100 s^{-1}) was achieved for the CGO slurry with high ceramic loading (CGO-M) and followed by NiO-CGO with 19 mPa s and the CGO slurry with 14 mPa s. Due to the lower shear thinning effect of the NiO-CGO and CGO-P slurry, the quality of these suspension is considered suitable, since the expected coating surface will smoothen the MgO support surface and enable the application of the thin film CGO layer (CGO-M).

5.4.1. Co-sintering of porous MgO support/dense CGO membrane layer

An important aspect in the fabrication of asymmetric multi-layers with a porous/dense structure is the co-sintering process. In co-sintering, a good match of the shrinkage or strain rate of the main structure, consisting of different membrane layers, needs to be achieved in order to avoid the development of excessive stresses during sintering, which can lead to mechanical failures or warpage in the case of planar structures [43]. For the co-sintering of a tubular support layer of MgO with a CGO membrane the differences in the starting powders (the sintering activity depends on the material and the starting powder's particle size) and the targeted final densities of the layers need to be considered. A thin membrane layer needs to be fully densified (to achieve 100 % gas tightness) on a sufficiently porous support layer (usually 25 to 40 %, depending on the support thickness and microstructure). An excellent tool to describe the shrinkage during a co-sintering process is optical dilatometry [38,79,80]. The densification and strain rate development of single green layers of a MgO extrusion mass and a dip-coating composition (after de-bindering) as function of sintering temperature are shown in **Fig. 23 (a)** and **(b)**, respectively

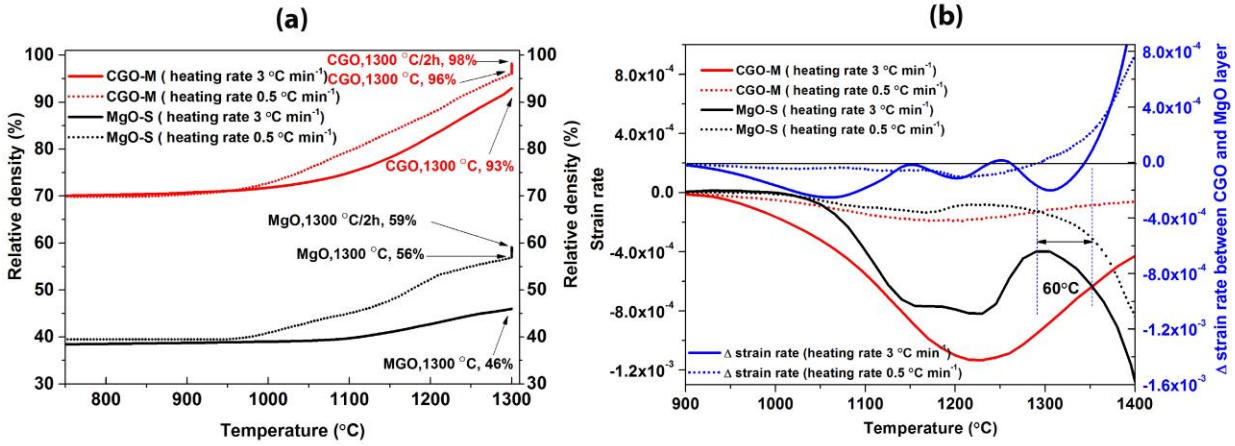

Fig. 23: (a) Densification and (b) strain rates of CGO membrane (CGO-M) and MgO support (MgO-S) layers, as well as strain rate difference between the two different layers for free sintering as function of sintering temperature. Measurements were performed at two different heating rates of 0.5 °C.min^{-1} (dotted lines): and 3 °C.min^{-1} (continuous lines) with an optical dilatometer TOMMI [81].

Fig. 23 (a) reveals that the MgO support structure has a significantly lower starting density (relative density) of about 38-40 % (or 60-62 % porosity) compared to a starting density of about 70 % for the CGO membrane layer. The low starting density of the MgO support (compared to the membrane) is desired and was

achieved by the use of thermoplastic binder and graphite as pore formers in the extrusion mass. The densification of the MgO support structure in a heating cycle is influenced by the heating rate (the total time to reach the final sintering temperature) and the isothermal holding time at the final sintering temperature. Thus, in **Fig. 23** (a) the MgO sintered with the slower heating rate (0.5 °C.min^{-1}) reaches almost 10 % higher final density (56 %) compared to the same material sintered with 3 °C.min^{-1} at a sintering temperature of 1300 °C. Applying additional holding time at 1300 °C further densifies the structure by about 3 %. Therefore, faster heating rates would favour more porous support structures. On the other hand, the densification curves of the CGO membrane layer reveal that the fast heating of 3 °C.min^{-1} to 1300 °C would only lead to a final density of about 93 %, densities of above 96 % could, however, be achieved with an isothermal holding time of a few hours. A slower heating of the CGO layer would lead to higher density.

Fig. 23 (b) shows the strain rates of the MgO and CGO layer at the two different heating rates (0.5 and 3 °C.min^{-1}) and the calculated strain rate differences for the two layers for both heating rates. From such data the formation of stresses between the layers can be estimated, and together with the shape change of complete, tubular bilayer structures the formation of stresses between the layers can be calculated. The strain rate difference between the MgO support and the CGO membrane layer in **Fig. 23** (b) is significantly increasing if the samples are heated faster (heating rate of 3 °C.min^{-1} compared to 0.5 °C.min^{-1}). A larger strain rate difference may drastically increase the risk of the formation of stress-induced defects and delamination. Especially, the larger strain rate difference between the layers in the low temperature sintering regime (900 to 1100 °C) would be critical in a bi-layer structure when the sample is still fragile and sintering necks start to form.

Therefore, if the stress levels do not lead to failure in the low temperature sintering region, a co-sintering with a fast heating rate towards a higher final sintering temperature (and shorter isothermal holding times) could lead to a bilayer structure with a porous support structure and a dense CGO layer. Furthermore, according to previous investigations by dilatometry, electron microscopy and mercury porosimetry [37], the densification between 1250 and 1400 °C is governed by the elimination of smaller submicron sized pores. This leads to shrinkage of the overall structure, but simultaneously also a growth and improved interconnectivity of larger macro pores (introduced by the addition of graphite pore former) which surprisingly resulted in improved pore connectivity and gas permeability of the support structure.

5.4.2. Microstructure of asymmetric MgO supported CGO membranes

After the successful completion of the co-sintering of the membrane, gas-leakage was tested to ensure that the membrane is free from processing defects. The test verified that the membranes were gas tight (for details on the gas leakage measurements refer to section 2.3). **Fig. 24** shows SEM images of thermally etched cross sections of the (a) full membrane, (b) interface of Ni-CGO and MgO porous layer after reduction, (c) dense CGO layer, (d) porous NiO-CGO layer and (e) porous MgO layer. Marco-defects or cracks have not been observed in the sample. **Fig. 24** (c) shows a cross section of the CGO layer thermally etched, showing well-densified CGO with grain sizes in the range of 0.5 to 1.5 µm. **Fig. 24** (d) shows the porous Ni-CGO layer. The grains in this layer are well interconnected with high open porosity and an average grain size of 1-1.5 µm. The MgO support layer did not show any evidence of anisotropy in the porosity distribution (see **Fig. 24** (e)). The measured porosity of the MgO layer was 42 % and the observed mean grain size was 2-3 µm. From **Fig. 24** (b), it can be seen that some densification has occurred at the interface due to strong interaction between NiO and MgO. It is reported in the literature that the Ni/MgO phase exhibits high catalytic activity in POM operation, since elemental nickel can be dispersed uniformly in the interface and eventually enhance the catalytic reaction [82]. Hence, the occurrence of densification in the interface will not affect the membrane performance. On the other hand it also improves the mechanical stability between the interfaces of the MgO and the Ni-CGO layers.

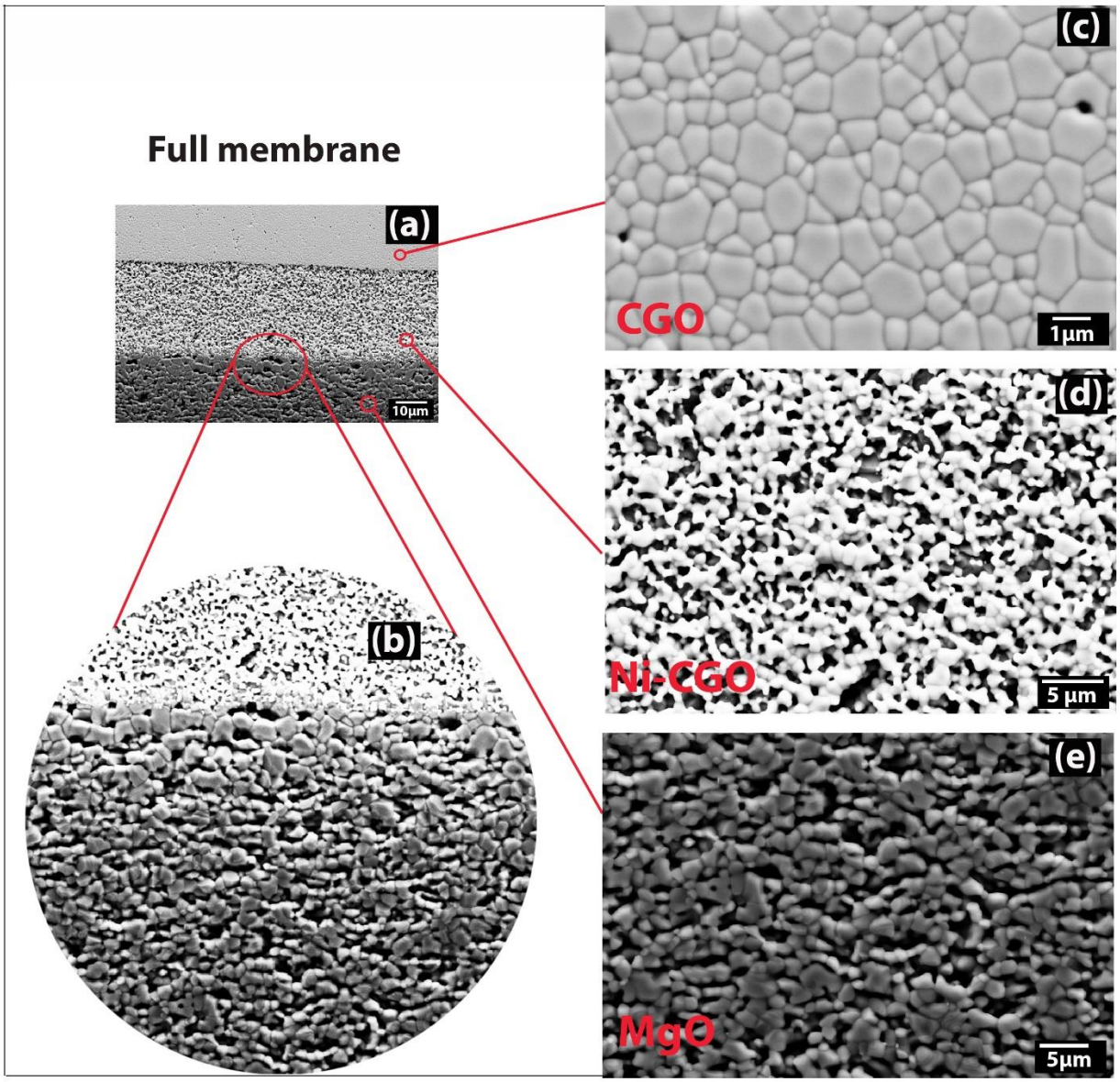

Fig. 24: SEM Micrographs of thermally etched surfaces of three different layers (a) full membrane, (b) the interface of the Ni-CGO and MgO porous layer after reduction, (c) dense CGO layer, (d) porous NiO-CGO layer and (e) porous MgO layer.

5.4.3. Experimental studies on sintering of bi-layered tubular membranes for model applications

Failure in asymmetric oxygen transport membranes do not necessarily origin from defects in the support structure (e.g. due to de-bindering of porous MgO supports as discussed in **Publication II**), but might also be caused by unfavorable densification behavior of different layers in a multi-layer structure during co-firing. Constrained sintering of tubular bi-layered structures is of general interest because it is being used in the development of various technologies. An analytical model has been developed by **TT Molla** (PhD student) to describe the densification and stress developments during constrained sintering of tubular bi-layered samples. For validating the analytical model, model input parameters, such as the shrinkage kinetics and viscous parameters for a bi-layered tubular supported ceramic oxygen membrane based on porous MgO and $Ce_{0.9}Gd_{0.1}O_{1.95-d}$ layers have been measured experimentally. This section discusses the experimental results of the bi-layered system compared to the results obtained by the analytical model.

For this study, the de-bindered bi-layered sample was pre-sintered/sintered at different temperatures (650 °C, 850 °C, 1000 °C, 1100 °C and 1300 °C) followed by cooling down to room temperature. The bi-layers were checked for defects after each respective temperature cycle and simultaneously the necessary data were collected for comparison with the model. **Fig. 25** shows a schematic cross section and a photo of the MgO tube with a dip-coated CGO layer after heat treatment to 650 °C.

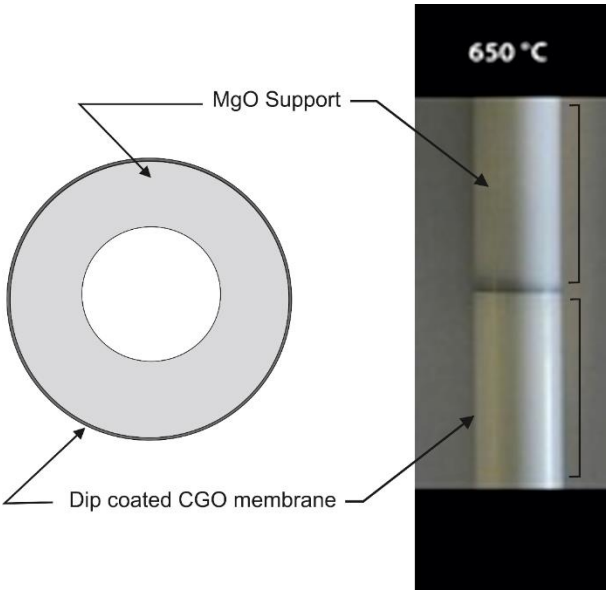

Fig. 25: Schematics of the cross section (left) and picture of the asymmetric bi-layer tubular sample (right) consisting of dip-coated CGO-membrane and MgO-support at 650 °C.

5.4.3.1. Evaluation of shrinkage and porosity by experiments and model

The shrinkage in each layer was calculated from the sample thickness after each thermal treatment. The sample thickness was measured using scanning electron microscopy, SEM (TM300, Hitachi, Japan by taking the average values of thickness from four measurements. Similarly, the porosities in each layer were calculated using the SEM images from the sample at each temperature.

To evaluate the shrinkage and porosity, **TT Molla** has established an analytical model using a Matlab program in which some material parameters need to be given. The cross section of a porous bi-layered tubular structure made of a support and a membrane as shown in **Fig. 26**. The tubular structure has the internal and external radii of r_i and r_o and an interfacial radius of r_f in between the support and membrane.

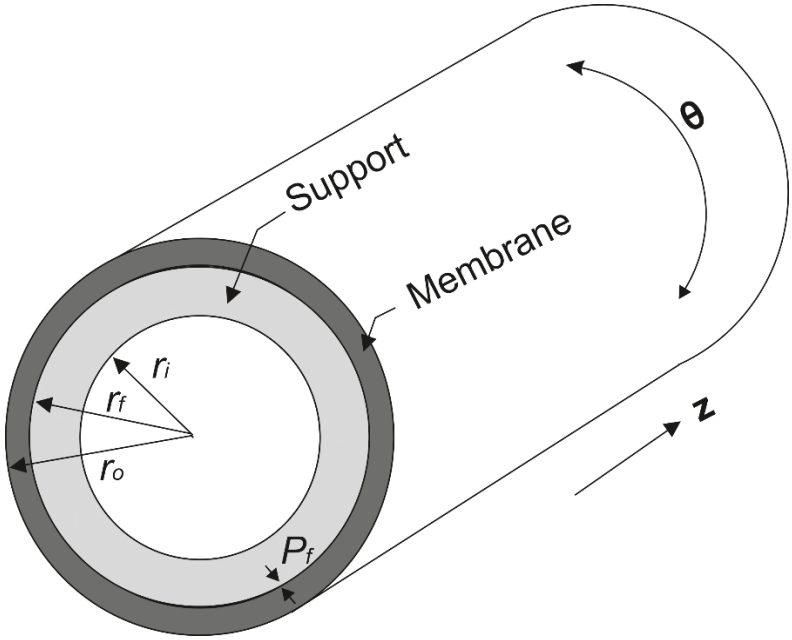

Fig. 26: Schematic cross section of porous bi-layered tubular structure.

In this model, it was considered that the viscous strain rate of an isotropically deforming body is directly proportional to the stress components, which indicates a direct correspondence between linear elasticity and linear viscous theories [83]. Therefore in this work, the analogy between linear elasticity and linear

viscous theories, the elastic-viscoelastic correspondence principle [84], has been used to describe the densification and stress developments during sintering of the porous bi-layered tubular structures. Further details about the model description and stress calculation can be found in **Joint publication IV (appendix IV).**

5.4.3.2. Shrinkage and porosity: comparison of experimental and model results

Fig. 27 shows the analytical model prediction for the linear shrinkage across the thickness of each layer, in comparison with the free shrinkage data and the measurements taken during the sintering of the tubular bi-layer. Comparisons of shrinkage in the constrained CGO membrane with the free CGO tape shows that the CGO membrane is exposed to tensile stresses, which hinder the densification during sintering of the tubular bi-layer. The constrained shrinkage in the MgO support is almost unaffected by the level of stresses generated in it. The results from the model agree well with the shrinkage measurements from the SEM images of the samples at four different temperatures. It is evident that the linear shrinkage in the CGO membrane dominates the sintering cycle, which exposes it to tensile stress from the MgO support for most of the time.

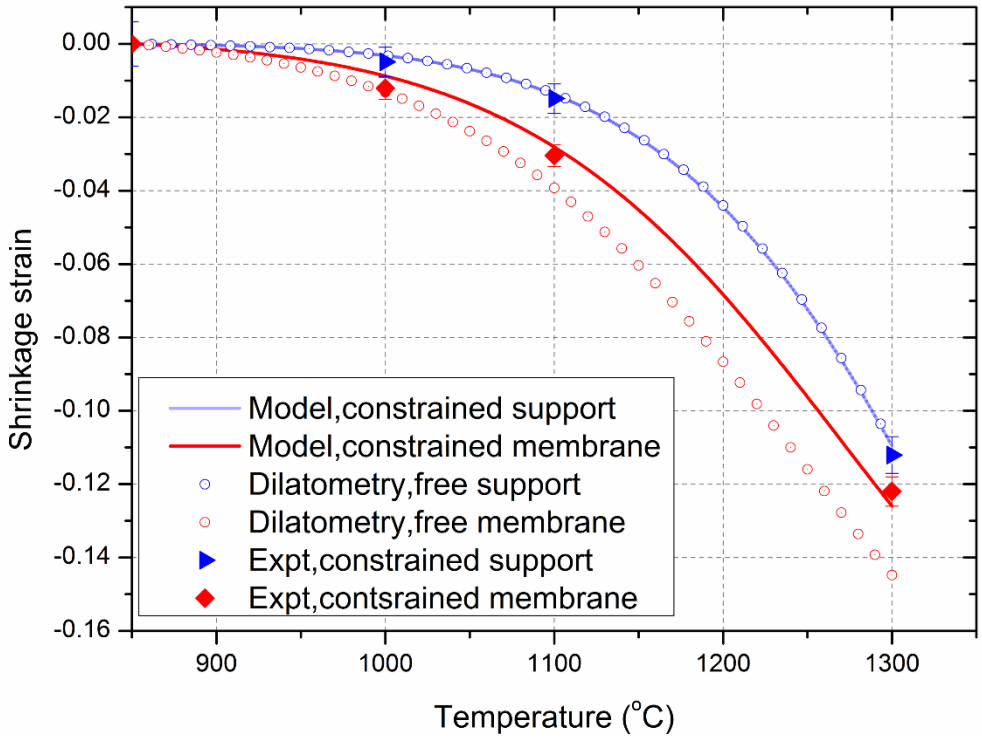

Fig. 27: Comparison of linear shrinkage in free and constrained sintering together with experimental measurements of constrained sintering.

The porosity evolutions in each layer during constrained sintering of the bi-layer tubular sample were measured using SEM images at four different temperatures. **Fig. 28** shows the examples of SEM images of the MgO support and the CGO membrane at 1100 °C. **Fig. 29** shows the comparison between results from the analytical model and measurement values with the standard deviation from the measurement. The standard deviations are deduced from the variations in the thickness observed from SEM images of the layers. Predictions from the analytical model agree well with the measured values in both the support as well as the membrane. Porosity evolution in the case of constrained bi-layered tubular structures is size dependent as the total stress varies with the radius of the sample during constrained sintering of tubular samples.

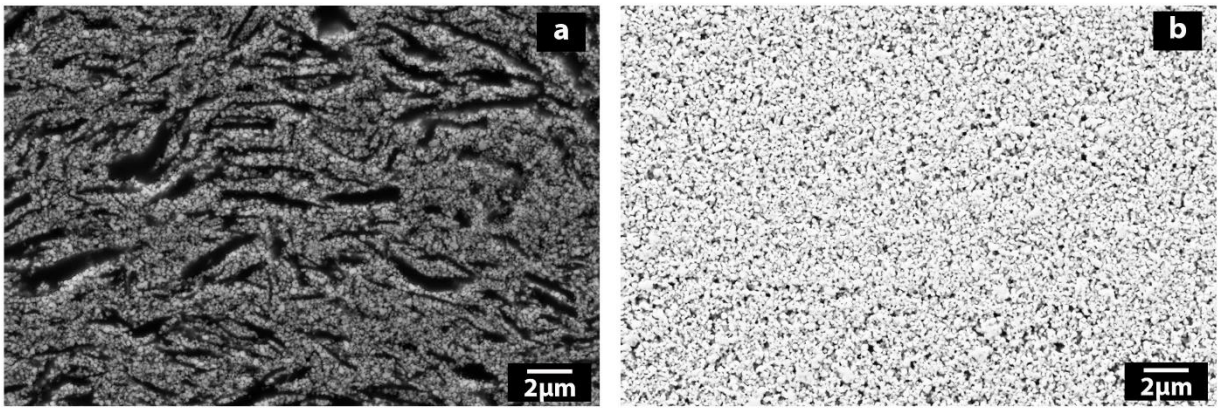

Fig. 28: SEM characterization of the bi-layered tubular sample after sintering to 1100 °C (a) MgO support and (b) CGO membrane.

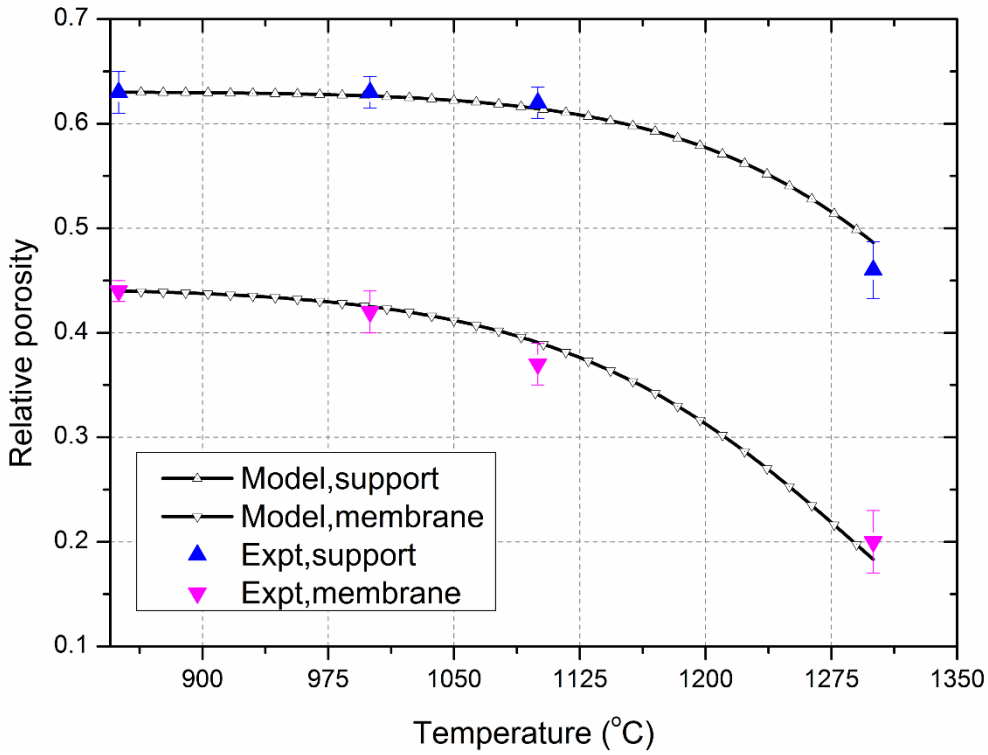

Fig. 29: Comparison of the evolution of porosity from model and experiment during constrained sintering of tubular bi-layer sample.

To conclude, the experimental sintering studies were compared with the analytical model developed by **TT Molla** to study and calculate the densification during sintering of bi-layered tubular supported ceramic oxygen membranes based on porous MgO and $Ce_{0.9}Gd_{0.1}O_{1.95-d}$ layers. It was found that results of shrinkage and porosity from the experiments agree well with the model. The following section **5.5** will discuss the about performance of the thin film ceria membrane.

5.5. Oxygen flux measurements in asymmetric MgO supported CGO membranes

Oxygen permeation measurements were conducted with the test setup illustrated in section **4.4**. For sealing the membrane sample and the transition pieces these were first heated with 500 Nml min^{-1} air on the outside of the tube to a temperature of 917 °C and then cooled to 650 °C. At 652 °C nitrogen was flowed on the inside of the tube at a rate of 100 Nml min^{-1}.

In order to avoid cracking of the membrane due to chemical expansion by subjecting it very fast to a very reducing environment, the membrane was reduced first with humidified hydrogen (app. 3 %) diluted with nitrogen at 650 °C. This was followed by varying the temperature and increasing the hydrogen flow and decreasing the nitrogen flow (see **Fig. 30**). **Fig. 30** shows the oxygen flux of the membrane as a function of the reciprocal temperature for different flows of nitrogen and humidified hydrogen. It is clear that an activation effect of the flux takes place at approximately 800 °C when changing from a gas mixture consisting of 50 Nml H_2:50 Nml N_2 to 100 Nml H_2:50 Nml N_2. The activation is attributed to an increased performance of the permeate activation layer containing Ni. There is a clear thermal dependence of the oxygen flux, and in pure hydrogen the activation energy of the flux is 82.3 kJ mol^{-1}. It is clearly seen that for an increasing inlet hydrogen concentration the oxygen flux also increases, which is attributed to an increase in driving force over the membrane resulting from the increased hydrogen concentration present in the permeate activation layer.

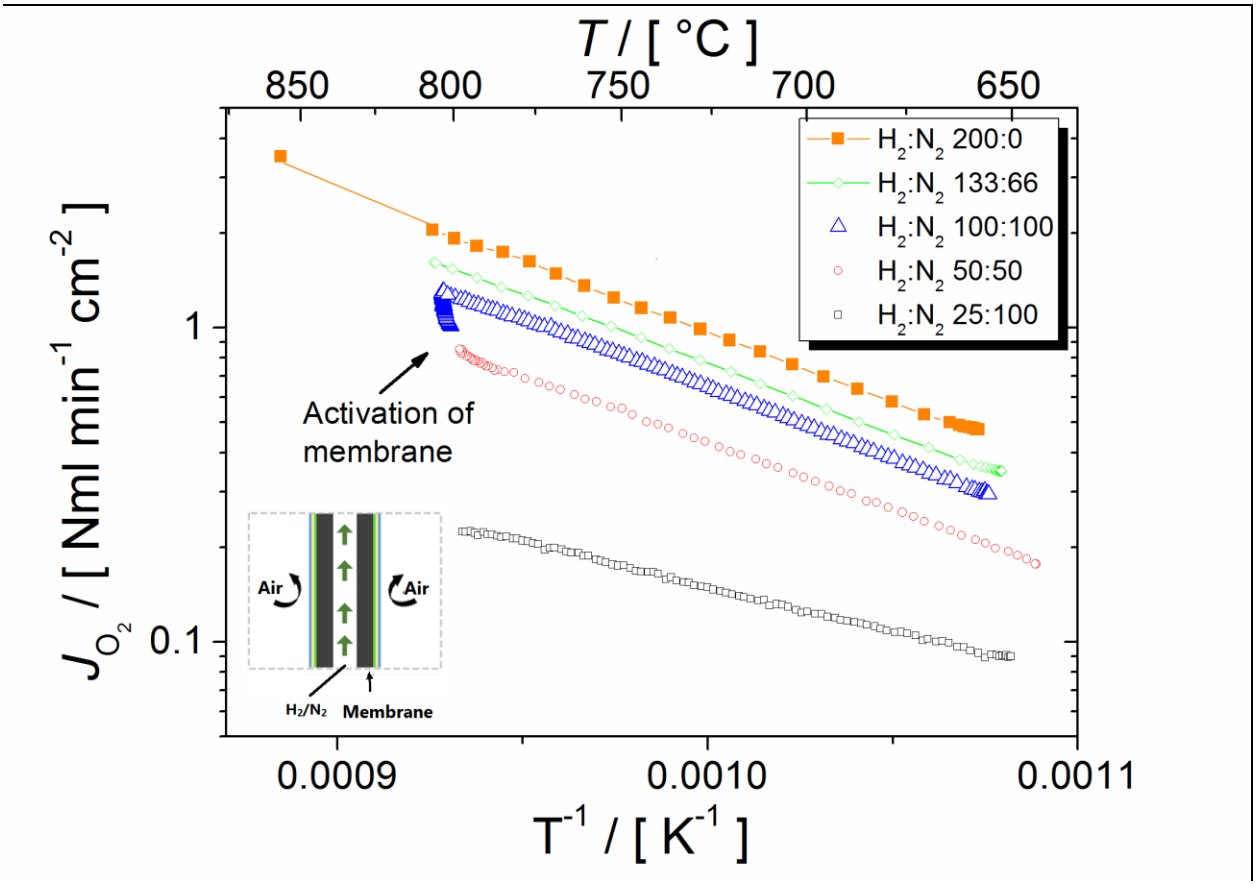

Fig. 30: Flux as function of reciprocal temperature for different hydrogen/nitrogen mixtures. The numbers in the caption all refer to the inlet volume flow of hydrogen and nitrogen in the unit Nml min^{-1}.

The membrane was also heated to higher temperatures than 856 °C in pure hydrogen. However, this resulted in significant condensation in the tubing leading to an unstable signal on the pO_2-sensor downstream the membrane, wherefore the flux values are highly scattered. There was, however, nothing that indicated that the Arrhenius dependency observed for the oxygen flux (see **Fig. 30**) changed. The membrane was held for approximately 80 h in pure hydrogen at 856 °C (±2 °C) without a measurable degradation in the flux.

Heating from 856 °C to 920 °C also resulted in a significantly higher flux, however, this was followed by a rapid deterioration of the flux, to a level below the 856 °C level. This large decrease is tentatively assigned to a coarsening effect of the Ni-CGO layer on the permeate side of the membrane. As it has previously been shown [85] that a redox-cycling of the anode of a solid oxide fuel cell can lead to an improved performance, this was also tried here. The sample was cooled to 650 °C and the anode was oxidized with air (approximately

24 h) and subsequently reduced again with hydrogen. **Fig. 31** shows the flux as a function of reciprocal absolute temperature prior to the high temperature treatment, after the high temperature treatment and after the redox-cycle. The permeate gas is in all cases 3 % humidified hydrogen. It is clear that the redox-cycling of the permeate Ni-CGO layer improves the oxygen flux through the membrane dramatically from 0.5 Nml min^{-1} cm^{-2} to 1.4 Nml min^{-1} cm^{-2} at 660 °C. Interestingly the activation energy changes from 68.6 kJ mol^{-1} (after the high temperature treatment) to 53.3 kJ mol^{-1} (after the redox-cycle). The flux reported in **Fig. 30** is thus to a large extend limited by the Ni-activation layer on the permeate side of the membrane.

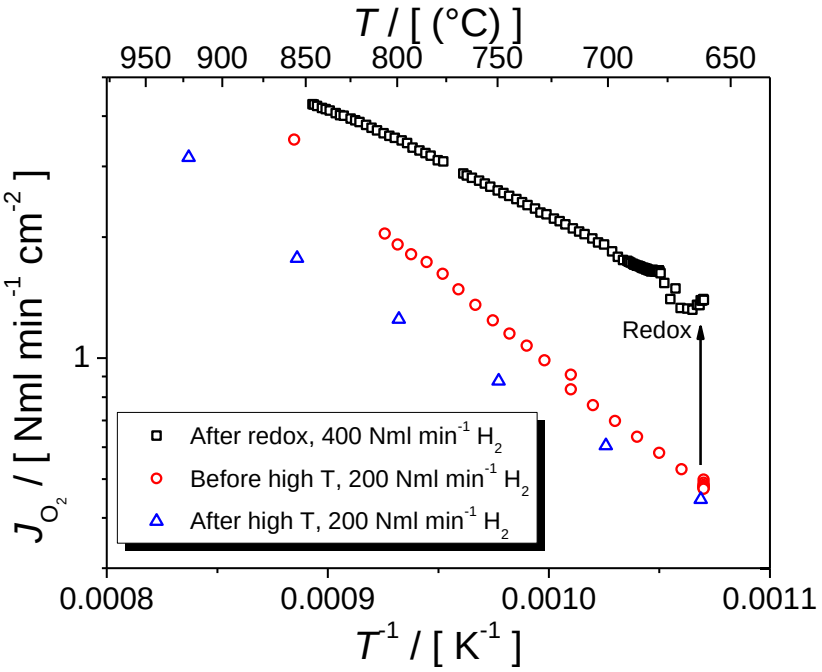

Fig. 31: Flux as a function of reciprocal temperature for three measurement series. Before a high temperature heat treatment at 920 °C, after a high temperature treatment at 930 °C and finally after the high temperature treatment but after a redox-cycling (air for 24 h) of the membrane component at 650 °C.

After the hydrogen tests the membrane was subjected to a mixture of methane (50 ml min^{-1}) and humidified hydrogen (3 % steam) (50 ml min^{-1}) even though this is well within a carbon forming regime, however, the flow from the membrane terminated after approximately 30 min of operation indicating a failure of the membrane.

An asymmetric tubular CGO membrane has been successfully prepared by an extrusion and dip-coating process. A gas-tight CGO membrane with a thickness of 31 µm was obtained. The optimized de-bindering and sintering regime with a very slow heating rate 0.25 °C min^{-1} and 0.5 °C min^{-1} was used to achieve gas tight thin membranes and desired porosity with catalytic and porous support layer. The MgO supported asymmetric CGO membrane exhibits gas permeation flux of 3.5 $ml.min^{-1}.cm^2$ at temperature of 856 °C with sweep gas (H_2) flow rate of 200 Nml min^{-1}. A redox-cycle of the Ni-CGO catalytic layer, did improve the permeation flux of the membrane, reaching 4 Nml min^{-1} cm^2 at 850 °C.

6. Summary and conclusion

Carbon dioxide (CO_2) is a greenhouse gas which is largely emitted from chemical, power generation and cement industries and pollutes the environment. Carbon capture and storage (CCS) is one approach for reducing CO_2 emissions in an attempt to overcome current global warming issues. Oxy-fuel power plants can be made more efficient and cleaner by combusting the coal using pure oxygen instead of air. Practically, pure oxygen is conventionally produced by cryogenic distillation in large scale or by pressure swing adsorption in small scale [1]. Oxygen transport membranes (OTMs) are promising as an alternative to the conventional processes of supplying oxygen into high temperature combustion processes and integrating them with higher efficiencies. By using pure oxygen, the NO_x emissions in exhaust gas can be eliminated, and remaining CO_2 and H_2O can be then more easily separated for CCS. Furthermore, OTM can be used as chemical reactors for gas reactions such as syngas production or oxidative coupling of methane (OCM). Especially, in chemical reactors, the OTMs need to withstand quite harsh conditions (high temperature, chemical reactions and corrosion).

Addressing some of these challenges related to the use of OTM in such demanding applications, it is the main aim of this thesis to develop a high performance asymmetric OTM based on ceria on a cheap support. An asymmetric OTM consists of different functional layers; a porous support, a catalytic and a dense membrane layer. The design and fabrication of all these layers should be done in a way such that they are chemically, structurally and thermally compatible. The support layer provides the mechanical stability to the thin membranes and should allow sufficient gas access to the catalysts close to the membrane surface. The porous support layer should have a high level of open porosity and low resistance to gas flow to support high membrane performance.

Hence, this work addresses the following objectives in fabrication and testing of the asymmetric ceria based OTM a) the optimization of thermoplastic feedstock that allows extrusion of porous MgO supports with low cost, suitable TEC and inertness, b) characterization of the extruded MgO membrane tube structures in respect to gas permeability and mechanical strength, c) full assembly of an asymmetric multi-layer membrane by dip-coating and co-sintering and its characterization by oxygen flux measurements.

A thermoplastic extrusion process was chosen for the fabrication of the MgO tubes (14 mm diameter and a thickness of 1 mm at green stage) to achieve the required thin walled structure with great dimensional accuracy and the required properties after co-sintering. In the first step different thermoplastic feedstock

compositions, consisting of a fine MgO powder, stearic acid as dispersant, pore former and thermoplastic binders were designed. They were analyzed by thermo gravimetry (TGA/DTA) to allow a smooth removal of organics during debindering and to avoid defect formation in the MgO tubes. Different critical temperature ranges for debindering were identified: 100-300 °C (removal of stearic acid, paraffin and PMMA), 300-500 °C (removal of Elvax polymer) and 500-800 °C (removal of graphite), a and slow heating rate of between 10 to 15 °C/h and isothermal holds were implemented at these temperatures to ensure structural integrity during the thermal treatment.

In the next step, the influence of feedstock composition (ratio between pore former, polymer and ceramic content) on the microstructure and the relevant properties of the MgO support structures for membrane applications was investigated, using kneading and warm pressing and subsequent sintering at 1275 °C for 2 h.

When the polymer content (Elvax, stearic acid) in the feedstock compositions was increased from 40 to 60 vol.%, only a small increase of porosity from 9 to 18 % was achieved. It was thus obvious that an increase in thermoplastic polymer would not result in sufficient porosity and higher polymer concentrations were detrimental for the form stability of the thin walled tubes during extrusion.

An increase of the pore-former content from 0 to 20 % created additional porosity from 14 to 47 %. Form-stable supports with a total porosity of 36 % and an average pore size ~0.33 µm could be prepared using a feedstock with 19 vol.% flaky graphite pore former, sintered at 1300 °C.

To understand the influence of the sintering temperature on the development of MgO support microstructure (porosity, pore size distribution, particle size), the gas permeability and mechanical properties, a thermoplastic compositions with flaky graphite as pore former was prepared and sintered at different temperatures between 1250 to 1400 °C. A significant, unexpected increase in gas permeation through the porous MgO supports was observed when the sintering temperature was increased from 1300 to 1400 °C, despite a significant decrease in the total porosity. This was explained by the growth and homogenization of the larger pores introduced by the pore former and by improved interconnectivity of the pores (broadening of the pore channels) due to densification.

Gas permeabilities of 1.4 to 3.1 $\times 10^{-16}$ m^2 at a ΔP of 2 bar were achieved for the temperatures 1300 and 1400 °C, respectively. However, these gas permeabilities of the support structure are still relatively low and

may limit the oxygen permeation flux if used in an asymmetric membrane structure with a high performance membrane layer.

Further investigations were carried out to improve the MgO support microstructure by introducing larger pores and reduce the number of bottle neck pores. This was achieved by introducing pore formers with larger particle size and different shape and particle size distribution. To characterize the supports' functional properties (gas permeability, mechanical strength and microstructure), porous tubular MgO supports (~11.4 mm diameter and a thickness of 800 µm) were prepared through thermoplastic extrusion using three different types of pore former i.e. flaky graphite, spherical graphite and PMMA (poly methyl methacrylate).

Supports prepared with the spherical type graphite as a pore former showed open interconnected pore structures, which resulted in high open porosities of about 42.5 % (5-13 % higher than other two supports) at 1300 °C.

The mechanical strength was characterized using 4-point bending of tubes cut in the axial direction. The Weibull moduli for MgO with spherical type graphite were the highest among the supports investigated. This suggests that the spread of flaw size distribution is the narrowest, which is desirable for a ceramic under application. The characteristic strength of the MgO support is 60 MPa at 850 °C, which is most likely sufficient for a mechanically robust support. Comparing the gas permeation values at the sintering temperature of 1300 °C (which was considered a suitable temperature for co-sintering with the membrane layer), the highest gas permeation value of 4.7 $\times 10^{-16}$ m^2 was achieved for MgO supports with spherical graphite. This is almost 40 % higher than MgO supports (19 % flaky graphite) with similar mechanical strength. In order to improve gas permeation values, further research was undertaken by choosing combinations of two pore formers (spherical graphite and PMMA) which resulted in high porosity of 55 % and high gas permeability of 4-4.5 $\times 10^{-15}$ m^2.

Finally, a full asymmetric tubular membrane has been successfully prepared. First, MgO tubes with optimized support properties were extruded, then dip-coating was used to apply a catalytic NiO-CGO layer (syngas catalyst), a CGO-LSC catalytic layer (air catalyst) and a CGO membrane layer, and finally the complete asymmetric tubular membranes were co-sintered. The catalytic layers were required to enhance the reduction kinetics of oxygen and the oxidation of hydrogen/methane, thereby allowing high oxygen permeation fluxes. Oxygen permeation measurements were conducted by flowing air on the feed side (outer side of the membrane) and hydrogen on the permeate side of the membrane.

The MgO supported asymmetric CGO membrane with a thickness of 30 µm revealed an oxygen permeation flux of 3.5 ml min^{-1} cm^{-2} at a temperature of 856 °C with a sweep gas (H_2) flow rate of 200 Nml min^{-1}.

After redox-cycling (reduction and oxidation) of the Ni-CGO catalytic layer, the permeation flux of the membrane was improved, reaching 4 Nml min^{-1} cm^2 at 850 °C. It is observed that activation energy for the reaction decreases from 68.6 kJ mol^{-1} (after high temperature treatment) to 53.3 kJ mol^{-1} (after redox cycle), which suggest that the improved performance is due to an improved catalytic activity of the Ni-CGO structure after the redox-cycle.

Finally, when the membrane was subjected to methane and humidified hydrogen mixtures, the membrane failed after 30 minutes of operation, most likely due to formation of carbon in the catalytic layer close to the CGO membrane surface, which eventually resulted in the detachment of the anode layer.

7. Outlook

In this work materials for an asymmetric ceramic membrane have been investigated for use in oxygen transport membranes (OTM). Magnesium oxide has been proposed as the porous membrane support for these asymmetric ceria based membranes due to its low cost and relatively high thermal expansion.

This study confirmed that the fabrication of a tubular, asymmetric membrane structure can be done using thermoplastic extrusion of the MgO support, followed by dip-coting of catalytic and membrane layers and subsequent co-sintering. Preliminary membrane tests showed promising performance.

This study provides a good basis for further R&D on such oxygen membranes. Suggestions for future studies are described below:

- Deeper investigations in the relationship between processing parameters, the MgO support microstructure (pore size, neck sizes, tortuosity) and the properties of the final support (gas permeability and mechanical strength) by advanced methods, such X-ray tomography or high resolution 3D electron microscopy and relevant microstructure modeling.
- Testing of the tubular MgO supported CGO membranes under more realistic conditions, such as real syngas production environments, on larger membrane area and in long-term tests.

8. References

[1] A. Kaiser, et al., J. Memb. Sci. 378 (2011) 51.

[2] B.J.P. Buhre, L.K. Elliott, C.D. Sheng, R.P. Gupta, T.F. Wall, Prog. Energy Combust. Sci. 31 (2005) 283.

[3] M.B. Toftegaard, J. Brix, P. a. Jensen, P. Glarborg, A.D. Jensen, Prog. Energy Combust. Sci. 36 (2010) 581.

[4] B. Belaissaoui, Y. Le Moullec, H. Hagi, E. Favre, Sep. Purif. Technol. 125 (2014) 142.

[5] M. Puig-Arnavat, S. Soprani, M. Søgaard, K. Engelbrecht, J. Ahrenfeldt, U.B. Henriksen, P.V. Hendriksen, RSC Adv. 3 (2013) 20843.

[6] S. Baumann, W. a. Meulenberg, H.P. Buchkremer, J. Eur. Ceram. Soc. 33 (2013) 1251.

[7] J. Sunarso, S. Baumann, J.M. Serra, W.A. Meulenberg, S. Liu, Y.S. Lin, J.C. Diniz, 320 (2008) 13.

[8] S. Baumann, J.M. Serra, M.P. Lobera, S. Escolástico, F. Schulze-Küppers, W. a. Meulenberg, J. Memb. Sci. 377 (2011) 198.

[9] P. Lemes-rachadel, G. Sachinelli, R. Antonio, F. Machado, D. Hotza, J. Carlos, (2013).

[10] J.M. Benito, a. Conesa, F. Rubio, M. a. Rodríguez, J. Eur. Ceram. Soc. 25 (2005) 1895.

[11] S. Smart, C.X.C. Lin, L. Ding, K. Thambimuthu, J.C.D. da Costa, Energy Environ. Sci. 3 (2010) 253.

[12] C. Zhang, Z. Xu, X. Chang, Z. Zhang, W. Jin, J. Memb. Sci. 299 (2007) 261.

[13] D. Bayraktar, F. Clemens, S. Diethelm, T. Graule, J. Van herle, P. Holtappels, J. Eur. Ceram. Soc. 27 (2007) 2455.

[14] H. Wang, Y. Cong, W. Yang, J. Memb. Sci. 209 (2002) 143.

[15] X. Zhu, S. Sun, Y. Cong, W. Yang, J. Memb. Sci. 345 (2009) 47.

[16] D.C. Zhu, X.Y. Xu, S.J. Feng, W. Liu, C.S. Chen, Catal. Today 82 (2003) 151.

[17] C.G. Fan, R.M. Wu, L.Z. Pei, Q.F. Zhang, Adv. Mater. Res. 105-106 (2010) 643.

[18] M.P. Lobera, J.M. Serra, S.P. Foghmoes, M. Søgaard, A. Kaiser, J. Memb. Sci. 385-386 (2011) 154.

[19] Y.Y. Wei, L. Huang, J. Tang, L.Y. Zhou, Z. Li, H.H. Wang, Chinese Chem. Lett. 22 (2011) 1492.

[20] C. Delbos, G. Lebain, N. Richet, C. Bertail, Catal. Today 156 (2010) 146.

[21] X. Zhu, Q. Li, Y. Cong, W. Yang, Catal. Commun. 10 (2008) 309.

[22] Y. Frolovaborchert, V. Sadykov, G. Alikina, a Lukashevich, E. Moroz, D. Kochubey, V. Kriventsov, V. Zaikovskii, V. Zyryanov, N. Uvarov, Solid State Ionics 177 (2006) 2533.

[23] S.J. Yoon, J. Goo Lee, Energy & Fuels 26 (2012) 524.

[24] H.J.M. Bouwmeester, Catal. Today 82 (2003) 141.

[25] J. Sunarso, S. Baumann, J.M. Serra, W.A. Meulenberg, S. Liu, Y.S. Lin, J.C. Diniz da Costa, J. Memb. Sci. 320 (2008) 13.

[26] S. Bose, C. Das, Mater. Lett. 110 (2013) 152.

[27] T. Nithyanantham, S. Biswas, N. Nagendra, S. Bandopadhyay, Ceram. Int. 40 (2014) 7783.

[28] A. Chroneos, B. Yildiz, A. Tarancón, D. Parfitt, J. a. Kilner, Energy Environ. Sci. 4 (2011) 2774.

[29] H.J.M. Bouwmeester, in:, P.J. Gellings, H.J.M. Bouwmeester (Eds.), CRC Handb. Solid State Electrochem., CRC Press Inc, Boca-Raton, Florida, 1997, pp. 481–555.

[30] A. Petric, P. Huang, F. Tietz, 135 (2000) 719.

[31] P.I. Cowin, C.T.G. Petit, R. Lan, J.T.S. Irvine, S. Tao, Adv. Energy Mater. 1 (2011) 314.

[32] W.. Zhu, S.. Deevi, Mater. Sci. Eng. A 362 (2003) 228.

[33] S.P. Jiang, S.H. Chan, J. Mater. Sci. 39 (2004) 4405.

[34] B.F. Zhao, R. Peng, C. Xia, (2008).

[35] A. Bose, Inorganic Membranes for Energy and Environmental Applications, Springer Science+Business, 2009.

[36] X. Tan, Y. Liu, K. Li, Ind. Eng. Chem. Res. 44 (2005) 61.

[37] D.K. Ramachandran, F. Clemens, a. J. Glasscock, M. Søgaard, a. Kaiser, Ceram. Int. 40 (2014) 10465.

[38] a. Kaiser, a. S. Prasad, S.P. Foghmoes, S. Ramousse, N. Bonanos, V. Esposito, J. Eur. Ceram. Soc. 33 (2013) 549.

[39] C. Chatzichristodoulou, M. Søgaard, J. Glasscock, A. Kaiser, S.P.V. Foghmoes, P.V. Hendriksen, J. Electrochem. Soc. 158 (2011) F73.

[40] P.L. Rachadel, J. Motuzas, G. Ji, D. Hotza, J.C. Diniz da Costa, J. Memb. Sci. 454 (2014) 382.

[41] X. Chang, C. Zhang, W. Jin, N. Xu, J. Memb. Sci. 285 (2006) 232.

[42] G. Etchegoyen, T. Chartier, P. Del-Gallo, J. Eur. Ceram. Soc. 26 (2006) 2807.

[43] G. Pećanac, S. Foghmoes, M. Lipińska-Chwałek, S. Baumann, T. Beck, J. Malzbender, J. Eur. Ceram. Soc. 33 (2013) 2689.

[44] P. Niehoff, S. Baumann, F. Schulze-Küppers, R.S. Bradley, I. Shapiro, W. a. Meulenberg, P.J. Withers, R. Vaßen, Sep. Purif. Technol. 121 (2014) 60.

[45] D. Bayraktar, F. Clemens, S. Diethelm, T. Graule, J. Van Herle, P. Holtappels, J. Eur. Ceram. Soc. 27 (2007) 2455.

[46] K. Kwok, L. Kiesel, H.L. Frandsen, M. Søgaard, P.V. Hendriksen, J. Eur. Ceram. Soc. 34 (2014) 1423.

[47] W.-S. Hsieh, P. Lin, S.-F. Wang, Int. J. Hydrogen Energy 38 (2013) 2859.

[48] Z. Liu, G. Zhang, X. Dong, W. Jiang, W. Jin, N. Xu, J. Memb. Sci. 415-416 (2012) 313.

[49] F. Handle, Extrusion in Ceramics, 2009.

[50] M.I. Michen, Co-Extrusion of Piezoelectric Ceramic Fibres Doktors Der Ingenieurwissenschaften Marina Ismael Michen, 2010.

[51] W. Jin, S. Li, P. Huang, N. Xu, J. Shi, 185 (2001) 237.

[52] C. Li, J. Memb. Sci. 226 (2003) 1.

[53] M. Ikeguchi, K. Ishii, Y. Sekine, E. Kikuchi, M. Matsukata, Mater. Lett. 59 (2005) 1356.

[54] T. Schiestel, M. Kilgus, S. Peter, K. Caspary, H. Wang, J. Caro, J. Memb. Sci. 258 (2005) 1.

[55] X. Xin, Z. Lü, X. Huang, X. Sha, Y. Zhang, W. Su, J. Power Sources 159 (2006) 1158.

[56] a. V. Kovalevsky, V.V. Kharton, F. Maxim, a. L. Shaula, J.R. Frade, J. Memb. Sci. 278 (2006) 162.

[57] Z. Chen, Z. Shao, R. Ran, W. Zhou, P. Zeng, S. Liu, 300 (2007) 182.

[58] V. Sadykov, V. Zarubina, S. Pavlova, T. Krieger, G. Alikina, a. Lukashevich, V. Muzykantov, E. Sadovskaya, N. Mezentseva, E. Zevak, Catal. Today 156 (2010) 173.

[59] C. Delbos, G. Lebain, N. Richet, C. Bertail, Catal. Today 156 (2010) 146.

[60] Q. Li, F. Li, Mater. Res. Bull. 48 (2013) 1160.

[61] X. Meng, W. Ding, R. Jin, H. Wang, Y. Gai, F. Ji, Y. Ge, D. Xie, J. Memb. Sci. 450 (2014) 291.

[62] R.. Mangalaraja, B.. Chandrasekhar, P. Manohar, Mater. Sci. Eng. A 343 (2003) 71.

[63] M. Lipińska-Chwałek, G. Pećanac, J. Malzbender, J. Eur. Ceram. Soc. 33 (2013) 1841.

[64] K. Kwok, H.L. Frandsen, M. Søgaard, P.V. Hendriksen, J. Memb. Sci. 453 (2014) 253.

[65] F. Jtilich, D.- Jtilich, 5 (1999) 129.

[66] F. Valdivieso, P. Goeuriot, P. Matheron, J. Nucl. Mater. 320 (2003) 1.

[67] H. Middleton, S. Diethelm, R. Ihringer, D. Larrain, J. Sfeir, J. Van Herle, J. Eur. Ceram. Soc. 24 (2004) 1083.

[68] M. Salehi, et.al., J. Memb. Sci. 443 (2013) 237.

[69] M.I. Corp, (2001).

[70] B. Münch, L. Holzer, J. Am. Ceram. Soc. 91 (2008) 4059.

[71] Abaqus, 6.12, (n.d.).

[72] Waloddi weibull, J. Appl. Mech. (1951).

[73] A. Sciences, P. Sciences, 12 (1977) 1426.

[74] a. Khalili, K. Kromp, J. Mater. Sci. 26 (1991) 6741.

[75] M. Lipinska-Chwalek, J. Malzbender, a. Chanda, S. Baumann, R.W. Steinbrech, J. Eur. Ceram. Soc. 31 (2011) 2997.

[76] M. Lipińska-Chwałek, L. Kiesel, J. Malzbender, J. Eur. Ceram. Soc. (2014).

[77] D. Vasanth, G. Pugazhenthi, R. Uppaluri, J. Memb. Sci. 379 (2011) 154.

[78] http://www.fuelcellmaterials.com/, (n.d.).

[79] D.-W. Ni, V. Esposito, C.G. Schmidt, T.T. Molla, K.B. Andersen, A. Kaiser, S. Ramousse, N. Pryds, J. Am. Ceram. Soc. 96 (2013) 972.

[80] T.T. Molla, H.L. Frandsen, R. Bjørk, D.W. Ni, E. Olevsky, N. Pryds, J. Eur. Ceram. Soc. 33 (2013) 1297.

[81] J. Baber, a. Klimera, F. Raether, J. Eur. Ceram. Soc. 27 (2007) 701.

[82] W. Dong, H. Roh, Z. Liu, K. Jun, S. Park, 22 (2001) 1323.

[83] R.K. Bordia, G.W. Scherer, 36 (1988) 2399.

[84] S. Mukherjee, G.H. Paulino, J. Appl. Mech. 70 (2003) 359.

[85] N. Oishi, a. Atkinson, N.P. Brandon, J. a. Kilner, B.C.H. Steele, J. Am. Ceram. Soc. 88 (2005) 1394.

9. Appendix

I-V : Publications

VI : Product costing

Publication I

"Tailoring the microstructure of porous MgO supports for asymmetric oxygen separation membranes: Optimization of thermoplastic feedstock systems"

Available online at www.sciencedirect.com

ScienceDirect

Ceramics International 40 (2014) 10465–10473

CERAMICS INTERNATIONAL

www.elsevier.com/locate/ceramint

Tailoring the microstructure of porous MgO supports for asymmetric oxygen separation membranes: Optimization of thermoplastic feedstock systems

D.K. Ramachandran[a,*], F. Clemens[b], A.J. Glasscock[a], M. Søgaard[a], A. Kaiser[a]

[a]*Department of Energy Conversion and Storage, Technical University of Denmark, Frederiksborgvej 399, Building 779, DK-4000 Roskilde, Denmark*
[b]*EMPA, Swiss Federal Laboratories for Materials Science and Technology, Laboratory for High Performance Ceramics, Ueberlandstrasse 129, CH-8600 Dübendorf, Switzerland*

Received 24 October 2013; received in revised form 13 February 2014; accepted 4 March 2014
Available online 17 March 2014

Abstract

Porous magnesium oxide (MgO) structures were prepared by thermoplastic processing for use as supports in asymmetric thin film oxygen transport membranes (OTMs). The open porosity, pore size distribution, and resulting gas permeability of the MgO structures were measured for different feedstock compositions and sintering temperatures. For a composition with 19 vol% graphite as a pore-former, sintering temperatures of 1300 °C and 1400 °C, resulted in support porosities of 36% and 26%, respectively, and gas permeabilities of 1.4×10^{-16} m^2 and 3.1×10^{-16} m^2. Electron microscopy showed that the unexpected increase in gas permeability at temperatures above 1300 °C was a result of the growth of macro-pores and the opening of bottle-neck pores which resulted in improved pore connectivity. Mercury intrusion porosimetry experiments confirmed an increase in average pore size for samples sintered above 1300 °C, despite a significant decrease in total porosity.

Keywords: Oxygen transport membranes (OTM); Magnesium oxide; Thermoplastic feedstock; Porous support; Microstructure

1. Introduction

Inorganic oxygen transport membranes (OTM) are of interest for high purity oxygen production and for integration into membrane reactors where high temperature oxygen is required [1]. Pure oxygen is used as a reactant/component in many industrial processes. Combustion of coal using oxygen instead of air removes nitrogen from the flue gas and makes subsequent CO_2 capture and sequestration significantly cheaper and more efficient. OTM technology has the potential to improve the process efficiency of a number of systems e.g., syngas production from methane [2–4]. In large-scale industrial syngas production, reactors operate in the temperature range of 700–1050 °C with a pressure between 2 MPa and 4 MPa to achieve significant conversion efficiencies, and have very reducing atmospheres containing aggressive gases such as CO, CO_2 and H_2S. Hence, the ceramic oxygen membrane materials and their auxiliary parts have to be both chemically and structurally stable in order to withstand these harsh conditions for long periods of time. Dense mixed oxide ion- and electron-conducting (MIEC) ceramics based on $Ce_{0.9}Gd_{0.1}O_{1.95-\delta}$ (CGO10) are promising materials for this application and have recently demonstrated high oxygen fluxes of 16 N ml min^{-1} cm^{-2} at 900 °C under syngas production conditions [5], using a 30 μm planar CGO10 membrane supported on a Ni-YSZ support typically used for solid oxide fuel cells [6,7].

There have been significant efforts devoted to fabricating strong and highly-permeable porous support materials for oxygen transport membranes. Both planar and tubular configurations have been investigated along with various methods for fabricating these structures [8–12] in order to achieve high quality components. Thermoplastic processing [13] followed by extrusion is a good method for producing tubular structures, thin walled parts with a thickness below 1 mm and with close dimensional tolerances can be achieved [14]. Also, it is possible to recycle the feedstock from defective parts and

*Corresponding author. Tel.: +45 4677 4800; fax: +45 4677 5858.
E-mail address: dhra@dtu.dk (D.K. Ramachandran).

http://dx.doi.org/10.1016/j.ceramint.2014.03.017
0272-8842/

reshape them. Using thermoplastic masses instead of water-based extrusion is advantageous as abrasion of the processing equipment (i.e., extruder, chamber, and die head parts) is significantly reduced due to the high polymer content.

A support material for the use in asymmetric oxygen transport membranes should have a low cost, high thermal and chemical stability in the harsh operating environment, and good mechanical properties at elevated temperatures. MgO satisfies these requirements [15,16] and is also non-toxic (unlike previously-reported perovskite and ceria-based materials) and is hence considered a good candidate for this application. MgO has relatively high thermal expansion coefficient (TEC) than other potential supports material such as YSZ or alumina [17]. However, the TEC of MgO is closer to the values for perovskites or ceria-based composites and it can be easily integrated with these membrane materials in order to prepare multi-layered structures without failures during processing as a result of expansion mismatches [18].

In addition, other factors relating to the processing, final microstructure, and use of the porous support need to be fulfilled:

(a) A total open porosity of 35–40% after sintering to achieve sufficient gas permeation (at a support thickness of 0.5 to 1 mm).
(b) For co-sintering of the support and the membrane layer it is important that the support layer has a similar sintering activity to the membrane layer to avoid cracking and defect formation during processing. This can be achieved by tailoring the particle size distribution of the raw ceramic powders.
(c) For the final application, a membrane layer and thin catalytic layers (with thicknesses between 10 and 50 μm) need to be deposited on the MgO support by dip-coating, a thermoplastic coating process or infiltration and the support needs to be compatible with these processing steps (not discussed in detail in this paper).

In this study we describe the preparation and characterization of porous magnesium oxide supports made by thermoplastic processing. The thermoplastic feedstock composition and sintering conditions were varied to investigate their effects on the microstructure and gas permeability of the final porous structure. The processing conditions were further optimized with respect to co-sintering of the MgO with a ceria-based membrane layer.

2. Experimental

2.1. Raw materials

MgO powder (Product # 12 R-0801, Inframat Advanced Materials, USA) was used for the preparation of the porous support along with a graphite powder (V-UF1 99.9, Graphit Kropfmühl AG, Germany) as a pore former. The raw MgO powder was calcined at 1000 °C to reduce the surface area of the powder. Then the powder was coated with stearic acid dispersed in 1-proponal and mixed for 24 h using a ball mill before drying at 90 °C. This stearic acid coating reduced the tendency of the fine MgO raw powder to adsorb water and agglomerate, and improved powder handling (e.g., significantly reduced dust formation during the kneading process). Heiber et al. also showed that feedstock properties could be improved using pre-coated powders [19]. Measurements of the particle size distribution (PSD) were undertaken using a particle size analyzer (LS 13320, Beckman colter, Inc., USA). BET surface areas of the powders were determined using an Autosorb-1 analyzer (Quantachrome Instruments, USA).

2.2. Feedstock preparation

In this study, the term "feedstock" refers to the mixture of thermoplastic and ceramic compounds used to prepare warm-pressed planar structures or extruded tubes. Previous studies [13] have shown that thermoplastic compositions designed for injection molding or thermoplastic extrusion can be shaped by warm-pressing and give similar microstructures to extruded samples (when the process was carefully controlled). Warm-pressed samples were used here to investigate the microstructural and permeation properties as they are a simple geometry suitable for most of the characterization methods and only a small amount of feedstock was required (unlike extrusion; the proposed method for preparing OTMs in the future).

Feedstocks of MgO were prepared from MgO powder, graphite, a thermoplastic binder (Elvax 250, Du Pont; USA), paraffin wax (Sigma-Aldrich, USA) as a plasticizer, and stearic acid (Sigma-Aldrich, USA) as a dispersant. This system was developed for injection molding by Trunec et al. [20] and later also applied for thermoplastic extrusion. A Plastograph N50 (Brabender, Germany) was used to prepare the thermoplastic feedstocks with an operating temperature of 100 °C. The compositions of the prepared feedstocks are summarized in Table 1.

2.3. Preparation of porous MgO samples

The various feedstocks with different composition were warm-pressed into rectangular planar structures (35 mm × 50 mm) with a thickness of 1–2 mm using a uniaxial press (Model TP600, Fortune). A load of 100 kN was applied for 2 min at 100 °C. After warm-pressing the samples were heat treated ("debindered") to remove the organic components and then sintered. These samples were used for thermogravimetry, dilatometry, and porosimetry experiments. The feedstock composition which was considered to have an optimized microstructure (MPG) was also extruded into tubes (14 mm outer diameter and 1 mm wall thickness) using a Brabender extruder 19/20DN in order to validate that the warm-pressing and extrusion of an identical feedstock did indeed produce MgO components with the same properties. The ability to achieve identical properties via different processing will of course depend on the type of binder system, pore former, and plasticizer used.

For the preliminary studies on feedstock development, all samples were warm-pressed and sintered at 1275 °C for 2 h with a heating rate of 30 °C/h. Additionally, the warm-pressed feedstocks were sintered at various temperatures between 1250 °C

and 1400 °C in order to investigate the influence of the sintering temperature on the final properties.

2.4. Characterization of the porous MgO samples

The properties of the different MgO feedstock compositions were characterized by dilatometry, density measurements, mercury intrusion porosimetry, permeability measurements, and electron microscopy, as described in detail in this section.

The geometrical densities of the warm-pressed samples were measured. The packing density of green (as-prepared) samples was calculated from the ratio between the measured green density and the expected green density (calculated by the density and volume fraction of each feedstock component).

Table 1
Feedstocks: (MP1-MP5) with various ceramic to polymer ratios and no pore former; (PG2-3) two different pore former contents with a constant ceramic concentration of 50 vol%; (MG1-4) different pore former contents with a constant polymer content of 45 vol%; and (MPG) final feedstock composition that was optimized for up-scaling.

Code	MgO content (vol%)	Polymer and additives (vol%)	Graphite (vol%)
Various ceramic contents (no pore former)			
MP1	60	40	–
MP2	55	45	–
MP3	50	50	–
MP4	45	55	–
MP5	40	60	–
Various pore former contents, constant MgO content 50 vol%			
MP3	50	50	0
PG2	50	45	5
PG3	50	40	10
Various pore former contents, constant polymer content 45 vol%			
MG1	50	45	5
MG2	45	45	10
MG3	40	45	15
MG4	35	45	20
Optimized feedstock composition			
MPG	39	42	19

The microstructure of the samples was studied using scanning electron microscopy (SEM) (SUPRA35, Carl Zeiss, Germany). The samples for the microstructural characterization were prepared using lap polishing with decreasing coarseness of sandpaper/polishing solution, where the last stage of polishing used 0.25 μm diamond paste.

A differential contact dilatometer (DIL 402 CD, Netzsch GmbH, Germany) was used to measure the sintering behavior and to characterize the densification behavior of the thermoplastic feedstocks. The samples were pellets cut from the warm-pressed sheets of MgO. An Al_2O_3 reference sample was measured simultaneously with the sample. The heating rate was 3 °C min^{-1} to a final temperature of 1450 °C. All experiments were conducted in air with a flow rate of 100 ml min^{-1}.

Porosimetry measurements were conducted using a mercury intrusion porosimeter (AutoPore IV 9510, Micromeritics, Norcross/GA, USA).

Gas permeation measurements were carried out using a system developed in-house. The setup consisted of a gas supply unit, a testing chamber and a unit for measuring the flow of the gas that permeates through the sample. A pressure difference across the sample was created using an electro-pneumatic pressure controller (Tescom, ER3000, USA). The flow of permeated gas was measured using an electronic flow meter (Agilent 5314, USA). The measurements were made with a pressure difference of 200 kPa at room temperature and with nitrogen as the permeate gas. Nitrogen was used for the experiments as it is safe and easy to work with and considered to give similar permeation data to oxygen (the gas of interest for OTM).

MgO supports (MPG) sintered at 1250 °C, 1300 °C, 1350 °C, and 1400 °C were used for the gas permeation measurements in order to quantify the gas permeability using the Darcy equation

$$j = -k/\mu \nabla P \quad (1)$$

where, k is the permeability (m^2), j is the flux (m^3/m^2 s), μ is the viscosity of the gas (Pa s), and ∇P is the pressure gradient (pressure (Pa)/sample thickness (m)).

Fig. 1 shows that the microstructure of MgO supports prepared by warm-pressing is comparable to that of an extruded tube made from the same feedstock MPG (sintering at 1300 °C for 2 h). Additionally, the properties of the warm-pressed and

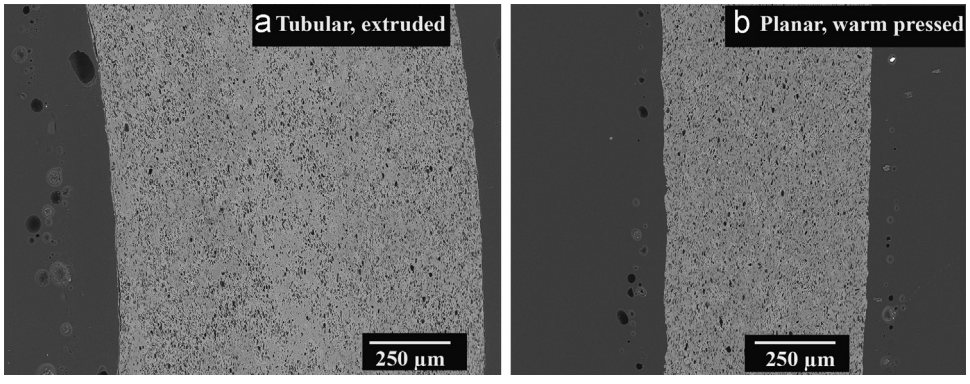

Fig. 1. SEM images of cross-sections of MgO supports (MPG) prepared by extrusion (tubular) and warm-pressing (planar), showing comparable microstructures.

extruded parts were identical with respect to gas permeability ($1.3 \pm 0.1 \times 10^{-16}$ m^2) and total open porosity ($36 \pm 1\%$), validating that the warm-pressing method is suitable for preparing samples for studying feedstock compositions for thermoplastic extrusion, as observed previously [13].

3. Result and discussion

3.1. Raw materials and feedstock composition

Table 2 summarizes the results of BET gas adsorption, particle size distribution (PSD), powder density and agglomeration factor (AF) for the raw powders. The agglomeration factor (AF) was calculated from the following equation [21].

$$AF = S_{BET} \times d50 \times \rho/6 \quad (2)$$

where, S_{BET}, d50 and ρ are specific surface area, median particle size, and powder density, respectively.

The uncalcined MgO powder had a very large surface area, (78 m^2/g as measured by BET), and consisted of extremely fine (nanometric) primary particles that could not be fully de-agglomerated by kneading or dispersion in stearic acid, as indicated by a very high agglomeration factor of 140. Calcining the MgO powder at 1000 °C for 10 h reduced the specific surface area by almost a factor of eight and the agglomeration factor by a factor of 14. Further de-agglomeration of the pre-calcined MgO powder was then achieved by coating with stearic acid and ball milling [13].

Another advantage of calcining the MgO powder was a reduction of the particle size distribution; both the D10 and the D90 were significantly reduced compared to the uncalcined powder. The selected graphite pore former had an average particle size (d50 above 11 μm) a factor of ~7 larger than that of the calcined MgO powder (see Table 2) in order to introduce large stable pores in the microstructure to increase gas permeation in the support.

Fig. 2 shows a ternary compositional diagram for the thermoplastic feedstocks. The white area represents recipes that were able to be processed whereas the compositions in the gray regions could not be prepared due to problems with the kneading, warm-pressing/extrusion or thermal treatment process.

For compositions with very high solids loading (MgO and graphite) of more than 65 vol% the feedstock could not be homogenized due to incomplete wetting of the polymer and a very high viscosity (referred to as the "unmixable region"). At very high polymer contents above 65 vol%, especially at high ratios of polymer to ceramic, the MgO structure deformed or collapsed during the shaping or heat treatment; this region is labeled "form instabilities". In the region in the center of the ternary diagram (where the polymer and graphite content exceeded 65 vol%) the prepared feedstocks were form-stable during extrusion but the MgO structures were not mechanically stable after sintering. Hence, only the white area of the compositional diagram, representing successful samples, was investigated in further detail. The data points in this region illustrate the three strategies for systematically studying the feedstock compositions (1) varying the polymer concentration (red data points, samples MP1-5), (2) increasing the pore former concentration with a fixed MgO content (blue data points, samples PG2-3) and (3) increasing the pore former concentration with a fixed polymer content (black data points, samples MG1-4).

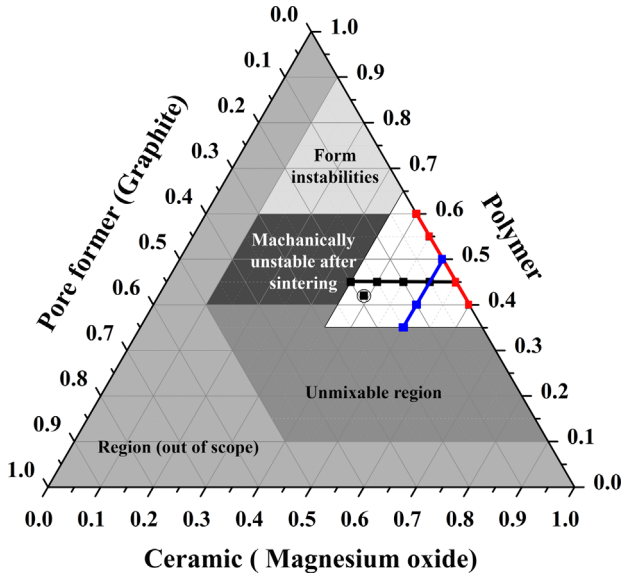

Fig. 2. Ternary compositional diagram for thermoplastic MgO feedstocks. The data points in the white operational window represent different studies where the following parameters were changed: (a) ceramic to polymer ratio (red squares: no graphite pore former), (b) graphite to polymer ratio (blue squares, 50 vol% ceramic) and pore former to ceramic ratio (black squares, 45 vol% polymer). A feedstock with optimized composition was then selected for further studies (circled square). (For interpretation of the references to color in this figure legend, the reader is referred to the web version of this article.)

Table 2
BET specific surface area, particle-size distribution (PSD), and the calculated agglomeration factor (AF) for MgO powder (uncalcined and calcined at 1000 °C) and graphite powder.

Powder	Specific surface area (m^2/g)	*PSD (μm)			Agglomeration factor (AF)
		D10	D50	D90	
MgO, uncalcined	78.0	0.510	2.99	40.8	140.0
MgO, 1000 °C, 10 h	10.8	0.187	1.53	6.07	10.0
Graphite	10.5	6.53	11.3	19.9	–

*PSD measured by laser diffraction after ball milling in ethanol for 24 h (see Section 2.1).

3.2. Influence of polymer content on the porosity

Feedstocks with different ratios of polymer to ceramic were prepared to investigate the influence of the polymer content on the formation of open porosity after sintering. Table 3 summarizes the compositions and properties of warm-pressed planar structures before organic removal (green state), and after sintering.

As expected, the shrinkage and the porosity of the sintered MgO increased gradually from 15% to 21% and from 9% to 18%, respectively, with increasing polymer content (40% to 60%). It is clear that the porosity can be adjusted by simply changing the powder/polymer ratio, which is an advantage of using thermoplastic processing. However, even at the highest polymer content of 60 vol% (the limit for producing a stable ceramic structure), the observed porosity of 18% is considered too low for sufficient gas permeability. Hence, the addition of a pore-former was required to create additional porosity. In Table 3 it can be seen that the packing density of the green warm-pressed samples increased gradually with increasing polymer content, clearly indicating that the flowability of the feedstocks increased. For MP1 with lowest polymer content of 40% the packing density of the green warm-pressed sample could be increased to values above 90% by further optimization of the pressing parameters (temperature and pressure) but this was not the main purpose of this study.

3.3. Influence of pore former (50 vol% ceramic)

In order to achieve high porosity values, the amount of pore former was gradually increased (replacing the polymer) at constant MgO powder concentration of 50 vol%, as shown by the blue line in Fig. 2. Table 4 shows that the porosity could be significantly increased from 13% to 31% by the addition of 10% graphite in the MgO feedstock. It can be seen that feedstock PG3 (with 10% graphite) had a low packing density in the green state of 0.88. This indicates that (under the conditions used here for warm-pressing), a polymer content of 40 vol% is too low to achieve a homogeneous green body without small air inclusions. Hence, for this system, it can be concluded that the lower limit of the polymer content is above 40% in order to avoid air inclusions in the feedstock and subsequent processing problems.

3.4. Influence of pore former content on support properties (constant polymer content of 45 vol%)

Table 5 shows the effect of graphite content (0–20 vol%) on the properties of the sintered MgO (constant polymer content of 45 vol%, sintered at 1275 °C). Comparing the compositions MP2, MG1 and MG2 with 0%, 5% and 10% graphite, respectively, the porosity increased almost linearly with the addition of graphite. It is worthwhile noting that the pore size distribution of the compositions changed from mono-modal to bi-modal at graphite concentrations above 10 vol%. Furthermore, the size of the second peak representing the larger pore sizes increased with increasing pore former content.

Also shown in Table 5 are the data for MPG (19 vol% graphite) which lie between those for MG3 and MG4 with respect to graphite content and final porosity. This composition was selected for further study as it porosity was within the targeted range (35–40%) and it showed the best overall behavior during processing (of the studied samples within the operational window shown in Fig. 2). Also, large quantities of MPG could be easily processed and hence this composition was considered suitable for up-scaling of the process in the future.

Table 3
Properties of MgO support layers with different polymer contents after sintering at 1275 °C for 2 h (*measured by Hg porosimetry).

Composition		Green state		Sintered state		
Code	Polymer	Density (g/cm^3)	Packing density[a]	Linear shrinkage (%)	*Porosity (%)	Pore size (μm)
MP1	40	2.22	0.88 ± 0.02	15.1	9.2	0.10
MP2	45	2.20	0.92 ± 0.02	15.7	13.5	0.07
MP3	50	2.12	0.94 ± 0.02	15.9	13.0	0.11
MP4	55	1.98	0.94 ± 0.02	17.9	13.5	0.12
MP5	60	1.90	0.96 ± 0.02	20.8	18.2	0.15

[a]Packing density at green state is defined here as the geometrical green density (column 3) compared to the expected green density calculated from the densities and concentrations of each component.

Table 4
Porosity and shrinkage of MgO supports sintered at 1275 °C for 2 h (constant ceramic content of 50 vol%) as a function of the graphite to polymer ratio.

Composition			Green state		Sintered state		
Code	Polymer	Graphite	Density (g/cm^3)	Packing density	Linear Shrinkage (%)	Porosity (%)	Pore size (μm)
MP3	50	0	2.12	0.94 ± 0.02	15.9	13.0	0.11
PG2	45	5	2.20	0.96 ± 0.02	15.1	17.1	0.14
PG3	40	10	2.08	0.88 ± 0.02	15.3	30.9	0.26

Table 5
Porosity and shrinkage of MgO supports sintered at 1275 °C for 2 h (constant polymer content of 45 vol%) as a function of the graphite to MgO ratio.

Composition				Green state		Sintered state			
Code	Ceramic	Polymer	Graphite	Density (g/cm^3)	Packing density	Shrinkage (%)	Porosity (%)	Pore size peaks* (μm)	
								P1	P2
MP2	55	45	0	2.19	0.92 ± 0.02	15.7	14.4	0.10	–
MG1	50	45	5	2.21	0.94 ± 0.02	15.1	16.0	0.15	–
MG2	45	45	10	2.20	0.98 ± 0.02	15.2	19.4	0.20	–
MG3	40	45	15	2.18	0.96 ± 0.02	14.9	32.5	0.21	0.36
MG4	35	45	20	2.03	0.96 ± 0.02	12.1	47.5	0.08	0.42
MPG	**39**	**42**	**19**	**2.08**	**0.94 ± 0.02**	**13.42**	**37.0**	**0.06**	**0.40**

*Bi-model pore size distribution (peaks labeled P1 and P2) was observed only when the graphite concentration was more than 10%.

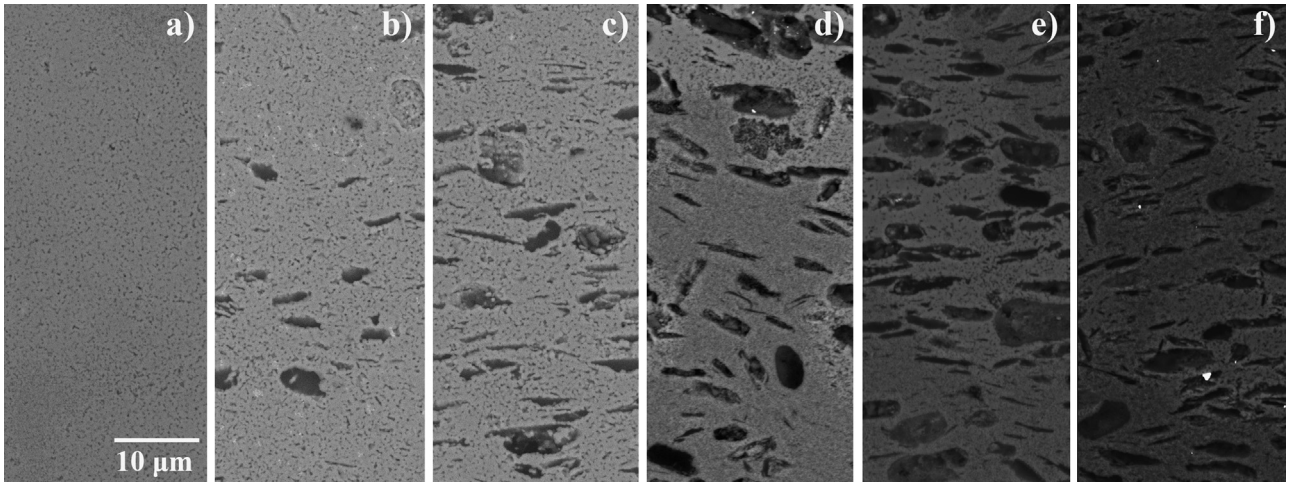

Fig. 3. SEM micrographs of MgO supports with various graphite contents (a) no graphite (MP2), (b) 5% graphite (MG1), (c) 10% graphite (MG2), (d) 15% graphite (MG3), (e) 20% graphite (MG4), and (f) 19% graphite (MPG). The samples were sintered at 1275 °C for 2 h.

Fig. 3 shows SEM images of polished cross-sections of the MgO supports MP2 and MG1 to MG4. An increase in the absolute porosity and the fraction of larger pores was observed when the amount of pore former was increased from 0 to 20 vol% (Fig. 3a–f). The graphite pore former produced the larger, elongated and oriented pores with sizes of several microns. The submicron porosity is from the removal of the polymer; these fine pores were also observed for composition MP2 (Fig. 3a), which contained no graphite.

3.5. Influence of sintering temperature

In the case where the MgO support will be co-sintered with a membrane layer, the densification behavior of the support during sintering must closely match that of the membrane to avoid mechanical failures e.g., cracking or delamination. Another challenge is to select a co-sintering temperature where the membrane can be fully densified while keeping sufficient porosity in the support. Hence, the densification behavior of the selected MgO feedstock (MPG) was investigated by dilatometry and compared to that of a CGO membrane sample (64 vol% CGO and 36 vol% polymer). The resulting densification curves in Fig. 4 show that more than 1300 °C is required for the membrane to reach a density above 85% (without an extended time at the sintering temperature). Further sintering experiments on CGO feedstocks showed that an isothermal holding time of about 2 h at1300 °C achieved a density of 95% of theoretical density, which is considered to be sufficiently dense for the application. Hence, it was necessary to investigate the effect of higher sintering temperatures and the 2 h holding time on the porosity of the MgO. This was done by sintering warm-pressed samples of MPG at 1250 °C, 1300 °C, 1350 °C or 1400 °C for 2 h and analyzing the resulting porosity by SEM.

Fig. 5 shows the microstructures of the MgO samples sintered at different temperatures. At a sintering temperature of 1250 °C (Fig. 5a) large elongated pores from the graphite are visible (8.7–16.6 μm in length and aspect ratios between 1.5 and 4.8). When the sintering temperature was increased these larger pores grew slightly, whereas the MgO matrix (skeleton) densified as the finer pores from the polymer were eliminated (Fig. 5b).

Hg porosimetry measurements were performed on the same MgO samples as shown in Fig. 5 to quantify the development

of the pore size distribution with sintering temperature. The pore size distributions of the MgO supports shown in Fig. 6 confirm the microstructural observations. For sintering temperatures of 1250 °C and 1300 °C bi-modal pore size distributions with two distinct peaks are observed; the first peak with an average size below 0.1 μm and the second peak including pores above 0.3 μm. This second peak is present for all four sintering temperatures. It is obvious that with increasing sintering temperature (from 1250 °C to 1350 °C) the smaller pores are completely eliminated from the MgO skeleton. As expected from the dilatometry measurements (Fig. 4), the porous MgO will sinter and densify at these temperatures and therefore the porosity below 0.1 μm will disappear. For the pores above 0.2 μm, the median pore diameter shifts from 0.3 to 0.7 when the final sintering temperature increased from 1250 °C to 1400 °C. The pore size distributions measured by Hg intrusion (Fig. 6) is significantly smaller compared to the microstructural observations (Fig. 5) and this discrepancy can be explained by the formation of bottleneck pores (e.g., submicron pores) which connect the larger (micrometer range) pores. In the Hg porosimetry technique the pore size is calculated from the pressure required to push the Hg through the sample and hence the bottleneck (smallest diameter of the pore) will give the measured pore size. Hence, the average pore size of samples with many bottleneck pores can be underestimated using this technique, which is why it was important also to view the microstructure.

The growth of the pores above 0.2 μm can be explained by the Oswald repining process; the bottleneck pore size increased

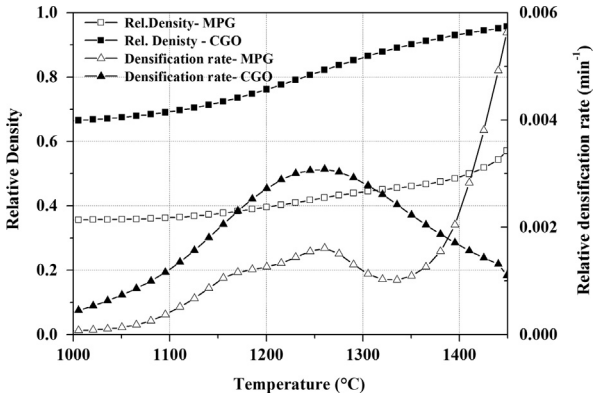

Fig. 4. Densification behavior as a function of temperature for an MgO sample (MPG) and a CGO membrane material measured by dilatometry (heating rate: 3 °C min^{-1}).

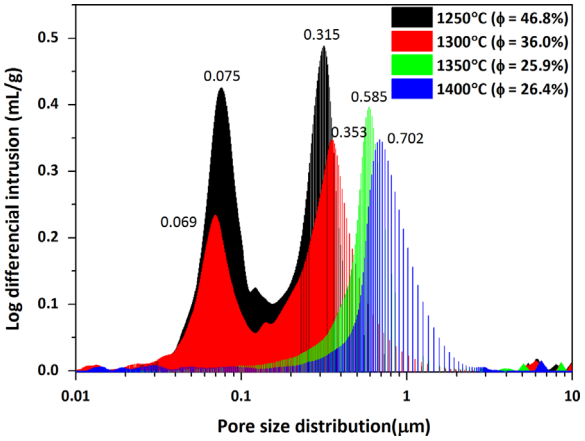

Fig. 6. Influence of the sintering temperature (T) on the pore size distribution of MgO supports (T=1250 °C, 1300 °C, 1350 °C and 1400 °C at 2 h holding time). The corresponding open porosity is denoted by ϕ.

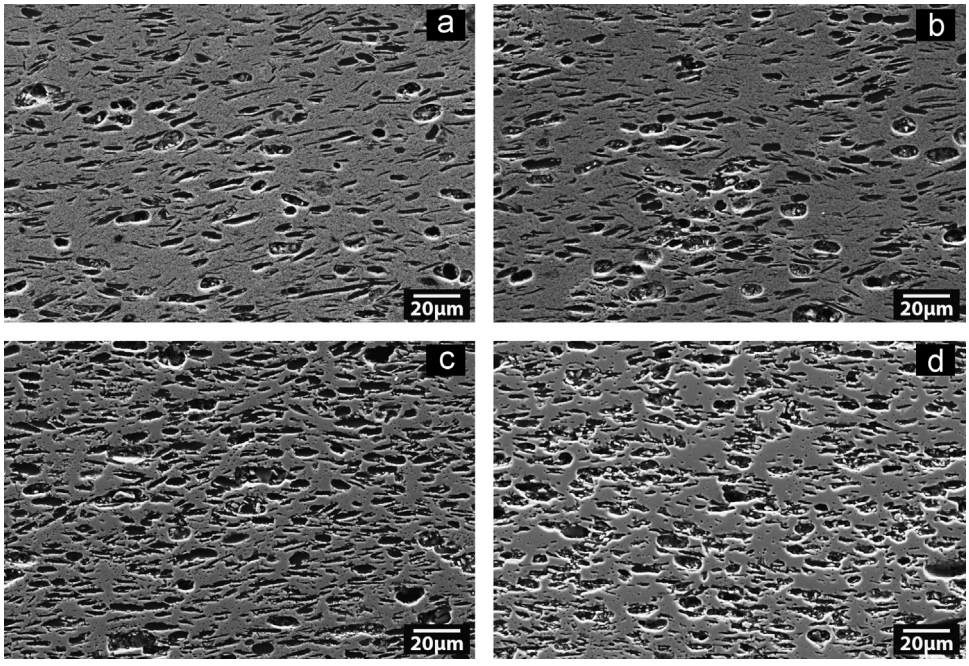

Fig. 5. SEM micrographs showing the densification and microstructural development of an MgO sample (MPG) at sintering temperatures of (a) 1250 °C, (b) 1300 °C, (c) 1350 °C and (d) 1400 °C (2 h isothermal holding time).

because of the densification of the MgO skeleton. The total porosity of the MgO samples as measured by Hg porosimetry is plotted as a function of sintering temperature in Fig. 6. As expected, the total porosity decreased with increasing sintering temperature until the sintering temperature reached 1350 °C. There was no further decrease in porosity observed at 1400 °C. The strong decrease in porosity in the temperature range 1250–1350 °C was a result of the elimination of the small pores in the MgO skeleton (as evidenced by the disappearance of the smaller pore size peak in Fig. 6).

3.6. Permeability of the MgO supports

Gas permeation measurements for the MPG samples were conducted in order to correlate the gas flow through the porous structure with the microstructure developed at different sintering temperatures. The permeability of the supports at ΔP of 200 kPa is plotted (left axis) as a function of the sintering temperature in Fig. 7a, along with the porosity of the supports (right axis).

The permeability was highest for the sample sintered at the lowest temperature of 1250 °C (with the bi-modal pore size distribution as shown in Fig. 6) and decreased by a factor of more than 3 for a sintering temperature of 1300 °C. Increasing the sintering temperature further to 1350 °C and 1400 °C did not further decrease the permeability as could be expected from the lower total porosity values. In fact the permeability of the sample sintered at 1400 °C was a factor of 2.5 larger than that of the sample sintered at 1350 °C. Considering the microstructural development discussed in the previous section, it is clear that the gas permeation depends not only on the total porosity, but also on the microstructure (pore size, pore shape and interconnectivity of the pores or "tortuosity"). Fig. 7b shows a significant increase in the volume fraction of the larger pores (above 0.5 μm) from below 20% to almost 90% when the sintering temperature was increased from 1300 °C to 1350 °C. Furthermore, the median pore size is more than doubled over the same range. Despite a reduction in the total porosity with increasing temperature, it is clear that the microstructures developed at higher sintering temperatures are beneficial for gas permeation (a higher fraction of large interconnected pores). This is a positive result with respect to co-sintering the MgO supports with CGO membranes; the evaluated sintering temperatures (above 1300 °C) required for densifying the CGO are not detrimental for gas permeability and are likely to be beneficial for the mechanical strength of the porous supports.

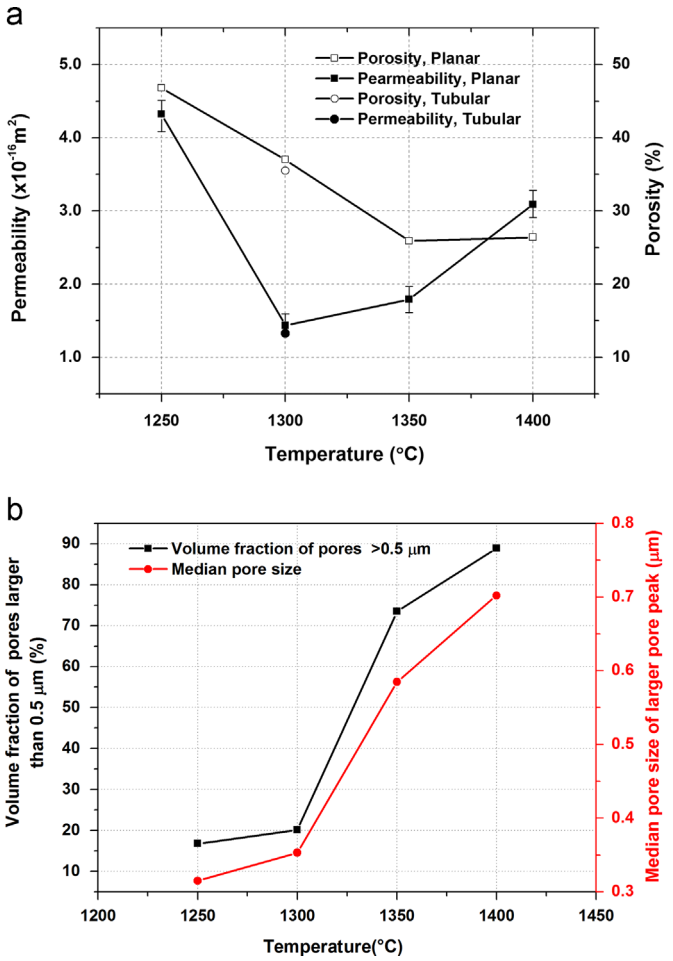

Fig. 7. (a) Gas permeability and total porosity in MgO supports and (b) volume fraction of pores larger than 0.5 μm and the median pore size of the larger pore size peak as functions of sintering temperature. Porosity and pore size distribution data are taken from the Hg porosimetry measurements.

4. Conclusion

Magnesium oxide has a relatively high thermal expansion coefficient compared to other structural ceramics, which makes it a suitable, generic support material for OTM materials such as perovskites or ceria-based materials. Supports with a high total porosity (up to 36%) and an average pore size ~0.5 μm were achieved using a feedstock with 19 vol% graphite pore former (particle size ~10 μm) and a sintering temperature of 1300 °C. A significant, unexpected increase in gas permeation through the porous MgO supports was observed when the sintering temperature was increased from 1300 °C to 1400 °C, despite a significant decrease in the total porosity. This was explained by the growth and homogenization of the larger pores introduced by the pore former and by improved interconnectivity of the pores (broadening of the pore channels) due to densification. The optimization of the MgO feedstock resulted in porous supports with suitable microstructures and sintering activity for co-sintering with CGO at temperatures between 1300 °C and 1400 °C. In the case where these MgO supports would be used with high-performance membrane layers (delivering oxygen fluxes of 10 ml min^{-1} cm^{-2} or more), these gas permeabilities of 1.4–3.1 × 10^{-16} m^2 may limit the performance of the membrane. Therefore further research is being undertaken to enlarge the average pore size of the MgO supports using alternative pore formers while optimizing the mechanical strength (e.g., using spherical graphite to form more homogenous pores). In addition, extrusion of these thermoplastic feedstocks is being undertaken to produce thin-walled porous MgO tubes onto which catalytic layers and ceria-based membrane layers can be applied by dip-coating and then co-sintered to produce fully functional OTMs.

Acknowledgments

The authors would like to thank the Danish Council for Independent Research, Technology and Production Sciences (FTP) which is part of The Danish Agency for Science, Technology and Innovation (FI) for financing this work within the OPTIMAC project (Project # 09–072888) and the DSF (Danish council for Strategic Research) for support within the project ENEFOX (Project #11-116387). Pernille Hedemark Nielsen and Marianne Nielsen are thankfully acknowledged for their assistance with the preparation of feedstocks, dilatometry analyses and Hg-porosimetry measurements.

References

[1] M. Salehi, F. Clemens, E.M. Pfaff, S. Diethelm, C. Leach, T. Graule, et al., A case study of the effect of grain size on the oxygen permeation flux of BSCF disk-shaped membrane fabricated by thermoplastic processing, J. Memb. Sci. 382 (2011) 186–193.

[2] X. Zhu, S. Sun, Y. Cong, W. Yang, Operation of perovskite membrane under vacuum and elevated pressures for high-purity oxygen production, J. Memb. Sci. 345 (2009) 47–52.

[3] C. Delbos, G. Lebain, N. Richet, C. Bertail, Performances of tubular $La_{0.8}Sr_{0.2}Fe_{0.7}Ga_{0.3}O_{3-\delta}$ mixed conducting membrane reactor for under pressure methane conversion to syngas, Catal. Today 156 (2010) 146–152.

[4] P.V. Hendriksen, P.H. Larsen, M. Mogensen, F.W. Poulsen, K. Wiik, Prospects and problems of dense oxygen permeable membranes, Catal. Today 56 (2000) 283–295.

[5] J. Sunarso, S. Baumann, J.M. Serra, W.A. Meulenberg, S. Liu, Y.S. Lin, et al., Mixed ionic-electronic conducting (MIEC) ceramic-based membranes for oxygen separation, J. Memb. Sci 320 (2008) 13–41.

[6] a. Kaiser, S. Foghmoes, C. Chatzichristodoulou, M. Søgaard, J.a. Glasscock, H.L. Frandsen, et al., Evaluation of thin film ceria membranes for syngas membrane reactors – preparation, characterization and testing, J. Memb. Sci. 378 (2011) 51–60.

[7] C. Chatzichristodoulou, M. Søgaard, J. Glasscock, A. Kaiser, S.P.V. Foghmoes, P.V. Hendriksen, Oxygen Permeation in thin, dense $Ce_{0.9}Gd_{0.1}O_{1.95-\delta}$ membranes II. Experimental determination, J. Electrochem. Soc. 158 (2011) F73.

[8] C. Zhang, Z. Xu, X. Chang, Z. Zhang, W. Jin, Preparation and characterization of mixed-conducting thin tubular membrane, J. Memb. Sci. 299 (2007) 261–267.

[9] D. Bayraktar, F. Clemens, S. Diethelm, T. Graule, J. Van Herle, P. Holtappels, Production and properties of substituted $LaFeO_3$-perovskite tubular membranes for partial oxidation of methane to syngas, J. Eur. Ceram. Soc. 27 (2007) 2455–2461.

[10] a. Chanda, B.X. Huang, J. Malzbender, R.W. Steinbrech, Micro- and macro-indentation behaviour of $Ba_{0.5}Sr_{0.5}Co_{0.8}Fe_{0.2}O_{3-\delta}$ perovskite, J. Eur. Ceram. Soc. 31 (2011) 401–408.

[11] D.C. Zhu, X.Y. Xu, S.J. Feng, W. Liu, C.S. Chen, La2NiO4 tubular membrane reactor for conversion of methane to syngas, Catal. Today 82 (2003) 151–156.

[12] R.Z. Liu, S.R. Wang, B. Huang, C.H. Zhao, J.L. Li, Z.R. Wang, et al., Dip-coating and co-sintering technologies for fabricating tubular solid oxide fuel cells, J. Solid State Electrochem. 13 (2008) 1905–1911.

[13] M. Salehi, E.M. Pfaff, R.M. Junior, C.P. Bergmann, S. Diethelm, C. Neururer, et al., $Ba_{0.5}Sr_{0.5}Co_{0.8}Fe_{0.2}O_{3-\delta}$(BSCF) feedstock development and optimization for thermoplastic forming of thin planar and tubular oxygen separation membranes, J. Memb. Sci. 443 (2013) 237–245.

[14] F. Clemens, Thermoplastic Extrusion for Ceramic Bodies, in: F. Händle (Ed.), Extrus. Ceram., Springer Verlag, Heidelberg, 2007, pp. 323–345.

[15] M. Lipińska-Chwałek, G. Pećanac, J. Malzbender, Creep behaviour of membrane and substrate materials for oxygen separation units, J. Eur. Ceram. Soc. 33 (2013) 1841–1848.

[16] K. Kwok, H.L. Frandsen, M. Søgaard, P.V. Hendriksen, Stress analysis and fail-safe design of bilayered tubular supported ceramic membranes, J. Memb. Sci. 453 (2014) 253–262.

[17] Y. Shiratori, YSZ–MgO composite electrolyte with adjusted thermal expansion coefficient to other SOFC components, Solid State Ion. 164 (2003) 27–33.

[18] F. Jtilich, D.- Jtilich, Therm. Expans. SOFC Mater. 5 (1999) 129–139.

[19] J. Heiber, F. Clemens, T. Graule, D. Hülsenberg, Thermoplastic extrusion to highly-loaded thin green fibres containing $Pb(Zr,Ti)O_3$, Adv. Eng. Mater. 7 (2005) 404–408.

[20] M. Trunec, J. Cihlar, Thermal removal of multicomponent binder from ceramic injection mouldings, J. Eur. Ceram. Soc. 22 (2002) 2231–2241.

[21] J. Heiber, F. Clemens, T. Graule, D. Hülsenberg, Influence of fibre diameter on the microstructure and the piezoelectric properties of PZT-fibres, Adv. Sci. Technol. 45 (2006) 2459–2463.

Publication II

"The role of sacrificial fugitives in thermoplastic extrusion feedstocks on properties of MgO supports for oxygen transport membranes"

Available online at www.sciencedirect.com
ScienceDirect
Journal of the European Ceramic Society xxx (2014) xxx–xxx
www.elsevier.com/locate/jeurceramsoc

The role of sacrificial fugitives in thermoplastic extrusion feedstocks on properties of MgO supports for oxygen transport membranes

D.K. Ramachandran [a,*], K. Kwok [a], M. Søgaard [a], F. Clemens [b], A.J. Glasscock [a], A. Kaiser [a]

[a] *Department of Energy Conversion and Storage, Technical University of Denmark, Frederiksborgvej 399, Building 779, DK-4000 Roskilde, Denmark*
[b] *EMPA, Swiss Federal Laboratories for Materials Science and Technology, Laboratory for High Performance Ceramics, Ueberlandstrasse 129, CH-8600 Dübendorf, Switzerland*

Received 16 August 2014; received in revised form 11 November 2014; accepted 16 November 2014

Abstract

Three different compositions of MgO compounds were investigated for use in oxygen transport membranes. Porous MgO supports were extruded using different kind (size, morphology and chemistry) of pore formers: A flaky graphite, a spherical graphite and ideal spheres of PMMA. The influence of the pore former on microstructure, gas permeation and the mechanical properties for various sintering temperatures were investigated. The gas permeation behavior of the MgO supports was highly dependent on pore neck size and total open porosity. MgO substrate, with 20% spherical graphite as a pore former, sintered at 1300 °C for 2 h, showed a total porosity of 42.5% and gas permeability of 4.7×10^{-16} m^2. Subsequently, the 4-point bending strengths of this substrate, scaled to an effective volume of 10 mm^3, were 77 and 60 MPa for room and operation temperature (850 °C). Both, permeation rate and mechanical strength is sufficient for using the support for further investigations in OTM.

Keywords: Porous MgO; Oxygen membrane; Microstructure; Mechanical strength; Gas permeability

1. Introduction

Carbon dioxide (CO_2) is one of the important greenhouse gases which is largely emitted from chemical, power generation and cement industries. Carbon capture and storage (CCS) is one approach for reducing CO_2 emissions in an attempt to overcome current global warming issues. Using carbon capture and storage a high CO_2 content in the exhaust gas is favoured. One possibility is using oxyfuel power plants in combination with pure oxygen instead of air for combustion process. Practically, pure oxygen is conventionally produced by cryogenic distillation in large scale or by pressure swing adsorption in small scale.[1] Oxygen transport membranes are a promising alternative for integration in high temperature combustion processes due to their high selectivity for oxygen and significantly lower efficiency losses.[2] With pure oxygen, the NO_x emissions in exhaust gas can be eliminated, since atmospheric nitrogen is separated from the air stream by the membrane before combustion process.[3–7] Therefore leaving only CO_2 and H_2O can be easily and cost effectively separated for CCS. In the last decade, intensive research has been dedicated to the preparation and characterization of monolithic oxygen transport membranes (OTM) to achieve high oxygen fluxes through thin planar or tubular membrane geometries.[8–13]

In comparison to monolithic membrane asymmetric OTM consists of different functional layers namely; porous support, catalytic and dense membrane layer. In order to fabricate an OTM all these layers should be tailored in a way that they are chemically, structurally and thermally compatible with each other. The support layer provides mechanical stability to the thin membranes and should ideally allow unrestricted gas access to the activation layers present on the membrane surface. Hence, the support layer of the membrane should have a high level of interconnected open porosity and minimal resistance to gas flow for better membrane performance. There have been many studies devoted to developing a porous support layer (both ceramic and

* Corresponding author. Tel.: +45 4677 4800; fax: +45 4677 5858.
E-mail addresses: dhra@dtu.dk, dhavaa@gmail.com (D.K. Ramachandran).

http://dx.doi.org/10.1016/j.jeurceramsoc.2014.11.014
0955-2219/

Table 1
Thermoplastic feedstock composition using different pore formers.

Code	Kneader temperature (°C)	MgO content (vol.%)	Polymer & additives (vol.%)	Pore former (vol.%)	Type of pore former
MP-FL	100	39	42	19	Flaky graphite
MP-SP	100	34	46	20	Spherical graphite
MP-PM	65	34	46	20	PMMA

metal-based materials) with planar and tubular structures[14–17] for high temperature membrane applications.

With respect to the mechanical properties, the number of studies is limited for support structures. There are some studies on BSCF materials where elastic modulus and toughness of porous BSCF were reported for both room and operation temperature.[18] Later, research activities include more candidate materials such as CGO and LSCF. For those mechanical properties like subcritical crack growth[16] and flexural strength[19] has been reported. Magnesium oxide (MgO) tubes were extruded and sintered as porous support layer (porosity of $36 \pm 5\%$) for membrane applications and the room temperature fracture strength of 36 ± 6 MPa was reported.[20] Similar values have been reported for porous CGO substrates.[21] It is worthwhile to mention that high temperature strength of porous supports is the critical issue to be characterized. K. Kwok et al.[19] proposed a high temperature testing methodology for tubular and planar ceramics to circumvent this difficult issue.

Beneath mechanical properties, OTM supports need to fulfill further requirements related to the final application and their implementation into a multi-layer structure (during ceramic processing). One very important property for application is a high gas permeability in the order of 10^{-15} m^2 to ensure transport of gasses through the relatively thick porous ceramic support layer.[22] The microstructure of the support (porosity, pore size distribution, grain size etc.) influences above properties and is strongly depending on the fabrication,[18] especially on sintering conditions. Thus it is important for implementation of a new type of support structure in an asymmetric OTM to have a more elaborated understanding of the relationship between processing, resulting microstructure and final support properties.

Considering the basic material properties, magnesium oxide is a cheap and readily available,[23,24] non-toxic raw material with a good thermal and chemical stability and a relative high thermal expansion coefficient suitable for many oxygen membrane materials (fluorites, perovskites and composites). In this work the development of porous magnesium oxide (MgO) supports for the use in tubular, asymmetric OTMs using different extrusion compositions will be described. Thin walled tubular MgO support structures were prepared, with a wall thickness below 1 mm after sintering, from thermoplastic feedstocks with different type of pore former and their mechanical properties, porosity and gas permeability as a function of pore former type, total open porosity and sintering temperatures for use OTM were investigated.

2. Experimental procedure

2.1. Raw powders

Feedstocks of MgO were prepared from MgO powder (Product #12R-0801, Inframat Advanced Materials, USA), pore former, a thermoplastic binder (Elvax 250, Du Pont; USA), paraffin wax (Sigma-Aldrich, USA) as a plasticizer, and stearic acid (Sigma-Aldrich, USA) as a dispersant. The MgO powder was first calcined and then coated with the stearic acid using 1-proponal as a solvent and then homogenized by ball milling with zirconia balls for 24 h. The solvent was removed from the MgO slurry by drying on a hot plate for 24 h at 90 °C. The stearic acid coating helps to interact better with polymeric binder to reduce the tendency of the fine MgO raw powder to adsorb water and further improved powder handling (e.g. significantly reduced dust formation during the kneading process).[25,26] Three type of pore formers were used in the feedstock composition namely; a graphite powder, flaky type (V-UF1 99.9, Graphit Kropfmühl AG, Germany) referred as (FL), another graphite spherical type (TIMREX® KS6, TIMCAL, Switzerland) referred as (SP) and PMMA (Poly methyl methacrylate, MR 10G, Exprix technologies, USA) referred as (PM).

2.2. Preparation of thermoplastic feedstock

It is worthwhile to mention that the composition of the three different feedstock vary depending on the used pore former material. Before this study, the feedstock with each pore former had to be optimized separately to be able to achieve a stable process (e.g. sufficient shaping capability and stable tube structure without deformation during extrusion, debinding and sintering). Table 1 shows thermoplastic extrusion feedstock compositions prepared using the three different pore formers. As shown in Table 1, all three types of ingredients were weighed and mixed in the kneader (Linden, Type BK20-Vol 500cc, Germany) in the following order to achieve homogeneous mixing. First, the kneader was heated to the operating temperature, filled with half of the MgO powder and allowed to run at a low speed of 10 rpm in order to transfer heat to the MgO powder and mill any larger aggregates. Next, the organic binder (Elvax 250 and paraffin wax) and the remaining MgO powder were added consecutively. After a homogeneous mixture was achieved (constant torque value), the pore former powder was added, and mixed further until the mixture was uniform.

Please cite this article in press as: Ramachandran DK, et al. The role of sacrificial fugitives in thermoplastic extrusion feedstocks on properties of MgO supports for oxygen transport membranes. J Eur Ceram Soc (2014), http://dx.doi.org/10.1016/j.jeurceramsoc.2014.11.014

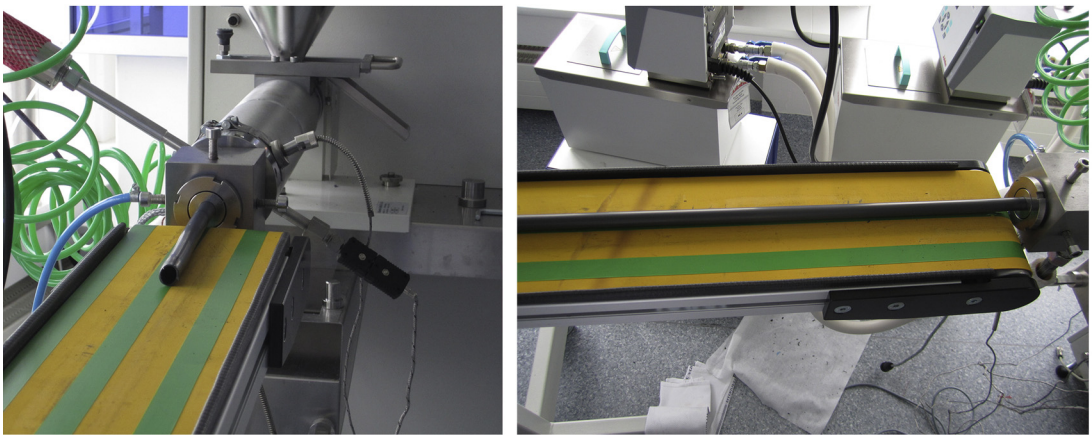

Fig. 1. The experimental extrusion of tubular device using thermoplastic feedstock.

2.3. Thermoplastic extrusion of thin walled support tubes

Thermoplastic extrusion was used to shape support tubes as the process is capable of producing thin walled, form-stable substrates suitable for further membrane processing by dip-coating process. The extruder (Model 19/20DN Brabender, Germany) in combination of oil baths were used to heat up the extruder chamber to 100 °C and the die head to 90 °C. The die head temperature was always kept 10 °C lower than the chamber temperature to ensure form stability of the tube at the exit of the die. An extruder speed of 10 rpm and a die assembly with inner and outer diameters of 12 mm and 14 mm, respectively, was used for all experiments. Feedstock (MP-PM) was extruded using lower temperatures (extruder chamber: 75 °C, die head: 70 °C) as the addition of a polymeric pore former produced a feedstock with lower viscosity at higher temperature. PMMA typically has a glass transition temperature at around 105 °C and it was necessary to optimize the extruder temperature to ensure a stable structure. Fig. 1 shows the image taken during thermoplastic extrusion process.

2.4. Debinding and sintering

Based on the thermo gravimetric experiments (discussed in Section 3.3), all three extruded feedstock compositions were debindered at different temperatures and heating rates which is presented in Fig. 2. After debinding, the samples were sintered at different sintering temperatures such as 1250 °C, 1300 °C, 1350 and 1400 °C with a heating rate of 30 °C h^{-1} in order to investigate the influence of the sintering temperature on the microstructure properties. For thermo gravimetric experiments are described in Section 2.5.

2.5. Material characterization

The properties of the different MgO feedstock compositions were characterized by thermal analysis, electron microscopy, Hg porosimetry, gas permeation and mechanical testing, as will be described in detail in this section.

A thermo-gravimetric balance (STA 409 CD, Netzsch GmbH, Germany) was used to study the decomposition behavior of the thermoplastic binder system (EVA, paraffin, stearic acid) and the three different pore formers in the MgO feedstock during debinding in air. All experiments were conducted with a heating rate of 1 °C min^{-1} and an air flow of 100 ml min^{-1}.

The microstructure of the samples was studied after sintering using scanning electron microscopy (SEM) (SUPRA35, Carl Zeiss, Germany). The samples for the microstructural characterization were prepared using lap polishing with decreasing coarseness of sandpaper/polishing solution, where the last stage of polishing was with a 0.25 μm diamond paste. Additionally, porosimetry measurements were conducted using a Pore Master (PR-60 GT, Micromeritics, USA). Samples with weights of 0.9 to 1.1 g were measured in a penetrometer with a 5 cm^3 bulb volume and a usable Hg volume in the penetrometer stem of 0.392 cm^3, allowing for a maximum measureable pore volume of 0.366 cm^3. All measurements were run between 5 Pa and 420 MPa translating into a measurement range of pore diameters between 240 μm and 0.003 μm.

Gas permeation measurements were carried out using an in-house built system device. The setup consists of a gas supply

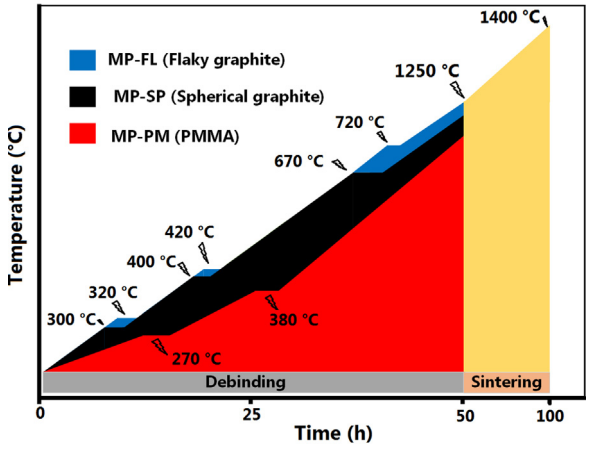

Fig. 2. Debinding cycle derived from thermo gravimetric experiments for all three supports; MP-FL (Flaky graphite), MP-SP (Spherical graphite) and MP-PM (PMMA).

Please cite this article in press as: Ramachandran DK, et al. The role of sacrificial fugitives in thermoplastic extrusion feedstocks on properties of MgO supports for oxygen transport membranes. *J Eur Ceram Soc* (2014), http://dx.doi.org/10.1016/j.jeurceramsoc.2014.11.014

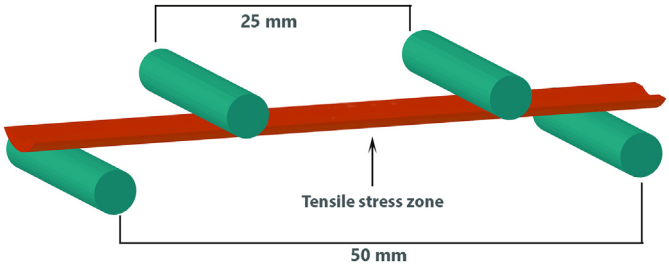

Fig. 3. Specimen geometry and loading configuration for strength testing.

unit, a testing chamber and a unit for measuring the flow of the gas that permeates the sample to be measured. The typical specimen size is a tubular supports with an area of approximately 10 to 20 cm^2. After sintering, the thickness of the different porous MgO support samples varies from 0.85 to 0.90 mm. A pressure difference across the samples was created using an electropneumatic pressure controller (Tescom, ER3000, USA). The flow of permeated gas was measured using a flow meter (Agilent, USA). The measurements were made with a pressure difference of 200 kPa at room temperature and with nitrogen as the permeate gas. MgO tubes sintered at 1300 °C were glued at one end to steel fixtures and to a polymer composite enclosure at the other. Then gas permeation measurements were carried out in order to quantify the gas permeability using the Darcy equation:

$$j = \frac{\kappa}{\mu}\nabla P \tag{1}$$

where k is the permeability (m^2), j is the flux ($m^3\,(m^2\,s)^{-1}$), μ is the viscosity of the gas (Pa s), and ∇P is the pressure gradient (pressure (Pa)/sample thickness (m)).

The elastic modulus and strength were measured by 4-point bending test of sectored specimens, which is a variant of the method developed.[19] Typically a large number (~30) of samples is used to investigate mechanical properties. Often this is time-consuming and therefore many reported strength values are based on a small sample number and are subjected to considerable uncertainties.[20,27] Sectored specimens were prepared by cutting the extruded tubes on the long axis into 4 quarters, each subtending an angle of 90°. The cut surfaces of the specimens were ground flat and then tested under four-point bending. The length of specimens is 60 mm.

A schematic of the specimen geometry and loading configuration is shown in Fig. 3. The distance between the loading pins is 25.0 mm. The support pin and the loading pin are separated by 12.5 mm. A large tensile stress zone is created in the middle bottom region of the specimen. The highest tensile stress is located away from the cut surfaces and therefore the measured strength data were not influenced by defects introduced by the machining.

All experiments were conducted using specially designed test equipment for continuous testing of multiple specimens under controlled environments. The test facility is described in detail in.[19]

Four-point bending tests were performed at room temperature and 850 °C in atmospheric air. The rate of downward movement of the actuator was 0.1 mm s^{-1}. The vertical displacement of the loading pins and the forces acting on the support pins were measured continuously.

The elastic modulus E was obtained from the load-displacement curve based on the Euler–Bernoulli beam theory,

$$E = \frac{P}{d}\frac{3La^2 + 2a^3}{6I} \tag{2}$$

where d is the vertical displacement of the loading pins, P is the applied force, and I is the second moment of area of the specimen cross section.

To obtain the strength of each specimen, the maximum stress corresponding to the applied force at fracture was computed by the finite element method using the commercial software Abaqus.[28] The calculated strength distribution was evaluated according to the conventional Weibull theory.[29] The probability of fracture P_f is given by

$$P_f = 1 - \exp\left(-\left(\frac{\sigma_{\max}}{\sigma_0}\right)^m\right) \tag{3}$$

where $\sigma_{\max}$ is the maximum tensile stress in the specimen. The linear regression method was used to compute the two Weibull parameters, namely the characteristic strength σ_0 and Weibull modulus m.

Since the stress distribution in the specimen is multi-axial, the principle of independent action[30] was employed in calculating the effective volume. This principle assumes that the principal stresses act independently on fracture, which leads to an effective volume expression given by

$$V_{\text{eff}} = \int_V \left(\frac{\sigma_1}{\sigma_{\max}}\right)^m + \left(\frac{\sigma_2}{\sigma_{\max}}\right)^m + \left(\frac{\sigma_3}{\sigma_{\max}}\right)^m \mathrm{d}V \tag{4}$$

where $\sigma_1, \sigma_2, \sigma_3$ are the three principal stresses, and V is the specimen volume. The effective volume was determined numerically from the computed stress distributions based on finite element analysis.

Weibull parameters were determined from a finite number of specimens invariably deviate from that of the parent population. The uncertainty in the measured Weibull parameters can be assessed by means of Monte Carlo simulations.[31] The confidence intervals for the measured characteristic strength and Weibull modulus were determined after carrying out 10,000 Monte Carlo runs for each set of tests.

3. Result and discussion

3.1. Characterization of raw materials and feedstocks for thermoplastic extrusion of MgO tubes

Fig. 4 shows SEM pictures of the raw materials that were used for preparation of thermoplastic feedstocks for extrusion. Fig. 4(a) shows the MgO powder that was pre-calcined at 1000 °C in order to improve de-agglomeration during milling and mixing and to avoid inhomogeneity in the final feedstock.[32] Three different types of pore formers, with quite different particle size and shape are shown in Fig. 4(b) to (d): Two types of graphite (named by the supplier as flaky graphite (b) and

Please cite this article in press as: Ramachandran DK, et al. The role of sacrificial fugitives in thermoplastic extrusion feedstocks on properties of MgO supports for oxygen transport membranes. *J Eur Ceram Soc* (2014), http://dx.doi.org/10.1016/j.jeurceramsoc.2014.11.014

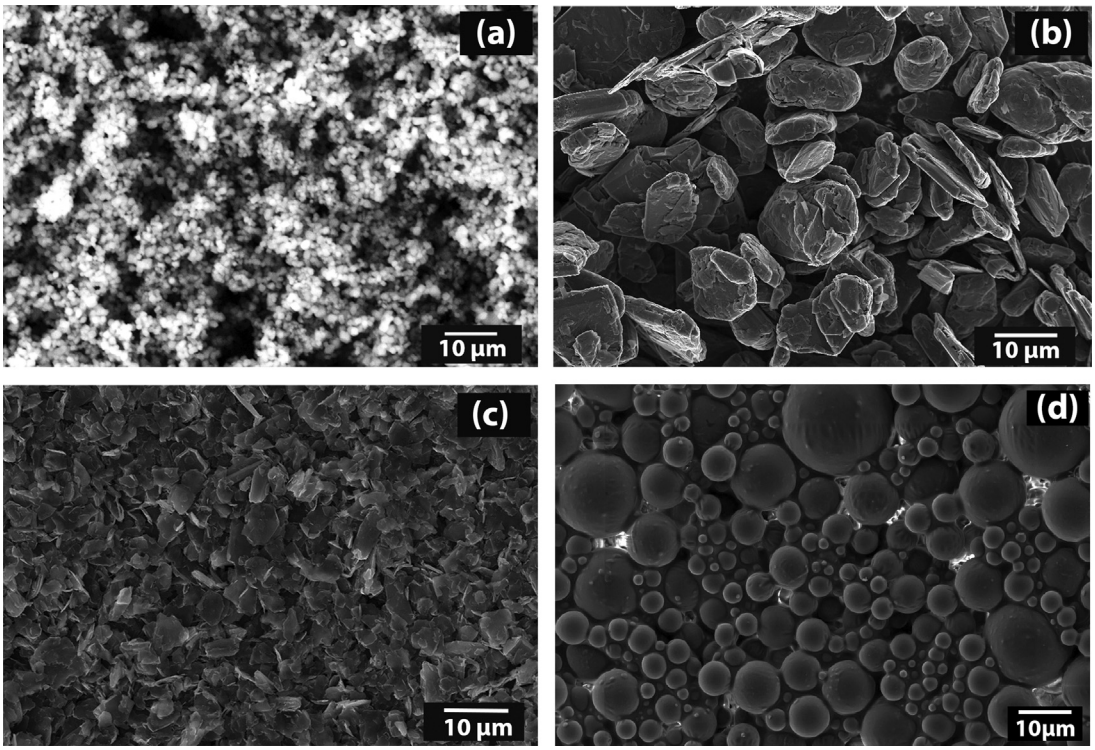

Fig. 4. SEM images of raw powders for preparation of thermoplastic feedstocks for extrusion: (a) MgO calcined at 1000 °C, (b) graphite powder, flaky (FL), (c) graphite powder, spherical (SP), and (d) PMMA (PM).

spherical graphite (c)) and PMMA. The influence of these different pore formers on processing, microstructure development (pore size, shape and distribution), gas permeability and mechanical strength are reported in the following sections.

From the particle size distribution (PSD) measurements, the mean particle size of the MgO powder and the pore formers were estimated using particle size analyzer (LS 13320, Beckman colter, Inc., USA). The uncalcined (as-received) MgO powder consisted of extremely fine (nanometric) primary particles that were aggregated into larger, irregular agglomerates (not shown here). Calcination of the MgO at 1000 °C resulted in reduction of the surface area and the measured PSD; the d50 value of the powder decreased from 2.99 μm to 1.53 μm after the processing.[32] A flaky graphite powder (FL) with an average particle size of about 11 μm was selected; this particle size is at least a factor of seven larger than the calcined MgO powder. The introduction of such large pore former particles was done with the intention of introducing sufficiently large pores in the sintered support, and hence achieving high gas permeation. With the same intention, another graphite powder (spherical, SP) with a mean particle size of 5.5 μm, and a PMMA pore former with 10.5 μm particle size were used to study the influence of the type and size of pore former on different MgO support properties (porosity, gas permeation and mechanical strength) after shaping and sintering.

In thermoplastic ceramic processing the debinding cycle is often critical and time consuming step. Relative large amounts of organics need to be removed before sintering step (Fig. 2). An incomplete or to quick debinding cycle will result in blister, cracks and voids which will negatively influence the mechanical strength. Thus, in this study thermogravimetric analysis was performed to identify decomposition temperatures of the organic components. Subsequently, the temperature profiles for debinding were optimized to ensure a very slow and smooth debinding and avoid the formation of any cracks/defects. Flaw-free ceramics are especially important for the study of the mechanical properties of the tubular membrane supports (reported in Section 3.3).

Fig. 5 shows the weight loss as a function of temperature for (a) the single components of the thermoplastic binder system and pore formers, as well as (b) the three MgO feedstocks (MP-FL, MP-SP and MP-PM). All feedstocks contain MgO powder, Elvax 250 as the main binder, paraffin wax as lubricant/binder and stearic acid as a dispersant.

The evaporation of the pure stearic acid and the decomposition of paraffin wax start rapidly at relatively low temperatures of around 160 °C, and 90% of the wax and stearic acid are removed in the narrow temperature range up to 300 °C. The Elvax250 decomposition starts slowly at a slightly higher temperature of about 250 °C, with the highest rate of weight loss occurring at temperatures between 400 °C and 500 °C. The polymeric pore former (PMMA) decomposes completely in the temperature range of 250 °C to 350 °C. This pore former is therefore removed before the debinding of the thermoplastic binder is completed. The mass loss curve for the pure graphite shows decomposition between 500 °C and 750 °C. In this case the pore former is removed at higher temperatures than the thermal decomposition temperature of the thermoplastic binder.

When the pore formers are mixed with MgO and thermoplastic additives (Fig. 5(b)), the decomposition peak for all feedstocks are broadened and slightly shifted to higher temperatures, first reaching complete decomposition at temperatures

Please cite this article in press as: Ramachandran DK, et al. The role of sacrificial fugitives in thermoplastic extrusion feedstocks on properties of MgO supports for oxygen transport membranes. *J Eur Ceram Soc* (2014), http://dx.doi.org/10.1016/j.jeurceramsoc.2014.11.014

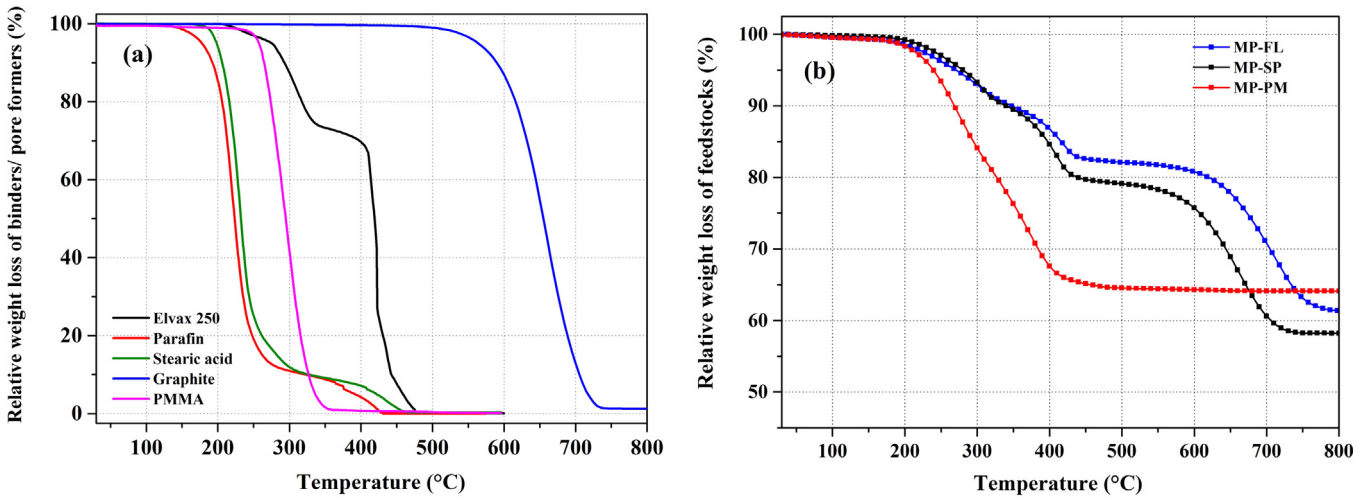

Fig. 5. (a) Thermogravimetric analysis (TGA) of the individual components; Elvax 250, paraffin wax, stearic acid, graphite and PMMA, (b) the binder removal of three different MgO feedstocks: MP-FL (graphite, flaky), MP-SP (graphite, spherical) and MP-PM (PMMA).

around 450 °C and 800 °C for PMMA and graphite pore formers, respectively. This shift can be explained by a slightly oxygen deficient atmosphere due to the binder decomposition in a densely packed MgO matrix that restricts the heat transfer and the removal of decomposition products (gases evolving during organic removal).[33]

The difference in decomposition temperature of organic compounds in the different feedstock can be better compared from the rate of the weight loss plotted in Fig. 6. The thermoplastic feedstocks that contain graphite (MP-FL and MP-SP) show a broader decomposition peak than the PMMA feedstock. The three distinct peaks are shifted slightly to higher temperatures for the graphite feedstock MP-FL which has slightly higher ceramic content (39 vol.% ceramic) compared to the MP-SP feedstock (34 vol.% ceramic). As discussed above, the shift in the decomposition peaks to higher temperatures for the MP-FL feedstock might be related to the a limited heat and air/oxygen transport inside the green body during organic removal.[33] According to the TG experiments, three different critical temperatures (320 °C, 420 °C, and 720 °C) where identified for MP-FL whereas the feedstock MP-SP has peak temperatures (300 °C, 400 °C, and 670 °C). Hence, a heating rate 15 °C h^{-1} and a dwell time of 1 h with at each of these temperatures was implemented in the debinding cycle to allow slow and complete stepwise decomposition of the polymer components, avoiding the formation of defects from degassing. In the case of the MP-PM feedstock, the debinding was more challenging due to the high polymer content (46 vol.% thermoplastic polymer and 20 vol.% PMMA) which decomposes in the temperature range of 200 to 420 °C. Fig. 6 shows distinct peaks for the MP-PM feedstock at 270 °C (assigned to a merging of the peaks from paraffin, stearic acid and PMMA) and at 375 °C (Elvax 250). Since the pore former of feedstock MP-PM leaves the green body in a very early stage of the debinding, the shape stability is lower in comparison to feedstocks with graphite as a pore former

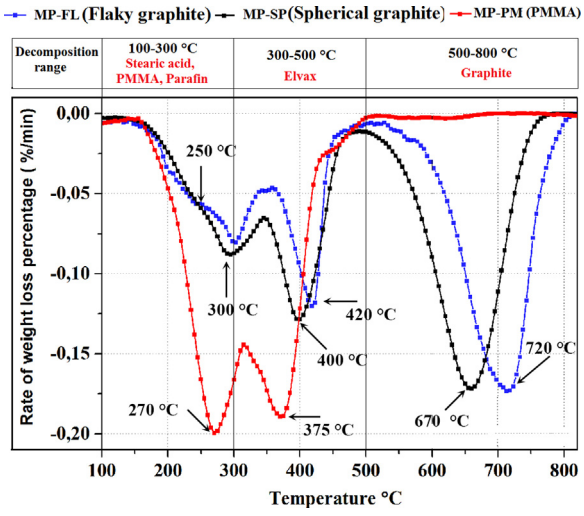

Fig. 6. Thermogravimetric analysis (TGA) of three thermoplastic MgO feedstocks: MP-FL, MP-SP and MP-PM. The major decomposition ranges for the different additives and pore formers are indicated; 100–300 °C (decomposition of stearic acid, paraffin and PMMA), 300–500 °C (decomposition of Elvax 250) and 500–800 °C (decomposition of graphite).

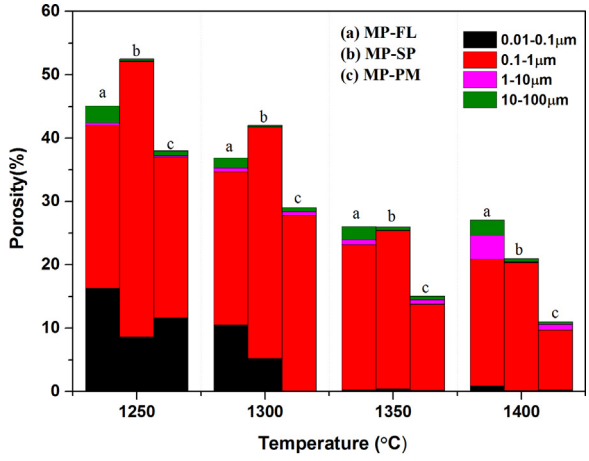

Fig. 7. Total porosity and pore size of the different MgO supports: (a) MP-FL, (b) MP-SP and (c) MP-PM sintering temperatures ranging from 1250 °C to 1400 °C.

Please cite this article in press as: Ramachandran DK, et al. The role of sacrificial fugitives in thermoplastic extrusion feedstocks on properties of MgO supports for oxygen transport membranes. *J Eur Ceram Soc* (2014), http://dx.doi.org/10.1016/j.jeurceramsoc.2014.11.014

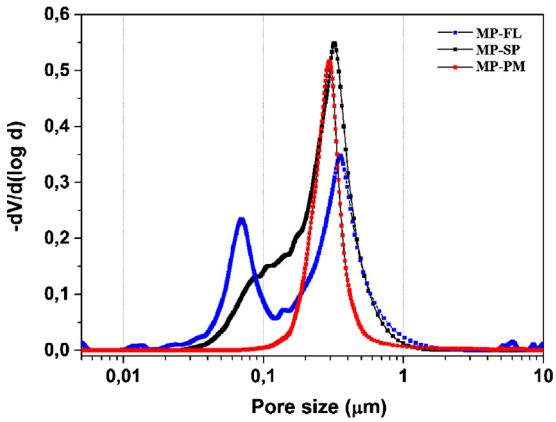

Fig. 8. Pore size distribution determined by Hg porosimetry for the different MgO supports (MP-FL, MP-SP and MP-PM) sintered at 1300 °C.

(MP-FL and MP-SP), and a slower heating rate needed to avoid shape deformation. Hence, a heating rate of 10 °C h^{-1} and a dwell of 2 h at each of the indicated temperatures (270 and 380 °C) were applied to achieve a successful debinding cycle of MP-PM.

3.2. Effect of sintering temperature on the evolution of the MgO support microstructures

After the optimized debinding cycle (see Section 2.4), the MgO supports were sintered for 2 h at several temperatures (1250 °C, 1300 °C, 1350 °C and 1400 °C) in order to evaluate the microstructural development. The porosity and the pore size distribution, measured by Hg intrusion, are presented in Fig. 7. This graph present porosity and four classes of poro size in order to visualize changes in the pore structure for the different pore formers depending on the sintering temperature. The highest porosity (52.5%) was achieved for MP-SP at 1250 °C that constitutes a large volume of small pores. Pores below 0.1 μm were eliminated by increase of sintering temperatures. As shown previously,[32] this class of pores sizes is related from the MgO particle network (e.g. MgO skeleton). A decrease of this pore size class can be explained by a sintering of the MgO skeleton through the collapse of these small pores. A sintering of the MgO skeleton does not only result in a decrease of the porosity. It also result in an increase of the lager pores as indicated in Fig. 7. For the MP-FL supports, the total porosity decreased with increasing sintering temperature, except between 1350 °C and 1400 °C, where the total porosity remained constant while the pore size increased. Furthermore these phenomena can be explained by further sintering and densification of MgO skeleton. Due to the larger pore size distribution and the constant porosity, it is thought that the MP-FL support sintered at 1400 °C should have better gas permeation properties than the support sintered 1350 °C. In the case of MP-SP, consistently decreasing porosity with increasing sintering temperature is observed, as well as a gradual increase in pore size. Meanwhile, the MP-PM showed very drastic changes in the pore size between 1250 and 1300 °C from elimination of pores below 0.1 μm, reducing the total porosity from 38 to 29%. The MP-PM support also shows similar trend MP-SP, but the total porosity is reduced to almost half of that of MP-SP at 1400 °C and there is no significant pore size enlargement observed after 1300 °C. This eventually confirms that the MP-PM has the least pore volume and poor connectivity, which may resist resulting in insufficient gas supply for the final application.

Previous investigations have been shown that 1300 °C seem to be a good compromise to achieve a dense CGO oxygen membrane on a tubular porous MgO support. In Fig. 8, the pore size distributions of the three different MgO supports sintered at 1300 °C are reported. For later applications the sintering temperature is most relevant, as it allows the densification of the active CGO membranes on the porous MgO support at low temperatures and high porosity. Fig. 8 shows a bimodal pore size distribution for MP-FL and monomodal distribution for MP-SP and MP-PM. It can easily be deduced that MP-SP should have a higher gas permeation value than other two supports, since it has similar mean pore size ~0.33 μm, but a total pore volume 5 to 13% higher than other two supports.

The microstructure (polished cross sections) as observed by electron microscopy are shown in Fig. 9 for all three different MgO supports sintered at 1300 °C. They all show different microstructures due the different debinding properties and particle sizes of the pore formers. Micrographs indicate that the support (MP-SP) has a better pore connectivity than all two supports which ideally enhances gas permeation value. This can be confirmed by the gas permeability measurements which is maximum for MP-SP and which will be discussed in Section 3.3. In the case of MP-PM, there are some big isolated pores which can be easily visualized Fig. 9(c) and the weak pore network eventually deteriorates the gas permeation properties.

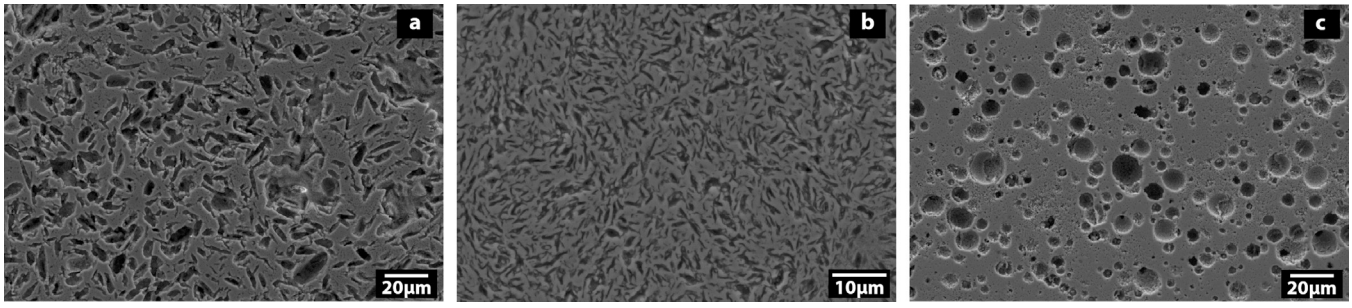

Fig. 9. SEM micrographs of polished cross sections of MgO supports sintered at 1300 °C (a) MP-FL, (b) MP-SP and (c) MP-PM.

Please cite this article in press as: Ramachandran DK, et al. The role of sacrificial fugitives in thermoplastic extrusion feedstocks on properties of MgO supports for oxygen transport membranes. *J Eur Ceram Soc* (2014), http://dx.doi.org/10.1016/j.jeurceramsoc.2014.11.014

Table 2
The pore size characteristics of three MgO support sintered at 1300 °C.

Code	Pore former (μm)	Pore size (image analysis) (μm)	Pore neck size (Hg porosimetry) (μm)	Size ratio (neck to pore) (%)
MP-FL	11.3	10.3	0.36	3.5
MP-SP	5.5	2.8	0.34	12.0
MP-PM	10.5	7.9	0.30	3.8

In order to calculate the mean pore size of MgO support from SEM 2D image, the image analysis MAT LAB program was used by simply selecting right threshold point in order to distinguish two different phases; ceramic and pore boundaries. It is also well known that the pore size determined by Hg porosimetry indicates pore neck size and it always underestimates the real pore size which is shown in SEM images. Table 2 shows the mean size of pore former, pore size, pore neck size (Hg porosimetry) and neck to pore ratio for all three supports sintered at 1300 °C.

Referring Table 2, it is important to calculate the neck to pore ratio as this value indicates how well the pores are connected with each other. It can be concluded that a higher neck to pore ratio was achieved for MP-SP (12%) whereas the ratio for the two other supports isunder 4%. Ultimately, the smaller pore and larger neck size of MP-SP improves mechanical strength and gas permeability respectively.

3.3. Mechanical and gas permeation properties of MgO supports

The mechanical properties of the three different MgO support tubes (MP-FL, MP-SP, and MP-PM,all sintered at 1300 °C) were evaluated by 4-point bending strength measurements at room temperature (25 °C) and at 850 °C which is a relevant operation temperature for an asymmetric ceria or ceria composite oxygen membrane.

The elastic modulus for the three different supports characterized at 25 °C and 850 °C are shown in Table 3. All load-displacement curves obtained from four-point bending tests are linear and reproducible over the all tests. The elastic moduli reported were determined by averaging results over all tests.

The difference in elastic moduli between the three different types of supports is due to the porosity difference. The dependence of the elastic modulus on porosity for ceramics can typically be described by an empirical relation[34]:

$$E = E_0 \quad \exp(-bp)$$

where E_0 is the elastic modulus at zero porosity, p is the porosity, and b is an empirical constant. Using the reported values for E_0 and b of dense MgO at room temperature [34], the empirical relation gives elastic moduli of 55.0 GPa, 41.0 GPa, and 80.0 GPa for MP-FL, MP-SP, and MP-PM, respectively. As shown in Table 3, the measured elastic moduli for MP-FL and MP-SP agree quite well with the empirical model, except for MP-PM for which the measured elastic modulus is lower than the empirical model prediction.

The elastic moduli for the three types of supports decrease slightly with temperature, of the order of 7–9 GPa. The measured elastic moduli are slightly lower than the range of 50–66 GPa given in the literature for MgO with a porosity of 36%.[20] For application as support materials, a low elastic modulus is preferred because a more compliant support induces smaller stresses in the membrane.[35,36]

The fracture strength distribution at 25 °C and 850 °C are plotted in Fig. 10(a) and (b), respectively. The corresponding Weibull moduli and characteristic strengths are summarized in Table 3, together with the effective volume of each test series and porosity of the supports. Limits of the 90% confidence interval are shown for the Weibull parameters in brackets.

Similar values for Weibull moduli were obtained for the three supports. This indicates that the spread of the critical flaw size distributions for the three supports are comparable. The Weibull moduli at 850 °C were found to be lower than those at 25 °C for all three supports. The differences are however within the limits of uncertainty due to finite sampling. Since the Weibull modulus is a measure of the spread of the critical flaw size, it is therefore not expected to correlate with temperature. Overall, the Weibull moduli for the three supports are typical for ceramics.

Table 3
Mechanical properties measured at 25 °C and 850 °C for MgO supports, sintered at 1300 °C. Numbers in brackets refer to limits of 90% confidence interval resulting from finite sampling.

Parameters	MP-FL*		MP-SP*		MP-PM*	
	25 °C	850 °C	25 °C	850 °C	25 °C	850 °C
Number of specimens	25	30	30	24	30	30
Elastic modulus [GPa]	49.89	42.39	42.51	34.56	51.60	43.01
Weibull modulus	7.75 (5.45–10.61)	5.12 (3.70–6.83)	8.97 (6.51–11.95)	6.35 (4.44–8.77)	8.74 (6.36–11.3)	5.45 (3.99–7.26)
Effective volume [mm^3]	6.91	10.82	5.53	7.67	5.68	9.06
Characteristic strength [MPa]	79.79 (76.14–83.47)	59.56 (55.90–63.42)	82.31 (79.39–85.33)	62.27 (58.76–65.84)	73.17 (70.56–75.88)	61.72 (58.16–65.47)
Porosity (%)	37		42		29	

* Sintering temperature for all samples was 1300°C with 2 h holding.

Please cite this article in press as: Ramachandran DK, et al. The role of sacrificial fugitives in thermoplastic extrusion feedstocks on properties of MgO supports for oxygen transport membranes. *J Eur Ceram Soc* (2014), http://dx.doi.org/10.1016/j.jeurceramsoc.2014.11.014

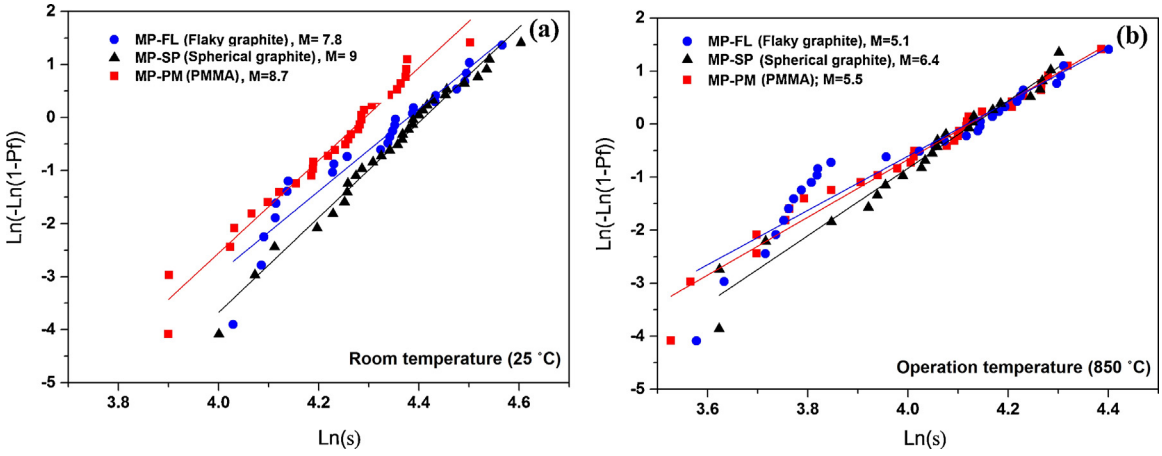

Fig. 10. Fracture probability of MgO supports at (a) room temperature (25 °C) and (b) membrane operation temperature (850 °C) for the three supports MP-FL (flaky graphite), MP-SP (spherical graphite) and MP-PM (PMMA) sintered at 1300 °C.

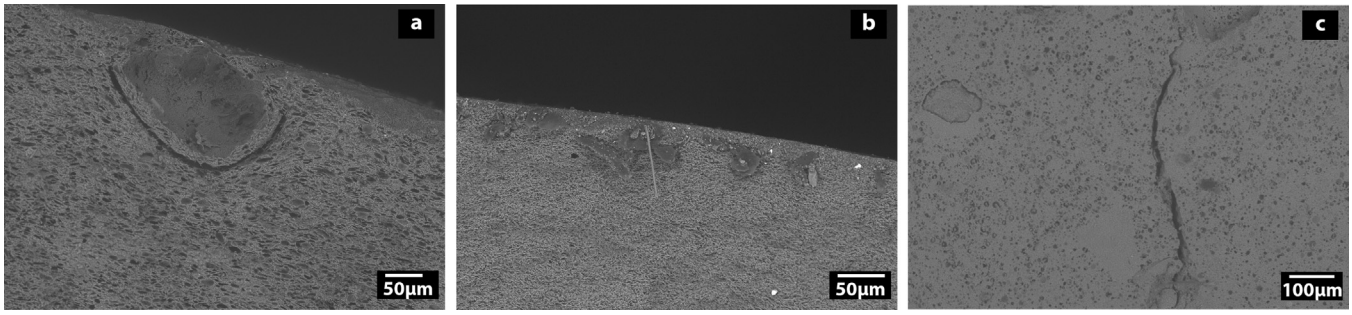

Fig. 11. Fracture surface and inhomogeneity in the microstructure of the tubular samples at the surface of (a) MP-FL, (b) MP-SP, and (c) MP-PM supports sintered at 1300 °C.

For each support, the effective volume at 850 °C is larger than that at 25 °C because of the lower Weibull modulus measured at the higher temperature. The differences in effective volumes between the supports are due to the difference in both the Weibull modulus and specimen dimensions.

To correctly compare the characteristic strengths of different supports, the measured strength values at different effective volumes in Table 3 need to be scaled to the same effective volume using the relation:

$$\left(\frac{\sigma_0'}{\sigma_0''}\right)^m = \frac{V_{\text{eff}}''}{V_{\text{eff}}'}$$

where σ_0' and σ_0'' are the characteristic strengths at the effective volumes V_{eff}' and V_{eff}''.

Table 4 shows the comparison of characteristic strength of different supports scaled to the same effective volume of 10 mm^3. All supports show a decrease in characteristic strength going from 25 °C to 850 °C. The drop in strength is primarily due to the reduction in elastic modulus with temperature.

At room temperature, MP-FL and MP-SP have similar characteristic strengths with a difference within the statistical uncertainty. The total open porosity difference of 6% between the two supports has little influence on the strength. Despite having the lower porosity (higher solid volume) the characteristic strength of MP-PM is lower than the other two supports. This suggests that the critical pore/flaw size is the strength-controlling factor in the supports.

Analysis of the fractured surfaces of the MP-FL and MP-SP supports in Fig. 11(a) and (b) reveal that locally dense spots (e.g. inhomogeneity in the MgO skeleton) are situated near the outer surface of the tubular supports. Cracks of a few hundred micrometers long surrounding the dense spots were observed. These cracks are likely to be resulted from the local mismatch of elastic moduli between the dense spots and the porous surrounding. Since the outer surface was subjected to tensile stress in the four-point bending tests, such dense spots were identified

Table 4
Characteristic strength of porous supports scaled to an effective volume of 10 mm^3.

Temperature (°C)	MP-FL (MPa)	MP-SP (MPa)	MP-PM (MPa)	BSCFZ[19] (MPa)
25	76.07	77.05	68.58	21.15
850	60.48	59.72	60.61	16.94

Please cite this article in press as: Ramachandran DK, et al. The role of sacrificial fugitives in thermoplastic extrusion feedstocks on properties of MgO supports for oxygen transport membranes. *J Eur Ceram Soc* (2014), http://dx.doi.org/10.1016/j.jeurceramsoc.2014.11.014

Table 5
The measured gas permeability of the MgO tubular supports at ΔP of 200 kPa.

	MP-FL	MP-SP	MP-PM
Darcian gas permeability (m^2)	1.25×10^{-16}	4.70×10^{-16}	1.0×10^{-17}

to be the fracture initiators. As shown in Fig. 11(c), even longer cracks were found in MP-PM than in MP-FL and MP-SP. The cracks are straight and oriented in the radial direction of the supports, and can extend as long as half of the support thickness. For all supports, cracks significantly larger than the pores can be identified. Fracture of specimens is therefore controlled by such inhomogeneity in the microstructure, and the pore geometry and distribution of the pore formers are expected to have only a minor effect in the characteristic strengths measured.

The gas permeability measurements were performed on MgO supports sintered at 1300 °C. The results of the MgO tubular supports at 200 kPa are presented in Table 5. This study indicates a strong correlation between the permeability and the open porosity, as expected. From Table 5, it is seen that the permeability is highest for the MgO support used spherical graphite as pore former (MP-SP). The achieved permeability value of 4.70×10^{-16} was almost 0.4–1.5 orders of magnitude higher than other two MgO supports. The reason for the higher permeability of MP-SP is due to the microstructures which contains high interconnected open porosity (ref Fig. 9). The decrease in permeability of other two supports originates from the decrease in porosity and the formation of randomly oriented larger elongated pores and isolated pores that may restrict the gas transport pathway.

4. Conclusion

Porous tubular MgO supports (14 mm diameter and a thickness of 1 mm) were developed through thermoplastic processing using three different types of pore former. The microstructure (pore size distributions, open porosity etc.) was investigated with respect to its influence on mechanical properties and the gas permeation. Thermoplastic processing was shown to be an easy route to produce porous structures and the level of porosity could be optimized to obtain a suitable support for OTM applications. Debinding studies were carried out in order to prepare stable and defect-free components. Three temperature regimes were identified as crucial areas where the polymers and pore former in the feedstock predominantly decompose. Hence dwell times of 1 h at each peak of these temperature regimes were implemented in the debinding cycle to allow slow and step-wise decomposition of the polymers and graphite powder. In the case of MP-PM, the temperatures 270 °C and 380 °C were observed to be critical temperatures and hence dwell time periods of 2 h were used at these temperatures to ensure complete organic removal. In the microstructural studies it was found that the supports prepared with spherical graphite as a pore former (MP-SP) showed open interconnected structures which resulted in higher open porosities about 42.5% at 1300 °C with a moderate gas permeation value. The mechanical strength was characterized using 4-point bending of tubes cut in the axial direction. The Weibull moduli for MgO with spherical type graphite (MP-SP) were the highest among the supports investigated. This suggests that the spread of flaw size distribution is the narrowest which is desirable for a ceramic under application. The characteristic strengths of MgO support (MP-SP) were 77 MPa and 60 MPa for room and membrane operating temperature which are likely sufficient for a mechanically robust support. Moreover, MgO support it preferred because it has no problems with high temperature redox reactions or carbon poising and cation diffusion which is typically observed in CGO and perovskite materials.[37,38] Comparing the gas permeation values at the same sintering temperature (1300 °C, considered suitable temperature of co-sintering with membrane layer in the future), the highest gas permeation value of 4.7×10^{-16} m^2 was achieved for MP-SP which is almost 40% higher than MP-FL supports with similar mechanical strength.

Acknowledgements

The authors would like to thank the Danish Council for Independent Research Technology and Production Sciences (FTP) which is part of The Danish Agency for Science. Technology and Innovation (FI) (Project no. 09-072888) for sponsoring the OPTIMAC research work. We would also like to acknowledge DTU-Division of Energy Conversion and Storage for the internally-funded project (BIO-OTM) under which the mechanical testing was performed. Pernille Hedemark Nielsen and Marianne Nielsen are thankfully acknowledged for preparation of feedstocks, dilatometry analzses and Hg-porosimetry measurements.

References

1. Belaissaoui B, Le Moullec Y, Hagi H, Favre E. Energy efficiency of oxygen enriched air production technologies: cryogeny vs. membranes. *Sep Purif Technol* 2014;**125**:142–50.
2. Puig-Arnavat M, Soprani S, Søgaard M, Engelbrecht K, Ahrenfeldt J, Henriksen UB. Integration of mixed conducting membranes in an oxygen–steam biomass gasification process. *RSC Adv* 2013;**3**:20843–54.
3. Lemes-rachadel P, Sachinelli G, Antonio R, Machado F, Hotza D, Carlos J. Current developments of mixed conducting membranes on porous substrates. *Mater Res* 2014:17.
4. Sammells AF, Schwartz M, Mackay RA, Barton TF, Peterson DR. Catalytic membrane reactors for spontaneous synthesis gas production. *Catal Today* 2000;**56**:325–8.
5. Dyer PN, Richards RE, Russek SL, Taylor DM. Ion transport membrane technology for oxygen separation and syngas production. *Solid State Ionics* 2000;**134**:21–33.
6. Leo A, Liu S, Diniz da Costa JC. The enhancement of oxygen flux on $Ba_{0.5}Sr_{0.5}Co_{0.8}Fe_{0.2}O_{3-\delta}$ (BSCF) hollow fibers using silver surface modification. *J Membr Sci* 2009;**340**:148–53.
7. Sunarso J, Baumann S, Serra JM, Meulenberg WA, Liu S, Lin YS. Mixed ionic–electronic conducting (MIEC) ceramic-based membranes for oxygen separation. *J Membr Sci* 2008;**320**:13–41.
8. Fan CG, Wu RM, Pei LZ, Zhang QF. Effect of sintering temperature on the behavior of oxygen permeation for $La_{0.6}Sr_{0.4}Co_{0.2}Fe_{0.8}O_{3-\delta}$ tubular membranes. *Adv Mater Res* 2010;**105–106**:643–6.
9. Watenabe K, Yuasa M, Kida T, Teraoka Y, Yamazoe N, Shimanoe K. High-performance oxygen-permeable membranes with an asymmetric structure using $Ba_{(0.95)}La_{(0.05)}FeO_{(3\text{-}delta)}$ perovskite-type oxide. *Adv Mater* 2010;**22**:2367–70.

Please cite this article in press as: Ramachandran DK, et al. The role of sacrificial fugitives in thermoplastic extrusion feedstocks on properties of MgO supports for oxygen transport membranes. *J Eur Ceram Soc* (2014), http://dx.doi.org/10.1016/j.jeurceramsoc.2014.11.014

10. Julian A, Juste E, Geffroy PM, Coudert V, Degot S, Del Gallo P. Elaboration of $La_{0.8}Sr_{0.2}Fe_{0.7}Ga_{0.3}O_{3-\delta}/La_{0.8}M_{0.2}FeO_{3-\delta}$ (M=Ca, Sr and Ba) asymmetric membranes by tape-casting and co-firing. *J Membr Sci* 2009;**333**:132–40.
11. Zhu DC, Xu XY, Feng SJ, Liu W, Chen CS. La_2NiO_4 tubular membrane reactor for conversion of methane to syngas. *Catal Today* 2003;**82**:151–6.
12. Meng X, Ding W, Jin R, Wang H, Gai Y, Ji F. Two-step fabrication of $BaCo_{0.7}Fe_{0.2}Nb_{0.1}O_{3-\delta}$ asymmetric oxygen permeable membrane by dip coating. *J Membr Sci* 2014;**450**:291–8.
13. Baumann S, Meulenberg WA, Buchkremer HP. Feature article manufacturing strategies for asymmetric ceramic membranes for efficient separation of oxygen from air. *J Eur Ceram Soc* 2013;**33**:1251–61.
14. Sarasketa-Zabala E, Otaegi L, Rodriguez-Martinez LM, Alvarez MA, Burgos N, Castro F. High temperature stability of porous metal substrates under highly humidified hydrogen conditions for metal supported solid oxide fuel cells. *Solid State Ionics* 2012;**222–223**:16–22.
15. Chen Z, Shao Z, Ran R, Zhou W, Zeng P, Liu S. A dense oxygen separation membrane with a layered morphologic structure. *J Membr Sci* 2007;**300**:182–90.
16. Zhou Y, Fukushima M, Miyazaki H, Yoshizawa Y, Hirao K, Iwamoto Y. Preparation and characterization of tubular porous silicon carbide membrane supports. *J Membr Sci* 2011;**369**:112–8.
17. Li S, Jin W, Huang P, Xu N, Shi J, Lin Y. Tubular lanthanum cobaltite perovskite type membrane for oxygen permeation. *J Membr Sci* 2000;**166**:51–61.
18. Lipinska-chwalek M, Malzbender J, Chanda A, Baumann S. Mechanical characterization of porous $Ba_{0.5}Sr_{0.5}Co_{0.8}Fe_{0.2}O_{3-d}$. *J Eur Ceram Soc* 2011;**31**:2997–3002.
19. Kwok K, Kiesel L, Frandsen HL, Søgaard M, Hendriksen PV. Strength characterization of tubular ceramic materials by flexure of semi-cylindrical specimens. *J Eur Ceram Soc* 2014;**34**:1423–32.
20. Lipińska-Chwałek M, Kiesel L, Malzbender J. Mechanical properties of porous MgO substrates for membrane applications. *J Eur Ceram Soc* 2014;**34**:2519–24.
21. Pećanac G, Foghmoes S, Lipińska-Chwałek M, Baumann S, Beck T, Malzbender J. Strength degradation and failure limits of dense and porous ceramic membrane materials. *J Eur Ceram Soc* 2013;**33**:2689–98.
22. Kaiser A, et al. Evaluation of thin film ceria membranes for syngas membrane reactors—preparation, characterization and testing. *J Membr Sci* 2011;**378**:51–60.
23. Hong L, Chen X, Cao Z. Preparation of a peroskite $La_{0.2}Sr_{0.8}CoO_{3-x}$ membrane on a porous MgO substrate. *J Eur Ceram Soc* 2011;**21**:2207–15.
24. Middleton H, Diethelm S, Larrain D, Sfeir J. Co-casting and co-sintering of porous MgO support plates with thin dense perovskite layers of $LaSrFeCoO_3$. *J Eur Ceram Soc* 2004;**24**:1083–6.
25. Ismael MR, Clemens F, Graule T, Hoffmann MJ. Effects of different thermoplastic binders on the processability of feedstocks for ceramic co-extrusion process. *Ceram Int* 2011;**37**:3173–82.
26. Heiber J, Clemens F, Graule T, Hülsenberg D. Thermoplastic extrusion to highly-loaded thin green fibres containing Pb(Zr, Ti)O_3. *Adv Eng Mater* 2005;**7**:404–8.
27. Pećanac G, Baumann S, Malzbender J. Mechanical properties and lifetime predictions for $Ba_{0.5}Sr_{0.5}Co_{0.8}Fe_{0.2}O_{3-\delta}$ membrane material. *J Membr Sci* 2011;**385–6**:263–8.
28. Abaqus 6.12 Documentation. Dassault Systemes Simulia Corporation; 2012.
29. Waloddi weibull. A statistical distribution function of wide applicability. *J Appl Mech* 1951;**18**:293–7.
30. De A, Jayatilaka S, Trustrum K. Statistical approach to brittle fracture. *J Mater Sci* 1977;**12**:1426–30.
31. Khalili A, Kromp K. Statistical properties of Weibull estimators. *J Mater Sci* 1991;**26**:6741–52.
32. Ramachandran DK, Clemens F, Glasscock AJ, Søgaard M, Kaiser A. Tailoring the microstructure of porous MgO supports for asymmetric oxygen separation membranes: optimization of thermoplastic feedstock systems. *Ceram Int* 2014;**40**:10465–73.
33. Salehi M, Clemens F, Graule T, Grobéty B. Kinetic analysis of the polymer burnout in ceramic thermoplastic processing of the YSZ thin electrolyte structures using model free method. *Appl Energy* 2012;**95**:147–55.
34. Spriggs RM, Brissette LA, Vasilos T. Effect of porosity on elastic and shear moduli of polycrystalline magnesium oxide. *J Am Ceram Soc* 1962;**45**:400.
35. Kwok K, Frandsen HL, Søgaard M, Hendriksen PV. Stress analysis and fail-safe design of bilayered tubular supported ceramic membranes. *J Membr Sci* 2014;**453**:253–62.
36. Kwok K, Frandsen HL, Søgaard M, Hendriksen PV. Mechanical reliability of geometrically imperfect tubular oxygen transport membranes. *J Membr Sci* 2014;**470**:80–9.
37. Yaremchenko AA, Kharton VV, Avdeev M, Shaula AL, Marques FMB. Oxygen permeability, thermal expansion and stability of $SrCo_{0.8}Fe_{0.2}O_{3-\delta}$–$SrAl_2O_4$ composites. *Solid State Ionics* 2007;**178**:1205–17.
38. Mogensen M, Sammes NM, Tompsett GA. Physical, chemical and electrochemical properties of pure and doped ceria. *Solid State Ionics* 2000;**129**:63–94.

Please cite this article in press as: Ramachandran DK, et al. The role of sacrificial fugitives in thermoplastic extrusion feedstocks on properties of MgO supports for oxygen transport membranes. *J Eur Ceram Soc* (2014), http://dx.doi.org/10.1016/j.jeurceramsoc.2014.11.014

Publication III

"Low cost porous MgO substrates for oxygen transport membranes"

Elsevier Editorial System(tm) for Materials Letters
Manuscript Draft

Manuscript Number: MLBLUE-D-14-03978

Title: Low cost porous MgO substrates for oxygen transport membranes

Article Type: Letter

Keywords: Porous MgO ceramics; Gas permeability; Membrane; Low cost supports; Thermoplastic system

Corresponding Author: Mr. Dhavanesan K Ramachandran,

Corresponding Author's Institution: Technical University of Denmark

First Author: Dhavanesan K Ramachandran

Order of Authors: Dhavanesan K Ramachandran; Martin Søgaard, PhD; Frank Clemens, PhD; Bhaskar Reddy Sudireddy, PhD; Andreas Kaiser, PhD

Abstract: This paper delineates the fabrication of porous magnesium oxide (MgO) ceramics with high porosity and gas permeability by warm pressing using pre-calcined MgO powder and fugitive pore former (combination of graphite and polymethyl methacrylate). Effect of pore former on the microstructure development of porous MgO ceramic substrates was subjected to investigation. The resultant microstructure consisted of large spherical and elongated pores with small interconnecting pores. The total porosity (55%), mean pore neck size (0.65 μm), and the associated gas permeability (4-4.5 x10-15 m2) of MgO substrates were measured and correlated. Economic analysis of the MgO substrates was performed and it was found that MgO was much cheaper compared to perovskite and fluorite materials

Suggested Reviewers: Liang Hong PhD
Associate Professor, Department of Chemical and Biomolecular Engineering, National University of Singapore
chehongl@nus.edu.sg
He has been working with inorganic catalytic materials and ceramic membrane for quite some years.

Kaustubha Mohanty PhD
Associate Professor, Department of Chemical Engineering, Indian Institute of Technology Guwahati
kmohanty@iitg.ernet.in
His research activity is focused on developing low cost ceramic membranes for water treatment and he acts as editor for number of journals. For further reference: http://www.iitg.ac.in/chemeng/KM.html

Marta Lipinska Chwalek PhD
Scientist, nstitute of Energy and Climate Research, Forschungszentrum Jülich
Marta.Lipinska-Chwalek@fz-juelich.de
She has been working with fabrication and characterization of porous ceramic membrane materials for past 10 years

DTU Energy Conversion

Dear editorial board of the Journal of Material Letters,

Enclosed please find the manuscript "**Low cost porous MgO substrates for oxygen transport membranes**", to be considered for publication in Material Letters.

In this manuscript, the development and characterization of a new porous magnesium oxide substrate with increased porosity and high permeability is presented for the application as membrane support for an asymmetric oxygen transport membrane. The economic analysis indicated that the developed MgO supports are almost 15-30 times cheaper compared to the perovskite and fluorite based support materials.

We believe that the preparation and characterization of cost-effective, porous ceramic support structures for use in asymmetric oxygen separation membranes is of interest to the readership of this journal.

We confirm that the work of this manuscript is original, unpublished and not being considered to be published elsewhere. All contributors, including funding sources are acknowledged. Thank you for your kind consideration of our paper and we look forward to your response.

On behalf of the authors,

Best regards,

Dhavanesan Kothanda Ramachandran

Ph.D. student

Department of Energy Conversion and Storage

Technical University of Denmark
DTU Energy Conversion
(Risø campus)

Frederiksborgvej 399
Building 779
DK-4000 Roskilde
Denmark

Tel.: +45 46 77 48 00
Fax: +45 46 77 58 58

dhra@dtu.dk
www.ecs.dtu.dk

Highlights

- Porous MgO substrate was developed through thermoplastic route using large particles of PMMA and graphite as pore-forming agent
- High gas permeability of $4x10^{-15}$ m^2 was achieved with a mean pore size of 0.65 µm.
- Cost-efficient porous MgO substrates for membrane applications.

Low cost porous MgO substrates for oxygen transport membranes

D. K. Ramachandran[1*], M. Søgaard[1], F.Clemens[2], B. R. Sudireddy[1], A. Kaiser[1]

[1]Department of Energy Conversion and Storage, Technical University of Denmark, Frederiksborgvej 399, Building 779, DK-4000 Roskilde, Denmark.

[2]Swiss Federal Laboratories for Materials Science and Technology, Ueberlandstrasse 129, CH-8600 Dübendorf, Switzerland

*Corresponding author, Tel.:+45 4677 4800; fax: +45 4677 5858. E-mail: dhra@dtu.dk, dhavaa@gmail.com

Abstract

This paper delineates the fabrication of porous magnesium oxide (MgO) ceramics with high porosity and gas permeability by warm pressing using pre-calcined MgO powder and fugitive pore former (combination of graphite and polymethyl methacrylate). Effect of pore former on the microstructure development of porous MgO ceramic substrates was subjected to investigation. The resultant microstructure consisted of large spherical and elongated pores with small interconnecting pores. The total porosity (55%), mean pore neck size (0.65 µm), and the associated gas permeability (4-4.5 x10^{-15} m^2) of MgO substrates were measured and correlated. Economic analysis of the MgO substrates was performed and it was found that MgO was much cheaper compared to perovskite and fluorite materials.

Keywords: Porous MgO ceramics; Gas permeability; Membrane; Low cost supports; Thermoplastic system

1. Introduction

Porous ceramic materials for high temperature engineering applications attracted significant attention due to their excellent thermal insulation properties originating from the unique combination of low density, low thermal conductivity, high thermal shock resistance and high refractoriness [1]. In catalytic membrane application, the function of the porous layer is to provide mechanical stability and unrestricted gas supply to the membrane interface for further catalytic reaction to occur. Often, in the preparation of oxygen transport membrane, the porous support layer for the membrane was made from the material similar to that of the membrane material in order to eliminate the thermal expansion mismatch issues [2]. The thickness of the porous support layer can be 25 to 50 times (~500 – 1000 μm) higher than the actual membrane layer (~20 μm), making the porous support as the major component in the membrane structure. It is thus important that a low cost material for porous support should be identified to minimize the cost of the membrane structure significantly to make it commercially viable. Magnesium oxide (MgO) is widely used in many industrial applications, mainly as refractory material, fireproofing construction material and catalyst [3]. The high thermal expansion, high thermal and chemical stability and low material cost of MgO made it attractive to use it as a support material [4,5].

There have been several methods employed to fabricate the MgO ceramic structures that included isostatic pressing, hot pressing, tape casting and extrusion for different applications [5–10]. The selection of shaping process depends on final application, cost-effectiveness for continuous production and scalability. It was demonstrated that both the warm pressing and extrusion processes resulted in similar final properties [9,11]. Extrusion process is also capable of producing stable and thin-walled components. Using warm pressing, porous MgO ceramics with a porosity of 36 vol. % and gas permeability of 1.4-3.1 × 10^{-16} m^2 were prepared. However, the permeability of the porous MgO layer requires significant improvement to be integrated into high performance oxygen transport membrane

[9]. The gas permeation capability of ceramic substrates can be improved by using appropriate pore former.

In this letter, porous MgO ceramic membranes were prepared using a combination pore formers (graphite and polymethyl methacrylate, henceforth referred to as PMMA) using warm-pressing technique. The effect of the fugitive pore former on the microstructure, porosity, pore size distribution and gas permeability of the porous MgO layer was investigated.

2. Experimental

2.1 Material and methods

Pre-calcined MgO powder (Inframat Advanced Materials, USA, d50 ~ 1.53 μm), graphite (Superior graphite, USA, d50 ~ 17.7 μm), Poly methyl methacrylate, PMMA (Exprix technologies, USA), a thermoplastic binder (Du Pont, USA), paraffin wax and stearic acid (Sigma-Aldrich, Germany) were used to prepare thermoplastic feedstock. MgO powder, polymer binder and pore former (graphite to PMMA ratio is 2:1 by volume) were fed into a kneader (Kneader N50, Brabender, Germany) in the volume ratio of 1.2: 1.5: 1. After kneading, the feedstock was shaped into planer substrate (dimension 35mm x50 mm x 1) by warm pressing (Fortune Isostatic Press-TP600, Frontijne Grotnes, Netherland) by applying a load of 100 KN at 100 ^{o}C. Subsequently, the warm pressed substrates were debindered slowly by employing a heating cycle of 15 °C/h and dwelling for 2 h at 250 °C, 400 °C and 650 °C. Further, the MgO substrates were sintered at 1300 °C for 2h in ambient condition with a heating rate of 30 °C/h.

2.2. Characterization

The phase identification of the pre-calcined MgO powder and sintered MgO porous structures was performed using X-ray diffraction (Bruker D8 diffractometer, Germany) with CuKα radiation over a 2θ range of 10–85°. The microstructure of the samples was recorded using scanning electron microscopy (SEM) (SUPRA35, Carl Zeiss, Germany). The porosity measurements were carried out using a mercury porosimeter, (Pore Master, PR-60 GT, Micromeritics, USA). Finally, gas permeation

measurements were carried out using an in-house built system. The flow of permeated gas across porous substrate was measured using a flow meter (Agilent, USA) for a pressure difference ranging from 25 kPa to 175 kPa. The gas permeability was calculated using the Darcy equation [9].

3. Results and Discussion:

Fig. 1 shows X-ray diffraction (XRD) patterns of pre-calcined, at 1000 °C for 10 h, MgO powder and sintered, at 1300 °C for 2 h, MgO substrate. All the reflections from the diffractograms of MgO powder and MgO sintered structure can be indexed to MgO periclase phase (JCPDS: 00-045-0946). No secondary phases were observed for both the samples after the heat treatments and no additional reflections were found after sintering the MgO structure compared to the pre-calcined powder. The clear and sharp reflections indicate the good crystallinity of the material.

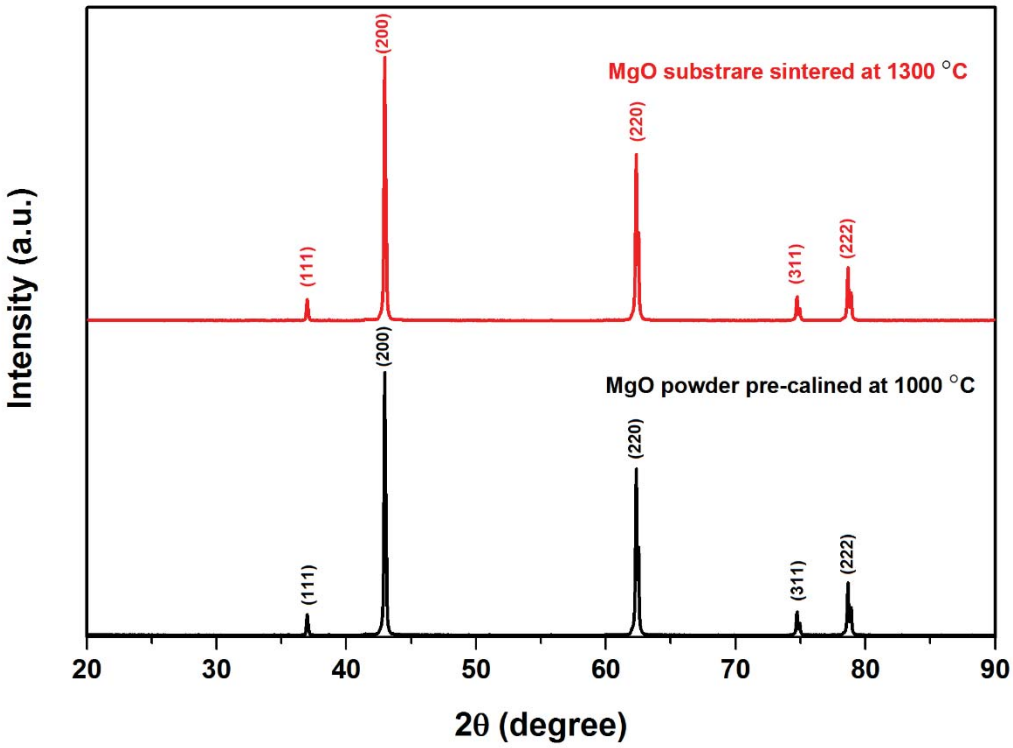

Fig. 1. X-ray diffraction patterns of MgO powder pre- calcined at 1000 °C and MgO substrate sintered at 1300 °C.

The microstructure of porous MgO substrates sintered at 1300 °C for 2 h in ambient is presented in **Fig. 2**. The micrographs at two different magnification indicate the wide range of pore sizes ranging from sub-micron to above 10 µm which are connected randomly. It can be seen that there are some spherical and elongated pores, those are originated from PMMA and graphite respectively. The small and elongated pores joined together to create the pore channel to enable the gas transport with minimal resistance within the structure. It is observed that there is a significant improvement in the mean pore size (~ 0.65 µm) and porosity (55 %) which is almost increased by 200% and 50%, respectively, compared to the values reported in our previous work [9]. Other main reason for considering the combination of two pore formers (graphite and PMMA) is in order to avoid the debindering defects as the each pore former has different degasification/ burnout temperatures, which helps to increase pore former content into the thermoplastic feedstock.

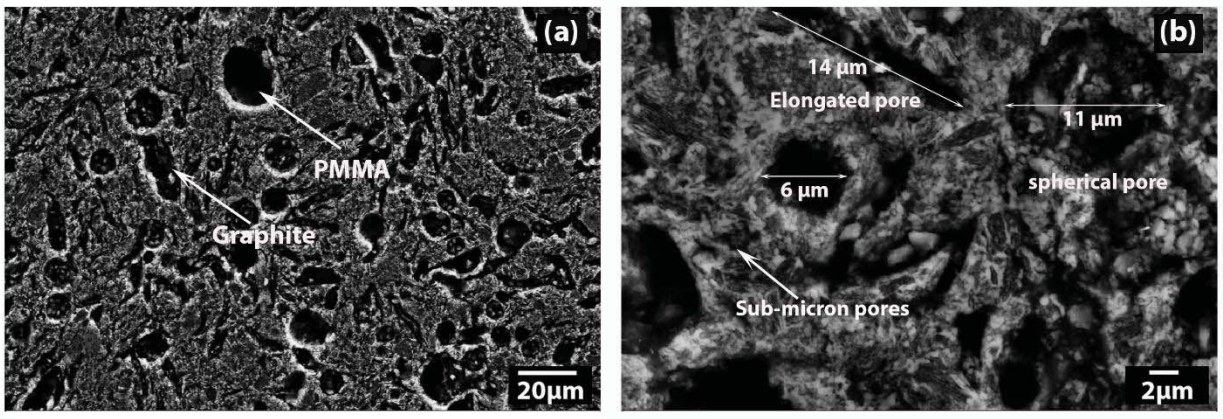

Fig. 2. SEM Micrographs of the porous MgO ceramics sintered at 1300°C for 2 h, (a) origin of the pores and (b) type of pores and size.

Porosity and gas permeability of the MgO substrates

Fig. 3 (a) shows the mercury (Hg) intrusion and extrusion measurement of MgO substrate sintered at 1300 °C. It is seen that as the intrusion pressure increases, only 2% of pore volume filled until pore neck size reaches 2 µm and then intruded volume started to increase drastically to 50 % with pore neck size

>0.65 µm. During Hg extrusion measurements, 2% of pore volume is extracted until pore cavity size reaches 0.3 µm, and further extracted volume is reached to 50% when pore size reaches 3 µm. Hysteresis (during intrusion and extrusion) is often observed due to large cavities being interconnected by smaller pore necks[12]. It can also be observed that almost one third of pore volume occupied with a pore size of >10 µm. From application point view, it is important to enlarge the pore neck size instead of increasing the pore/cavity size for better gas permeability.

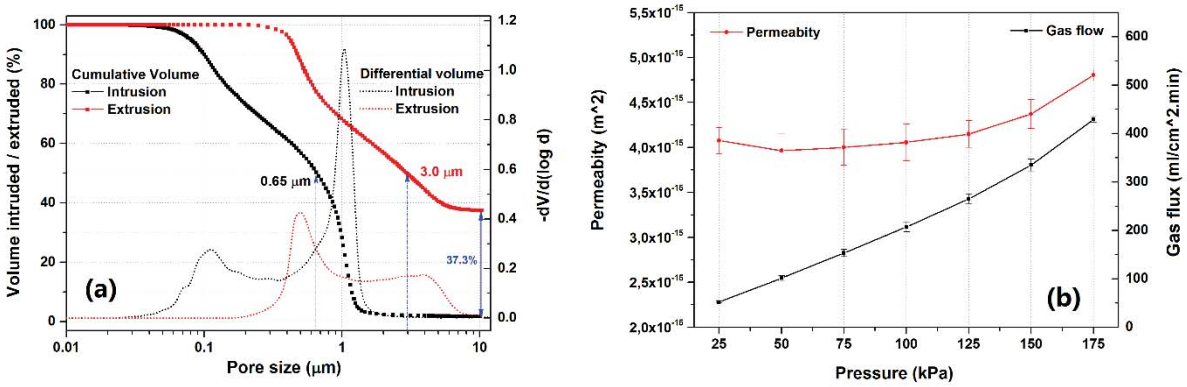

Fig. 3. (a) the cumulative and differential intruded volume in different pore sizes for the porous MgO sintered substrate, (b) the measured gas permeability and gas flow as function of ΔP from 25 to 175 kPa.

Fig. 3 (b) shows the measured gas flux and the calculated permeability as a function of pressure difference (ΔP) across the porous substrate. The measured gas flux versus the pressure difference curve showed an almost linear trend for all ΔP. Increasing the pressure from 25 kPa to 150 kPa, did not result in significant changes in permeability and there was no influence from the pressure gradient. An increase in gas permeability was observed when pressure was reached beyond 150 kPa; this increase was attributed to the elevation of gas access to small pores in the support and this enhanced the gas permeation. The MgO substrates exhibits a gas permeation value of about 4-4.5 $x10^{-15}$ m^2 which is almost 7 to 8 times higher than to the acceptable range [13]. The high permeability measured on the

MgO support forms the basis for further studies on integrating these substrates into high performance perovskite and fluorite based membrane materials.

Cost analysis

The cost analysis of porous MgO support was done by considering a small size production facility located in India with monthly production capacity ~ 3 tones (2000 m^2) finished goods. In membrane cost calculation, all costs involved in the production processes should be assessed carefully to make a better estimate which is presented in **Table 1.** The direct cost involves mainly the costs associated with the manufacturing of the product such as, bill of materials and routing (operation and manpower) cost. Moreover, indirect costs (utilities, rent, audit and administrative staff) are included into the product cost which is considered to be 50% of WIP (work in progress) cost. Finally, membrane cost is assessed to be 150\$/m^2 including pricing factor of 10 times. In comparison with fluorite and perovskite material, MgO is 15-30 times cheaper in term of material cost which makes MgO economic to be considered as low cost support material for asymmetric oxygen transport membrane [14].

Table 1 about here

4. Conclusions

Porous MgO ceramic substrates with high porosity of 55% was prepared by warm pressing using pre-treated MgO powder along with graphite and PMMA pore-formers. The mean pore neck and pore cavity sizes of the sintered MgO substrates, was about 0.65 μm and 3 μm respectively. The microstructure and porosimetry experiments indicate broad pore size distribution with good pore-connectivity, resulting in high gas permeation value of about 4-4.5 $x10^{-15}$ m^2. The estimated product cost of porous MgO substrates was about 150\$ per square meter, making them cost efficient membrane supports for oxygen transport membranes.

5. Acknowledgements

The authors would like to thank the Danish Council for Independent Research Technology and Production Sciences (FTP) which is part of The Danish Agency for Science. Technology and Innovation (FI) (Project # 09-072888) for sponsoring the **OPTIMAC** research work. Pernille Hedemark Nielsen is thankfully acknowledged for preparation polished cross sections for SEM analysis.

6. References

[1] A.R. Studart et.al., J. Am. Ceram. Soc. 89 (2006) 1771.

[2] S. Baumann et.al., J. Eur. Ceram. Soc. 33 (2013) 1251.

[3] H. Jeon, D.J. Kim, S.J. Kim, J.H. Kim, Fuel Process. Technol. 116 (2013) 325.

[4] Y. Shiratori, Solid State Ionics 164 (2003) 27.

[5] H. Middleton et.al., J. Eur. Ceram. Soc. 24 (2004) 1083.

[6] F. Valdivieso et.al., J. Nucl. Mater. 320 (2003) 1.

[7] L. Hong, X. Chen, Z. Cao, J. Eur. Ceram. Soc. 21 (2001).

[8] R.W. Rice, W.R. Grace, J. Am. Ceram. Soc. 8 (1993).

[9] D.K. Ramachandran et.al., Ceram. Int. 40 (2014) 10465.

[10] M. Lipińska-Chwałek et.al., J. Eur. Ceram. Soc. (2014).

[11] M. Salehi, et.al., J. Memb. Sci. 443 (2013) 237.

[12] S. Lowell, J.. Shields, M.I. Corp, J. Colloid Interface Sci. 80 (1981) 192.

[13] A. Kaiser et al., J. Memb. Sci. 378 (2011) 51.

[14] http://www.fuelcellmaterials.com

List of Tables:

Table 1: Membrane cost analysis production of a sample size of 2000 m^2

Details	**Total for 2000 m^2 (USD)**	**Cost/m^2 (USD)**
Raw materials cost	12500	6.25
Process wastage (20 % of RM cost)	2500	1.25
Production cost	5000	2.5
Indirect cost (50 % of WIP cost)	10000	5.0
Total cost	30000	**15.0**
Pricing factor (5-10 times)		**(75-150 $)**

Publication IV

"Modeling constrained sintering of bi-layered tubular samples"

Available online at www.sciencedirect.com
ScienceDirect
Journal of the European Ceramic Society xxx (2014) xxx–xxx
www.elsevier.com/locate/jeurceramsoc

Modeling constrained sintering of bi-layered tubular structures

Tesfaye Tadesse Molla [a,*], Dhavanesan Kothanda Ramachandran [a], De Wei Ni [a], Vincenzo Esposito [a], Francesca Teocoli [a], Eugene Olevsky [b], Rasmus Bjørk [a], Nini Pryds [a], Andreas Kaiser [a], Henrik Lund Frandsen [a]

[a] *Technical University of Denmark, Department of Energy Conversion and Storage, Risø Campus, Frederiksborgvej 399, P.O. Box 49, Building 779, 4000 Roskilde, Denmark*

[b] *San Diego State University, Mechanical Engineering Department, 5500 Campanile Dr., San Diego, CA 92182-1323, USA*

Received 3 September 2014; received in revised form 8 October 2014; accepted 12 October 2014

Abstract

Constrained sintering of tubular bi-layered structures is being used in the development of various technologies. Densification mismatch between the layers making the tubular bi-layer can generate stresses, which may create processing defects. An analytical model is presented to describe the densification and stress developments during sintering of tubular bi-layered samples. The correspondence between linear elastic and linear viscous theories is used as a basis for derivation of the model. The developed model is first verified by finite element simulation for sintering of tubular bi-layer system. Furthermore, the model is validated using densification results from sintering of bi-layered tubular ceramic oxygen membrane based on porous MgO and $Ce_{0.9}Gd_{0.1}O_{1.95-d}$ layers. Model input parameters, such as the shrinkage kinetics and viscous parameters are obtained experimentally using optical dilatometry and thermo-mechanical analysis. Results from the analytical model are found to agree well with finite element simulations as well as measurements from sintering experiment.

Keywords: Constrained sintering; Tubular bi-layer; Oxygen membrane; Sintering; Stress

1. Introduction

Functionally graded tubular multi-layered ceramic structures are being used in the development of tubular type of solid oxide fuel cells and gas separation technologies.[1–5] A tubular multi-layer structure with thin film oxygen transport membrane layer on a porous support offers improved performance due to reduced thickness of the separation layer. Mechanical and dimensional stability together with the opportunity to use cost effective shaping processes for mass production such as extrusion and dip coating are some of the other reasons to use tubular multi-layers.[1–3] Nevertheless, an important and critical step in the manufacturing of such tubular multi-layers is the simultaneous sintering of the different layers (co-sintering), which is required to densify the green structure and give it higher strength.[4] Processing defects like cracks, delaminations and coating peel-offs are some of the problems associated with sintering of tubular multi-layer samples. Such defects are believed to occur mainly due to the transient stress development inside the structure in response to the differential shrinkage in the constituent layers, i.e. the layer with faster shrinkage rate is constrained by the slowly shrinking layer resulting in constrained sintering. In order to produce defect free tubular multi-layered structures, it is important to control and optimize the transient stress generation during the entire sintering process. Thus, it is necessary to develop a model to understand development of stresses and densification mechanisms.

The problem of transient stresses during sintering of *planar* multi-layer structures including camber development in asymmetric multi-layers has been addressed in numerous publications.[6–20] Generally to model densification and stress generations during co-firing of planar multi-layered samples, the continuum theory of sintering has been used.[6,7] The porous

* Corresponding author at: Frederiksborgvej 399, P.O. Box 49, Building 778, 4000 Roskilde, Denmark. Tel.: +45 2074 5931; fax: +45 4677 5858.
E-mail address: ttmo@dtu.dk (T.T. Molla).

http://dx.doi.org/10.1016/j.jeurceramsoc.2014.10.010
0955-2219/

structure has then assumed to have a linear viscous behavior, where the viscous strain rate is directly proportional to the applied load.[6] The total deformation in the sintering body is thus equal to the sum of the viscous strain rate and internal shrinkage rate, which is driven by a hydrostatic potential often referred to as the sintering stress.[21]

Timoshenko and Goodier provided an analytical elastic solution for stresses in a single layered tube exposed to a gradient in internal strain (e.g. thermal or chemical).[22] In addition, Lamé derived the stress field in a tube exposed to an external pressure.[23] Recently Kwok et al. generalized those analytical expressions in Refs. 22,23 for elastic materials to describe stress developments in bi-layered tubular supported oxygen membranes under internal and external pressures.[24] For bi-layer structures, Kwok et al. assumed the pressure in Lamé's model as the interaction pressure between the two monolithic tubular layers, which may arise due to mismatch in the internal strains of the layers. In this work, Kwok et al. tried to analyze elastic stress developments due to gradient and mismatch in the chemical and/or thermal strains during operations of bi-layered tubular structures, for example, in oxygen separation applications.[24]

Based on the analogy between linear elasticity and linear viscous models, the methodology used by Kwok et al. to analyze elastic stresses could be extended for linear viscous materials and a time dependent analysis. This is made by invoking the analogy between internal strains (thermal or chemical) in the elastic materials and free shrinkage rates in the viscous materials. The mechanical viscous properties are then defined for a given temperature and microstructure during the sintering cycle. During sintering of porous bi-layered tubular body, mismatch in the densification rate between the two layers can develop stresses. If the sintering bodies in the tubular bi-layer system are modeled by linear viscous materials, the mismatch in the internal shrinkage rate between the two layers should be directly proportional to the development of stress. By doing so, it is possible to model the development of stresses and densification in each layer during sintering of bi-layered tubular structures.

Therefore, an analytical model describing stress developments and densification during constrained sintering of bi-layered tubular structures has been developed in this work. In order to verify the analytical model, finite element simulations for constrained sintering of bi-layered tubular sample is performed. The analytical model is also validated using constrained sintering experiment of tubular bi-layered oxygen membrane based on porous magnesium oxide (MgO) and $Ce_{0.9}Gd_{0.1}O_{1.95-d}$ (CGO) layers. Model input parameters such as the shrinkage kinetics and viscous parameters of the individual layers of the tubes are obtained experimentally using optical dilatometry and a thermo-mechanical analysis (TMA) respectively.

2. Experimental

2.1. Raw powders

Three types of powders were used for the preparation of asymmetric tubular membrane structures: (1) MgO powder (Product # 12R-0801, Inframat Advanced Materials, USA) and (2) a graphite powder (V-UF1 99.9, Graphit Kropfmühl AG, Germany) as a pore former, both for the porous support; and (3) CGO (GDC10-TC, Fuel Cell Materials, USA) for the dense membrane layer. The raw ceramic powders (MgO, CGO) were pre-calcined at 1000 °C with a heating rate of 100 °C/h for 10 h to reduce the surface area of the powder and hence reduce the sintering activity. The specific surface areas of the calcined MgO and CGO powders were measured by the BET method to be 10.8 m^2/g and 4.3 m^2/g with a particle size of d50: ~1.5 μm (d10: ~0.2 μm, d90: ~6.0 μm) and d50: ~2.1 μm (d10: ~0.9 μm, d90: ~7.7 μm) respectively.

2.2. Layer preparation

MgO feedstocks for thermoplastic extrusion were prepared from MgO powder, graphite, a thermoplastic binder (Elvax 250, Du Pont, USA), paraffin wax (Sigma–Aldrich, USA) as a plasticizer, and stearic acid (Sigma–Aldrich, USA) as a dispersant. The MgO feedstocks were extruded into tubes (14 mm outer diameter and 1 mm wall thickness) using a Brabender extruder 19/20DN to prepare the porous membrane support layer. The feedstock optimization with respect to the form stability, shrinkage behavior as well as additional information on the layer preparation can be found in our previous work.[25]

For the dense membrane layer, first the pre-calcined CGO powder was dispersed in an ethanol based suspension with polyvinylpyrrolidone (PVP, Sigma–Aldrich, USA) as dispersant and polyvinylbutyral (PVB, Sukisui chemicals, Japan) as binder. The resulting slurry for the dip coating was homogenized by ball milling for 72 h. The slurry for the preparation of the dense membrane was dip coated on the extruded MgO tubes at a constant speed of 2.5 mm/s in a controlled atmosphere. The green densities of the extruded and dip coated layers were measured on the basis of mass and volume measurements. The relative density of the sample was calculated from the ratio between the measured density and the theoretical density of the powder. The theoretical densities of MgO and CGO used are 3.6 and 7.2 g/cm^3 respectively.[25]

2.3. Sintering procedures

The heat treatment procedure for the tubular asymmetric bi-layered samples consists of (1) a constant heating rate (iso-rate) with a ramp of 0.25 °C/min for the de-binding cycle from room temperature to 650 °C and (2) an iso-rate ramp of 0.5 °C/min for the sintering cycle from 650 °C to a maximum of 1300 °C. Various bi-layers were heated with the same heating profile to different temperatures of 250 °C, 450 °C, 650 °C, 850 °C, 1000 °C, 1100 °C and 1300 °C, followed by cooling down to room temperature with the rate of 1 °C/min. The bi-layers were checked for defects after each respective temperature cycle and simultaneously the necessary data were collected for comparison with model. Fig. 1 shows a schematic cross section and a photo of the MgO tube with a dip coated CGO layer after heat treatment to 650 °C.

Please cite this article in press as: Molla TT, et al. Modeling constrained sintering of bi-layered tubular structures. *J Eur Ceram Soc* (2014), http://dx.doi.org/10.1016/j.jeurceramsoc.2014.10.010

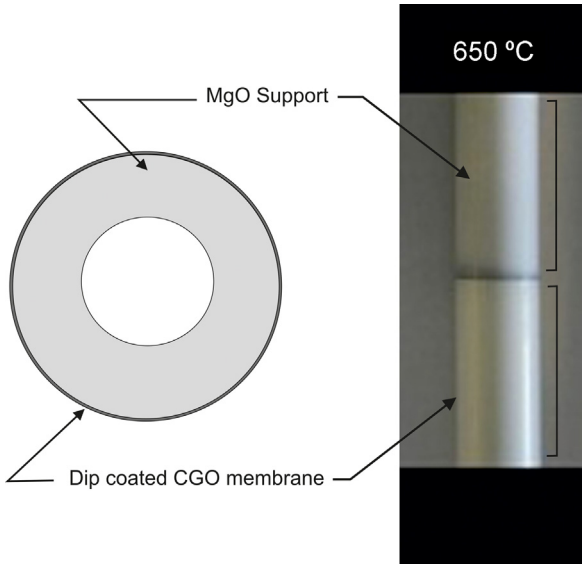

Fig. 1. Schematics of the cross section (left) and photo of a tubular asymmetric MgO support/CGO membrane bi-layer (right) after heat treatment to 650 °C.

The shrinkage in each layer was calculated from the sample thickness after each thermal treatment. The sample thickness was measured using scanning electron microscopy, SEM (TM3000, Hitachi, Japan). After de-binding, a fractured surface of the cross section was analyzed for the microstructure characterization and thickness measurement. The samples sintered above 850 °C were imbedded in a polymer and afterwards polished. The polished cross sections were then used for measuring the shrinkage of MgO and CGO layer. The average values of thickness were determined from four measurements. Similarly, the porosities in each layer were calculated using the SEM images from the fractured surfaces of the sample. Table 1 shows the different dimensions and porosity values of the layers measured at the initial and final (1300 °C) stage of the sintering cycle.

By using the raw materials of both MgO and CGO described above, free standing tapes of each layer were prepared to measure the free shrinkage kinetics and viscosity. The heat treatment profile used for bi-layered tubular supported membrane is also applied while measuring the shrinkage and viscosity of each tape. For free sintering of individual layers, optical dilatometry (TOMMI, Fraunhofer ISC, Würzburg, Germany) results were collected for each sample size with time and temperature. Assuming isotropic shrinkage, the densification strains are calculated from the linear shrinkage data. Details of the methodologies used in the sample's processing and optical dilatometry can be found in Ni et al.[26]

Table 1
Parameters of MgO and CGO layers before and after sintering of the tubular bi-layer at 1300 °C.

	Initial	Final
External diameter of CGO (mm)	14.42 ± 0.10	12.61 ± 0.61
Thickness of CGO (μm)	26.80 ± 0.30	23.55 ± 0.91
Thickness of MgO (μm)	1002 ± 6.10	886.76 ± 4.52
Relative porosity of CGO	0.44 ± 0.01	0.20 ± 0.03
Relative porosity of MgO	0.63 ± 0.02	0.46 ± 0.03

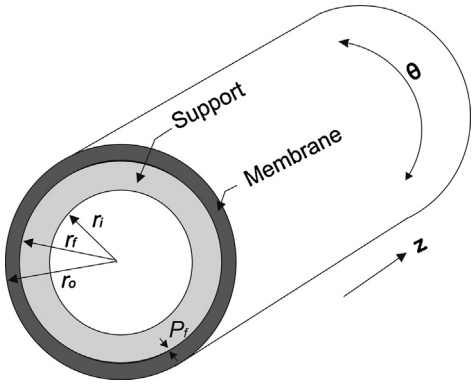

Fig. 2. Schematic representation of the porous bi-layered tubular structure.

The viscosities of MgO and CGO during sintering were determined using cyclic loading dilatometry with the help of thermo-mechanical analyzer (TMA 402 F1 Hyperion, Netzsch, Germany). The details of the methodology used are explained in Ref. 27. For thermo-mechanical analysis, two layers with a final thickness of 1 mm for each material were shaped and cut into 20 mm × 5 mm bars. Specimens were fired continuously in air at a heating rate of 0.25 °C/min from room temperature to 700 °C and held for 2 h to ensure the burn-out of all organics. During the measurement, the samples were heated in air from room temperature at a heating rate of 0.5 °C/min applying a superimposed 8-min cyclic squared profile. The maximum load was 8 mN. The load was applied by a trapezoidal push rod at the center of the beam with 5 mm width and span of 1 cm. The deflection changes were measured with an accuracy of ±0.125 nm.

3. Model development

Consider the cross section of porous bi-layered tubular structure made of support and membrane as shown in Fig. 2. The tubular structure has the internal and external radii of r_i and r_o and an interfacial radius of r_f in between the support and membrane. For analysis of densification and deformation of sintering bodies, the continuum theory of sintering can be used.[6,7,21] According to Bordia and Scherer a constitutive equation based on linear viscous behaviors is quite appropriate to use for porous bodies during sintering.[6,7] In this theory, the viscous strain rate of isotropically deforming body is directly proportional to the stress components. There is also a direct correspondence between linear elasticity and linear viscous theories, where the viscous mechanical properties of the porous body can be defined either by bulk and shear viscosities or by uni-axial viscosity and viscous Poisson's ratio.[6] Therefore in this work, the analogy between linear elasticity and linear viscous theories, the elastic-visco elastic correspondence principle,[28] has been used to describe the densification and stress developments during sintering of the porous bi-layered tubular structures.

The length of the tube is assumed to be very large compared to the thickness of each layers, and hence plane strain analysis can be applied. Stresses develop only in the principal directions

Please cite this article in press as: Molla TT, et al. Modeling constrained sintering of bi-layered tubular structures. *J Eur Ceram Soc* (2014), http://dx.doi.org/10.1016/j.jeurceramsoc.2014.10.010

i.e. tangential, rr, radial, $\theta\theta$, and axial, zz, axis, as all the shear stresses vanish because of axisymmetry.

During sintering, stress in the support as well as in the membrane can develop because of:

1. The gradient of the internal free shrinkage rate, $\dot{\varepsilon}^f$, in each layer and
2. The interfacial pressure, P_f, that develop due to the mismatch in the shrinkage rates between the two layers.

Employing the correspondence between linear elasticity and linear viscous materials, the expressions in[24] can be adapted to linear viscous materials. In the case of a sintering tubular body, the internal strain, ε, can be replaced by the internal shrinkage rate, $\dot{\varepsilon}^f$. Table 2 summarizes how the equations for linear elastic model have been transformed into linear viscous materials.

In the expressions given in Table 2, the subscript s and m indicates the support and membrane, where as the superscript, ε, indicates stresses due to the internal strain in the elastic case or free strain rate, $\dot{\varepsilon}^f = d\varepsilon^f/dt$, in the linear viscous case. As it is shown in Table 2, the stress expressions for linear viscous materials are found by replacing the Young's modulus and Poisson's ratio, E and ν, in the elastic model by uni-axial viscosity and viscous Poisson's ratio, η and ν'. Note that the expressions provided here represent stress/force balance of a viscous media at the specific geometry or radius, r, and not the time derivative of the elastic solution.

The stresses, σ, in the radial and tangential directions due to the interfacial pressure, P_f, that develops because of the mismatch in the shrinkage rate between the two layers, can be calculated based on expressions provided by Lame[23] as:

$$\sigma^P_{rr,s} = \frac{P_f r_f^2}{r_f^2 - r_i^2} - \frac{P_f r_f^2 r_i^2}{(r_f^2 - r_i^2) r^2} \tag{1}$$

$$\sigma^P_{\theta\theta,s} = \frac{P_f r_f^2}{r_f^2 - r_i^2} + \frac{P_f r_f^2 r_i^2}{(r_f^2 - r_i^2) r^2} \tag{2}$$

$$\sigma^P_{rr,m} = \frac{-P_f r_f^2}{r_0^2 - r_f^2} - \frac{-P_f r_0^2 r_f^2}{(r_0^2 - r_f^2) r^2} \tag{3}$$

$$\sigma^P_{\theta\theta,m} = \frac{-P_f r_f^2}{r_0^2 - r_f^2} + \frac{-P_f r_0^2 r_f^2}{(r_0^2 - r_f^2) r^2} \tag{4}$$

Here the superscript, P, indicates that stresses are from the interfacial pressure, whereas the subscripts s and m are again for the support and membrane. To calculate the stress components in Eqs. (1)–(4), first the interfacial pressure has to be determined at each time during the sintering cycle based on the mismatch in the shrinkage rate, $\dot{\varepsilon}^f_{mis}$, between the two layers. To determine this, the continuity of tangential strain rate, $\dot{\varepsilon}_{\theta\theta}$, at the interface between the support and membrane can be applied as suggested by Kwok et al.[24] This implies:

$$\dot{\varepsilon}_{\theta\theta,s} = \dot{\varepsilon}_{\theta\theta,m} \quad \text{at} \quad r = r_f \tag{5}$$

The boundary condition in Eq. (5) gives the interfacial pressure, P_f, as:

$$P_f = \frac{1}{S_1}\dot{\varepsilon}^f_{mis} \tag{6}$$

where S_1 and $\dot{\varepsilon}^f_{mis}$ are given by:

$$S_1 = \frac{1 - \nu'^2_m}{\eta_m}\frac{r_0^2 + r_f^2}{r_0^2 - r_f^2} + \frac{1 - \nu'^2_s}{\eta_s}\frac{r_f^2 + r_i^2}{r_f^2 - r_i^2} + \frac{(1 + \nu'_m)\nu'_m}{\eta_m} - \frac{(1 + \nu'_s)\nu'_s}{\eta_s} \tag{7}$$

$$\dot{\varepsilon}^f_{mis} = \frac{2(1 + \nu'_m)}{r_0^2 - r_f^2}\int_{r_f}^{r_0} r\dot{\varepsilon}^f_m dr - \frac{2(1 + \nu'_s)}{r_f^2 - r_i^2}\int_{r_i}^{r_f} r\dot{\varepsilon}^f_s dr \tag{8}$$

Note that the dot sign above the variable represents the time derivative of the quantity i.e. $\dot{x} = dx/dt$. For the details of the derivations, please refer to the work by Kwok et al.[24]

The total stress components, σ, in the radial, rr, and tangential, $\theta\theta$, directions can thus be given by Eqs. (9) and (10) where the subscript, $j = s$ or m.

$$\sigma_{rr,j} = \sigma^P_{rr,j} + \sigma^\varepsilon_{rr,j} \tag{9}$$

$$\sigma_{\theta\theta,j} = \sigma^P_{\theta\theta,j} + \sigma^\varepsilon_{\theta\theta,j} \tag{10}$$

For derivation of the axial stress components, the axial strain rate components are assumed to be independent of the radius in the bi-layer structures and the stresses can be written as[24]:

$$\sigma_{zz,s} = \eta_s(\dot{\varepsilon}_{zz} - \dot{\varepsilon}^f_s) + \nu'_s(\sigma_{rr,s} + \sigma_{\theta\theta,s}) \tag{11}$$

$$\sigma_{zz,m} = \eta_m(\dot{\varepsilon}_{zz} - \dot{\varepsilon}^f_m) + \nu'_m(\sigma_{rr,m} + \sigma_{\theta\theta,m}) \tag{12}$$

Here $\dot{\varepsilon}_{zz}$ is the axial strain rate in the bi-layer, which can be calculated from the force balance equilibrium in the axial direction, see Eq. (13) where F_{axial} represents the axial force.

$$F^s_{axial} + F^m_{axial} = 0$$
$$\int_{r_i}^{r_f} 2\pi r\sigma_{zz,s} dr + \int_{r_f}^{r_0} 2\pi r\sigma_{zz,m} dr = 0 \tag{13}$$

Substituting Eqs. (11) and (12) into Eq. (13), the axial strain rate can be found as:

$$\dot{\varepsilon}_{zz} = \frac{1}{S_2}\left[2(\nu'_m - \nu'_s)P_f r_f^2 + 2\eta_m\int_{r_f}^{r_0} r\dot{\varepsilon}^f_m dr + 2\eta_s\int_{r_i}^{r_f} r\dot{\varepsilon}^f_s dr\right] \tag{14}$$

Here the factor S_2 is given by:

$$S_2 = \eta_m(r_0^2 - r_f^2) + \eta_s(r_f^2 - r_i^2) \tag{15}$$

The equations up until now are adapted from the general elastic solution in Ref. 24 to linear viscous materials in order to calculate the stress levels at a given time during the sintering cycle. The stresses at each time step are then used to calculate the constraint related strain rates so as to update the porosity, radii and thickness of each layer.

Please cite this article in press as: Molla TT, et al. Modeling constrained sintering of bi-layered tubular structures. *J Eur Ceram Soc* (2014), http://dx.doi.org/10.1016/j.jeurceramsoc.2014.10.010

Table 2
The analogy between linear elasticity and linear viscous materials for stress at a given radius, r.

Linear elastic[24]	Linear viscous
$\sigma^{\varepsilon}_{rr,s} = \frac{E_s}{1-\nu_s}\left[\frac{r^2-r_i^2}{(r_f^2-r_i^2)r^2}\int_{r_i}^{r_f} r\varepsilon_s dr - \frac{1}{r^2}\int_{r_i}^{r} r\varepsilon_s dr\right]$	$\sigma^{\varepsilon}_{rr,s} = \frac{\eta_s}{1-\nu_s}\left[\frac{r^2-r_i^2}{(r_f^2-r_i^2)r^2}\int_{r_i}^{r_f} r\dot{\varepsilon}_s^f dr - \frac{1}{r^2}\int_{r_i}^{r} r\dot{\varepsilon}_s^f dr\right]$
$\sigma^{\varepsilon}_{\theta\theta,s} = \frac{E_s}{1-\nu_s}\left[\frac{r^2+r_i^2}{(r_f^2-r_i^2)r^2}\int_{r_i}^{r_f} r\varepsilon_s dr + \frac{1}{r^2}\int_{r_i}^{r} r\varepsilon_s dr - \varepsilon_s\right]$	$\sigma^{\varepsilon}_{\theta\theta,s} = \frac{\eta_s}{1-\nu_s'}\left[\frac{r^2+r_i^2}{(r_f^2-r_i^2)r^2}\int_{r_i}^{r_f} r\dot{\varepsilon}_s^f dr + \frac{1}{r^2}\int_{r_i}^{r} r\dot{\varepsilon}_s^f dr - \dot{\varepsilon}_s^f\right]$
$\sigma^{\varepsilon}_{rr,m} = \frac{E_m}{1-\nu_m}\left[\frac{r^2-r_f^2}{(r_0^2-r_f^2)r^2}\int_{r_f}^{r_0} r\varepsilon_m dr - \frac{1}{r^2}\int_{r_f}^{r} r\varepsilon_m dr\right]$	$\sigma^{\varepsilon}_{rr,m} = \frac{\eta_m}{1-\nu_m'}\left[\frac{r^2-r_f^2}{(r_0^2-r_f^2)r^2}\int_{r_f}^{r_0} r\dot{\varepsilon}_m^f dr - \frac{1}{r^2}\int_{r_f}^{r} r\dot{\varepsilon}_m^f dr\right]$
$\sigma^{\varepsilon}_{\theta\theta,m} = \frac{E_m}{1-\nu_m}\left[\frac{r^2+r_f^2}{(r_0^2-r_f^2)r^2}\int_{r_f}^{r_0} r\varepsilon_m dr + \frac{1}{r^2}\int_{r_f}^{r} r\varepsilon_m dr - \varepsilon_m\right]$	$\sigma^{\varepsilon}_{\theta\theta,m} = \frac{\eta_m}{1-\nu_m'}\left[\frac{r^2+r_f^2}{(r_0^2-r_f^2)r^2}\int_{r_f}^{r_0} r\dot{\varepsilon}_m^f dr + \frac{1}{r^2}\int_{r_f}^{r} r\dot{\varepsilon}_m^f dr - \dot{\varepsilon}_m^f\right]$

3.1. Obtaining the porosity evolution

By dividing each layer through n equal points and by using numerical integrations, it is possible to find all the stresses components at each point in time and hence calculate the corresponding viscous strain rates over the thickness, $\dot{\varepsilon}^v$, in each layer as:

$$\dot{\varepsilon}^v_{rr,j} = \frac{1}{\eta_j}\left[\sigma_{rr,j} - \nu_s'(\sigma_{\theta\theta,j} + \sigma_{zz,j})\right] \tag{16}$$

$$\dot{\varepsilon}^v_{\theta\theta,j} = \frac{1}{\eta_j}\left[\sigma_{rr,j} - \nu_s'(\sigma_{rr,j} + \sigma_{zz,j})\right] \tag{17}$$

Here again the subscript, j, can be of either for the substrate, s, or membrane, m.

The total strain rate in the radial, rr, tangential, $\theta\theta$, and axial, zz, axis and the corresponding volumetric strain rate, $\dot{e}$, in either the support or membrane can be updated as:

$$\dot{\varepsilon}_{rr,j} = \dot{\varepsilon}^f_j + \dot{\varepsilon}^v_{rr,j} \tag{18}$$

$$\dot{\varepsilon}_{\theta\theta,j} = \dot{\varepsilon}^f_j + \dot{\varepsilon}^v_{\theta\theta,j} \tag{19}$$

$$\dot{\varepsilon}_{zz,j} = \dot{\varepsilon}_{zz} \tag{20}$$

$$\dot{e}_j = \dot{\varepsilon}_{rr,j} + \dot{\varepsilon}_{\theta\theta,j} + \dot{\varepsilon}_{zz,j} \tag{21}$$

Therefore the porosity in each layer can be updated based on the conservation of mass that relates the volumetric strain rate, $\dot{e}$, to the porosity, θ_p, as[21]:

$$\dot{\theta}_{p,j} = \dot{e}_j(1-\theta_{p,j}) \tag{22}$$

The uni-axial viscosity is obtained experimentally, see Section 2. But the viscous Poisson's ratio, ν', is updated based on the instantaneous porosity of each layer at each time step using:[18,21]

$$\nu' = \frac{3\psi-\varphi}{6\psi+\varphi} \quad \text{where} \quad \psi = \frac{2}{3}\frac{(1-\theta_p)^3}{\theta_p} \quad \text{and}$$

$$\varphi = (1-\theta_p)^2 \tag{23}$$

3.2. Obtaining the thickness evolution

The total tangential strain rate, $\dot{\varepsilon}_{\theta\theta}$, can be described using the expression given in Eq. (24).[22] Here, V_r, the radial deformational velocity field and $\partial V_t/\partial\theta$ is the change in the tangential velocity field with an angle θ, which vanishes for an axisymmetric body in cylindrical $r-\theta-z$ coordinate system.

$$\dot{\varepsilon}_{\theta\theta} = \frac{V_r}{r} + \frac{1}{r}\frac{\partial V_t}{\partial\theta} \tag{24}$$

By using the tangential strain rates from Eq. (19), the deformational velocity field, V_r, is calculated from Eq. (24) across the thickness of the layer. The corresponding thicknesses of the layers are updated based on the updated internal, interfacial and external radii. Note that during the sintering cycle, the above equations are solved in a time dependent manner where the shrinkage rate, mechanical properties and the geometrical parameters are updated for each time step.

3.3. Finite element model

To verify the analytical model described above, a two dimensional finite element model for the constrained sintering of bi-layered tubular structure has been developed using ABAQUS™. With the help of creep user subroutine the total inelastic strains and porosity evolutions during sintering has been defined based on the Skorohod Olevsky viscous sintering model (SOVS).[21] Details about the implementation of the SOVS theory into ABAQUS™ with the help of creep user subroutines to model sintering of multi-layers are reported in Molla et al.[29]

Only one quarter of the cross sectional domain is modeled because of symmetry of the geometry, loading and boundary conditions. The domain was discretized using eight noded plane strain elements (commonly referred to as CPE8 in the ABAQUS element library) with an element size of 50 and 13 μm for the support and membrane respectively. Symmetry boundary conditions are imposed on the truncated ends of the finite element model.

4. Results and discussion

The analytical model for constrained sintering of bi-layered tubular structure explained in Section 3 is implemented using a Matlab program. The initial values of the stresses are determined by the initial gradient of free shrinkage rate in each layer and the differential shrinkage rate between the two layers. The development of stresses and densification in each layer together with geometrical parameters (the different radii in the bi-layer

Please cite this article in press as: Molla TT, et al. Modeling constrained sintering of bi-layered tubular structures. *J Eur Ceram Soc* (2014), http://dx.doi.org/10.1016/j.jeurceramsoc.2014.10.010

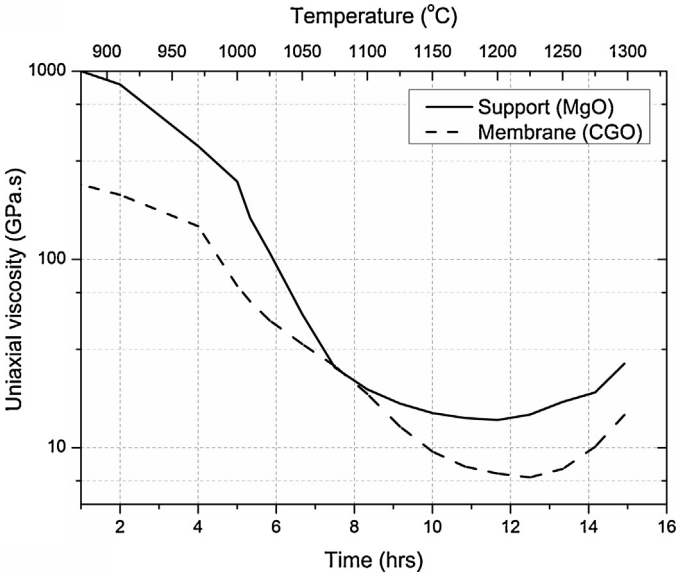

Fig. 3. Uni-axial viscosity of MgO and CGO tapes as a function of time and temperature during constant heating rate of 0.5 K/min.

system and thicknesses) are calculated. The stress calculations from the analytical model are verified with the help of the finite element model developed to simulate the constrained sintering of bi-layered tubular sample. Furthermore, the shrinkage results from the analytical model are compared with SEM measurements made during the sintering experiment of tubular samples. From the dilatometry data (see Fig. 7), densification starts first in CGO layer and hence the bi-layer model simulations are performed beginning from the temperature wherein the CGO membrane starts to densify, i.e. the analysis starting point is at about 850 °C, which distinguishes the pure sintering densification stage of the processing avoiding the debinding and initial sintering period when no essential shrinkage is present.

Fig. 3 shows results for the uni-axial viscosity of both MgO and CGO as function of temperature obtained using the data collected from the TMA analysis. The uni-axial viscosities of both tapes show rapid drop at lower sintering temperatures and remain more or less constant as the temperature increases. The trend in the viscosity variation for the sintering temperatures is similar with the observations reported for most porous ceramic oxides during densification.[8,19,27]

4.1. Development of stresses

The tangential stress (often called hoop stress) evolution at the external surfaces of each layer i.e. at $r = r_f$ in the case of the MgO support and at $r = r_o$ in the case of CGO membrane is calculated from the analytical model. Fig. 4 shows comparison of results from the analytical and finite element simulations. As it is shown the hoop stresses from the analytical model agree very well with predictions from numerical simulations. The hoop stresses are shown to be maximum at the beginning of the sintering process, wherein the membrane and support are exposed to tensile and compressive stresses respectively.

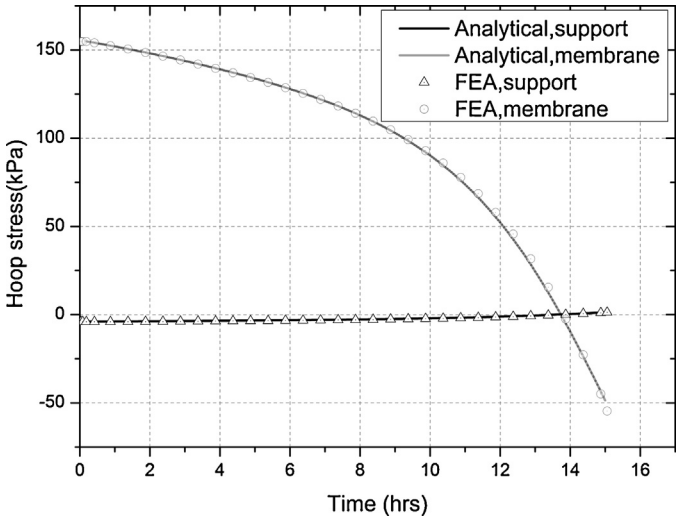

Fig. 4. The evolution of the maximum hoop stress in the support (at $r = r_f$) and membrane (at $r = r_o$) during the sintering cycle.

During the sintering cycle, the hoop stresses evolve and finally the membrane and support will be in compression and tension respectively. The hoop stress in the membrane is quite large compared to stresses in the support, which are usually the main causes for hindering the densification in the CGO membrane. This means that the hoop stress is also the main cause for defects like cracks and peel-offs.

Similarly the analytical model predictions for the evolutions of radial stresses in both layers have been compared with the respective stress values from the numerical simulations as shown in Fig. 5. Here also, the MgO support is initially exposed to compressive radial stress and evolves to tensile stress in time. Generally the magnitude of radial stresses in both layers is very small compared to the hoop stress throughout the sintering cycle. Such observations again show that, most of the processing defects occur due to the hoop stresses at the beginning of the

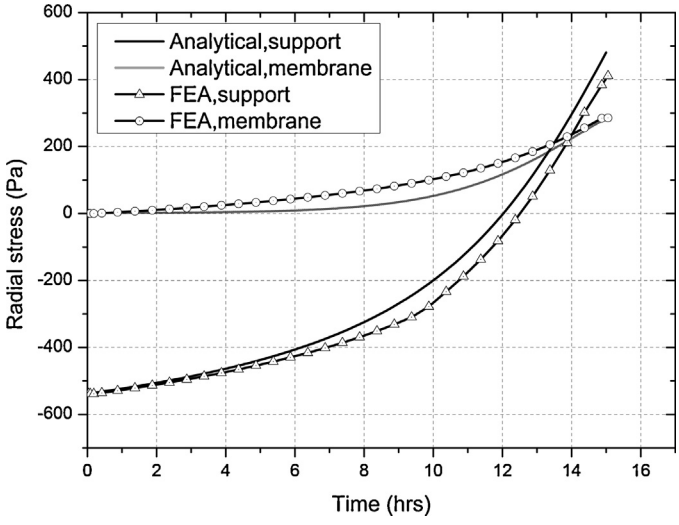

Fig. 5. The evolution of radial stress in the support (at $r = r_f$) and membrane (at $r = r_o$) during the sintering cycle.

Please cite this article in press as: Molla TT, et al. Modeling constrained sintering of bi-layered tubular structures. *J Eur Ceram Soc* (2014), http://dx.doi.org/10.1016/j.jeurceramsoc.2014.10.010

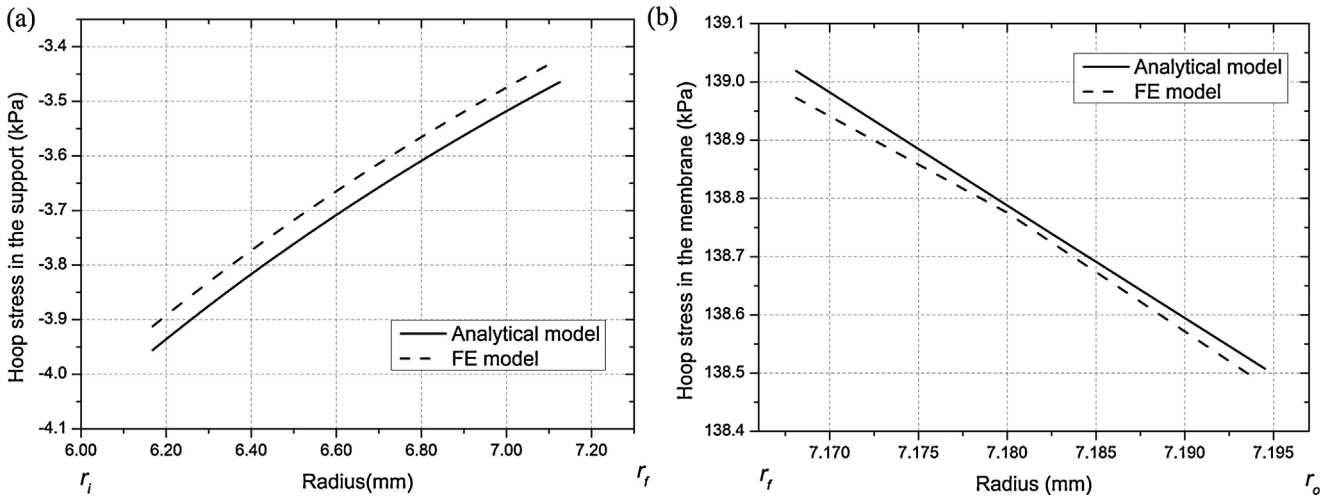

Fig. 6. Hoop stress variation across the radius (a) MgO support and (b) CGO membrane.

sintering cycle as the magnitudes of radial stresses are almost insignificant in both layers.

In addition to stress evolutions in time, the variation of the hoop stress across the radius of each layer for a given time has been invetigated using both the analytical as well as numerical simulations. Fig. 6(a) and (b) shows the hoop stress variation across the radius of the support and membrane around the early stage of the sintering ($t \approx 4$ h or $T \approx 970$ °C). Again a good agreement of the stress calculations from the analytical and numerical models are obitained as shown in Fig. 6. The maximum deviation between the analytical and finite element models, in this case is close 1.24%. Note here that, the variations of the stresses are plotted as a function of radius from the inner, r_i, to interfacial, r_f, in case of the support and from the interfacial, r_f, to outer, r_o, in case of the membrane at the given time.

The analytical model and the finite element simulations are in good agreement for all stresses during constrained sintering of tubular bi-layered structure. The strains and displacements also compare well in the two models. Therefore the analytical model provides a very good alternative to a circumstantial finite element analysis (FEA). In the present study, results from the finite element simulations are observed not to vary significantly for further refinement of the mesh. In the following, the evolutions of shrinkage, porosity and shape of the bi-layered sample

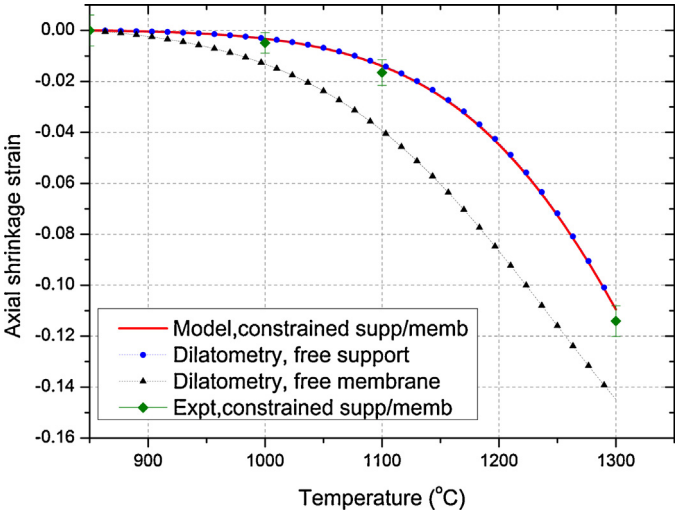

Fig. 7. Comparison of linear shrinkage strains during free sintering and axial strain during constrained sintering together with experimental measurements of axial strains in the tubular bi-layer sample.

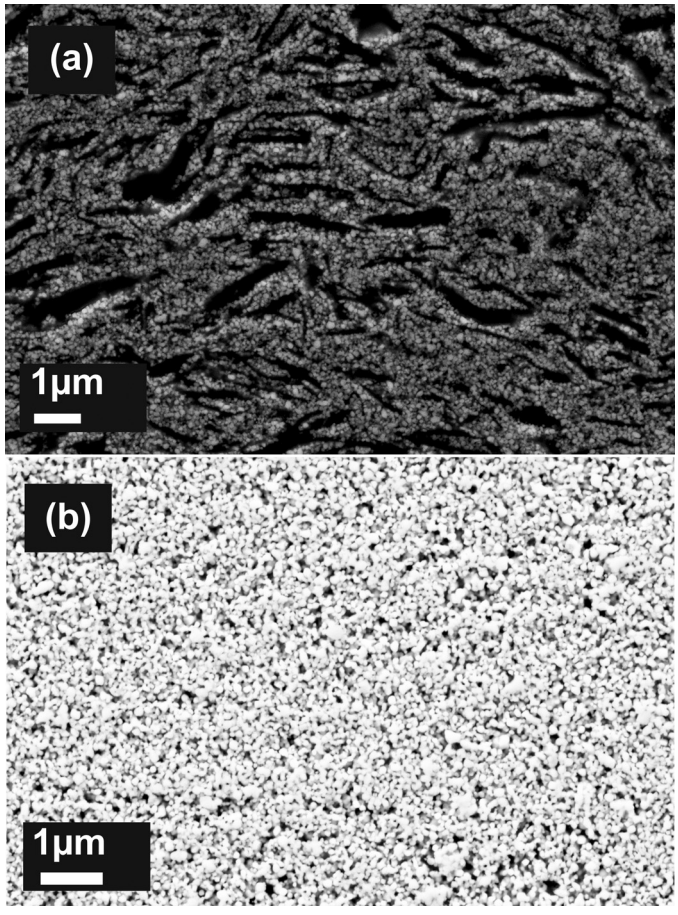

Fig. 8. SEM characterization of the bi-layered tubular sample after sintering to 1100 °C (a) MgO support and (b) CGO membrane.

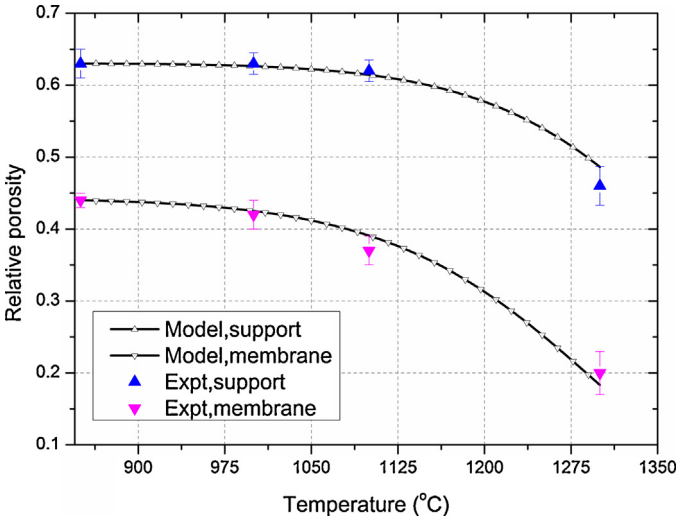

Fig. 9. Comparison of the evolution of porosity from model and experiment during constrained sintering of tubular bi-layer sample.

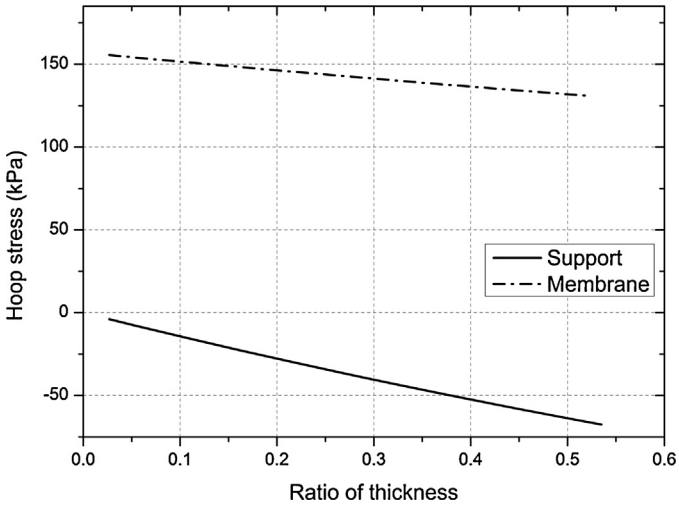

Fig. 11. Variation of hoop stress with ratio of thickness of the layers (CGO-membrane to MgO-support) at the beginning of the sintering cycle.

from experiment are compared with results from the analytical model.

4.2. Shrinkage

Fig. 7 shows the analytical model prediction for the axial shrinkage, ε_{zz}, across the length of the bi-layer in comparison with free shrinkage data and the measurements taken during the sintering of tubular bi-layer. Comparison of axial shrinkage in the constrained CGO membrane with the free CGO tape shows that the CGO membrane is exposed to tensile stresses, which hinder the densification during sintering of the tubular bi-layer. The constrained shrinkage in the MgO support is almost unaffected by the level of stresses generated in it. Results from the model agree well with the shrinkage measurements from SEM images of the samples at four different temperatures. It is evident that the linear shrinkage in the CGO membrane dominates the sintering cycle, which exposes it to tensile stress from the MgO support.

4.3. Porosity evolution

The porosity evolutions in each layer during constrained sintering of the bi-layer tubular sample were measured using SEM images at four different temperatures. Fig. 8 shows the example of SEM images of MgO support and CGO membrane at 1100 °C. From the analytical model, Eq. (22) is used to update the porosity in time. Fig. 9 shows the comparison between results from the analytical model and measurement values with the standard deviation from the measurement. The standard deviations are deduced from the variations in the thickness observed from SEM images of the layers. Predictions from the analytical model agree well with the measured values in both the support as well as membrane. Porosity evolution in the case of constrained bi-layered tubular structures is size dependent as the total stress

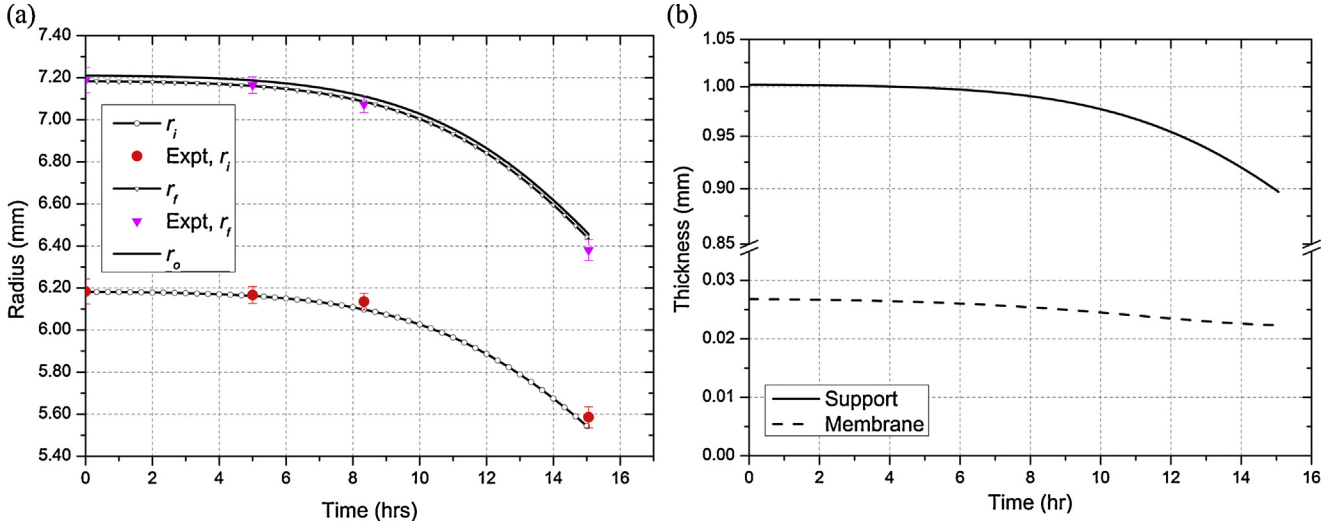

Fig. 10. Evolution of geometrical parameters during the sintering cycle: (a) the different radii in the bi-layer and (b) thickness.

Please cite this article in press as: Molla TT, et al. Modeling constrained sintering of bi-layered tubular structures. *J Eur Ceram Soc* (2014), http://dx.doi.org/10.1016/j.jeurceramsoc.2014.10.010

varies with the radius of the sample during constrained sintering of tubular samples.

4.4. Evolution of shape

In addition to densifications, the geometrical parameters of the tubular samples were also calculated using the analytical model. Fig. 10(a) shows the evolutions of the internal, r_i, interfacial, r_f, and external, r_o, radii of the bi-layer sample during the entire sintering cycle. Experimental values, deduced from measurements of the interface diameter and thickness of the MgO support at four temperatures, are also in good agreement with the model. The model predictions for the thickness evolution of each layer have also been shown in Fig. 10(b).

Processing defects such as axial cracks and peel-offs of the coating or membrane often occur due to the transient hoop stress, which is maximum at the beginning of the sintering process as shown in Fig. 4. This is similar with processing flaw generations during constrained sintering of planar multi-layers.[30] The densification and stress analysis during constrained sintering of tubular bi-layer structures would help to optimize stresses, for example, as a function of thickness of the support or membrane. Fig. 11 shows an example of variation of the maximum hoop stress as function of ratio of thickness (i.e. radial thickness of the CGO membrane to the MgO support). For the sample analyzed in this study, increasing the thickness ratio between the two layers would not only slightly decrease the hoop stress in the membrane but also increases the compressive hoop stress on the support. The increase of compressive hoop stress on the support can have an effect on the final size of the sample. Sometimes the dimensions are of course set by the application of the tubular structure, and the possibility for tuning these parameters might not be available.

5. Conclusion

A closed form analytical model based on the analogy between linear elastic and linear viscous theories has been developed to describe densification and stress development during sintering of tubular bi-layered samples. Stresses during constrained sintering of tubular bi-layered structures develop not only due to mismatch in the shrinkage rate of the layers but also because of the radial gradients in the internal shrinkage rate of each layer. The developed analytical model is first verified by finite element simulation for the constrained sintering of tubular bi-layer system. Furthermore, the analytical model is validated using densification results from sintering of bi-layered tubular supported ceramic oxygen membranes based on porous MgO and $Ce_{0.9}Gd_{0.1}O_{1.95-d}$ layers. Results from the analytical model agree well with finite element simulations as well as measurements from the experiment.

In general, the radial stresses in the bi-layered tubular structures are very small throughout the sintering cycle as compared to the hoop stresses. Processing defects like axial cracks and coating peel-offs mainly occur due to the hoop stress which is maximum at the beginning of the sintering cycle. The model provided in this study could be used to minimize the transient stress generations during constrained sintering of tubular bi-layered structures.

Acknowledgments

The authors would like to acknowledge the support of the Danish Council for Independent Research Technology and Production Sciences (FTP) which is part of The Danish Agency for Science, Technology and Innovation (FI) (Project # 09-072888). The support of US National Science Foundation Division of Civil, Mechanical Systems, and Manufacturing Innovations (NSF grant No. CMMI 1234114) is also gratefully appreciated.

References

1. Powell J, Assabumrungrat S, Blackburn S. Design of ceramic paste formulations for co-extrusion. *Powder Technol* 2013;**245**:21–7.
2. Bredesen R, Jordal K, Bolland O. High-temperature membranes in power generation with CO_2 capture. *Chem Eng Process* 2004;**43**:1129–58.
3. Zhang C, Xu Z, Chang X, Zhang Z, Jin W. Preparation and characterization of mixed-conducting thin tubular membrane. *J Membr Sci* 2007;**299**:261–7.
4. Liu Z, Zhang G, Dong X, Jiang W, Jin W, Xu N. Fabrication of asymmetric tubular mixed-conducting dense membranes by a combined spin-spraying and co-sintering process. *J Membr Sci* 2012;**415–416**:313–9.
5. Salehi M, Pfaff E, Junior R, Bergmann C, Diethelm S, Neururer C, et al. $Ba_{0.5}Sr_{0.5}Co_{0.8}Fe_{0.2}O_{3-\delta}$ (BSCF) feedstock development and optimization for thermoplastic forming of thin planar and tubular oxygen separation membranes. *J Membr Sci* 2013;**443**:237–45.
6. Bordia R, Scherer G. On constrained sintering-I, constitutive model for a sintering body. *Acta Metall* 1988;**36**(9):2393–7.
7. Bordia R, Scherer G. On constrained sintering-II, comparison of constitutive models. *Acta Metall* 1988;**36**(9):2399–409.
8. Cai P, Green D, Messing G. Constrained densification of alumina/zirconia hybrid laminates: 1. Experimental observations of processing defects. *J Am Ceram Soc* 1997;**80**(8):1929–39.
9. Cai P, Green D, Messing G. Constrained densification of alumina/zirconia hybrid laminates: 2. Viscoelastic stress computation. *J Am Ceram Soc* 1997;**80**(8):1940–8.
10. Kanters J, Eisele U, Rodel J. Co-sintering simulation and experimentation: case study of nanocrystalline zirconia. *J Am Ceram Soc* 2001;**84**(12):2757–63.
11. Ollagnier J, Green D, Guillon O, Roedel J. Constrained sintering of a glass ceramic composite: II. Symmetric laminate. *J Am Ceram Soc* 2009;**92**(12):2900–6.
12. Ollagnier J, Guillon O, Roedel J. Constrained sintering of a glass ceramic composite: I. Asymmetric laminate. *J Am Ceram Soc* 2010;**93**(1):74–81.
13. Chang J, Guillon O, Roedel J, Kang S. Characterization of warpage behaviour of Gd-doped ceria/NiO-yttria stabilized zirconia bi-layer samples for solid oxide fuel cell application. *J Power Sources* 2008;**185**(2):759–64.
14. Lu G, Sutterlin R, Guppta T. Effect of mismatched sintering kinetics on camber in a low-temperature cofired ceramic package. *J Am Ceram Soc* 1993;**76**(8):1907–14.
15. Muecke R, Menzler N, Buchkremer H, Stoever D. Cofiring of thin zirconia films during SOFC manufacturing. *J Am Ceram Soc* 2009;**92**(1):S95–102.
16. Kim J, Rudkin R, Wang X, Atkinson A. Constrained sintering kinetics of 3YSZ films. *J Eur Ceram Soc* 2011;**31**(13):2231–9.
17. Olevsky E, Molla T, Frandsen H, Bjork R, Esposito V, Ni D, et al. Sintering of multilayered porous structures: Part I. Constitutive models. *J Am Ceram Soc* 2013:1–9.
18. Frandsen H, Olevsky E, Molla T, Esposito V, Bjork R, Pryds N. Modeling sintering of multi-layers under influence of gravity. *J Am Ceram Soc* 2013;**96**(1):80–9.

Please cite this article in press as: Molla TT, et al. Modeling constrained sintering of bi-layered tubular structures. *J Eur Ceram Soc* (2014), http://dx.doi.org/10.1016/j.jeurceramsoc.2014.10.010

19. Molla T, Frandsen H, Bjørk R, Ni D, Olevsky E, Pryds N. Modeling kinetics of distortion in porous bi-layered structures. *J Eur Ceram Soc* 2013;**33**(7):1297–305.
20. Ni D, Esposito V, Schmidt C, Molla T, Andersen K, Kaiser A, et al. Camber evolution and stress development of porous ceramic bilayers during co-firing. *J Am Ceram Soc* 2013;**96**:972–8.
21. Olevsky E. Theory of sintering: from discrete to continuum. *Mater Sci Eng R-Rep* 1998;**23**(2):41–100.
22. Timoshenko S, Goodier J. *Theory of elasticity*. New York, USA: McGraw-Hill Book Company; 1951.
23. Lamé G. *Leçons sur la théorie mathématique de l'élasticité des corps solides*. Bachelier; 1852.
24. Kwok K, Frandsen H, Søgaard M, Hendriksen P. Stress analysis and fail-safe design of bi-layered tubular supported ceramic membranes. *J Membr Sci* 2014;**453**:253–62.
25. Ramachandran D, Clemens F, Glasscock A, Søggard M, Kaiser A. Tailoring the microstructure of porous MgO supports for asymmetric oxygen separation membranes: optimization of thermoplastic feedstock systems. *Ceram Int* 2014;**40**:10465–73.
26. Ni D, Schmidt C, Teocoli F, Kaiser A, Andersen K, Ramousse S, et al. Densification and grain growth during sintering of porous $Ce_{0.9}Gd_{0.1}O_{1.95}$ tape cast layers: a comprehensive study on heuristic methods. *J Eur Ceram Soc* 2013;**33**:2529–37.
27. Teocoli F, Esposito V. Viscoelastic properties of doped-ceria under reduced oxygen partial pressure. *Scr Mater* 2014;**75**: 82–5.
28. Mukherjee S, Paulino G. The elastic–viscoelastic correspondence principle for functionally graded materials. *J Appl Mech-TransASME* 2003;**70**(3):359–63.
29. Molla TT, Ni DW, Bulatova R, Bjørk R, Bahl C, Pryds N, Fransen HL. Finite element modeling of shape distortions during sintering of bi-layers. *J Am Ceram Soc* 2014;**97**(9):2965–72.
30. Bordia R, Jagota A. Cracks growth and damage in constrained sintering. *J Am Ceram Soc* 1993;**76**(10):2475–85.

Please cite this article in press as: Molla TT, et al. Modeling constrained sintering of bi-layered tubular structures. *J Eur Ceram Soc* (2014), http://dx.doi.org/10.1016/j.jeurceramsoc.2014.10.010

Publication V

"Tubular multilayer fabrication and performance of a doped ceria oxygen membrane on a low cost MgO support"

Elsevier Editorial System(tm) for Membrane Science
Manuscript Draft

Manuscript Number:

Title: Fabrication and performance of a tubular ceria based oxygen membrane on a low cost MgO support

Article Type: Full Length Article

Keywords: Asymmetric Membrane; Dip coating; MgO support; CGO membrane; Oxygen flux

Corresponding Author: Mr. Dhavanesan K Ramachandran,

Corresponding Author's Institution: Technical University of Denmark

First Author: Dhavanesan K Ramachandran

Order of Authors: Dhavanesan K Ramachandran; Martin Søgaard, PhD; Frank Clemens; Andreas Kaiser

Abstract: A 30 μm thin-film tubular CGO (Ce0.9Gd0.1O1.95-δ) membrane with catalytic layers on both sides has been prepared by dip coating on a low cost, porous magnesium oxide (MgO) support. The MgO support was fabricated through a thermoplastic extrusion process. Support, thin membrane and catalytic layers were sintered in individual steps at temperatures between 1250 to 1300 °C to achieve a controlled removal of binder and organic additives and to obtain the desired, defect free microstructure. The prepared asymmetric tubular CGO membrane has been tested at elevated temperatures (up to 900 °C) using atmospheric air and N2, H2 for the feed and sweep side respectively. At the end of the experiment methane was fed on the sweep side. The oxygen permeation was 4 Nml min-1 cm-2 at 850 °C using H2 on one side and air on the other side. SEM analysis after the membrane test indicates detachment of the catalytic layer on the permeate side most likely due to carbon formation as the membrane was tested with methane/humidified hydrogen mixture.

Suggested Reviewers: Wanqin JIN PhD
Professor, College of Chemistry and Chemical Engineering, Nanjing University of Technology
wqjin@njtech.edu.cn

Marie-Laure Fontaine PhD
Senior Scientist, Sustainable Energy Technology, SINTEF Materials and Chemistry
Marie-Laure.Fontaine@sintef.no

Kiyoshi Hirao PhD
Senior Scientist, Advanced Manufacturing Research Institute (AMRI), National Institute of Advanced Industrial Science and Technology (AIST), Japan
k-hirao@aist.go.jp

Cover Letter
Click here to download Cover Letter: Cover letter.pdf

DTU Energy Conversion

Dear editorial board of the Journal of Membrane Science,

Enclosed please find the manuscript "**Fabrication and performance of a tubular ceria based oxygen membrane on a low cost MgO support**", Dhavanesan Kothanda Ramachandran, Martin Søgaard, Frank Clemens, and Andreas Kaiser, to be submitted as a research work in Journal of Membrane science.

This article describes the fabrication and testing of a thin-film tubular CGO ($Ce_{0.9}Gd_{0.1}O_{1.95-\delta}$) membrane on a low cost, porous magnesium oxide (MgO) support by extrusion, dip-coating and catalyst infiltration. Critical steps in the fabrication (i.e. co-sintering of porous MgO support and dense membrane layers) were optimized and resulted in an asymmetric membrane with an oxygen flux of 4 Nml/min cm^2 under reducing conditions. The demonstrated oxygen flux is an important step towards the use of such a mixed conducting membrane in chemical (syngas) reactors.

We believe that the preparation and characterization of cost-effective asymmetric oxygen separation membranes is of interest to the readers of this journal

We confirm that the work of this manuscript is original, unpublished and not being considered for publication elsewhere. All contributors, including funding sources are acknowledged. Thank you for your kind consideration of our paper and we look forward to your response.

On behalf of the authors,
Best regards,
Dhavanesan Kothanda Ramachandran
Ph.D student
Department of Energy Conversion and Storage

Technical University of Denmark
DTU Energy Conversion
(Risø campus)
Frederiksborgvej 399
Building 779
DK-4000 Roskilde
Denmark
Tel.: +45 46 77 48 00
Fax: +45 46 77 58 58
dhra@dtu.dk
www.ecs.dtu.dk

Highlights:

- A low cost Magnesium oxide (MgO) substrate was developed for use as a support layer for the membranes.
- A defect free tubular asymmetric oxygen transport membrane was successfully prepared through extrusion and dip-coating.
- Oxygen flux performance of 4 Nml/min cm^2 under reducing environments was achieved for a 30 µm thick asymmetric CGO membrane supported by MgO.

Technical University of Denmark
DTU Energy Conversion
(Risø campus)

Frederiksborgvej 399
Building 779
DK-4000 Roskilde
Denmark

Tel.: +45 46 77 48 00
Fax: +45 46 77 58 58

dhra@dtu.dk
www.ecs.dtu.dk

Fabrication and performance of a tubular ceria based oxygen membrane on a low cost MgO support.

D. K Ramachandran[1*], M. Søgaard[1], F.Clemens[2], A. Kaiser[1]

[1]Department of Energy Conversion and Storage, Technical University of Denmark, Frederiksborgvej 399, Building 779, DK-4000 Roskilde, Denmark.

[2]EMPA, Swiss Federal Laboratories for Materials Science and Technology, Laboratory for High Performance Ceramics, Ueberlandstrasse 129, CH-8600 Dübendorf, Switzerland

*Corresponding author, Tel.:+45 4677 4800; fax: +45 4677 5858. E-mail: dhra@dtu.dk, dhavaa@gmail.com

Abstract

A 30 µm thin-film tubular CGO ($Ce_{0.9}Gd_{0.1}O_{1.95-\delta}$) membrane with catalytic layers on both sides has been prepared by dip coating on a low cost, porous magnesium oxide (MgO) support. The MgO support was fabricated through a thermoplastic extrusion process. Support, thin membrane and catalytic layers were sintered in individual steps at temperatures between 1250 to 1300 °C to achieve a controlled removal of binder and organic additives and to obtain the desired, defect free microstructure. The prepared asymmetric tubular CGO membrane has been tested at elevated temperatures (up to 900 °C) using atmospheric air and N_2, H_2 for the feed and sweep side respectively. At the end of the experiment methane was fed on the sweep side. The oxygen permeation was 4 Nml min^{-1} cm^{-2} at 850 °C using H_2 on one side and air on the other side. SEM analysis after the membrane test indicates detachment of the catalytic layer on the permeate side most likely due to carbon formation as the membrane was tested with methane/humidified hydrogen mixture.

Keywords; **Asymmetric Membrane, Dip coating, MgO support, CGO membrane, Oxygen flux.**

1. Introduction

Gadolinium doped Ceria, CGO, is widely used in high temperature electrochemical devices such as solid oxide fuel/electrolysis cells (SOFC/SOEC), membranes and flue gas purification devices. The high phase stability of CGO under both oxidizing and reduction atmospheres and the high ionic conductivity, makes CGO an interesting material for an Oxygen Transport Membrane (OTM). An OTM is a gas-tight component permeable only to oxygen, giving 100 % theoretical selectivity. The use of such membranes to provide oxygen for different industries i.e. steel, cement and syngas production, can improve the energy efficiency in the production cycle and further in some cases facilitate an easier CO_2 capture and sequestration. Developing a high performance OTM-system is a challenging task as material development, ceramic processing and system integration must be considered.

The oxygen permeation flux of various fluorite structured membrane materials for wide range of membrane thickness (50 to 2000 μm) have been reported [1]. In order to achieve fluxes that are of commercial interest for most of the large scale applications it is clear that thin film membranes with thicknesses below <100 μm must be prepared. Such thin membrane are typically not mechanically stable. In order to reduce the membrane thickness without sacrificing mechanical properties of the overall component, an asymmetric membrane configuration can overcome the problems associated with mechanical stability. Previously, Kaiser et al. [2], have reported oxygen fluxes of more than 10 Nml min^{-1} cm^{-2} at 850 °C on a 30 μm thick planar CGO membrane supported by a Ni-YSZ cermet support. The different layers were prepared by tape casting and subsequent lamination. The CGO membrane showed good thermal and chemical stability at syngas operation conditions.

When the membrane layer gets below a certain characteristic thickness, the catalytic processes on the surface of the membrane might become a limiting factor of the membrane performance. In order to improve the oxygen flux further the surface exchange kinetics have to be enhanced on both sides of the membrane, which is typically done using electro-catalytic materials. Ni–$Ce_{0.9}Gd_{0.1}O_{1.95}$ (Ni–CGO), ceramic-metal composites (cermet) have been widely used as electro catalytic material in SOFCs [3,4] in which the metallic form of Ni acts as catalyst for fuel oxidation and provides electronic conductivity, whereas CGO not only acts as a matrix to support the catalyst but it also transports oxygen ions out from the structure [5–7]. Moreover, a Ni-CGO cermet can easily be combined with a CGO membrane instead of using the traditional yttria stabilized zirconia (YSZ) due to the thermal expansion coefficients (TEC) of YSZ (i.e. ~10.5×10^{-6} K^{-1}) which is significantly lower than that of CGO and MgO [8,9].

Perovskites structured materials such as (La,Sr)(Co,Fe)O_3 have been vastly used as oxygen reduction catalysts in SOFC and for OTMs [10]. It has also been demonstrated that electrodes with very high catalytic activity can be prepared by infiltration of these materials into porous ionic conducting backbone structures [11]. Additionally, Zhao et al. [12], have reported that LSC catalytic layers prepared by this route show remarkable performance in terms of high resistance to thermal cycling and thermal shock due to using of impregnated nano catalytic particles rather than bulk particles.

For the preparation of asymmetric membranes, a planar structure configuration is usually chosen because of the simple fabrication [13–15]. Changing to a tubular design has some advantages compared to a planar design especially in terms of mechanical strength when the component is in a temperature gradient. Additionally, the sealing of tubular components, especially if high pressure is considered much less difficult [16–19]. Some studies on the preparation and testing of an asymmetric tubular perovskite membrane structure have been reported earlier [20–24]. In these studies identical materials for dense layers and porous supports were mainly used. Recently Liu et al. [24], demonstrated that a crack-free asymmetric tubular perovskite membrane with a thickness of 20 μm could be prepared using extrusion and a spray drying processing step. With the asymmetric design the oxygen flux performance was almost 1.35 times higher than with the symmetric configuration and the membrane was stable under low pO_2 conditions over 200 h. It is evident to see that the membrane performance and stability could be improved by an asymmetric configuration. Moreover, to the author's knowledge studies are not available that deal with the preparation and testing of asymmetric tubular CGO membranes for use in syngas reactors or in similar applications. Hence this work contribute to closing the research gap in this area.

This present work addresses the preparation and characterization of a gastight membrane layer of $Ce_{0.9}Gd_{0.1}O_{1.95-\delta}$ (CGO10), supported on a porous MgO tubular substrate. On each side of the CGO membrane a catalytic layer is present in order to improve the electro-catalytic reaction. The optimization of the de-bindering and sintering cycle is optimized as to allow for an effective removal of binder organics and co-sintering of a defect free asymmetric membrane multi-layer structure. The oxygen permeation flux for the tubular, MgO supported CGO membrane is measured in the temperature range of 750–900 °C under conditions relevant for syngas operation.

2. Material and methods

Fig. 1 (a) shows a schematic of the prepared asymmetric tubular membrane architecture in which the porous MgO support was fabricated using thermoplastic extrusion and the membrane and catalytic layers were prepared through a dip-coating process from stabilized ceramic suspensions. This was followed by impregnation of catalytic material into the porous backbone on the outside of the membrane. **Fig. 1** (b)-(e) shows photographs of tubular membranes after each progressing steps. The process starts from the extrusion of tubes, followed by dip coating and sintering of the catalytic layer (NiO-CGO), membrane layer (CGO) and porous CGO backbone layer for impregnation of nano particles of LSC.

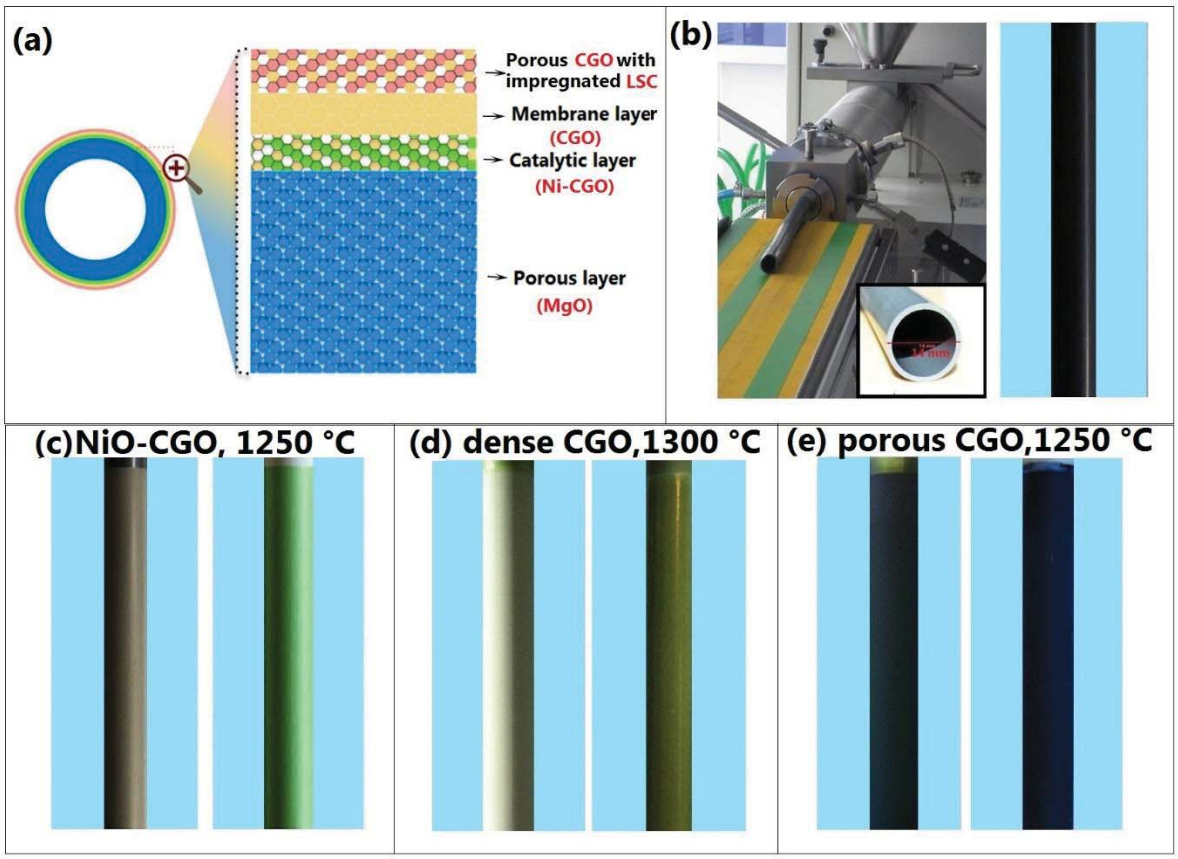

Fig. 1: (a) Schematic of the manufactured asymmetric tubular membrane including the used materials, (b) MgO tubes after thermoplastic extrusion, (c) Catalytic layer of NiO-CGO after coating and pre-sintering, d) Dense CGO membrane layer after coating and sintering, e) Membrane after coating and sintering of porous CGO layer with infiltration of LSC nano particles.

2.1 Thermoplastic extrusion of MgO support tubes

The preparation of the tubular MgO support includes powder processing, kneading, thermoplastic extrusion and finally the thermal de-bindering and sintering. First the MgO powder (Product # 12R-0801, Inframat Advanced Materials, USA) was pre-calcined at 1000 °C for 10 h in order to reduce the surface area of the powder. The pre-calcined MgO powder, graphite powder (TIMREX® KS6, TIMCAL, Switzerland), thermoplastic binder (Elvax 250, Du Pont; USA), and paraffin wax (Sigma-Aldrich, USA) as a plasticizer was mixed in a kneader (Linden, Type BK20, Germany). The graphite powder is used as a pore former. The feedstock composition consists of 34 vol.% MgO, 46 vol.% thermoplastic binders & additives and 20 % graphite. The feedstock optimization with respect to the form stability, shrinkage behavior during extrusion and the sintering process as well as additional information on the preparation, can be found in our previous work [25]. The kneaded feedstock was shaped into a tube using a die assembly of Ø = 14 mm outer diameter and Ø = 12 mm inner diameter by using an extruder (Model 19/20DN, Brabender, Germany). An oil bath was used to maintain a temperature of 110 °C and 100 °C for the extruder chamber and die head, respectively. An extruder speed of 10 RPM was used during the entire extrusion step as this was found to be the optimal speed with respect to extruded form stability during the processing.

2.2 Preparation of functional layers

2.2.1 Slurry preparation

Three different slurries have been prepared: i) a CGO slurry for the dense membrane layer (CGO-D) ii) a CGO slurry for the porous infiltration layer on the feed side (CGO-P) iii) a NiO-CGO slurry for the activation layer on the permeate side. The slurry compositions are listed in **Table 1**. For the rheology measurement of dip-coating ceramic suspensions, a rheometer (MCR302, Anton Paar, Sweden) was used. For the dense CGO membrane preparation, a pre-calcined CGO powder (high solid loading –10 vol.% for better densification) was dispersed in an ethanol based suspension with polyvinylpyrrolidone (PVP) as dispersant and polyvinylbutyral (PVB) as binder. The resulting slurry for the dip coating was homogenized by ball milling for 72 h. For the preparation of the catalytic layer on the permeate side, a NiO-CGO (60:40 wt.%) based cermet was used.. This NiO-CGO suspension (total solid loading 5-6 vol.%) was prepared with low viscosity in order to cover the MgO tube surface properly and to produce a very thin layer. For the preparation of the catalytic layer on the feed side of the membrane, a porous CGO backbone has been established from the porous CGO suspension using dip coating process. This slurry contains about 20

wt.% of graphite pore former in order to create porosity. Later a water based solution of the nitrates corresponding to a nominal composition of $La_{0.6}Sr_{0.4}CoO_{3-\delta}$ (LSC) has been prepared. The reason for using this technique is that the catalytic activity can be enhanced by infiltration of nano particles of these materials into porous backbone structure, since the small of amount material used will not diminish the total porosity of the structure. For rheology measurements of the developed dip-coating ceramic suspensions, a rheometer (MCR302, Anton Paar, Sweden) was used.

Table 1. Composition of NiO-CGO, dense (CGO-D) and porous (CGO-P) ethanol based suspensions.

Components	**NiO-CGO (60:40)**	**CGO-D**	**CGO-P**
Nickel oxide	5-6 vol.%	---	---
CGO (Low surface area) pre-calcined at 1000°C		10 vol.%	4-5 vol.%
Surfactant, PVP K10	3 vol.%	4 vol.%	5 vol.%
Graphite	---	---	20 vol.%
Binder, PVB K90	3 vol.%	5-6 vol.%	5-6 vol.%

2.2.2 Preparation of the functional layers

For the dip coating of the three functional layers, an in-house constructed dip coater has been used. The dip coating speed can be controlled accurately by a step engine, thereby allowing a very precise control of the thickness and evenness of the coatings. As shown in **Fig. 1**, the catalytic layer of NiO-CGO was coated on the green MgO tube and pre-sintered at 1250 °C, followed by dip coating and sintering of the dense CGO membrane (CGO-M) and finally the porous CGO layer.

The porous MgO layer was prepared by thermoplastic extrusion of the feedstock containing ~66 vol.% of binder organics and fugitive pore former. It is very difficult to simultaneously carry out the binder burn out and ensure the densification of the CGO membrane in the same sintering cycle due to the amount of gasses formed. Therefore in order to remove the organic media, a de-bindering and sintering cycle has been developed which is followed by additional cycles. **Fig. 2** shows the sintering profile for the MgO substrate and the co-sintering of the three functional layers such as the NiO-CGO layer, the dense CGO layer and the porous CGO layer. Optimized heating rates of 0.25 °C min^{-1} and 0.5 C min^{-1} were used in the 1^{st} cycle for the de-bindering and the sintering regime, respectively. A holding time of one hour at 300 °C,

400 °C and 670 °C was implemented during the de-bindering cycle to ensure complete removal of organic matter. The temperature was further raised to 1250 °C in order to initiate the partial sintering with the NiO-CGO layer and to improve the mechanical strength for safe handling for the subsequent dip coating.

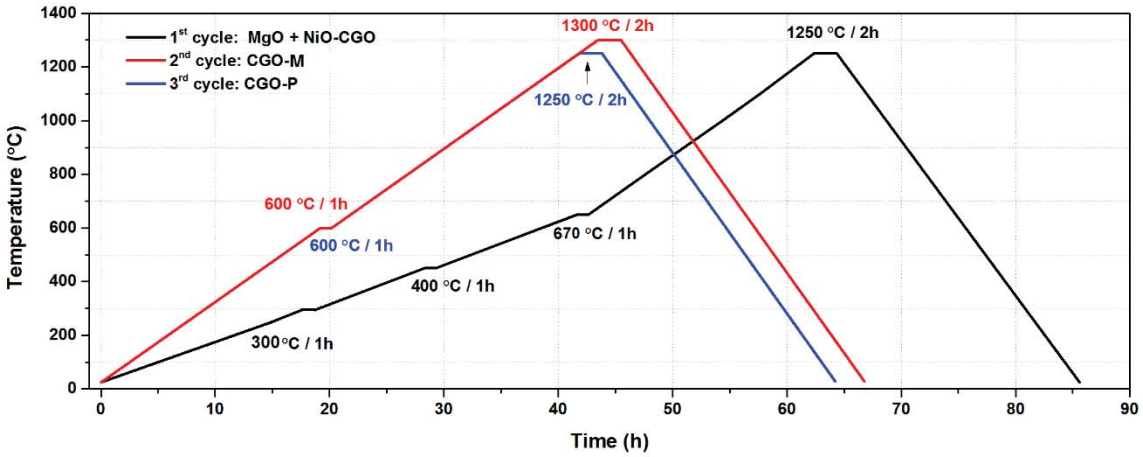

Fig. 2: De-bindering and sintering cycles used for co-sintering of tubular membrane.

Before coating of the membrane CGO layer, the pre-sintered sample was coated again with a single coating of the NiO-CGO suspensions in order to close any pores that may have developed during the pre-sintering of the NiO-CGO layer. The CGO membrane suspension was coated twice in order to improve the chances of gas tightness of the dense membrane layer and to obtain a final sintered thickness of approx. 20 to 30 µm. After the coating, a heating rate of 0.5 °C min^{-1} has been employed for the 2nd cycle and a dwelling period of 1 h at 600 °C was applied to binder removal and later elevated to 1300 °C for 2 h (as shown in **Fig. 2**).

Finally, the outer (porous) CGO layer is dip coated on the already sintered CGO dense layer. The component was sintered at 1250 °C for 2 h. Subsequently, an aqueous solution (1 M) of the nitrates corresponding to the nominal composition ($La_{0.6}Sr_{0.4}CoO_{3-\delta}$) was impregnated into the porous CGO layer 4 times and it was thermally treated at 200 °C after each impregnation. Finally, the infiltrated component was de-bindered at 400 °C before the membrane testing.

To analyze the shrinkage behavior of the porous and dense layers of the membrane, dilatometry experiments were carried out. For this analysis (an optical dilatometer, TOMMI, Fraunhofer ISC, Würzburg, Germany), warm pressed MgO feedstocks and a pressed pellet of the CGO from dried powder of CGO-M slurry was used after de-bindering at 900 °C. The linear shrinkage (dl/L_0) was monitored in situ continuously during the heating and cooling cycles and the shrinkage of the sample was corrected using

the thermal expansion coefficient (TEC) determined from the cooling part of the shrinkage curve. Considering the warm pressed pellets isotropic, the relative densities (ρ) are calculated as a function of temperature from optical dilatometry results using the following equation [26].

$$\rho(T) = \rho_g \left(1 - \frac{dl}{L_0}\right)^{-3} \quad (1)$$

where ρg is the relative density of green sample.

2.3. Oxygen permeation measurement

Before the oxygen permeation measurement, the membrane gas tightness has been tested using an in-house developed equipment. In this equipment the membrane is immersed in ethanol and the inside of the membrane is pressurized with nitrogen to 4 bar. The gas tightness of the membrane was verified as no bubbles could be visually observed.

Oxygen permeation measurements were conducted with the test setup illustrated in **Fig. 3**. The tubular membrane is connected to alumina tubes via alumina transition pieces. The transition pieces and the sample are mounted at room temperature using a glass ceramic paste consisting of Na_2O: 17.8 mol.%, Al_2O_3: 9.4 mol.%, and SiO_2: 72.8 mol.% and an organic solvent. Upon heating to approximately 900 °C this glass ceramic paste can flow and seals the transition piece to both the membrane and the alumina tubes. The temperature near both ends of the tubular sample is monitored by two thermocouples located inside the transition pieces. Due to the length of the sample and the transition pieces, a temperature difference of approximately 10 °C was measured at high temperature (900 °C). The alumina tubes connecting the tubular membrane sample were connected to the gas supply system of the rig. The lower alumina tube (permeate/sweep inlet) connects to the gas supply system where a variety of gasses can be prepared/supplied. An in-house constructed oxygen sensor (Nernst sensor) is connected to the inlet of the sweep gas supply.

The upper alumina tube (permeate/sweep outlet), is also connected to an oxygen partial pressure sensor and a mass flow meter. On the feed side of the membrane (outer side of the membrane) a gas flow of 30 NL/h air was present during the experiment. On the permeate side of the membrane, different flows of nitrogen/hydrogen mixtures where utilized in order to characterize the membrane performance as a function of the flow rate. The oxygen flux through the membrane was calculated using the mass balance from the flow of the sweep gas and the inlet and outlet oxygen partial pressures of the sweep gas [27]. It

should be noted that there is a slight overpressure on the permeate side of the membrane wherefore gaseous oxygen transferred from permeate stream via leaks/pinholes is very limited.

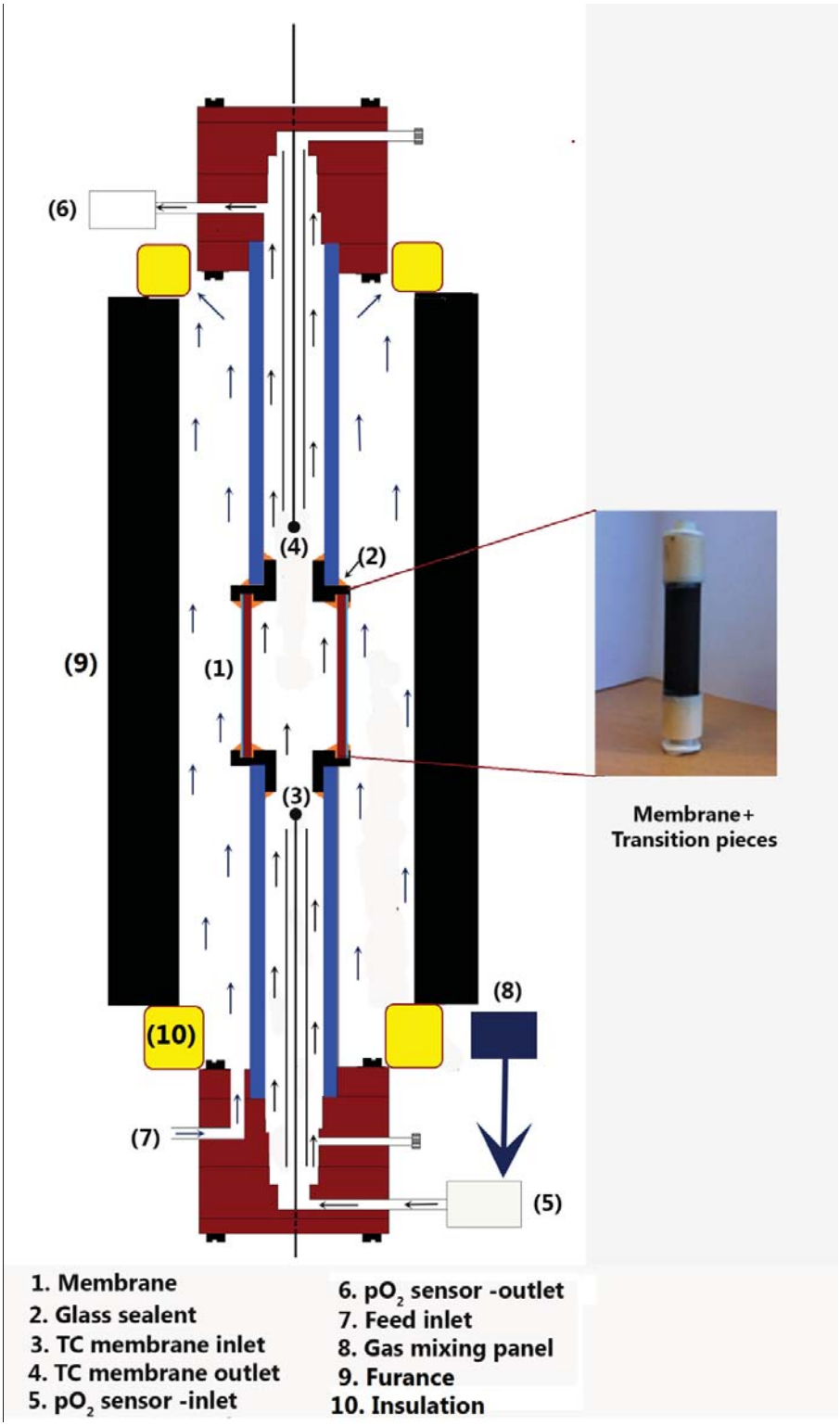

Fig. 3: Schematic of membrane rig setup.

3. Result and discussion

3.1. Rheological behavior of CGO-M, NiO-CGO and CGO-P ceramic suspensions for dip-coating

The rheological behavior of the three suspensions: CGO slurry for the dense membrane layer (CGO-D); CGO slurry for the porous layer (CGO-P); slurry for the catalytic layer (NiO-CGO) have been characterized as to give information on the expected quality of the layer thickness and the smoothness of the coated surface. The viscosity (η) was calculated from the measured value of the shear stress (τ) over a range of shear rates (γ) from 0 to 100 s^{-1}. **Fig. 4** shows that the CGO suspension prepared with high solid loading (CGO-M) for preparation of the dense membrane layer has a shear thinning behavior. The other two slurries for the porous catalytic layers (NiO-CGO and CGO-P) show a very low shear thinning behavior indicating that the coating thickness will only be slightly influenced by the coating speed. At a shear rate of 100 s^{-1}, the CGO slurry with high ceramic loading (CGO-M) shows the highest viscosity of 37 mPa s followed by NiO-CGO with 19 mPa s and the CGO slurry with 14 mPa s. Due to the lower shear thinning effect of the NiO-CGO and CGO-P slurry, the quality of these suspension is considered suitable as the expected coating surface will smoothen the MgO support surface to enable the application of the thin film CGO layer (CGO-M).

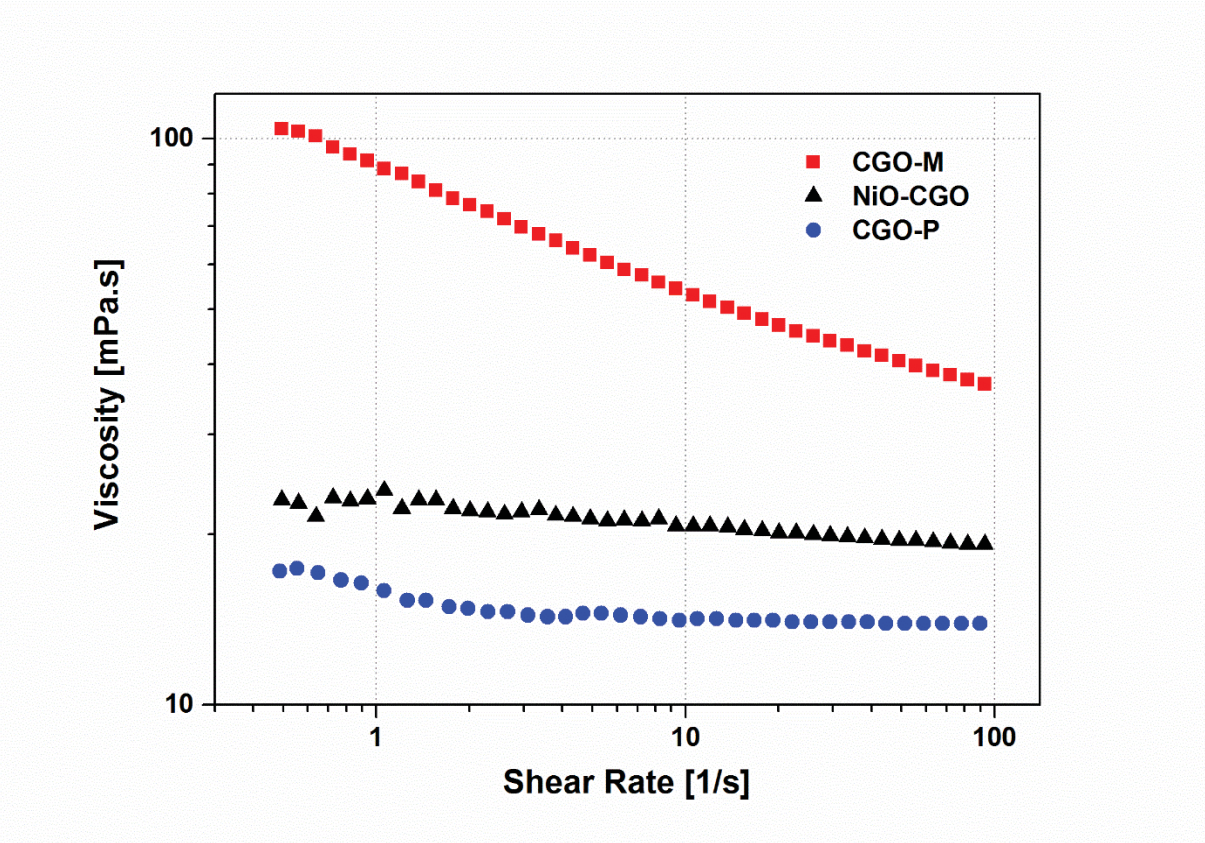

Fig. 4: Viscosity of various ceramic suspensions as function of shear rate.

3.2 Co-sintering of porous MgO support/dense CGO membrane layer

An important aspect in the fabrication of asymmetric multi-layers with a porous/dense structure is the co-sintering process. In co-sintering, a good match of the shrinkage and strain rate of the membrane structure, consisting of different layers, need to be achieved in order to avoid the development of excessive stresses during sintering which can lead to mechanical failures or warpage in the case of planar structures [28]. For the co-sintering of a tubular support layer of MgO with a CGO membrane the differences in the starting powders and targeted final densities of the layers need to be considered. A thin membrane layer needs to be fully densified (to achieve 100 % gas tightness) on a sufficiently porous support layer (usually 25 to 40 %, depending on support thickness and microstructure).

In the present work the shrinkage, final density and potential distortion of ceramic multilayer systems during the co-sintering process have been measured using optical dilatometry [29–31]. The densification and strain rate development of single green layers of a MgO extrusion mass and a dip coating

composition (after de-bindering) as function of sintering temperature are shown in **Fig. 5 (a)** and **(b)**, respectively.

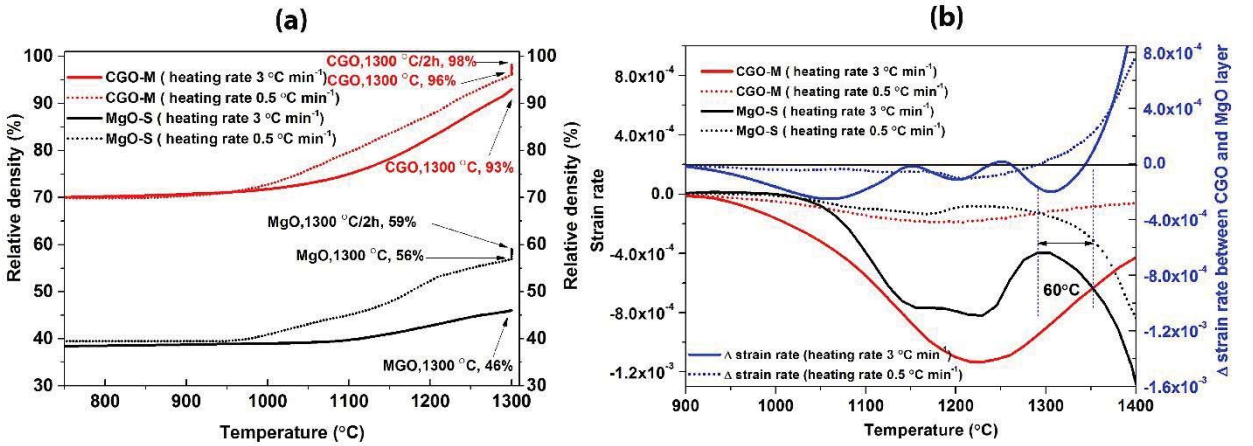

Fig. 5: (a) Densification and (b) strain rates of CGO membrane (CGO-M) and MgO support (MgO-S) layers and, as well as strain rate difference between the two different layers for free sintering as function of sintering temperature. Measurements were performed at two different heating rates of 0.5 °C min^{-1} (dotted lines): and 3 °C min^{-1} (continuous lines) with an optical dilatometer TOMMI [32].

Fig. 5 (a) reveals that the MgO support structure has a significantly lower starting density (relative density) of about 38-40 % (or 60-62 % porosity) compared to a starting density of about 70 % for the CGO membrane layer. The low starting density of the MgO support (compared to the membrane) is desired and was achieved by the use of thermoplastic binder and graphite as pore formers in the extrusion mass. The densification of the MgO support structure in a heating cycle is influenced by the heating rate (the total time to reach the final sintering temperature) and the isothermal holding time at the final sintering temperature. Thus, in **Fig. 5**(a) the MgO sintered with the slower heating rate (0.5 °C min^{-1}) reaches almost 10% higher final density (56 %) compared to the same material sintered with 3 °C min^{-1} at a sintering temperature of 1300 °C. Applying additional holding time at 1300 °C further densifies the structure by approximately 3%. Therefore, faster heating rates would favor more porous support structures. On the other hand, the densification curves of the CGO membrane layer reveal that the fast heating of 3 °C min^{-1} to 1300 °C would only lead to a final density of 93 %, densities of 96 % could, however, be achieved with an isothermal holding time of a few hours. A slower heating of the CGO layer would lead to higher density.

Fig. 5 (b) shows the strain rates of the MgO and CGO layer at the two different heating rates (0.5 and 3 °C min^{-1}) and the calculated strain rate differences for the two layers for both heating rates. From such data the formation of stresses between the layers can be estimated, and together with the shape change of complete, tubular bilayer structures the formation of stresses between the layers can be calculated. Such modeling is reported elsewhere [33] and here we just briefly describe the strain curves and their relevance.

The strain rate difference between the MgO support and the CGO membrane layer in **Fig. 5** (b) is significantly increasing if the samples are heated faster (heating rate of 3 °C min^{-1} compared to 0.5 °C min^{-1}). A larger strain rate difference may drastically increase the risk of the formation of stress-induced defects and delamination. Especially, the larger strain rate difference between the layers in the low temperature sintering regime (900 to 1100 °C) would be critical in a bi-layer structure when the sample is still fragile and sintering necks start to form.

The strain rate curves in **Fig. 5** (b) indicate that after the onset of sintering at about 900 °C the CGO membrane layer is shrinking faster than the MgO support until temperatures of about 1300 °C when the CGO layer is getting fully densified and the shrinkage rate of the CGO layer is declining. Above temperatures of about 1300 °C the MgO support shrinks faster than the CGO membrane layer (crossing points between the two strain rate curves). Interestingly, this cross over point is shifted from temperatures of 1300 °C to 1360 °C if the heating rate is increased from 0.5 to 3 °C min^{-1}.

Therefore, if the stress levels do not lead to failure in the low temperature sintering region, a co-sintering with a fast heating rate towards a higher final sintering temperature (and shorter isothermal holding times) could lead to a bilayer structure with a porous support structure and a dense CGO layer. Furthermore, according to previous investigations by dilatometry, electron microscopy and mercury porosimetry [25], the densification between 1250 and 1400 °C is governed by the elimination of smaller submicron sized pores. This leads to shrinkage of the overall structure, but simultaneously also a growth and improved interconnectivity of larger macro pores (introduced by the addition of graphite pore former) which surprisingly resulted in improved pore connectivity and gas permeability of the support structure.

Previous work on such MgO supports with a porosity of 42 % have shown that for these structures a gas permeability (Darcy) of about 4.2×10^{-16} m^2 can be reached [25] which need to be improved to avoid gas transport limitations for membrane layers with high oxygen fluxes above 10 ml $min\ cm^{-2}$. With a specific

high temperature mechanical test rig the mechanical strength of extruded MgO support tubes was determined with 77 MPa at room temperature and 60 MPa at 850 ˚C [34]. These strength values are considered to be sufficient for the membrane application. Nevertheless, these type of strength measurements need also to be performed on fully assembled MgO supported CGO membranes to exclude a reduction in strength due to defect formation during co-sintering.

3.3. Microstructure of asymmetric MgO supported CGO membranes

After successful completion of the co-sintering of the membrane, gas-leakage was tested to ensure that the membrane is free from processing defects. The test verified that the membranes were gas tight (for details on the gas leakage measurements refer to section 2.3). **Fig. 6** shows SEM images of thermally etched cross sections of the (a) full membrane, (b) interface of Ni-CGO and MgO porous layer after reduction, (c) dense CGO layer, (d) porous NiO-CGO layer and (e) porous MgO layer. Marco-defects or cracks have not been observed in the sample. **Fig. 6** (c) shows a cross section of the CGO layer thermally etched, showing well densified CGO with grain sizes in the range of 0.5 to 1.5 µm. **Fig. 6** (d) shows the porous Ni-CGO layer. The grains in this layer are well interconnected with high open porosity and an average grain size of 1-1.5 µm. The MgO support layer did not show any evidence of anisotropy in the porosity distribution (see **Fig. 6** (e)). The measured porosity of the MgO layer was 42 % and the observed mean grain size was 2-3 µm. From **Fig. 6** (b), it can be seen that some densification has occurred at the interface due to strong interaction between NiO and MgO. It is reported in the literature that the Ni/MgO phase exhibits high catalytic activity in POM (partial oxidation of methane) operation as elemental nickel can be dispersed uniformly in the interface and eventually enhance the catalytic reaction [35]. Hence, the occurrence of densification in the interface will not affect the membrane performance. On the other hand it also improves the mechanical stability between the interfaces of the MgO and the Ni-CGO layers which was confirmed by SEM image shown in **Fig. 9** in which the crack was observed inside Ni-CGO layer and not in the interface. **Table 2** shows the mean thicknesses of the membrane functional layer measured from SEM cross sections.

Table 2. The measured thicknesses of functional layers through SEM images

Layer	MgO	Ni-CGO	CGO-M	CGO-P
Thickness (µm)	819±11	28±0.6	31±0.5	23±1.0

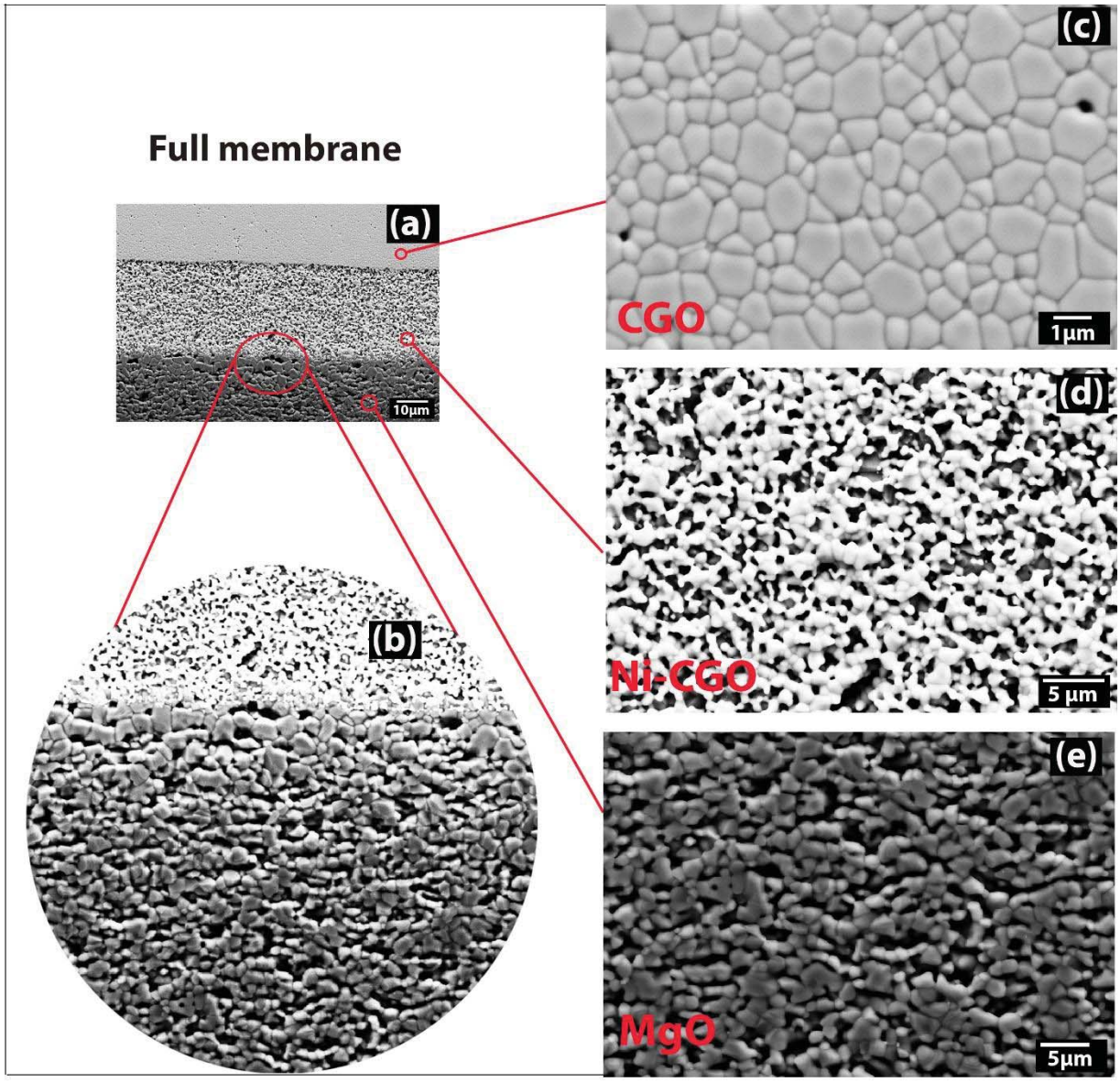

Fig. 6: SEM Micrographs of thermally etched surfaces of three different layers (a) full membrane, (b) interface of the Ni-CGO and MgO porous layer after reduction, (c) dense CGO layer, (d) porous NiO-CGO layer and (e) porous MgO layer.

3.4 Oxygen flux measurements in asymmetric MgO supported CGO membranes

The performance of fully assembled, asymmetric multi-layer membranes based on MgO support and the CGO membrane and catalytic layers was finally determined by oxygen permeation measurements, as described in section 2.3.

For testing the quality of the sealing (between the membrane sample and the transition pieces connecting it with the test rig), the test rig was first heated with 500 Nml min^{-1} air on the outside of the tube to a temperature of 917 °C and then cooled to 650 °C. At 652 °C nitrogen was flowed on the inside of the tube with 100 Nml min^{-1}. The pO_2 of the inlet was 2.6×10^{-5} atm and the outlet showed a pO_2 of 2.5×10^{-4} atm, corresponding to a flux of 2.1×10^{-3} Nml min^{-1} cm^{-2}. The low oxygen flux indicates that as expected the CGO membrane does not have high electronic conductivity at relatively oxidizing conditions at low temperature and also shows that only small amounts of oxygen leaks into the permeate stream.

By subjecting the CGO membrane to very fast changes in the oxygen partial presseure one can risk failure due to the chemical expansion. A slow change is therefore preferred as the membrane may relax to some extend via creep. The membrane was therefore first reduced with humidified hydrogen (app. 3 %) diluted with nitrogen at 650 °C. This was followed by varying the temperature and increasing the hydrogen flow and decreasing the nitrogen flow (see **Fig. 7**). **Fig. 7** shows the oxygen flux of the membrane as a function of the reciprocal temperature for different flows of nitrogen and humidified hydrogen. At approximately 800°C the gas mixture was changed from 50 Nml H_2:50 Nml N_2 to 100 Nml H_2:50 Nml N_2. This result in an increase in the oxygen flux and is marked on **Fig. 7**. as an activation of the membrane.The activation is attributed to an increased performance of the permeate activation layer containing Ni and it is not considered unlikely that it is first at this point the permeate activation layer is fully reduced. There is a clear thermal dependence of the oxygen flux and in pure hydrogen the activation energy of the flux is 82.3 kJ mol^{-1}. It is clearly seen that for an increasing inlet hydrogen concentration the oxygen flux also increases, which is attributed to an increase in driving force over the membrane resulting from the increased hydrogen concentration present in the permeate activation layer.

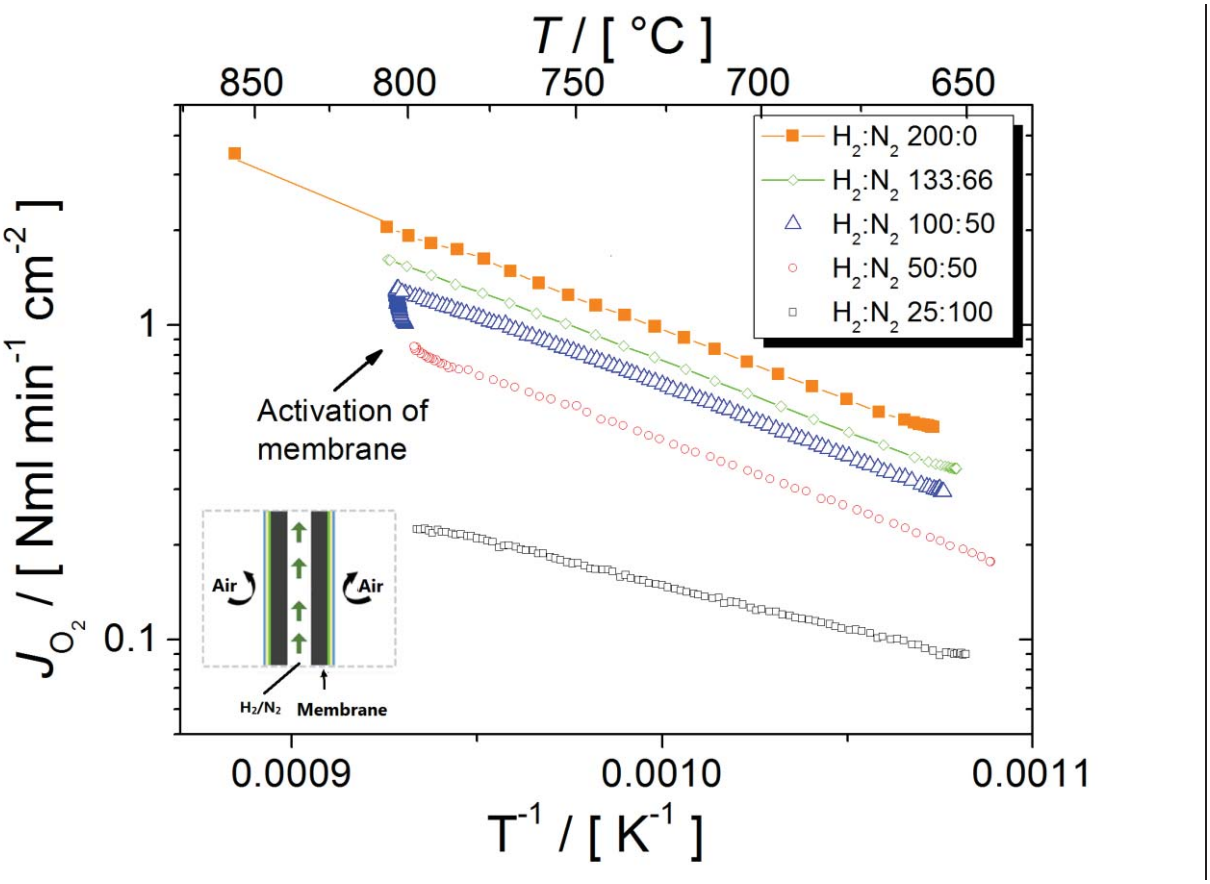

Fig. 7: Flux as function of reciprocal temperature for different hydrogen/nitrogen mixtures. The numbers in the caption all refer to the inlet volume flow of hydrogen and nitrogen in the unit Nml min^{-1}.

The membrane was also heated to higher temperatures than 856 °C in pure hydrogen. However, this resulted in significant condensation in the tubing leading to an unstable signal on the pO_2-sensor downstream the membrane, wherefore the flux values are highly scattered. There was, however, nothing that indicated that the Arrhenius dependency observed for the oxygen flux (see **Fig. 7**) changed. The membrane was held for approximately 80 h in pure hydrogen at 856 °C (±2 °C) without a measurable degradation in the flux.

Heating from 856 °C to 920 °C also resulted in a significantly higher flux, however, this was followed by a rapid deterioration of the flux, to a level below the 856 °C level. This large decrease is tentatively assigned to a coarsening effect of the Ni-CGO layer on the permeate side of the membrane. As it has previously been shown [36] that a redox-cycling of the anode of a solid oxide fuel cell can lead to an improved performance, this was also tried here. The sample was cooled to 650 °C and the anode was oxidized with air (approximately 24 h) and subsequently reduced again with hydrogen. **Fig. 8** shows the flux as a

function of reciprocal absolute temperature prior to the high temperature treatment, after the high temperature treatment and after the redox-cycle. The permeate gas is in all cases 3 % humidified hydrogen. It is clear that the redox-cycling of the permeate Ni-CGO layer improves the oxygen flux through the membrane dramatically from 0.5 Nml min^{-1} cm^{-2} to 1.4 Nml min^{-1} cm^{-2} at 660 °C. Interestingly the activation energy changes from 68.6 kJ mol^{-1} (after the high temperature treatment) to 53.3 kJ mol^{-1} (after the redox-cycle). The flux reported in **Fig. 7** is thus to a large extend limited by the Ni-activation layer on the permeate side of the membrane. The observed activation energy of 53.3 kJ mol^{-1} is significantly below that of both typical anode processes and cathode processes [11,37]. It is in the range of theat expected for ionic conduction through the CGO membrane, however, it seems unlikely that the flux is limited by the ionic conductivity through the membrane [38] , It is more likely that the low activation energy is an artifact due to the Ni-electrode re-coarsening when increasing the temperature.

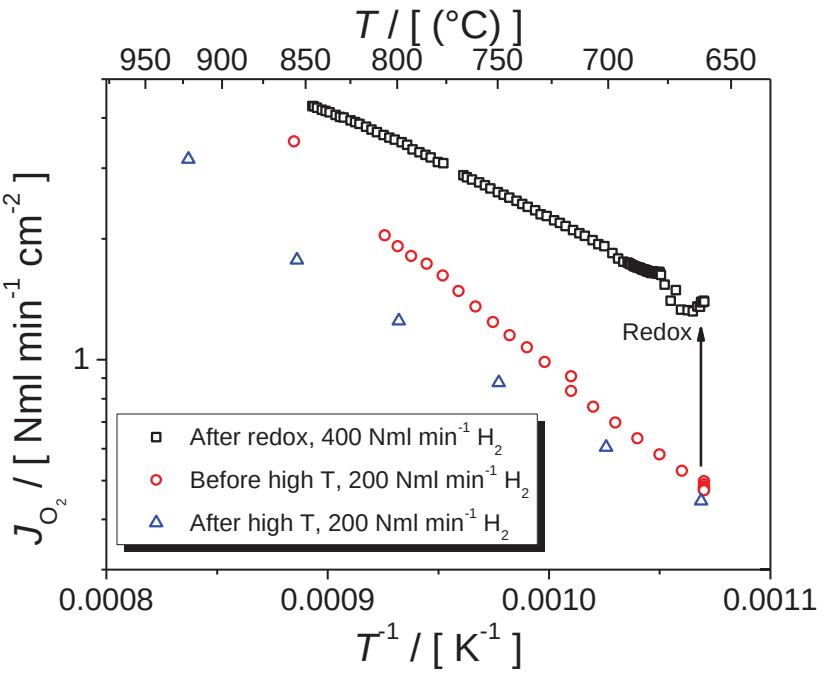

Fig. 8: Flux as a function of reciprocal temperature for three measurement series. Before a high temperature heat treatment at 920 °C, after a high temperature treatment at 930 °C and finally after the high temperature treatment but after a redox-cycling (air for 24 h) of the membrane component at 650 °C.

After the hydrogen tests the membrane was subjected to a mixture of methane (50 ml min^{-1}) and humidified hydrogen (3 % steam) (50 ml min^{-1}) even though this is well within a carbon forming regime,

however, the flow from the membrane terminated after approximately 30 min of operation indicating a failure of the membrane.

Fig. 9 shows micrographs of asymmetric tubular CGO membrane after oxygen permeation tests and removal from the test housing. After the full treatment cycle, including tests in methane, the CGO membrane layer has completely detached from the porous MgO support within the porous Ni-CGO layer. The SEM analysis supports that carbon formation at the Ni-CGO activation layer could be a likely reason for the failure observed [39].

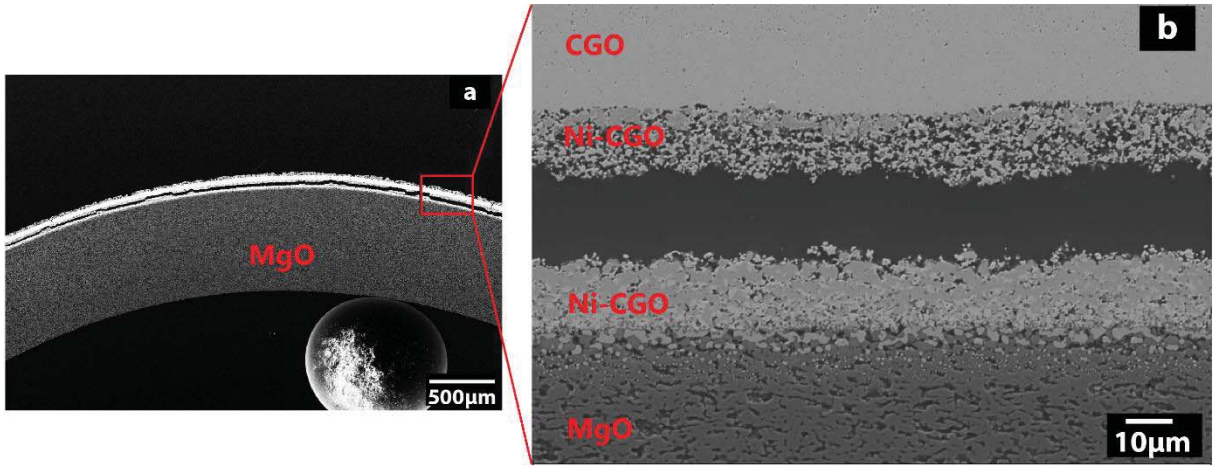

Fig. 9: SEM micrograph of the MgO supported CGO10 membrane after testing and removal from the test housing. After testing, a complete detachment of layers occurs in between NiO-CGO layer due to inter-diffusion and propitiation of Ni particles on MgO layer.

Conclusion

An asymmetric tubular CGO membrane has successfully been prepared by an extrusion and dip-coating process. A gas-tight CGO membrane with a thickness of about 30 µm was obtained. The optimized de-bindering and sintering regime with a very slow heating rate of 0.25 °C min^{-1} and 0.5 °C min^{-1} was used to achieve gas tight thin membranes and desired porosity within catalytic and porous support layers. The MgO supported asymmetric CGO membrane resulted in an oxygen permeation flux of 3.5 Nml min^{-1} cm^2 at temperature of 856 °C with sweep gas (H_2) at a flow rate of 200 Nml min^{-1}. A redox-cycle of the Ni-CGO catalytic layer improved the permeation flux of the membrane, reaching 4 Nml min^{-1} cm^2 at 850 °C. A decrease of activation energy suggest that this improvement in performance is due to an improved catalytic activity of the Ni-CGO structure after redox-cycle. Performance tests in methane/humidified

hydrogen mixtures indicated the occurrence of anode layer detachment most likely due to carbon formation.

Acknowledgement

The authors would like to thank the Danish Council for Independent Research Technology and Production Sciences (FTP) which is part of The Danish Agency for Science, Technology and Innovation (FI) (Project # 09-072888) for sponsoring the OPTIMAC research work.

References

[1] J. Sunarso, S. Baumann, J.M. Serra, W.A. Meulenberg, S. Liu, Y.S. Lin, et al., Mixed ionic – electronic conducting (MIEC) ceramic-based membranes for oxygen separation, 320 (2008) 13–41.

[2] A. Kaiser, et al., Evaluation of thin film ceria membranes for syngas membrane reactors—Preparation, characterization and testing, J. Memb. Sci. 378 (2011) 51–60.

[3] P.I. Cowin, C.T.G. Petit, R. Lan, J.T.S. Irvine, S. Tao, Recent Progress in the Development of Anode Materials for Solid Oxide Fuel Cells, Adv. Energy Mater. 1 (2011) 314–332.

[4] B. Steele*, Materials for IT-SOFC stacks 35 years R&D: the inevitability of gradualness?, Solid State Ionics. 134 (2000) 3–20.

[5] W.. Zhu, S.. Deevi, A review on the status of anode materials for solid oxide fuel cells, Mater. Sci. Eng. A. 362 (2003) 228–239.

[6] S.P. Jiang, S.H. Chan, A review of anode materials development in solid oxide fuel cells, J. Mater. Sci. 39 (2004) 4405–4439.

[7] D. a. Macedo, G.L. Souza, B. Cela, C. a. Paskocimas, A.E. Martinelli, F.M.L. Figueiredo, et al., A versatile route for the preparation of Ni–CGO cermets from nanocomposite powders, Ceram. Int. 39 (2013) 4321–4328.

[8] M. Pihlatie, Stability of Ni–YSZ composites for solid oxide fuel cells during reduction and re-oxidation, n.d.

[9] F. Jtilich, D.- Jtilich, Thermal Expansion of SOFC Materials, 5 (1999) 129–139.

[10] A. Petric, P. Huang, F. Tietz, Evaluation of La – Sr – Co – Fe – O perovskites for solid oxide fuel cells and gas separation membranes, 135 (2000) 719–725.

[11] a. Samson, M. Søgaard, R. Knibbe, N. Bonanos, High Performance Cathodes for Solid Oxide Fuel Cells Prepared by Infiltration of $La_{0.6}Sr_{0.4}CoO_{3-\delta}$ into Gd-Doped Ceria, J. Electrochem. Soc. 158 (2011) B650.

[12] B.F. Zhao, R. Peng, C. Xia, LSC-based electrode with high durability for IT-SOFCs, (2008).

[13] O. Buchler, J. Serra, W. Meulenberg, D. Sebold, H. Buchkremer, Preparation and properties of thin $La_{1-x}Sr_xCo_{1-y}Fe_yO_{3-\delta}$ perovskitic membranes supported on tailored ceramic substrates, Solid State Ionics. 178 (2007) 91–99.

[14] S. Baumann, W. a. Meulenberg, H.P. Buchkremer, Manufacturing strategies for asymmetric ceramic membranes for efficient separation of oxygen from air, J. Eur. Ceram. Soc. 33 (2013) 1251–1261.

[15] Z. Chen, Z. Shao, R. Ran, W. Zhou, P. Zeng, S. Liu, A dense oxygen separation membrane with a layered morphologic structure, 300 (2007) 182–190.

[16] M.E. Navarro, X.G. Capdevila, M. Morales, J.J. Roa, M. Segarra, Manufacturing of anode-supported tubular solid oxide fuel cells by a new shaping technique using aqueous gel-casting, J. Power Sources. 200 (2012) 45–52.

[17] U.-J. Yun, J.-W. Lee, S.-B. Lee, T.-H. Lim, S.-J. Park, R.-H. Song, et al., Fabrication and Operation of Tubular Segmented-In-Series (SIS) Solid Oxide Fuel Cells (SOFC), Fuel Cells. 12 (2012) 1099–1103.

[18] Kendall K -SOFC.pdf, (n.d.).

[19] D. Bayraktar, F. Clemens, S. Diethelm, T. Graule, J. Van herle, P. Holtappels, Production and properties of substituted LaFeO3-perovskite tubular membranes for partial oxidation of methane to syngas, J. Eur. Ceram. Soc. 27 (2007) 2455–2461.

[20] C.G. Fan, R.M. Wu, L.Z. Pei, Q.F. Zhang, Effect of Sintering Temperature on the Behavior of Oxygen Permeation for $La_{0.6}Sr_{0.4}Co_{0.2}Fe_{0.8}O_{3-\delta}$ Tubular Membranes, Adv. Mater. Res. 105-106 (2010) 643–646.

[21] C. Delbos, G. Lebain, N. Richet, C. Bertail, Performances of tubular La0.8Sr0.2Fe0.7Ga0.3O3−δ mixed conducting membrane reactor for under pressure methane conversion to syngas, Catal. Today. 156 (2010) 146–152.

[22] H. Wang, Y. Cong, W. Yang, Investigation on the partial oxidation of methane to syngas in a tubular Ba0.5Sr0.5Co0.8Fe0.2O3−δ membrane reactor, Catal. Today. 82 (2003) 157–166.

[23] a. V. Kovalevsky, V.V. Kharton, F.M.M. Snijkers, J.F.C. Cooymans, J.J. Luyten, F.M.B. Marques, Oxygen transport and stability of asymmetric SrFe(Al)O3−δ-SrAl2O4 composite membranes, J. Memb. Sci. 301 (2007) 238–244.

[24] Z. Liu, G. Zhang, X. Dong, W. Jiang, W. Jin, N. Xu, Fabrication of asymmetric tubular mixed-conducting dense membranes by a combined spin-spraying and co-sintering process, J. Memb. Sci. 415-416 (2012) 313–319.

[25] D.K. Ramachandran, F. Clemens, a. J. Glasscock, M. Søgaard, a. Kaiser, Tailoring the microstructure of porous MgO supports for asymmetric oxygen separation membranes: Optimization of thermoplastic feedstock systems, Ceram. Int. 40 (2014) 10465–10473.

[26] D.W. Ni, E. Olevsky, V. Esposito, T.T. Molla, S.P. V. Foghmoes, R. Bjørk, et al., Sintering of Multilayered Porous Structures: Part II-Experiments and Model Applications, J. Am. Ceram. Soc. 96 (2013) 2666–2673.

[27] C. Chatzichristodoulou, M. Søgaard, J. Glasscock, A. Kaiser, S.P.V. Foghmoes, P.V. Hendriksen, Oxygen Permeation in Thin, Dense Ce0.9Gd0.1O1.95-δ Membranes II. Experimental Determination, J. Electrochem. Soc. 158 (2011) F73.

[28] G. Pećanac, S. Foghmoes, M. Lipińska-Chwałek, S. Baumann, T. Beck, J. Malzbender, Strength degradation and failure limits of dense and porous ceramic membrane materials, J. Eur. Ceram. Soc. 33 (2013) 2689–2698.

[29] D.-W. Ni, V. Esposito, C.G. Schmidt, T.T. Molla, K.B. Andersen, A. Kaiser, et al., Camber Evolution and Stress Development of Porous Ceramic Bilayers During Co-Firing, J. Am. Ceram. Soc. 96 (2013) 972–978.

[30] T.T. Molla, H.L. Frandsen, R. Bjørk, D.W. Ni, E. Olevsky, N. Pryds, Modeling kinetics of distortion in porous bi-layered structures, J. Eur. Ceram. Soc. 33 (2013) 1297–1305.

[31] a. Kaiser, a. S. Prasad, S.P. Foghmoes, S. Ramousse, N. Bonanos, V. Esposito, Sintering process optimization for multi-layer CGO membranes by in situ techniques, J. Eur. Ceram. Soc. 33 (2013) 549–556.

[32] J. Baber, a. Klimera, F. Raether, In situ measurement of dimensional changes and temperature fields during sintering with a novel thermooptical measuring device, J. Eur. Ceram. Soc. 27 (2007) 701–705.

[33] T.T. Molla, D.K. Ramachandran, D.W. Ni, F. Teocoli, A. Kaiser, N. Pryds, et al., Constrained Sintering of Bi-layered Tubular Structures, J. Am. Ceram. Soc. Am. Ceram. Soc. (2014).

[34] D.K. Ramachandran, K. Kwok, M. Søgaard, F. Clemens, A.J. Glasscock, A. Kaiser, Design and characterize functional properties of porous MgO supports for oxygen transport membranes, To Be Submitt. (2014).

[35] W. Dong, H. Roh, Z. Liu, K. Jun, S. Park, Hydrogen Production from Methane Reforming Reactions over Ni / MgO Catalyst, 22 (2001) 1323–1327.

[36] N. Oishi, a. Atkinson, N.P. Brandon, J. a. Kilner, B.C.H. Steele, Fabrication of an Anode-Supported Gadolinium-Doped Ceria Solid Oxide Fuel Cell and Its Operation at 550oC, J. Am. Ceram. Soc. 88 (2005) 1394–1396.

[37] T. Ramos, M. Sogaard, M.B. Mogensen, Electrochemical Characterization of Ni/ScYSZ Electrodes as SOFC Anodes, J. Electrochem. Soc. 161 (2014) F434–F444.

[38] C. Chatzichristodoulou, M. Søgaard, P. V. Hendriksen, Oxygen Permeation in Thin, Dense Ce0.9Gd0.1O1.95-δ Membranes I. Model Study, J. Electrochem. Soc. 158 (2011) F61.

[39] H. Timmermann, D. Fouquet, a. Weber, E. Ivers-Tiffée, U. Hennings, R. Reimert, Internal Reforming of Methane at Ni/YSZ and Ni/CGO SOFC Cermet Anodes, Fuel Cells. 6 (2006) 307–313.

Product costing

"Economic analysis of the porous MgO support layer for membrane applications"

1. Organization structure

The organization is structured as a Pvt. Ltd and named **Hi5Cer** Pvt. Ltd, registered as a domestic company under Income-tax Act196 in India. The company is capable of producing porous ceramics material for advanced applications. It produces approx. 36 tones (24 kilo. m^2) of finished goods annually.

1.1. Organization chart

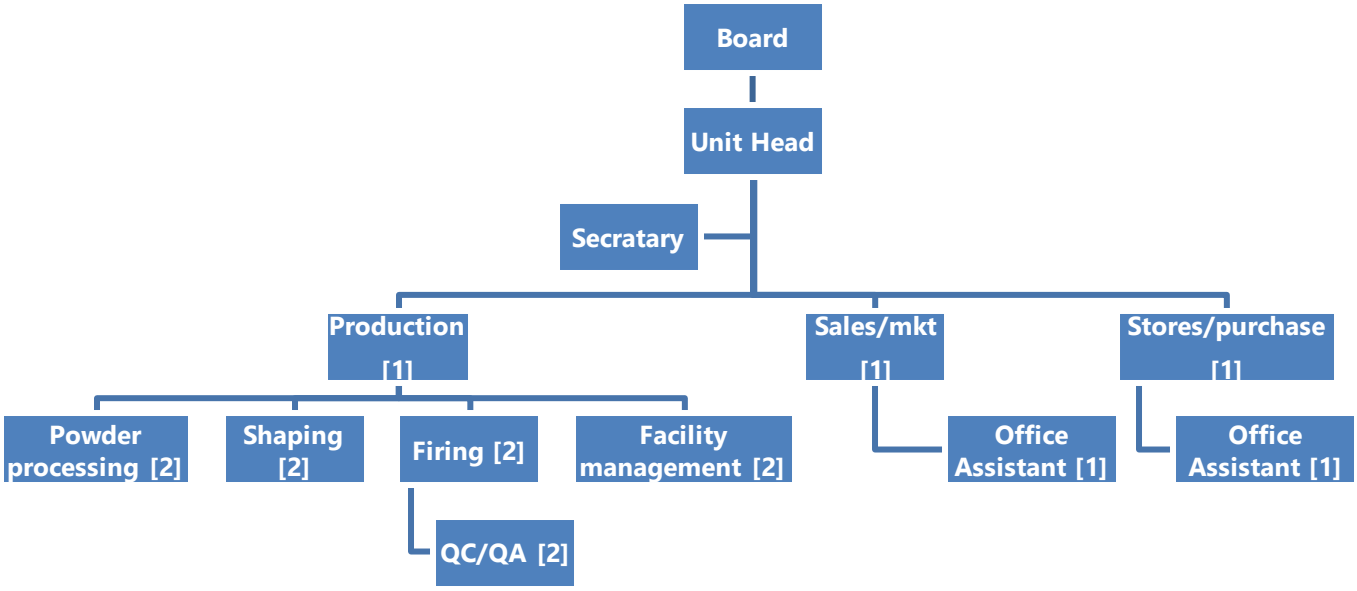

Fig.1: Organization chart of production facility with annual production of 36 MT porous ceramic substrates. The number in square brackets indicates number of man powers involved in a specific role.

2. Cost calculations

This document will describe how the product cost for the porous ceramics materials was calculated by considering a small-sized production facility with a monthly production capacity of approximately 3 tones (2 k. m^2) finished goods.

All costs involved in the production processes should be assessed carefully to make a better estimate on the product cost. The associated costs for this estimate are classified into two broad categories;

1. Direct cost
2. Indirect cost

2.1. Direct cost

The direct cost involves mainly the costs directly associated with the manufacturing of the product, such as material (bill of materials) and routing (operation and manpower) cost. The following section will describe in more detail how these costs were calculated.

2.1.1. Bill of materials (BOM)

The purchasing price of the raw material will normally be based on the consignment size. Table 1 shows the cost of materials based on the procurement of 5 tonnes of materials collectively.

Table: 1 List of required materials and their price.

BOM	Composition Wt%	Cost /kg (DKK)	Total cost (DKK)
M1	60	20	1200
M2	10	40	400
M3	10	30	300
M4	20	30	600
	100	per 100 kg	2500
		per Kg	**25**

2.1.2. Process wastage

In the manufacturing unit, there is always some production waste relating to the processing step. It is important to account for these kind of wastages and to be considered them while calculating the product or production cost.

Table 2: Process wastage at each processing step.

Operation	Percentage
Milling	4-5 %
In-process	8-10 %
At final inspection	5-8 %
Total	**17-23 %**

Table 2 shows that the process steps can be divided into 3 categories, namely: (1) milling, (2) in-process and (3) at final inspection, and indicates the wastage for each group. The process wastage cost for each of the groups was calculated from the raw materials (BOM) cost. Finally, 20 % of the raw materials cost is considered as the total process wastage cost.

2.1.3. Production Estimation

Table 3 shows that the raw materials consumption for daily and monthly production. The associated raw materials cost is 2500 DKK and 75000 DKK for daily and monthly production, respectively.

Table 3: Monthly production estimation and associated raw materials cost.

	Daily production	**Monthly production**
Weight (kg)	100	3000
Surface area (m^2)	66	2000
Material cost (DKK)	**2500**	**75000**

2.1.4. Man power cost

The routing lists the operations needed to manufacture a product. It estimate the costs incurred to complete a successful operation and includes man cost, which is one of the main element to be used to calculate production costs. It must be kept in mind that the company is setup in India, so the salary and remuneration will be considerably lower than at the Danish market.

Table 4: List of man power needed for each functional area and the employees' monthly wages.

	Number	Monthly salary (DKK)	Monthly cost (DKK)	Annual cost (DKK)
Administration				
Unit Head	1	5000	5000	60000
Secretary	1	1200	1200	14400
Production				
1) Highly skilled	1	3400	3400	40800
2) Semi-skilled	7	1500	10500	126000
3) Helpers	3	900	2700	32400
Sale and Marketing				
1) Highly skilled	1	2800	2800	33600
2) Assistant	1	900	900	10800
Commercial				
1) Highly skilled	1	2500	2500	30000
2) Assistant	1	1000	1000	12000
Total	**17**		**30000**	**360000**

2.3. Indirect cost

Indirect costs are grouped under fixed costs, and will usually be constant for a wide range of output and its services that the organization delivers. It may be difficult to determine precisely how the activities of each and every supporting people and indirect costs do not vary substantially within certain production volumes or other indicators of activity. The following are considered to be fixed costs:

Utilities

Rent

Audit and legal services

Administrative staff

Equipment rental

Normally, manufacturing industries follow the rule of thumb of considering the contribution of indirect cost in the product costing to about 40-50 % of the total direct costs.

2.4. Product cost estimation

Table 5 shows the economic anlysis of porous MgO supports for membrane applications. The direct costs involves mainly the costs directly associated with the manufacturing of the product such as the cost of materials, man power and process wastages. Moreover, indirect costs (utilities, rent, audit and administrative staff) are included into the product cost, and are considered to be 50 % of WIP (work in progress) cost. Finally, the membrane cost is assessed to be 150 \$/m^2 including a pricing factor of 10.

Table 5: Porous MgO supports cost analysis from production of a sample size of 2000 m^2

Details	**Price per 2000 m^2 (DKK)**	**Price per m^2 (DKK)**	**Price per m^2 (USD)**
Raw materials cost	75000	37.5	6.25
Process wastage (20 % of RM cost)	15000	7.5	1.25
Man power	30000	15	2.5
Indirect cost (50 % of WIP cost)	60000	30	5.0
Total cost	**180000**	**90**	**15**
Pricing factor	**5-10 times**	**450-900**	**75-150**